

AFCRL-67-0128

DEPARTMENT OF METEOROLOGY
UNIVERSITY OF CALIFORNIA
LOS ANGELES, CALIFORNIA

Diagnostic Studies of Weather Systems
of Low and High Latitudes (Rossby Number < 1)

T. N. Krishnamurti
Principal Investigator

AF 19(628)-4777

Period covered
30 November 1964 - 30 November 1966

Project No. 6698

Task No. 669802

Final Report

DISTRIBUTION OF THIS DOCUMENT IS UNLIMITED

Prepared for

AIR FORCE CAMBRIDGE RESEARCH LABORATORIES
OFFICE OF AEROSPACE RESEARCH
UNITED STATES AIR FORCE
BEDFORD, MASSACHUSETTS 01730

This work was also supported by E.S.S.A. Grant
Number: Cwb 11210, National Meteorological Center
and from N.A.S.A. Grant Number: NsG 237-62

Acquisition Document
SOT

65053
N67-30784 N67-30790
(ACCESSION NUMBER)
363 (PAGES)
AP-650533 (NASA CR OR TMX OR AD NUMBER)
CR 05513
(THRU)
3 (CODE)
20 (CATEGORY)

FACILITY FORM 602

DEPARTMENT OF METEOROLOGY
UNIVERSITY OF CALIFORNIA
LOS ANGELES, CALIFORNIA

Diagnostic Studies of Weather Systems
of Low and High Latitudes (Rossby Number < 1)

T. N. Krishnamurti

Principal Investigator

AF 19(628)-4777

Period covered
30 November 1964 - 30 November 1966

Project No. 6698

Task No. 669802

Final Report

DISTRIBUTION OF THIS DOCUMENT IS UNLIMITED

Prepared for

AIR FORCE CAMBRIDGE RESEARCH LABORATORIES
OFFICE OF AEROSPACE RESEARCH
UNITED STATES AIR FORCE
BEDFORD, MASSACHUSETTS 01730

This work was also supported by E.S.S.A. Grant
Number: Cwb 11210, National Meteorological Center
and from N.A.S.A. Grant Number: NsG 237-62

Abstract

A theory of a general balance model for small Rossby numbers, including effects of latent heat, friction and terrain is presented with some applications in high and low latitudes.

List of Topics

- I. A diagnostic balance model for studies of weather systems of low and high latitudes. (Rossby Number < 1)
- T. N. Krishnamurti 1-41 ✓
- II. A study of a developing wave cyclone.
- T. N. Krishnamurti 1-52 ✓
- III. Numerical calculation of three dimensional trajectories utilizing the balanced horizontal and vertical motions.
- Jan Paegle 1-21 ✓
- ~~IV.~~ A study of a non-developing easterly wave.
- David Baumhefner 1-160 ✓
- ~~V.~~ A study of a developing easterly wave.
- T. N. Krishnamurti and Julia Nogues 1-37 ✓
- VI. A calculation of percentage area covered by convective clouds from moisture convergence.
- T. N. Krishnamurti 1-24 ✓

Project Personnel

Principal Investigator:

1. T. N. Krishnamurti

Graduate Students:

2. David Paul Baumhefner
3. Julia Nogues
4. Jan Paegle
5. Allen Tangren

Undergraduate Students:

6. Steve Esbensen
7. Mike Borowski
8. Peter Baumhefner

Part time Computer Programmers:

9. Ruby Wen
10. Peter Heinrich
11. Robert M. Coie

Drafting Aid:

12. George Apostolides
13. Glen McKenzie

N67 - 30785

A Diagnostic Balance Model for Studies of Weather
Systems of Low and High Latitudes (Rossby Number < 1)

By T. N. Krishnamurti

1. Introduction

A diagnostic balance model can be used to describe the three dimensional motion, temperature, pressure and moisture fields consistent with a system of scaled dynamical equations.

In the following we are presenting dynamical equations that are valid for a small Rossby number theory, Lorenz (1960) and Phillips (1963) have discussed the essential scale analysis and energetics of this system of equations. In the middle latitudes, cyclone scale disturbances belong to this class, namely

$$R_o = U/fL < 1$$

However the possible application of a dynamical system where $R_o > 1$ in low latitudes is questionable.

The model can be applied with considerable confidence to study weather systems of the tropics that are found north of 5° North latitude and that have not reached hurricane strength. There are a large class of tropical disturbances outside of the intertropical convergence zone and the hurricanes where the Rossby number is still < 1 and the expansion theory is hence valid.

In a typical easterly wave, for instance,

$$U \approx 10 \text{ mps}$$

$$f \approx 0.5 \times 10^{-4} \text{ sec}^{-1}$$

$$L \approx 10^6 \text{ meters}$$

$$R_o \approx 0.2 < 1$$

If we deal with disturbances closer to the equator or of wavelengths smaller than a 1000 km or much larger wind speeds then this analysis would not apply.

The types of weather disturbances we deal with here satisfy the criteria of small Rossby number. We will be examining two wave

perturbations in a basic easterly flow, one of which develops into a tropical storm while the other remains undisturbed. In these examples our interest is in the initial-pre hurricane stage. An examination of large scale motion, temperature pressure and moisture distribution is needed for any search of instability mechanism that may be important in the subsequent developments to large Rossby number phenomena.

The diagnostic balance model is a very powerful tool for studying the role of a number of rather complex mechanisms that describe the instantaneous state of the atmosphere. The formulation of the model for the middle latitudes is somewhat different from that in the tropics for at least two essential reasons.

i) The non-divergent stream function of the horizontal velocity field for middle latitude systems can in general be obtained from a solution of a balance equation for a prescribed distribution of the geopotential height field. An analysis of the geopotential height field is not easily possible in the tropics and a wind field is required to obtain a stream function which corresponds to the observed relative vorticity distribution.

ii) Heating functions describing effects of latent heat release can be handled rather easily if dynamical ascent of absolutely stable air is producing condensation. This is generally true of the large scale precipitation from stable non-convective cloud systems. The heating function can in such cases be defined non-zero if,

- i) Atmosphere is absolutely stable.
- ii) Relative humidity is near 100%
- iii) Air is rising on a large scale.

These conditions are generally met in the middle latitudes. In the tropics heating functions have to be defined for convective type of

cloud forms. A formal parameterization of the cumulus-scale heating should perhaps be carried out in somewhat the same way as it is done for studies of tropical storms, e.g. Kuo (1965). In the tropics a heating function may be defined if

- i) Atmosphere is conditionally unstable
- ii) Net moisture convergence in vertical columns > 0 .

While we have separated the middle latitudes and the tropics in two broad categories for defining heating function, in the real atmosphere there is a large overlap generally, and this must be borne in mind in treating weather systems. For instance, along the fronts of a middle latitude cyclonic disturbances all of the tropical conditions will generally be satisfied and a heating function in such regions should be accordingly defined. The problem thus becomes somewhat too complicated. For the present, we have made this broad division between the high and low latitude disturbances.

2. The balance equation

The quasistatic equation of motion with pressure as a vertical coordinate may be written in the form, (A list of symbols appears in Table 1)

$$\frac{\partial \mathbf{W}}{\partial t} + (\mathbf{W} \cdot \nabla) \mathbf{W} + \omega \frac{\partial \mathbf{W}}{\partial p} - f \mathbf{W} \times \mathbf{k} = -g \nabla Z + \mathbf{F} \quad (1)$$

$$\frac{R}{p} \theta \left(\frac{p}{p_0} \right)^{R/C_p} = -g \frac{\partial Z}{\partial p} \quad (2)$$

The continuity equation may be written in the form

$$\nabla \cdot \mathbf{W} = - \frac{\partial \omega}{\partial p} \quad (3)$$

The first law of thermodynamics is expressed by the relation,

$$C_p \frac{T}{\theta} \left[\frac{\partial \theta}{\partial t} + \mathbf{v} \cdot \nabla \theta + \omega \frac{\partial \theta}{\partial p} \right] = H \quad (4)$$

Where H is the diabatic heating per unit mass of air.

In the formulation of a diagnostic balance model, vorticity and divergence equations are derived from equations (1) and (2). From considerations of scale analysis, certain terms involving the time derivatives of divergence and advection by the divergent part of the wind are dropped generally, Lorenz (1960), Phillips (1963).

By defining,

$$W = k \times \nabla \psi - \nabla \chi$$

Where ψ and χ define a stream function and a velocity potential.

We may write the vorticity and the divergence equations by the relations.

$$\begin{aligned} \frac{\partial}{\partial t} \nabla^2 \psi = & -J(\psi, \zeta_a) + \nabla \chi \cdot \nabla \zeta_a + \zeta_a \nabla^2 \chi - \omega \frac{\partial}{\partial p} \nabla^2 \psi \\ & - \nabla \omega \cdot \nabla \frac{\partial \psi}{\partial p} - g \frac{\partial}{\partial p} \left[\frac{\partial \tau_y}{\partial x} - \frac{\partial \tau_x}{\partial y} \right] \end{aligned} \quad (5)$$

$$\nabla \cdot f \nabla \psi = \nabla^2 \phi - 2J\left(\frac{\partial \psi}{\partial x}, \frac{\partial \psi}{\partial y}\right) \quad (6)$$

The frictional force is retained at the 1000 millibar surface, and is defined in terms of stresses τ_x and τ_y .

$$\tau_x = C_D \rho U \sqrt{U^2 + V^2} \quad (7)$$

$$\tau_y = C_D \rho V \sqrt{U^2 + V^2} \quad (8)$$

Where U and V are the total horizontal wind components on a pressure surface. The non-divergent stream function in the following is obtained from equation (6) for a given geopotential ϕ , for the high latitude weather systems. The method of solution is the same as that given in Shuman (1957), except when the equation is hyperbolic over part of the area of interest, in which case we have solved the

equation,

$$\nabla \cdot f \nabla \psi = \nabla^2 \phi - 2 J (U_g, V_g) \quad (9)$$

Comparison of the two stream functions obtained from equations (6) and (9) for an example with no hyperbolic regions showed very slight differences in the stream functions. Equation (9) may hence be used to evaluate the stream function when there are limited hyperbolic regions. The ellipticity condition is frequently expressed by the relation

$$\nabla^2 \psi > f/2 \quad (10)$$

This relation is generally satisfied by the solution over most regions except where the magnitude of the anticyclonic relative vorticity is large. For the low latitude system relative vorticity $\nabla^2 \psi$ is obtained from the analysed wind field (isotach and isogan distribution)

$$\nabla^2 \psi = \frac{\partial V^0}{\partial x} - \frac{\partial U^0}{\partial y} \quad (11)$$

where U^0 and V^0 are the zonal and meridional components of the observed wind. This stream function is then assumed to be related to a geopotential height distribution from the balance equation,

$$\nabla^2 \phi = \nabla \cdot f \nabla \psi + 2 J \left(\frac{\partial \psi}{\partial x}, \frac{\partial \psi}{\partial y} \right) \quad (12)$$

There are several numerical problems that are encountered in the actual solution of these boundary value problems, we shall discuss these in some detail in the other sections.

The thermodynamic energy equation (4) may be combined with an equation of state,

$$\pi = \frac{RT}{p \theta} \quad (13)$$

and a relation for a static stability parameter,

$$\sigma = - \frac{RT}{p\theta} \frac{\partial \theta}{\partial p} = - \pi \frac{\partial \theta}{\partial p} \quad (14)$$

to obtain the following equation,

$$\pi \frac{\partial \theta}{\partial t} = - \pi J(\psi, \theta) + \pi \nabla \chi \cdot \nabla \theta + \sigma \omega + \frac{HR}{C_p p} \quad (15)$$

The ω - equation of a general balance model is obtained by combining equation (5), (6) and (15). It is expressed by the following three equations for ω , χ and $\frac{\partial \psi}{\partial t}$.

$$\begin{aligned} \nabla^2 \sigma \omega + f^2 \frac{\partial^2 \omega}{\partial p^2} &= f \frac{\partial}{\partial p} J(\psi, \zeta_a) + \pi \nabla^2 J(\psi, \theta) \\ &- 2 \frac{\partial}{\partial t} \frac{\partial}{\partial p} J\left(\frac{\partial \psi}{\partial x}, \frac{\partial \psi}{\partial y}\right) - f \frac{\partial}{\partial p} (\zeta \nabla^2 \chi) \\ &+ f \frac{\partial}{\partial p} g \frac{\partial}{\partial p} \left[\frac{\partial \tau_y}{\partial x} - \frac{\partial \tau_x}{\partial y} \right] - \frac{R}{C_p p} \nabla^2 H_L \\ &- \frac{R}{C_p p} \nabla^2 H_S + f \frac{\partial}{\partial p} \left(\omega \frac{\partial}{\partial p} \nabla^2 \psi \right) \\ &+ f \frac{\partial}{\partial p} \left(\nabla \omega \cdot \nabla \frac{\partial \psi}{\partial p} \right) - f \frac{\partial}{\partial p} \left(\nabla \chi \cdot \nabla \zeta_a \right) \\ &- \pi \nabla^2 (\nabla \chi \cdot \nabla \theta) - \beta \frac{\partial}{\partial p} \frac{\partial}{\partial y} \frac{\partial \psi}{\partial t} \quad (16) \end{aligned}$$

$$\nabla^2 \chi = \frac{\partial \omega}{\partial p} \quad (17)$$

$$\begin{aligned} \nabla^2 \frac{\partial \psi}{\partial t} &= - J(\psi, \zeta_a) - g \frac{\partial}{\partial p} \left[\frac{\partial \tau_y}{\partial x} - \frac{\partial \tau_x}{\partial y} \right] \\ &+ \nabla \chi \cdot \nabla \zeta_a + \zeta_a \nabla^2 \chi \\ &- \nabla \omega \cdot \nabla \frac{\partial \psi}{\partial p} - \omega \frac{\partial}{\partial p} \nabla^2 \psi \quad (18) \end{aligned}$$

Equations (16), (17) and (18) are solved by numerical techniques, and a discussion of these solutions is a major part of this report. There are several problems that are encountered in the solution of the equations that are of interest.

- i) Proper boundary conditions for ω , χ , and $\frac{\partial \psi}{\partial t}$.
- ii) Ellipticity of the three equations, validity of boundary value techniques.
- iii) Finite difference analogues of the three equations.
- iv) Formulation of heating terms, sensible and latent heat for stable and unstable situations.
- v) Formulation of surface friction.
- vi) Inclusion of Terrain effects.
- vii) Interpretation of results.

3. The development problem

For a simple quasi-geostrophic theory (adiabatic, frictionless flow) the individual change of vorticity is given by the convergence of mass

$$\frac{d \zeta_a}{d t} = f_o \frac{\partial \omega}{\partial p} \quad (19)$$

Vertical motion in a quasi-geostrophic theory is given by the ω -equation,

$$\nabla^2 \sigma_{(p)} \omega + f_o^2 \frac{\partial^2 \omega}{\partial p^2} = f_o \frac{\partial}{\partial p} \mathbf{W} \cdot \nabla \zeta_a - \nabla^2 \mathbf{W} \cdot \nabla \frac{\partial \phi}{\partial p} \quad (20)$$

The two forcing functions of an ω - equation are:

- i) Differential vorticity advection,
- and ii) Laplacian of thermal advection.

Given the ϕ distribution for several map times the instantaneous distribution of vertical motions can be determined from a

solution of the ω - equation. If three dimensional trajectories are constructed utilizing these velocities then the observed change in vorticity along the trajectory may be related to the computed convergence and we may hence determine the map features that contribute to vertical motions and convergence. Sutcliffe's (1947) and Petterssen's (1956) development criteria are essentially quasi-geostrophic development formula that pursue this sort of reasoning.

In a general balance model this problem becomes somewhat more complicated. Having obtained the ψ and χ distribution of a balance model, the horizontal velocity components

$$U = -\frac{\partial \chi}{\partial x} - \frac{\partial \psi}{\partial y} \quad (21)$$

$$V = -\frac{\partial \chi}{\partial y} + \frac{\partial \psi}{\partial x} \quad (22)$$

and the p - components for several map times may be used to construct three dimensional trajectories, Paegle (1966). Along such trajectories various development terms of the vorticity equation may be tabulated and a listing of various baroclinic mechanisms producing rising motions and convergence can be made. All of this information becomes very useful for studying the storm development problem. This has been a major motivation for pursuing this investigation.

4. Forcing functions of the balance ω - equation

The quasi-geostrophic ω - equation contains two forcing functions, while the general balance ω - equation, presented here, has 12 forcing functions. At first sight it is not quite obvious that an analysis should be carried this far, however as we shall show the contribution by several of these terms is quite large and yields information that is not obtainable from a quasi-geostrophic model.

The forcing functions are:

1. $f \frac{\partial}{\partial p} J(\psi, \zeta_a)$ Differential vorticity advection by the non-divergent part of the wind.
2. $\pi \nabla^2 J(\psi, \theta)$ Laplacian of thermal advection by the non-divergent part of the wind.
3. $-2 \frac{\partial}{\partial t} \frac{\partial}{\partial p} J\left(\frac{\partial \psi}{\partial x}, \frac{\partial \psi}{\partial y}\right)$ We label this term as a differential deformation effect (explained later).
4. $-f \frac{\partial}{\partial p} (\zeta \nabla^2 \chi)$ Differential divergence effects of a balance model.
5. $f \frac{\partial}{\partial p} g \frac{\partial}{\partial p} \left[\frac{\partial \tau_y}{\partial x} - \frac{\partial \tau_x}{\partial y} \right]$ Effects of frictional stresses.
6. $-\frac{R}{C_p p} \nabla^2 H_L$ Effects of latent heat.
7. $-\frac{R}{C_p p} \nabla^2 H_S$ Effects of sensible heat transfer from water surfaces to the atmosphere.
8. $f \frac{\partial}{\partial p} \left(\omega \frac{\partial}{\partial p} \nabla^2 \psi \right)$ Differential vertical advection of vorticity.
9. $f \frac{\partial}{\partial p} \left(\nabla \omega \cdot \nabla \frac{\partial \psi}{\partial p} \right)$ Differential turning of vortex tubes.
10. $-f \frac{\partial}{\partial p} \{ \nabla \chi \cdot \nabla \zeta_a \}$ Differential advection of vorticity by the divergent part of the wind.
11. $-\pi \nabla^2 \{ \nabla \chi \cdot \nabla \theta \}$ Laplacian of thermal advection by the divergent part of the wind.
12. $-\beta \frac{\partial}{\partial p} \frac{\partial}{\partial y} \frac{\partial \psi}{\partial t}$ Contribution by the beta term of the vorticity equation.

The complete problem is solved with and without terrain effects to estimate terrain contribution. It might have been desirable to include the terrain effects as an internal forcing function. The pressure frame (x, y, p) is somewhat artificial near the lower

boundary due to reduction of data to sea level, and this boundary condition at best is only a compromise for the real problem of up and down-slope motion of air. An earth frame, where the earth's surface is a coordinate surface, would be more desirable for inclusion of terrain boundary condition, but the problem becomes many times more complicated when all the terms of the balance model are retained.

The problem, as we have posed^{it}/, contains 12 internal forcing functions and one external forcing function.

In all cases the following qualitative rule is found important for interpreting vertical motion contribution. If a forcing function F_i is greater than zero then in the vicinity of this region its contribution will be rising motions. There are exceptions to this rule but generally this is true.

It is thus easy to verify the relation between rising and sinking motion and the vorticity and thermal advection patterns. Synoptic experience and results of simple quasi-geostrophic ω -equation solutions have verified the inverse relationship between these forcing functions and the sign of rising or sinking motion. It must however be noted that the two terms of the quasi-geostrophic theory do not exactly correspond to the first two terms of a balance model. The stream function for the former case is the geostrophic stream function $\frac{gZ}{f_0}$ while for the later case it is the balance non-divergent stream function. Besides, in the quasi-geostrophic theory f is replaced by f_0 and the static stability σ is a function of pressure only, while in the balance model the contribution from the first two terms arise for variable f and $\sigma(x, y, p)$.

A qualitative interpretation of terms 1,2,8,9,10 and 11 can be made in a similar manner. The heating terms 6 and 7 will be positive if H_L and H_S are positive and will in general contribute

rising motions. The forms of these functions H_L and H_S are discussed in a separate section. Frictional stresses (term 5) will contribute rising motions in regions of cyclonic relative vorticity and sinking motions in regions of anticyclonic relative vorticity.

The deformation and the divergence terms (3 and 4) do not appear in the quasi-geostrophic theory but are large (as we shall demonstrate later) and their interpretation is somewhat difficult.

$$\text{Let } D_1 = \frac{\partial U_\psi}{\partial x} - \frac{\partial V_\psi}{\partial y} \quad (23)$$

$$\text{and } D_2 = \frac{\partial V_\psi}{\partial x} + \frac{\partial U_\psi}{\partial y} \quad (24)$$

define the two components of the deformation field. Then we can show that

$$-(\nabla^2 \chi)^2 D_1^2 + D_2^2 - \zeta^2 = -4 J(U_\psi, V_\psi) \quad (25)$$

In the vicinity of intensifying frontal zones the magnitude of deformation generally increases and the contribution by the term

$-2 \frac{\partial}{\partial t} \frac{\partial}{\partial p} J(U_\psi, V_\psi)$ will be expected to be large. Much further analysis of this term is needed.

The divergence term strongly modifies the vertical motion distribution produced by the leading 2 terms in regions where ζ is large. This is easy to see from the form of the forcing function,

$-f \frac{\partial}{\partial p} \zeta \nabla^2 \chi$. Let $\zeta > 0$ in a region of strong sinking motion at low levels $\zeta \nabla^2 \chi < 0$ and at upper levels $\zeta \nabla^2 \chi > 0$, hence

$-f \frac{\partial}{\partial p} \zeta \nabla^2 \chi > 0$ and will contribute rising motion and oppose the two leading terms. The converse holds in regions of strong rising motions.

The β term (12) is the least important of all of the terms listed above.

We have not included any radiative effects in the analysis presented here, the assumption has been that measures of the instantaneous tendencies of atmospheric variables for synoptic scale motions can be made without invoking these effects. This may prove to be wrong. We shall next discuss some of the more detailed aspects of heating, friction and terrain effects in the model.

5. The heating function of the ω - equation

In the ω - equation the forcing function of heating terms is written in the form,

$$F_H = - \frac{R}{C_p} \nabla^2 H \quad (26)$$

where H is defined through the first law of thermodynamics as the rate of heating per unit mass of air

$$C_p \frac{T}{\theta} \frac{d\theta}{dt} = H \quad (27)$$

In our analysis we have restricted H to contain the effects of sensible heat transfer from the water surfaces H_S , and the effects of release of latent heat H_L in the free atmosphere, thus $H = H_S + H_L$.

a) Sensible heat

Transfer of sensible heat from ocean surface is very important in examples of strong polar outbreaks of cold air over warm oceans. We have included a heat flux equation defined by the empirical relation,

$$F_S = C (T_w - T_a) V \quad (28)$$

Jacobs (1951) used a value $C = 4.7 \times 10^{-3}$, when the units of the various quantities are,

$$F_S \approx \text{cal/cm}^2/\text{minute}$$

$$V \approx \text{meters/sec}$$

$$T_w - T_a \approx {}^\circ\text{C}$$

The rate of heating H_S is measured as a convergence of flux, i.e.

$$H_S = g \frac{\partial F_S}{\partial p} \quad (29)$$

We have assumed $F_S = 0$ above the 900 millibar in our studies, thus the forcing function for the ω - equation at the 900 millibar surfaces has the form,

$$\begin{aligned} F_{HS} &= - \frac{R}{C_p p} g \nabla^2 \frac{F_{S(1000)}}{\Delta p} \\ &= - \frac{R g}{C_p p \Delta p} \nabla^2 F_{S(1000)} \end{aligned} \quad (30)$$

The forcing function has dimension $\text{sec}^{-3} \text{mb}^{-1}$, thus F_S should have the dimension millibar meter sec^{-1} . Hence we may write,

$$F_S = 32.9 \times 10^{-3} V(T_w - T_a) \text{ mb meter sec}^{-1} \quad (31)$$

and

$$F_{HS} = 4.5953 \times 10^{-7} \nabla^2 V(T_w - T_a) \text{ in units of sec}^{-3} \text{mb}^{-1}. \quad (32)$$

A crude measure of the vertical velocity near the 1000 millibar surface can be made by writing,

$$\omega_S = - \frac{4.5953 \times 10^{-7}}{\sigma} V(T_w - T_a) \text{ in units of mbs/sec.} \quad (33)$$

If we assume typical values of the wind speed ($V = 10 \text{ mps}$), sea-air temp difference ($T_w - T_a = 1^\circ\text{C}$) and static stability ($\sigma = 0.02 \text{ meter}^2 \text{ sec}^{-2} \text{ mb}^{-2}$) then we obtain,

$$\omega_S \approx - 2.3 \times 10^{-4} \text{ mb/sec}$$

which is a rising motion of about 0.3 cm/sec . The corresponding convergence $\frac{\partial \omega_S}{\partial p}$ and rate of production of vorticity at the sea

level will thus be a small quantity. In strong polar outbreaks V can be as large as 25 mps and $(T_w - T_a)$ as large as 10°C , and σ may be quite variable, corresponding contribution to vertical motions near the 1000 millibar surface may well exceed 1 cm/sec. In our studies the forcing function for the sensible heat is given by the expression,

$$F_{HS} = -4.5953 \times 10^{-7} \nabla^2 V(T_w - T_a). \quad (34)$$

In the non-linear balance model static stability is permitted to vary in the $x - y - p$ space thus a realistic measure of the effect of sensible heat is possible. It must however be noted that the empirical coefficients of the Jacobs transfer formula are not very reliable and such calculations need considerable refinement.

b) Latent heat

The following static stability parameters are relevant to our studies.

$$\sigma = - \frac{RT}{p \theta} \frac{\partial \theta}{\partial p} \quad (\text{dry}) \quad (35)$$

and
$$\sigma_e = - \frac{RT}{p \theta_e} \frac{\partial \theta_e}{\partial p} \quad (\text{moist}) \quad (36)$$

where θ_e is the equivalent potential temperature defined by the relation,

$$\theta_e = \theta_e^{Lq_S/C_p T} \quad (37)$$

The relation between σ_e and σ is given by the approximate relation,

$$\sigma_e = \sigma - \frac{RL}{C_p p} \frac{\partial q_S}{\partial p} \quad (38)$$

Since $\frac{\partial q_S}{\partial p}$ is large in the lower latitudes and in the lower troposphere below 700 mbs generally, σ_e can be negative or

positive depending on the magnitude of the second term in equation (38). According to parcel ascent considerations we define stability by the inequalities;

- | | |
|-------------------|-------------------------|
| i) $\sigma > 0$ | Absolutely stable. |
| $\sigma_e > 0$ | |
| ii) $\sigma > 0$ | Conditionally unstable. |
| $\sigma_e < 0$ | |
| iii) $\sigma < 0$ | Absolutely unstable. |
| $\sigma_e < 0$ | |

The dry static stability is regarded as a function $\sigma(p)$ in quasi-geostrophic models. In the non-linear balanced model static stability is permitted to vary in the three dimensions.

In our studies of synoptic scale motions we do not have to deal with absolutely unstable regions, but inequalities i) and ii) do appear. Middle latitude temperature distributions are characterized by relation i), and tropical flow below 700 mbs satisfy the relation ii) generally. In summer large areas of the lower troposphere as far north as 40° latitude can be conditionally unstable, and in winter time during periods of strong polar outbreaks tropical latitudes may be absolutely stable on the synoptic scale.

For the absolutely stable case we define a heating function H_L by the relation,

$$H_L = -L \omega \frac{\partial q_s}{\partial p} \quad (39)$$

provided the air is near saturated, rising and $\sigma_e > 0$. Since the effective static stability is positive, the ω equation remains elliptic. For the conditionally unstable case we evaluate a heating function by parameterizing the sub-grid scale heating as a function of the net convergence of moisture on the synoptic scale, essentially along the

lines of Charney and Eliassen (1964), or Kuo (1965).

$$\text{Let } I = \frac{1}{g} \int_{p_B}^{p_T} \nabla \cdot q \nabla p - \frac{\omega_B q_B}{g} \quad (40)$$

I gives a measure of net convergence of moisture in vertical columns extending from the top of the friction layer (subscript B) to the top of the atmosphere (subscript T).

The corresponding heating function H_L may be written as,

$$H_L = L g \frac{1}{q_{SB}} \frac{\partial q_S}{\partial p} A I \quad (41)$$

where A is an arbitrary coefficient, and measures the fraction of I that will go into the formation of convective elements. A direct calculation of this coefficient can be made in a manner shown by Kuo (1965), as we show in another section Krishnamurti (1966). The corresponding forcing function is given by the expression,

$$-\frac{R}{C_p p} \nabla^2 H_L = -\frac{RLg}{C_p p} \nabla^2 \frac{1}{q_{SB}} \frac{\partial q_S}{\partial p} A I \quad (42)$$

This relation was used in the tropical investigations discussed in this report.

In Kuo's formulation H is expressed by the relation,

$$H = \frac{C_p}{\Delta t} a (T_S - T) ,$$

where T_S , Δt and a are defined in Krishnamurti (1966).

Hence we may write:

$$\text{Forcing function} = -\frac{R}{p \Delta t} \nabla^2 a (T_S - T) \quad (43)$$

A crude measure of large scale vertical velocity arising from the parameterization of cumulus scale motion may be obtained by equating,

$$\nabla^2 \sigma \omega \approx - \frac{R}{p \Delta t} \nabla^2 a (T_S - T)$$

or

$$\omega \approx - \frac{R}{p \Delta t \sigma} a (T_S - T)$$

Typical magnitudes are:

$$R \approx \frac{2000}{7} \text{ meter}^2 \text{ sec}^{-2} \text{ degree}^{-1}$$

$$p \approx 500 \text{ mb}$$

$$\Delta t \approx 7200 \text{ sec}$$

$$\sigma \approx 0.02 \text{ meter}^2 \text{ sec}^{-2} \text{ mb}^{-2}$$

$$a \approx 0.05$$

$$T_S - T \approx 1 \text{ degree}$$

Hence

$$\omega \approx -2 \times 10^{-4} \text{ mb/sec}$$

or

$$W \approx 0.25 \text{ cm/sec rising motion}$$

The corresponding mid tropospheric vertical velocity is very small. Formal solutions of ω - equations (without the crude approximations) do indeed yield vertical motion of this order or somewhat smaller in most of the tropical investigations we have investigated.

6. Surface friction

The contribution by friction is introduced in the vorticity and the ω equations by defining a surface stress at the 1000 millibar surface according to relations,

$$\tau_x = C_D \rho U \sqrt{U^2 + V^2}$$

$$\tau_y = C_D \rho V \sqrt{U^2 + V^2}$$

where C_D is a non-dimensional drag coefficient assumed equal to 2.5×10^{-3} . The local change of relative vorticity by the frictional stress is given by the relation,

$$\left(\frac{\partial}{\partial t} \nabla^2 \psi \right)_F = \frac{\partial}{\partial x} \left(-g \frac{\partial \tau_y}{\partial p} \right) - \frac{\partial}{\partial y} \left(-g \frac{\partial \tau_x}{\partial p} \right)$$

The corresponding forcing function for the ω - equation is given by the relation

$$\begin{aligned} F_F &= -f \frac{\partial}{\partial p} \left(\frac{\partial}{\partial t} \nabla^2 \psi \right)_F \\ &= fg \left[\frac{\partial^3 \tau_y}{\partial x \partial p^2} - \frac{\partial^3 \tau_x}{\partial y \partial p^2} \right] \end{aligned} \quad (44)$$

$\left(\frac{\partial}{\partial t} \nabla^2 \psi \right)_F$ is estimated at the 1000, 800, 600, 400 and 200 millibar surfaces, while F_F is evaluated at the 900, 700, 500 and the 300 millibar surfaces. The pressure derivative of the stress is evaluated by assuming the stress to vanish at the 900 millibar surface and above. The equation for $\left(\frac{\partial}{\partial t} \nabla^2 \psi \right)_F$ and F_F may, for convenience, be expressed in the form:

$$\begin{aligned} \left(\frac{\partial}{\partial t} \nabla^2 \psi \right)_F &= g \left[\frac{\partial}{\partial y} \frac{\tau_x}{100} - \frac{\partial}{\partial x} \frac{\tau_y}{100} \right] \\ &= \frac{10 C_D g}{R} \left[\frac{\partial}{\partial y} \frac{U \sqrt{U^2 + V^2}}{T} - \frac{\partial}{\partial x} \frac{U \sqrt{U^2 + V^2}}{T} \right] \end{aligned} \quad (45)$$

and

$$F_F = -\frac{f C_D g}{10 R} \left[\frac{\partial}{\partial y} \frac{U \sqrt{U^2 + V^2}}{T} - \frac{\partial}{\partial x} \frac{V \sqrt{U^2 + V^2}}{T} \right] \quad (46)$$

The quantity in the brackets is evaluated from the divergent and the non-divergent component of the wind and the temperature at the 1000 millibar surface. The manner by which the divergent part of the wind is evaluated in successive approximation procedure is discussed in another section. Since the choice of the value of the drag coefficient is very important in equations (45) and (46), it is somewhat unfortunate that a value based on earlier studies is the best that can be done at this stage. This is not very critical for middle latitude storms where, as we shall see, frictional vertical motion in cyclonic disturbances is around 1-2 cm/sec at the lower levels and damps very rapidly with height. This vertical motion is generally overpowered by the vertical motions induced by the baroclinic dynamics and latent heat. This effect however becomes very important in the tropics because low level wind speeds still are about the same order (10 mps) density of air is still about the same and for a drag coefficient of 2.5×10^{-3} units, vertical velocities produced by frictional stresses are of the same order or larger than those produced by the weak baroclinic dynamics of the tropical weather systems.

7. Terrain (up and downslope) vertical motions

Terrain effect is introduced at the 1000 mb surface as a lower boundary condition,

$$\begin{aligned} \omega_T &= -g \frac{1000}{RT} \left[U \frac{\partial h}{\partial x} + V \frac{\partial h}{\partial y} \right] \\ &= -g \frac{1000}{RT} \left[J(\psi, h) - \nabla \chi \cdot \nabla h \right] \end{aligned} \quad (47)$$

where T , ψ and χ are the values at the 1000 millibar surface and h is a smoothed terrain height obtained from a study of Berkofsky and Bertoni (1955). ω_T was used as a lower boundary condition in our studies at the 1000 millibar surface during the relaxation of the ω equation. This lower boundary effect varies each time a new value of χ is estimated, the second term is generally much smaller than the first, and a numerical scheme exhibits a rapid convergence. (A discussion of the manner in which ψ , ω , χ and $\frac{\partial \psi}{\partial t}$ are evaluated is given elsewhere.)

8. Map projection--grid mesh lengths

The tangent plane equations are integrated over a lambert conformal map projection or a Mercator map projection in our studies.

a) Lambert conformal projection

Map factor M is given by the relation,

$$M = \frac{0.5}{\sin(90 - \bar{\phi})} \left[\frac{\tan \{ (90 - \bar{\phi})/2 \}}{0.2679} \right]^{0.716} \quad (48)$$

where $\bar{\phi}$ is the latitude. $M = 1$ for $\phi = 30$ or 60 degrees.

Distances on the earth's surface DX and DY , along the zonal and meridional directions are divided by M to obtain distances in the map projection. In these studies $DX = 2.5$ degrees longitude and $DY = 2.5$ degrees latitude.

b) Mercator map projection

The corresponding expression for M is given by the relation,

$$M = \sin 85 \operatorname{cosec} (90 - \bar{\phi}) \quad (49)$$

In these studies $DX = 2$ degrees longitude and $DY = 2$ degrees latitude.

In the dynamical equation, map projection modifies the differential operators, e.g.

Earth	\equiv	Map
$\frac{\partial}{\partial x}$	\equiv	$M \frac{\partial}{\partial x}$
$\frac{\partial}{\partial y}$	\equiv	$M \frac{\partial}{\partial y}$
$\frac{\partial^2}{\partial x^2}$	\equiv	$M^2 \frac{\partial^2}{\partial x^2} + M \frac{\partial M}{\partial x} \frac{\partial}{\partial x}$
$\frac{\partial^2}{\partial y^2}$	\equiv	$M^2 \frac{\partial^2}{\partial y^2} + M \frac{\partial M}{\partial y} \frac{\partial}{\partial y}$

These operators are used throughout these studies in a consistent manner.

Along the zonal (X) direction there are 33 grid points, along the meridional (Y) direction there are 15 grid points and 5 levels in the vertical direction.

9. The concept of partitioning of various effects in diagnostic balanced models

Consider the system of partial differential equations,

$$\nabla^2 \sigma \omega + f^2 \frac{\partial^2 \omega}{\partial p^2} = A(\psi) + B(\psi) + L_1(\omega, \chi, \frac{\partial \psi}{\partial t}, \psi) +$$

$$L_2(\omega, \chi, \frac{\partial \psi}{\partial t}, \psi) + \dots + L_n(\omega, \chi, \frac{\partial \psi}{\partial t}, \psi)$$
(50)

$$\nabla^2 \chi = \frac{\partial \omega}{\partial p}$$
(51)

$$\nabla^2 \frac{\partial \psi}{\partial t} = M_1(\omega, \chi, \psi) + M_2(\omega, \chi, \psi) + \dots +$$

$$M_n(\omega, \chi, \psi).$$
(52)

where $A(\psi)$, $B(\psi)$ are the leading forcing function of the problem and $\psi(x, y, p)$ is prescribed. $L_1, L_2, L_n, M_1, M_2, \dots, M_n$ are operators defining various terms of a general balance problem.

The corresponding quasi-geostrophic problem is defined by a single equation

$$\nabla^2 \sigma(p) \omega + f_o^2 \frac{\partial^2 \omega}{\partial p^2} = A(\psi) + B(\psi) \quad (53)$$

For homogeneous boundary conditions,

$$\omega = 0 \quad \text{at } x = x_1, x_2$$

$$y = y_1, y_2$$

$$\text{and } p = p_1, p_2$$

we may write the quasi-geostrophic problem into the following two equations,

$$\nabla^2 \sigma(p) \omega_A + f_o^2 \frac{\partial^2 \omega_A}{\partial p^2} = A(\psi) \quad (54)$$

$$\text{and } \nabla^2 \sigma(p) \omega_B + f_o^2 \frac{\partial^2 \omega_B}{\partial p^2} = B(\psi) \quad (55)$$

$$\text{where } \omega_A + \omega_B = \omega \quad (56)$$

A partitioning of vertical motion is thus possible for a quasi-geostrophic problem, ω_A is a contribution to the vertical motion from the forcing function $A(\psi)$ which may be the differential vorticity advection effects and ω_B the contribution by the thermal effects. Such a partitioning cannot in general be done using inhomogeneous boundary conditions (like terrain contributions) because they will enter into both ω_A and ω_B and the relation $\omega = \omega_A + \omega_B$ will not hold.

A problem of inhomogeneous boundary condition can however be transformed into a problem with homogeneous boundary condition by redefining a dependent variable ω^* as a function of ω and the boundary effects. This is somewhat simple for the quasi-geostrophic case but becomes very complicated when we deal with the general balance model. Hence the partitioning that we shall discuss deals with the problem of homogeneous boundary conditions.

For the general balance problem there are at least two interesting ways of partitioning vertical motion distribution, which yield convergent solutions for ω , χ and $\frac{\partial \psi}{\partial t}$.

Problem 1 Let $L_1 = L_2 = \dots = L_n = 0$, solve

$$\nabla^2 \sigma \omega^1 + f^2 \frac{\partial^2 \omega^1}{\partial p^2} = A(\psi) + B(\psi) \quad (57)$$

and obtain ω^1 , a first guess solution. This first guess should in general give the principal results, as is the case for the small Rossby number theory.

Next we write,

$$\nabla^2 \chi^1 = \frac{\partial \omega^1}{\partial p} \quad (58)$$

$$\text{and } \nabla^2 \left(\frac{\partial \psi}{\partial t} \right)^1 = M_1(\omega^1, \chi^1, \psi) + \dots + M_n(\omega^1, \chi^1, \psi) \quad (59)$$

solutions for χ^1 and $\left(\frac{\partial \psi}{\partial t} \right)^1$ are then evaluated for the homogeneous boundary conditions, and $\omega^2, \chi^2, \left(\frac{\partial \psi}{\partial t} \right)^2, \dots, \omega^n, \chi^n, \left(\frac{\partial \psi}{\partial t} \right)^n$ are then successively evaluated by retaining all the terms on the right side. Numerical convergence is defined by a set of small numbers ϵ_1, ϵ_2 and ϵ_n such that finite difference analogues of equations (50), (51) and (52) are satisfied to this degree of tolerance

error. This is a numerical procedure that has been found to converge in a large number of examples where a distribution of $\psi(x, y, p)$ is assumed given.

The preceding discussion tacitly assumes that the equations for ω , χ and $\frac{\partial \psi}{\partial t}$ are always elliptic. The ω - equation can be hyperbolic if the static stability changes sign over portions of regions of interest. A problem quite frequently encountered when conditionally unstable regions are treated as though they were absolutely stable, in which case the effective moist static stability is < 0 over such regions. The ω - equation can become hyperbolic, through cross differentiation terms like the twisting terms,

$f \frac{\partial}{\partial p} \nabla \omega \cdot \nabla \frac{\partial \psi}{\partial p}$ especially if the vertical and the horizontal grid distances are small. This difficulty is not encountered in studies of large scale flow of the atmosphere. In order to assure an elliptic boundary-value problem in the conditionally unstable regions one should treat the effect of heating in a special manner, as for instance it is being done for tropical storm studies, Kuo (1965).

Having obtained a convergent solution for ω , χ and $\frac{\partial \psi}{\partial t}$ the partitioning of the vertical velocity may be carried out in the following manner.

$$\nabla^2 \omega_A + f^2 \frac{\partial^2 \omega_A}{\partial p^2} = A(\psi) \quad (60)$$

$$\nabla^2 \omega_B + f^2 \frac{\partial^2 \omega_B}{\partial p^2} = B(\psi) \quad (61)$$

$$\nabla^2 \omega_n + f^2 \frac{\partial^2 \omega_n}{\partial p^2} = L_n(\omega, \chi, \frac{\partial \psi}{\partial t}, \psi) \quad (62)$$

where ω_A and ω_B determine the contributions from the two principal forcing functions and ω_n are the contributions from n other terms. This partitioning has the feature that

$$\omega = \omega_A + \omega_B + \sum_{n=1}^N \omega_n \quad \text{which is the total vertical}$$

velocity, and it yields considerable information regarding baroclinic processes that are part of the complex atmospheric phenomenon. The operator on the left hand side contains the same terms as in the quasi-geostrophic theory, hence this manner of partitioning may be considered a natural extension of the quasi-geostrophic problem.

Problem 2. Another mechanistic view of the partitioning problem is as follows. We write three equations in the form,

$$\nabla^2 \sigma \omega + f^2 \frac{\partial^2 \omega}{\partial p^2} + \sum_n L_n(\omega, \chi, \frac{\partial \psi}{\partial t}, \psi) = A(\psi) + B(\psi) \quad (63)$$

$$\nabla^2 \chi = \frac{\partial \omega}{\partial p} \quad (64)$$

$$\nabla^2 \frac{\partial \psi}{\partial t} = \sum_n M_n(\omega, \chi, \psi) \quad (65)$$

In this formulation non-linear terms like the twisting term, advections by the divergent part of the wind etc. appear on the left hand side of the ω - equation. Their nature is similar to that of complex differential operators, except that not all of these operators contain ω explicitly. The pertinent question that one might ask with this formulation is what individual total contribution to ω arise from $A(\psi)$ and $B(\psi)$ respectively. There is no simple iterative scheme for solving this problem when the operator L_n appears on the left hand

side, though the correct answer to the question raised here can be obtained by the following procedure.

Solve the system of equations

$$\nabla^2 \sigma \omega + f^2 \frac{\partial^2 \omega}{\partial p^2} = A(\psi) + \sum_n L_n(\omega, \chi, \frac{\partial \psi}{\partial t}, \psi) \quad (66)$$

$$\nabla^2 \chi = \frac{\partial \omega}{\partial p} \quad (67)$$

$$\nabla^2 \frac{\partial \psi}{\partial t} = \sum_n M_n(\omega, \chi, \psi) \quad (68)$$

by dropping $B(\psi)$, by pursuing exactly the same procedure as in problem 1 outlined earlier. Let the final values of ω be $\omega(A_\psi)$.

Next a solution of the system of equations,

$$\nabla^2 \sigma \omega + f^2 \frac{\partial^2 \omega}{\partial p^2} = B(\psi) + \sum_n L_n(\omega, \chi, \frac{\partial \psi}{\partial t}, \psi) \quad (69)$$

$$\nabla^2 \chi = \frac{\partial \omega}{\partial p} \quad (70)$$

$$\nabla^2 \frac{\partial \psi}{\partial t} = \sum_n M_n(\omega, \chi, \psi) \quad (71)$$

is obtained. Let the final values be $\omega = \omega(B_\psi)$. Then $\omega = \omega(A_\psi) + \omega(B_\psi)$ will give the unique total vertical velocity provided there are no quadratic or higher order non linearities in L_n and M_n , in our problem this would at least require a slight reformulation of the friction terms.

In meteorological terminology we have in this second problem, modified the contribution to the rising motion by the

differential vorticity advection and the thermal advection by building up the complex operators on the left hand side. This partitioning may in some ways be more realistic because now we have the same form of the two forcing functions as in the quasi-geostrophic problem on the right hand side. It is however somewhat hard to physically perceive why, for instance, frictional stresses or latent heat should modify the vertical motions produced by differential vorticity advection, and there are a number of such other questions that are hard to answer. I have preferred to determine the partitioning according to problem 1 discussed above because the individual contributions to the vertical motions by a number of forcing functions, in addition to the two (of the quasi-geostrophic theory) on the right hand side, are determined in a unique manner. The information gained by this procedure does yield considerable insight into the role of the individual mechanisms.

It might be asked why not portray fields of the forcing functions themselves rather than the partitioned vertical motion? The forcing functions by themselves are very cellular. The ω -field on the other hand is better defined. This is analogous, for instance, to a relation between $\nabla^2 \psi$ and ψ . The former (vorticity) is more cellular while the ψ field may exhibit long waves. The forcing functions are proportional to $\nabla^2 \sigma \omega$.

In closing this section it would be relevant to point out a relation between $A(\psi)$ and $B(\psi)$ for a quasi-geostrophic problem.

Consider the quasi-geostrophic problem in the form

$$\nabla^2 \sigma(p) \omega_A + f_o^2 \frac{\partial^2 \omega_A}{\partial p^2} = f_o \frac{\partial}{\partial p} \mathbf{W} \cdot \nabla \zeta_a \quad (72)$$

$$\text{and } \nabla^2 \sigma(p) \omega_B + f_o^2 \frac{\partial^2 \omega_B}{\partial p^2} = - \nabla^2 \mathbf{W} \cdot \nabla \frac{\partial \phi}{\partial p} \quad (73)$$

If we define the geostrophic wind by the relation

$$\mathbf{V} = \frac{1}{f_o} \mathbf{k} \times \nabla \phi \quad (74)$$

on the right hand sides of the above two equations, we may rewrite these equations in the form,

$$\begin{aligned} \nabla^2 \sigma(p) \omega_A + f_o^2 \frac{\partial^2 \omega_A}{\partial p^2} &= -\frac{Rg}{f_o p} [J(T, \nabla^2 Z) + J(Z, \nabla^2 T)] \\ &\quad + f_o \beta \frac{\partial V_g}{\partial p} \end{aligned} \quad (75)$$

and

$$\nabla^2 \sigma(p) \omega_B + f_o^2 \frac{\partial^2 \omega_B}{\partial p^2} = -\frac{Rg}{f_o p} [J(T, \nabla^2 Z) - J(Z, \nabla^2 T)] \quad (76)$$

where V_g is the south-north component of the geostrophic wind.

In deriving these expressions, terms of the form,

$$\frac{2gR}{f_o p} \left[J \left(\frac{\partial Z}{\partial x}, \frac{\partial T}{\partial x} \right) + J \left(\frac{\partial Z}{\partial y}, \frac{\partial T}{\partial y} \right) \right]$$

have been neglected for purposes of interpretation. It can be easily shown that this term is in general somewhat smaller than the two other terms. The beta term usually gives a very small contribution to the vertical motion, hence we may write the total ω - equation of the quasi-geostrophic problem in the form,

$$\nabla^2 \sigma(p) \omega + f_o^2 \frac{\partial^2 \omega}{\partial p^2} = \frac{-2Rg}{f_o p} J(T, \nabla^2 Z) \quad (77)$$

The term on the right hand side (advection of vorticity by the thermal wind) appears in the classical development formula of Sutcliffe (1947), it determines the essential regions of large scale rising and sinking motions. It might be asked why partition baroclinic vertical motions into ω_A and ω_B when their corresponding forcing functions are somewhat related to each other.

If the advection of thermal vorticity by the mean geostrophic wind is zero, then the two contributions ω_A and ω_B will be nearly identical, a phenomenon frequently observed in the initial stages of development of a diffluent upper trough.

If on the other hand, the advection of vorticity by the thermal wind is small then the total vertical motion will be negligible, the vorticity and the thermal contributions nearly cancelling each other, a phenomenon frequently observed near occluding cold fronts where vorticity advection aloft contributes to rising motions and is nearly cancelled by the cold advection and associated sinking motions. In a baroclinic frontal cyclone in the final stages of development (as we shall show from drawings) thermal advection determines most of the sinking and rising motion distribution, implying that

$$J(T, \nabla^2 Z) + J(Z, \nabla^2 T) \approx 0$$

The foregoing discussion suggests the following more instructive problem,

$$\nabla^2 \sigma(p) \omega_C + f_o^2 \frac{\partial^2 \omega_C}{\partial p^2} = \frac{-Rg}{f_o p} J(T, \nabla^2 Z) \quad (78)$$

$$\nabla^2 \sigma(p) \omega_D + f_o^2 \frac{\partial^2 \omega_D}{\partial p^2} = \frac{-Rg}{f_o p} J(Z, \nabla^2 T) \quad (79)$$

The solutions of the above pair of equations will in general yield considerable information regarding the importance of synoptic processes during cyclone development. Here we may note that

$$2 \omega_C = \omega \quad \text{Total vertical motion,}$$

$$\omega_C + \omega_D = \omega_A \quad \text{Vorticity contribution,}$$

$$\text{and} \quad \omega_C - \omega_D = \omega_B \quad \text{Thermal contribution.}$$

10. Numerical computation procedures

The following discussion requires a basic knowledge of Fortran programming. The computer program for the general balance model is written in the Fortran IV language. It uses the overlay feature, several links are part of this program.

Link 0 Contains a number of frequently used subroutines.

- i) $\partial Q / \partial x$
- ii) $\partial Q / \partial y$
- iii) $\frac{\partial Q}{\partial p}$
- iv) $\nabla^2 Q$
- v) $J(P, Q)$
- vi) $\nabla P \cdot \nabla Q$
- vii) $P = Q + R \cdot S$
- viii) $P = -f \cdot \frac{\partial}{\partial p} \cdot Q$
- ix) $P = Q \cdot R \cdot S$
- x) General relaxation subroutine for solving problems of

the kind,

$$\nabla^2 PQ + R \frac{\partial^2 Q}{\partial p^2} = T$$

where P , Q , R and T are three dimensional matrices prescribed over $33 \times 15 \times 5$ or $33 \times 15 \times 4$ grid points. S is a defined constant. Subroutines (i) through (vi) contain finite difference analogs for frequently used differential operators. Subroutines (vi) and (ix) are frequently used sum and product of three dimensional arrays, the arbitrary parameter S enables considerable flexibility of use. The subroutine (viii) is frequently used in the iterative sequence relating terms of the vorticity equation with terms of the ω - equation, here f stands for a variable coriolis parameter.

Subroutine (x) is used for solution of ω , χ and $\frac{\partial \psi}{\partial t}$ with the following calling arguments.

$\omega \rightarrow Q = \omega, P = \sigma, R = f, T = \text{forcing function},$

$\chi \rightarrow Q = \chi, P = 1, R = 0, T = \text{forcing function},$

$\frac{\partial \psi}{\partial t} \rightarrow Q = \frac{\partial \psi}{\partial t}, P = 1, R = 0, T = \text{forcing function}.$

The relaxation procedure is the Liebman-forward-extrapolation technique with over relaxation coefficients which are determined by trial and error, and are found to be different for ω , χ and $\frac{\partial \psi}{\partial t}$.

The use of link 0 greatly minimizes the possibility of errors because the master control program and other links mostly contain calling statements of these subroutines of link 0. It thus becomes important that the formulation of the differential operators are written correctly with appropriate finite difference analogs in this link.

Link 1. It is a non-divergent stream function program. For the tropical examples it calls the relaxation subroutine (x) of Link 0,

$$Q = \psi, P = 1, R = 0 \quad \text{and} \quad T = \frac{\partial V}{\partial x} - \frac{\partial U}{\partial y}.$$

For the middle latitude weather systems a complete relaxation program for the following equation is kept in this link.

$$\nabla \cdot f \nabla \psi = \nabla^2 \phi - 2 J \left(\frac{\partial \psi}{\partial x}, \frac{\partial \psi}{\partial y} \right)$$

if the solution diverges because of ellipticity condition not being met at all points. Then the following equation is solved automatically,

$$\nabla \cdot f \nabla \psi = \nabla^2 \phi - 2 J (U_g, V_g)$$

and indicated so.

Link 2 Prepares the three dimensional distribution of temperature, potential temperature, dry static stability and absolute vorticity. Table II shows the structure of scratch tapes for the general balance problem. At the end of the computations this link produces the first six items of tape 3 and the entire list of tape 10. Tape 10 contains several repeated fields. The particular order was designed for the needs of the later links and as a fast access to the variables like ψ , θ and ζ_a , this prevents frequent rewinding of tapes. This ordering was mainly arrived at through discussion with Mr. Robert M. Coie, a senior programmer at Douglas Aircraft Company, Long Beach, California, who has assisted in various aspects of the coding of this problem.

Link 3 It is an initialization program that precedes the major relaxation of ω , χ and $\frac{\partial \psi}{\partial t}$. The first 7 items of tape 9, the first two items of tape 4 and the first item of tape 1 are prepared by this link. Tape 9 contains the following 7 fields in sequence, terrain height in meters, a storage for junk field contains the field of $\frac{\partial \psi}{\partial t}$ subsequently, rotational components of the wind U_ψ , V_ψ , q specific humidity, saturation specific humidity, a stability parameter that modifies the dry static stability. Tape 4 contains the forcing functions of the ω -equation. The first two are functions of ψ , ζ_a and θ and are evaluated in this link.

These are respectively differential vorticity advection and the laplacian of thermal advection. Tape 1 contains the various terms of the vorticity equation. At this stage the first term, vorticity advection, is computed and placed in the beginning of the tape.

Link 4 Contains subroutines for computation of forcing functions of the ω - equation, vorticity equation, continuity equation and the sum of the forcing functions. These are placed on tapes 4 and 1 as indicated in Table 2. This link calls the relaxation of ω , χ and $\frac{\partial \psi}{\partial t}$ in sequence and this process is repeated till convergence criteria are met.

Some of the varying fields are computed during the iteration process and placed in their respective storage places on the tapes. This includes most of tapes 4 and 1. Items 8 and 9 on tape 9 are respectively the net moisture convergence in vertical columns and the percent area occupied by convective clouds. These fields are computed for the changing velocity field and are needed for an evaluation of heating terms of the ω - equation.

ω_1 is the first approximation to the vertical velocity obtained from the two leading terms. ω_T and χ_T are the final values of ω and χ . ω_1 , ω_T and χ_T are placed on tape 3.

Link 5 A calculation of the total horizontal velocity U , V their directions and total speeds DD , VV are made and binary records are entered on tape 3. ω_{i1} through ω_{i12} contain the results of the partitioned vertical velocity without terrain effects. These are evaluated by calling the relaxation subroutine of link zero 12 times. Tape 3 is a history tape of the problem, the contents of tapes 9, 4 and 1 are copies on the tape at the termination of this link.

The program is currently written for IBM 7094 for a mesh of $33 \times 15 \times 5$ which takes about 40 minutes to evaluate all the fields.

Fields like ω , χ and $\frac{\partial \psi}{\partial t}$ are always kept in core with only three additional three dimensional storage arrays. The unused core on the IBM 7094 is around 7,000, which is available for considerable expansion of array sizes or of the programs.

Tape 3 is further used for research purposes, e.g. analyzing maps of desired fields, cross-sections, energy studies and trajectories. All of this is carried out by a series of separate program decks that are not a part of the above mentioned links.

Other computational features are: Z , ψ , χ , $\frac{\partial \psi}{\partial t}$, U_ψ , V_ψ , U , V , ζ_a , $\nabla^2 \chi$ and all of the forcing functions of the vorticity equation appear at the 1000, 800, 600, 400 and the 200 mb surface. ω , T , θ , q , q_s and all of the forcing functions of the omega equation appear at the 900, 700, 500 and the 300 mb surface. There is no staggering of the grid in the horizontal. All horizontal space differences are taken over a distance of two grid points. The truncation error of Jacobean, Laplacian and $\nabla P \cdot \nabla Q$ are of the order of the square of the grid distance. These difference operators are taken over 9 grid points. Boundary conditions of the problem are:

$$\psi = -\frac{gZ}{f} \quad \text{at} \quad y = y_1 \quad \text{and} \quad y = y_2$$

$$\omega = 0 \quad \text{at} \quad y = y_1 \quad \text{and} \quad y = y_2$$

$$\omega = 0 \quad \text{at} \quad p = 100 \text{ mb.}$$

$$\omega = 0 \quad \text{or} \quad -g\rho \mathbf{V} \cdot \nabla h \quad \text{at} \quad p = 1000 \text{ mb.}$$

$$\chi = 0 \quad \text{at} \quad p = y_1 \quad \text{and} \quad y = y_2$$

$$\frac{\partial \psi}{\partial t} = 0 \quad \text{at} \quad y = y_1 \quad \text{and} \quad y = y_2$$

where y_1 and y_2 refer to the northern and southern walls. Along x - axis there is a cyclical continuity.

The following concluding note on a normalizing procedure for general relaxation problems is relevant here:

The equations of the form,

$$\nabla^2 PQ + R \frac{\partial^2 Q}{\partial p^2} = T$$

are assumed to be elliptic here. Let the finite difference analog of this equation be written by the equation,

$$\text{Residue} = \nabla^2 PQ + R \frac{D^2 Q}{D p^2} - T \quad (80)$$

where $\nabla^2 PQ$ and $\frac{D^2 Q}{D p^2}$ are the finite difference analogs for

$\nabla^2 PQ$ and $\frac{D^2 Q}{D p^2}$ respectively. In order to use the same general form of the Liebmann forward extrapolation technique, equation (80) may be rewritten in the form,

$$\text{Normalized Residue} = \left(\nabla^2 PQ + R \frac{D^2 Q}{D p^2} - T \right) \frac{1}{(P |\nabla^2|)} \quad (81)$$

The normalizing factor is the inverse of the coefficient of Q where $(|\nabla^2|)$ is the magnitude of the finite difference del square operator. It is a function of grid lengths and the map projection scale factors.

In the iterative procedure of the Liebmann relaxation, during each scan Q is modified by the relation,

$$Q = Q + \alpha \cdot \text{Normalized Residue} \quad (82)$$

where α is the over-relaxation coefficient.

This procedure converges very rapidly provided a trial search is made to determine the optimum magnitude of α . No textbook rules

determine the values of α in a general problem. α is found to vary for different grid distances, static stabilities, ranges of coriolis parameters. In these studies we have used

$$\begin{aligned}\psi &\rightarrow \alpha = 0.31 \\ \omega &\rightarrow \alpha = 0.37 \\ \chi &\rightarrow \alpha = 0.47 \\ \frac{\partial \psi}{\partial t} &\rightarrow \alpha = 0.47\end{aligned}$$

for the middle latitude winter storm studies. In the tropics values differ somewhat on the lower side.

11. Some concluding remarks

The general balance model for diagnostic studies is a useful platform for meteorological research. There are several problem areas where much further work will be required.

i) Restriction to small Rossby number theory ($R_o < 1$) can perhaps be avoided by carrying the solutions of the general balance equations as input in a primitive equation prediction model. Short range forecasts with a primitive equation program yields useful synoptic information for $R_o > 1$.

ii) The formulation of heating, friction and terrain requires much more work. The presentation in this report is a first order formulation based on what is now found in standard textbooks.

iii) Input data: Analysis of fields like Z , DD , VV , T or q in sparse data regions will remain for some time the art of a skilled synoptic analyst. The skilled analyst will perhaps utilize satellite cloud and radiation information to supplement conventional data and perform an analysis where his experience will undoubtedly play an important role. Once the input fields are somewhat satisfactorily defined it becomes a mathematical problem, and the results apply to the subjectively obtained input. Objective analysis techniques are still very unsatisfactory in sparse data regions and much further work

will be required before it will meet the eye. Each field like wind, moisture and pressure should be separately examined by an objective analysis program.

Table 1

List of Symbols, Units and Typical Magnitudes

Note: We use the following fundamental units throughout our report:

Millibar α meter β sec γ degree δ . The table contains the symbol, meaning of symbol, values of $\alpha, \beta, \gamma, \delta$ and a typical atmospheric magnitude of the quantity in those units, * denotes very wide range of magnitudes.

Symbol	Meaning of symbol	α	β	γ	δ	Magnitude
f	coriolis parameter	0	0	-1	0	10^{-4}
u	zonal velocity of total balance wind	0	1	-1	0	10
v	Meridional velocity of total balance wind	0	1	-1	0	10
w	Vertical velocity	1	0	-1	0	10^{-3}
ρ	Density of air	1	-2	2	0	10^{-2}
x	Distance along zonal direction	0	1	0	0	10^3
y	Distance along meridional direction	0	1	0	0	10^3
p	Pressure, vertical coordinate distance	1	0	0	0	10^2
f_0	Mean value of Coriolis parameter	0	0	-1	0	10^{-4}
σ	Dry static stability	-2	2	-2	0	10^{-2}
σ_e	Moist static stability	-2	2	-2	0	10^{-3} *
R	Gas constant	0	2	-2	-1	2000/7
c_p	Specific heat of air of constant pressure	0	2	-2	-1	10^3
c_v	Specific heat of air at constant volume	0	2	-2	-1	5000/7

Table 1 (continued)

g	acceleration of gravity	0 1 -1 0	10
k	unit vector in the vertical direction	0 1 0 0	1
T	air temperature	0 0 0 1	300
θ	Potential temperature	0 0 0 1	300
v	Horizontal velocity vector	0 1 -1 0	10
v_ψ	Rotational part of horizontal wind vector	0 1 -1 0	10
v_x	Divergent part of horizontal wind vector	0 1 -1 0	1
β	Northward variation of Coriolis parameter	0 -1 -1 0	10^{-11}
z	Height of constant pressure surfaces	0 1 0 0	6000^*
ϕ	Geopotential of constant pressure surfaces	0 2 -2 0	$6 \times 10^9^*$
ψ	Rotational part of the horizontal wind	0 1 -2 0	10^8
χ	Velocity potential	0 1 -2 0	10^6
∇	Del operator	0 -1 0 0	10^{-3}
∇^2	Laplacian operator	0 -2 0 0	10^{-7}
J	Jacobian operator	0 -2 0 0	10^{-7}
π	Symbol for $\frac{RT}{p\theta}$	-1 2 -2 -1	0.3^*
$F_i, A(\psi), B(\psi)$	Forcing function of ω equation	-1 0 -3 0	10^{-16}^*
q	Specific humidity	0 0 0 0	10^{-3}
q_s	Saturation specific humidity	0 0 0 0	10^{-3}
ζ_a	Absolute vorticity	0 0 -1 0	10^{-4}

Table 1

S	Relative vorticity	0 0 -1 0	10^{-4}
L	Latent heat	0 2 -2 0	10^6
D_1, D_2	Components of deformation	0 0 -1 0	10^{-4}
H	Heating function	0 2 -3 0	10^{-2}
F_s	Sensible heat flux	1 1 -1 0	10^{-1}
I	Net moisture convergence	1 -1 1 0	10^{-6}
T_x, T_y	Frictional stress	1 0 0 0	10^{-3}
ω_T	Terrain induced vertical motion	1 0 -1 0	10^{-3}
M	Map scale factor	0 0 0 0	1.0
$\bar{\phi}$	Latitude	0 0 0 0	1.0

14

Scratch tape storage for multilevel balance model					
	3	9	4	1	10
∇	R	$f_{\partial p}^2 \tau(\psi, \zeta_a)$	$- \tau(\psi, \zeta_a)$	ψ	θ
Σ	J	$\pi \nabla^2 \tau(\psi, \theta)$	$- g \frac{\partial}{\partial p} [\frac{\partial \tau_y}{\partial x} - \frac{\partial \tau_x}{\partial y}]$	ζ_a	ζ_a
T	u_ψ	$f_{\partial p}^2 g \frac{\partial}{\partial p} [\frac{\partial \tau_y}{\partial x} - \frac{\partial \tau_x}{\partial y}]$	$\nabla x \cdot \nabla \zeta_a$	ψ	ψ
θ	v_ψ	$-\frac{R}{q_p} \nabla^2 H_s$	$\zeta_a \nabla^2 x$	ψ	ψ
ζ_a	q	$-\beta \frac{\partial}{\partial p} \frac{\partial}{\partial y} \frac{\partial \psi}{\partial t}$	$-\nabla \omega \cdot \nabla \frac{\partial \psi}{\partial p}$	ψ	θ
ω	q_s	$-2 \frac{\partial}{\partial t} \frac{\partial}{\partial p} \tau(\frac{\partial \psi}{\partial x}, \frac{\partial \psi}{\partial y})$	$-\omega \frac{\partial}{\partial p} \nabla^2 \psi$	ψ	ψ
ω_t	$\frac{R}{c_p} L \frac{\partial q_s}{\partial p}$	$-f \frac{\partial}{\partial p} (\nabla x \cdot \nabla \zeta_a)$	SUM		
x_t	I	$-f \frac{\partial}{\partial p} (\zeta \nabla^2 x)$			
u		$-f \frac{\partial}{\partial p} (-\nabla \omega \cdot \nabla \frac{\partial \psi}{\partial p})$			
v		$-f \frac{\partial}{\partial p} (-\omega \frac{\partial}{\partial p} \nabla^2 \psi)$			
DD		$-\pi \nabla^2 (\nabla x \cdot \nabla \theta)$			
w_{i1}		$-\frac{R}{q_p} \nabla^2 H_L$			
w_{i2}		SUM			
\dots					
w_{in_2}					
Tape 9					
Tape 4					
Tape 1					

List of References

- Berkofsky, L., and E. A. Bertoni, 1955: Mean Topographic Charts for the Entire Earth. *Bulletin of American Meteorological Society*, Vol. 36, pp. 350-354.
- Charney, J., and A. Eliassen, 1964: On the Growth of the Hurricane Depression. *Journal of Atmospheric Sciences*, Vol. 21, pp. 68-75.
- Kuo, H. L., 1965: On formation and Intensification of Tropical Cyclones through Latent Heat Release by Cumulus Convection. *Journal of Atmospheric Sciences*, Vol. 22, pp. 40-63.
- Jacobs, W. C., 1951: Large Scale Aspects of Energy Transformation over the Oceans. *Compendium of Meteorology*, American Meteorological Society. Boston, Mass.
- Krishnamurti, T. N., 1966: A Calculation of Percentage Area Covered by Convective Clouds from Moisture Convergence. Final Report to AFCRL, Department of Meteorology, University of California, Los Angeles. AF 19(628) AFCRL-67-0128.
- Lorenz, E. N., 1960: Energy and Numerical Weather Prediction. *Tellus*, Vol. 12, pp. 364-373.
- Paegle, J., 1966: Numerical Calculation of Three Dimensional Trajectories Utilizing the Balanced Horizontal and Vertical Motions. Final Report to AFCRL, Department of Meteorology, University of California, Los Angeles. AF 19(628) AFCRL-67-0128.
- Petterssen, S., 1956: *Weather Analysis and Forecasting*, Vol. 1, Chapter 16, pp. 320-338. The McGraw-Hill Book Company, New York.
- Phillips, N. A., 1963: Geostrophic Motion. *Reviews of Geophysics*. Vol. 1, pp. 123-176.
- Shuman, F. G., 1957: Numerical Methods in Weather Prediction. The Balance Equation. *Monthly Weather Review*, Vol. 85, No. 10, pp. 329-332.
- Sutcliffe, R. C., 1947: A Contribution to the Problem of Development. *Quarterly Journal of Royal Meteorological Society*. 73, pp. 370-383.

N67-30786

A Study of a Wave Cyclone Development

By T. N. Krishnamurti

1. Introduction

The case study deals with a frontal cyclone development over the midwestern United States. Analysis of following fields were carried out for April 12 and 13, 1964.

- i) Geopotential heights of standard constant pressure surfaces.
- ii) Specific humidity at standard constant pressure surfaces.
- iii) Cloud cover using conventional and Tiros data.

The following calculations were carried out for four map times of storm development.

- i) Three dimensional motion field using a two level quasi-geostrophic model (adiabatic).
- ii) Three dimensional motion field using a 5-level linear balance model (adiabatic)
- iii) Three dimensional motion field using a 5-level general balance model, including effects of terrain, friction and heating.
- iv) Partitioning of vertical motion for the various models.
- v) Three dimensional trajectories and interpolation of development terms along the trajectory.

Since approximately 10^4 two dimensional fields are computed and stored as binary records on magnetic tapes, it becomes quite a difficult task to isolate important features and portray them for illustration purposes. Not all map times showing the development of any feature is shown in the following. A selection of some of the important features are made, but it is quite possible that some important information has thus been omitted in the following discussions.

2. Description of synoptic situation during wave cyclone development

The case study was selected because of a development that followed the well known criteria of the two level quasi-geostrophic theory. In the upper levels there was a well marked diffluent trough initially Figure 1 (April 12, 1964 00Z) with a strong north westerly flow in the rear of the upper trough, and weaker winds ahead of it. From simple barotropic considerations such a diffluent trough is expected to produce a stronger curvature and a drop in the 500 millibar height field due to a transformation of shear vorticity into curvature vorticity. In this case considerable development of the 500 millibar height field is noticed with an increase in the magnitudes of the absolute vorticity due to baroclinic processes. At the surface levels, Figure 2, there was a considerable development of a weak lee trough into a 975 millibar low over Minnesota. We are depicting four map times at intervals of 12 hours, these may be approximately labeled to indicate the,

- i) diffluence stage,
- ii) open wave stage,
- iii) pre-occlusion stage,
- and iv) occlusion stage.

The trough initially over the lee of the Rockies, moves a distance of about 1000 nautical miles over a period of 36 hours. Since the major development takes place in a region well covered with data it is possible to obtain detailed three dimensional analysis of the geopotential height distributions. The surface low develops somewhat slowly in the first 24 hours and a rapid development follows




in the last 12 hours.

Figure 3 shows the geopotential heights and the isotachs of the total wind for the four map times at the 200 mb surface. Unlike in the tropics, the upper level maps near the jet stream level in middle latitude give limited qualitative information. There was a strong polar jet stream behind the upper trough at the first map time, the jet stream moves faster than the wave, and a large part of the strong winds were equally well distributed on both sides of the upper trough by the last map time. The 500 millibar surface shows a more distinct change from a diffluent to a confluent system, a feature very typical during rapid cyclogenesis. Maps of specific humidity show a moist tongue extending well north to 40° North extending from the gulf of Mexico during all map times.

Figure 4 shows the distribution of total precipitable water for the four map times. This distribution was obtained from the fields of specific humidity at several levels using Simpsons rule of numerical integration in the vertical. This integrated map is not directly used in any of the subsequent calculations, however the fields of specific humidity are used in the determination of heating terms. The integrated map is useful for discussion purposes. It shows a quasi-stationary moist tongue which may have played an important role in the development through precipitation, latent heat release, attendant rising motions and low-level convergence distributions. These are some of the questions that we hope to examine in the next sections. Precipitation amounts were small prior to April 13 00Z. In the next 12 hours several stations reported 1 to 2 inches of rain along the northern part of the moist tongue.

We overlooked this precipitation when we first examined the regular surface synoptic reports. A re-examination of the hourly precipitation data over a large number of hourly recording stations in Minnesota showed that precipitation was indeed high in the last 12 hours.

Figure 5 illustrates nephanalysis for the 4-map times. Conventional data (synoptic reports for four map times) as well as satellite information (pictures and radiation measurements from channels II and V for ORBITS 4398-4399 4412-4427-4428 and 4413 (only radiation) 4414 (only pictures) of Tiros VII have been used. See Figure (5). The conventional data have been mostly taken into account but wherever satellite information was available it was taken to support or complete the analysis.

The type of clouds (m limit of low clouds; m limit of middle clouds and m limit of high clouds) as well as their amount (  ) regions covered with more than 50% by low middle and high clouds respectively) have been considered. From the nephanalysis we find that low cloudiness is found in the north western part of the country, Pacific and parts of the frontal system.

Wherever a zone with two types of cloudiness is found, shaded regions determine the dominant type and a line is drawn enclosing the region of both types. Thus in eastern Canada and Minnesota there is a dominating zone of stratus, strato cumulus and fracto stratus that prevents seeing higher clouds, this is also confirmed by satellite information, therefore the line mm (middle clouds) is included. There is a good correlation between region of heavy overcast with the fields of total precipitable water Figure 4. At the first map time there was a region of overcast extending from

the Gulf of Mexico to the north up to 40° latitude. The organization of the pattern of cloud cover during the occlusion stage from an initial chaotic state is an interesting feature of this figure. Cloud patterns are generally interesting to look at when they are part of a vigorous isolated weather system; if there are several weak systems patterns tend to be chaotic. This is generally true of any synoptic feature of atmospheric dynamics. Detailed synoptic studies of many interacting systems, in a domain of interest, usually leaves a number of unanswered questions.

Figure 6 illustrates the distribution for 4 map times of the vertical motions at the 500 millibar surface obtained from a multilevel linear balance model. The unit of vertical velocity throughout this report is 10^{-5} millibars/sec. This corresponds to approximately 0.013 cm/sec. Of interest in the vertical motion distributions are the large sinking motions behind the diffluent trough at the first map time. The maximum sinking intensity is close to 500 units, maximum intensity of rising motions is only 200 units. The gradual increase in the intensity of the rising and sinking motions in the developing storm is worthy of note. The pattern of rising and sinking motions at the last map time is a classic illustration of the dipole centers during the occlusion stage.

3. A comparison of the geostrophic VS the balanced non-divergent wind fields

The balance equation for the non-divergent stream function is given by the equation,

$$\nabla \cdot f \nabla \psi = \nabla^2 \phi - 2 \mathcal{J}\left(\frac{\partial \psi}{\partial x}, \frac{\partial \psi}{\partial y}\right)$$

There are several approximations of interest here. i) If the second term on the right hand side is dropped and f is replaced by f_0 , a mean value of the coriolis parameter, then the stream function ψ describes geostrophic motions, Phillips (1963). ii) If f is treated as a variable and the second term is not retained then ψ_L describes what is frequently called a linear-balanced non-divergent stream function. iii) If the geostrophic stream function is used to evaluate the second term on the right hand side and f is treated as a variable then ψ_{N1} is called a semi-geostrophic balance stream function. iv) If no approximations are made then ψ_{N2} is called the complete non-divergent balanced stream function. This balance equation has been analysed by several meteorologists over the past 10 years. Petterssen found this form of the equation in 1936 in his studies of the kinematic properties of the wind fields.

It is of interest to a synoptic meteorologist to find out if large non-geostrophic motions can still be non-divergent. In 1951 Bjerknes discussed the non-geostrophic motions downwind from an unstable ridge in the upper flow patterns. One of his findings was that, the wind which is nearly in gradient balance and hence super geostrophic in the ridges, comes down in a north westerly flow and cuts towards higher pressure as it acquires a geostrophic adjustment. Such flow fields have been found in the initial states of several of our synoptic investigations of baroclonic frontal cyclone developments. We find that most of this non-geostrophic motion, is a non-divergent contribution. An hence it is especially meaningful to compare for instance these four, i) through iv), stream functions listed above.

Figure (7) depicts Ψ_L , Ψ_{N1} and Ψ_{N2} the linear balanced, semi-geostrophic and the complete balanced stream function shown by solid lines in the three drawings. The dashed lines in all these three drawings show the 200 millibar height field during the occlusion state of the wave cyclone. It is not possible to illustrate such drawings for several map times and for several map times and for several levels, though such information would be very illustrative and pertinent. This depiction of the stream function fields is not quite satisfactory for visual comparisons with the height distributions because the quantities we are most interested in are the speed and directions of the non-geostrophic departures in the non-divergent flow. We have estimated the speeds from these stream functions and the following results were obtained.

Cross isobaric flow is a minimum for the linear balanced stream function Ψ_L , the amplitudes of the waves in the westerlies for the \bar{Z} and Ψ_L fields are very nearly the same. However the magnitude of the linear balanced wind is considerably larger near regions of strongly curved flow, in such regions Ψ_L overestimates the magnitude of the wind. This effect is especially pronounced in the lower troposphere where closed centers are more in number, typical magnitudes of linear balanced wind are nearly twice as large as the geostrophic or the observed wind. We made some attempts to use the linear balanced stream function to evaluate the divergent part of the wind ∇_x and the vertical motion ω from a linear balanced model. The magnitudes of the vorticity and the thermal advection were somewhat too large and unreasonably large rising and sinking motions were found

near closed centers. Since the governing equation for the non-divergent stream function is linear this result should become apparent from an analysis of the problem for an analytic distribution of the geopotential height field.

The winds obtained from the semi-geostrophic stream function ψ_{N1} and the complete non-divergent stream function ψ_{N2} have speeds very close to the observed or the geostrophic wind. The fields of these stream functions are very similar, there is considerable cross-isobaric flow in these two representations. The non-divergent wind cuts towards higher pressure in the north-westerly current and towards lower pressure in the south-westerly flow. The amplitude of the non-divergent stream function is somewhat larger than that of the geopotential heights. This feature may be observed in Figure (7) very distinctly in the region south of 40°N . Typical magnitudes of the non-geostrophic departures are as large as 14 mps. We have also re-examined a case study reported recently by Newton and Palmen (1963) on the non-geostrophic winds in a long wave in the westerly current. Similar results were obtained as for the case study we have presented here.

In summarizing it may be stated that a large part of the upper tropospheric cross-isobaric flow frequently observed in baroclinic disturbances may be explained from the non-divergent part of the total wind.

4. Partitioning of baroclinic vertical motions in the two level quasi-geostrophic model

We refer here to the simple ω -equation of the quasi-geostrophic dynamics applied to 2-levels, the 1000 and 500 millibar surfaces.

The baroclinic development of the wave cyclone was well marked with intense centers of sinking and rising motions of air in the middle troposphere. A line was drawn for the four map times through the axis of maximum rising and sinking motions in Figure (2) and a partitioning of the vertical motion at the 500 millibar was carried out to resolve its two components:

i) Contribution by differential vorticity advection, ω_1 .

ii) Contribution by the Laplacian of thermal advection, ω_2 .

In general, since cold air is sinking and warm air is rising, the axis in question here marks the line along which a maximum contribution to the release of potential energy takes place for each stage of the storm development.

From earlier synoptic investigations of Petterssen (1956) the lee cyclone development is described to follow along the rather well accepted rule: If a region of strong upper positive vorticity advection were found to overlies an open wave cyclone at the sea-level, then the wave cyclone will intensify. In terms of the ω -equation Petterssen's rule may be re-expressed as follows: In the initial stages of a cyclone development differential vorticity advection is important and in later stages as the cyclone advects warm and cold air by its circulation, Laplacian of thermal advection would increase. This has been an accepted rule of synoptic meteorologists for a considerable time. This rule is also in accordance with a principle generally used in current weather map discussions regarding the intensification of a diffluent upper trough and the associated surface cyclone development, see Figures 1 and 2. Here again the synoptic rules are that the initial intensification

processes are quasi-barotropic and the baroclinic processes, namely the thermal effects, became important only somewhat later.

The proposed partitioning of the vertical motions during the various stages of the storm development will be very important in verifying the validity of these synoptic principles quantitatively. Figure (8a) shows the partitioning at the diffluent trough stage. The solid line indicates the total vertical motions, the dashed line the thermal term and the dash-dotted line the differential vorticity advection term. During this stage air is sinking behind the upper diffluent trough, strongest sinking motion $\approx 550 \times 10^{-5}$ millibars/sec which corresponds to about 8 cm/sec at the 500 millibar surface. The rising motion ahead of the trough is very weak and of the order 1 cm/sec. The interesting aspect of the partitioning at this stage is that both the thermal term (cold air advection) and the vorticity advection give about equal contribution at this time. Hence we must conclude that at the initial diffluence stage both the vorticity and the thermal mechanisms are operating with about equal intensity, the latter by no means is negligible. This conclusion could have been drawn from an examination of the isothermal patterns below the upper trough which reveal a lag of the thermal trough with respect to the pressure trough and attendant large cold advection. An examination of Figures 8 b, c and d show the gradual increase of the sinking and rising motions along the line under investigation. During the open wave stage Figure 8 b both terms contribute about equally in the rising air whose intensity has increased to about 5.5 cm/sec, in the sinking branch the thermal contribution is somewhat larger. There is an

interesting phase lag between the two terms (represented in this manner) and there are regions in the vicinity of the trough where the two effects cancel. During the pre-occlusion stage the storm has a larger baroclinic effect evidenced by the much larger magnitudes of the thermal term. At the occlusion stage sinking motions acquire intensities near 13 cm/sec and rising motions near 11 cm/sec. The sinking motion is mostly a thermal contribution, weak sinking motions about 10% are contributed by the differential vorticity advection. Ahead of the trough most of the rising motion, about 65%, is contributed again by warm air advection. At this stage the thermal trough was somewhat ahead of the upper pressure trough. This is substantiated by the latitude of the zero vertical motion in the two terms.

Figure (9) shows the distribution maps of ω , ω_1 and ω_2 for the final map time and one may observe the relative importance of the baroclinic mechanisms. The total rising motion is largely a thermal contribution over most of the map. This implies that $J(T, \nabla^2 z) \approx -J(z, \nabla^2 T)$ when the baroclinic disturbance is most intense the advection of vorticity by the thermal wind is nearly equal and opposite to the advection of thermal vorticity by the geostrophic wind. This is not quite true in the vicinity of the upper trough where the vorticity contribution is somewhat large. This study has been repeated for seven examples of extratropical storms in none of which, the contribution by thermal advection was small initially. All of these storms were studied over continental United States.

5. Results of partitioning of vertical motions from the multi level balance model

a) Differential vorticity advection

A map of corresponding vertical motion is displayed in Figure 10 (top), only the last map time is included in the list of illustrations. Vertical motions are somewhat cellular but the major features include rising air ahead of the upper trough and sinking behind. There is a considerable separation between the regions of largest upward and downward vertical motions. Largest rising motion are of the order -500×10^{-5} mb/sec over Minnesota, north of the surface low. This corresponds to about 7 cm/sec. The intensity of the largest sinking motions is in the lee of the Rockies and is of the same intensity. This pattern of rising motion contribution is not quite similar to the contribution by differential vorticity advection in a 2-level quasi-geostrophic model, Figure 9 (bottom right). These differences can arise due to at least four reasons.

- i) Static stability being variable in the balance model.
- ii) Differential advections take into account the strong jet stream at the 300 mb surface in the balance model.
- iii) Balance stream function Ψ_N is different from the geostrophic stream function, gZ/f_0 .
- iv) Coriolis parameter f is variable in the balance model.

Of these iii) and iv) cannot account for the large differences in the two models, especially magnitudes of the order of 300×10^{-5} mb/sec in the lee of the Rockies. It cannot be explained in terms of the variable static stability because in the cold

air ∇ is larger in the balance model hence ω would tend to become smaller by this effect. The product of ∇ times ω is approximately in-variant in these models. The large difference is best explained by (ii) namely better vertical resolution in the multi level balance model. These large differences are found in the region of the strong jet stream; the differential vorticity advection of the balance model does take these features into account.

b) Laplacian of thermal advection

The thermal contribution to rising and sinking motion is large, Figure 10 (bottom) as we shall see from the remaining terms, it is the dominant term. Sinking motion in the cold air behind the surface front acquires magnitudes close to 1200×10^{-5} mb/sec downward motion at the 500 millibar surface. This field is somewhat different from the corresponding quasi-geostrophic contribution, Figure 9 (bottom left). The balance wind, used for advection of the thermal field, is closer to the gradient and the actual wind which is subgeostrophic near low centers. The large differences near the low center cannot be explained by this difference in the stream functions. Part of this difference is still due to the stream functions used in the two calculations. In the quasi-geostrophic calculation the stream function refers to 750 millibar surface, while for the multi level balance model it corresponds to the 500 millibar surface. Another reason for the difference is the intensity of cold advection which was stronger at the upper levels.

c) Deformation and divergence contributions

The contribution to the vertical velocity by the deformation and divergence effects, Figure 11, are somewhat similar near the low center. They both counteract

the rising and sinking contributions produced by the two leading terms. The large rising center, southwest of lake Michigan has an intensity close to -300 units, which is approximately 4 cm/sec rising motion at the 500 millibar surface. It is thus clear that these terms are very important in the storm dynamics. The deformation term is generally very small away from the storm, however there are several centers > 100 units in the divergence contribution. In general the divergence contribution counteracts the contribution by the two leading terms Figure 10 over most regions. Both of these terms do not appear in the quasi-geostrophic theory, and hence these results are quite significant.

d) Frictional and terrain contributions

Drag coefficient C_D is equal to 2.5×10^{-3} , in this study. Largest frictional vertical motion, Figure 12, are of the order 10^{-3} mb/sec at the 900 mb

In regions of cyclonic low level relative vorticity rising motion is well organized, and in regions of anticyclonic vorticity sinking motion is found. This is to be expected for this simple formulation of the frictional stress terms.

Figure 12 (bottom) shows the horizontal distribution of the frictional contribution, shown by solid lines, and the surface pressure field (± 5 mb isobars) are indicated by dashed lines. Both terrain and the frictional contribution decay rapidly with height. Figure 13 shows an example of the vertical distribution of the damping of the frictional vertical velocity taken at a grid point. Whether indeed such frictional vertical velocities exist over land areas can not be checked very easily, it is however comforting to note that the total picture of the mid tropospheric vertical velocity is not altered by more than 10% when frictional and terrain effects

are introduced. Danielssen (1966) has compared the magnitudes of mid tropospheric vertical motion obtained from isentropic trajectory calculation and those obtained from solutions of our balanced model (without terrain and friction) and found very good agreement. It leads us to conclude that the effect of friction and terrain should be very small ($\ll 10^{-3}$ mb/sec) in the middle troposphere and hence the formulation presented here is perhaps not very unrealistic. The corresponding contribution at other map times were quite similar. Terrain effects were larger at the first map time behind the upper trough and contributed significantly to the total sinking motion and the associated lee development.

e) Contribution by release of latent heat

Partitioning of latent heat contribution is carried out by setting,

$$\nabla^2 \sigma \omega_L + f^2 \frac{\partial^2 \omega_L}{\partial p^2} = \frac{RL}{c_p p} \nabla^2 \omega \frac{\partial q_s}{\partial p}$$

ω_L is the contribution by latent heat and ω is the vertical velocity obtained by solving the complete balance equations. We may write,

$$\omega = \omega_L + \omega_R$$

where ω_R is the contribution by the remaining terms. We may rewrite the

ω -equation of this problem in the form,

$$\nabla^2 \sigma_\epsilon \omega_L + f^2 \frac{\partial^2 \omega_L}{\partial p^2} = \frac{RL}{c_p p} \nabla^2 \omega_R \frac{\partial q_s}{\partial p}$$

This equation will be elliptic if $\sigma_\epsilon > 0$. Calculations are made assuming no conditionally unstable regions. This requires an adjustment of the effective static stability,

$$\sigma_\epsilon = \sigma - \frac{RL}{c_p p} \frac{\partial q_s}{\partial p}$$

In regions, where $\nabla \epsilon < 0$ we have arbitrarily set $\nabla \epsilon = 0.1 \nabla$, this artificial setting was carried out at few grid points south of 30°N near the Gulf of Mexico in the moist and warm tongue of air. As we have mentioned earlier this is the region where a special form of heating function should have been evaluated in terms of parameterization of cumulus scale motion. We hope to present such results in the near future.

Figure 14 shows the contribution to the vertical velocity from latent heat at the 900, 700, 500 and 300 millibar surfaces. The results show that the latent heat contribution is very large, > 500 units, and comparable to the first two. The corresponding contribution at the first three map times was much smaller. The rising motion center gradually moves eastward, Figure 6, while the moisture field is quasi-stationary. The significance of these vertical motions to the intensification of the surface pressure field during the last 12 hours becomes clearer from this analysis. The magnitude of low level convergence and the product of absolute vorticity and convergence is large in the vicinity of the intensifying low. The patterns of rising motion, Figure 14, show that even at 300 millibar surface latent heat contributions are of the order -50×10^{-5} mb/sec. This corresponds to about 1 cm/sec rising motion. Another feature of the ω -equation, not quite understood here, is the sinking motion distribution that spreads out away from regions of heating. It is not obvious whether the real atmosphere indeed has this feature! The intensity of the sinking motion is quite small. This numerical feature is found

in both high and low latitude investigations where the nature of the heating terms are quite different.

f) An overall look at all the terms

Table 1 shows a distribution of vertical motion at the 500 mb surface along a line taken parallel to the upper trough and 5° longitude east or down wind from the trough. Different points from left to right on Table 1 are taken from south to north. They may be identified easily from the figures of individual charts presented earlier.

Partitioning shows the following features of interest. Ahead of the upper trough vorticity advection (1) contributes rising motion at all points; to the south cold air advection (2) produces sinking motion while to the north the first two terms are in phase. This is a very typical feature of the thermal and vorticity contribution in the near occlusion stage in extratropical storm. Ahead of the trough contribution by the deformation term (3) is large and cuts down the intensity of rising motion. The divergence term (4) counteracts the rising and sinking motion of the total picture; its contribution along this line are not as strong as they are usually found behind intense cold fronts. Frictional contribution (5) above the surface is rising motion, intensity about $6/10$ cm sec. The contribution by latent heat (6) is very large north of the surface low, shows a large point value, a feature typical of heating distribution. Lake water temperatures were analyzed to examine their contribution to development through sensible heat transfer (7) this was a very small effect in this storm and is almost negligible at the 500 millibar

surface. The vertical motions from vertical advection (8) and the twisting terms (9) are small, the latter is in phase with the vorticity advection (1) contribution while the former is out of phase. The two contributions (8) and (9) have a tendency to cancel each other. The contributions by the vorticity (10) and thermal (11) advection by the divergent part of the wind are both very small over all regions. The beta term (12) is the smallest of all of the contributions and contributes less than 1/10 cm/sec rising or sinking motion. The partitioning was done without terrain effects. A comparison of the total without terrain effects (sum of partitioned ω) and the solution of the complete problem with the terrain is shown in the last two rows of Table 2. Terrain contribution damp with height rapidly hence the totals in the last two rows (at 500 mb surface) are nearly identical.

Table 1 and the charts presented earlier give an insight into the processes and important mechanisms in the middle troposphere. We have only displayed a small part of information. Many such charts are available at several levels of the troposphere where the ratio of the relative magnitudes are not the same as what we have portrayed in Table 1.

Figure (15) shows a distribution of the vertical velocity, ω , at the 500 millibar surface from the complete balance model including the 12 internal forcing functions and one external (terrain) boundary forcing function. There are four results of importance that may be compared at this stage: (April 13, 12Z 1964)

- i) Two level quasi-geostrophic ω , Figure 9 (top left).
- ii) Multi level linear-balance ω , Figure 6 (bottom right).

iii) Multi level balance ω containing sum of two leading terms,
Figure 15 (bottom).

and iv) Multi level balance ω containing sum of all terms, Figure 15
(top).

It is of interest to note that the patterns of total vertical velocity are similar in all cases; the intensities are somewhat different. Inclusion of latent heat increases the rising motion; and the deformation and divergence effects cut down the intensity of sinking motion in the complete model.

6. On the development of the April storm

Analysis of the forcing functions of the ω -equation, their individual contribution to rising motion, and an examination of the distribution of different terms of the vorticity equations enables us to draw the following description of the storm development.

The initial development April 12 00Z - April 12 12Z was at upper levels behind the diffluent trough. Strong sinking motions are produced by differential vorticity advection, Laplacian of thermal advection and the terrain effects. Above the level of non-divergence (near 500 mbs) in this sinking region a strong field of horizontal convergence exists. Parcels moving south-eastward experience a strong production of absolute vorticity in this region. The development at upper levels results in a drop of surface pressure field ahead of the upper trough.

The final surface development between April 13 00Z - 12Z is contributed by differential vorticity advection, Laplacian of thermal advection, latent heat and surface friction. Parcels moving through the lower levels experience strong convergence in the rising motion produced by these effects. The product of $\frac{\partial \omega}{\partial p}$ and ζ_a is indeed very large and these factors contribute significantly. The divergence and deformation effects counteract the development and have a significant effect on the storm dynamics. Some of the other forcing functions that appear to be small in the instantaneous picture may have contributed significantly over longer time scales. Such questions can only be answered by examining a prediction approach to this problem.

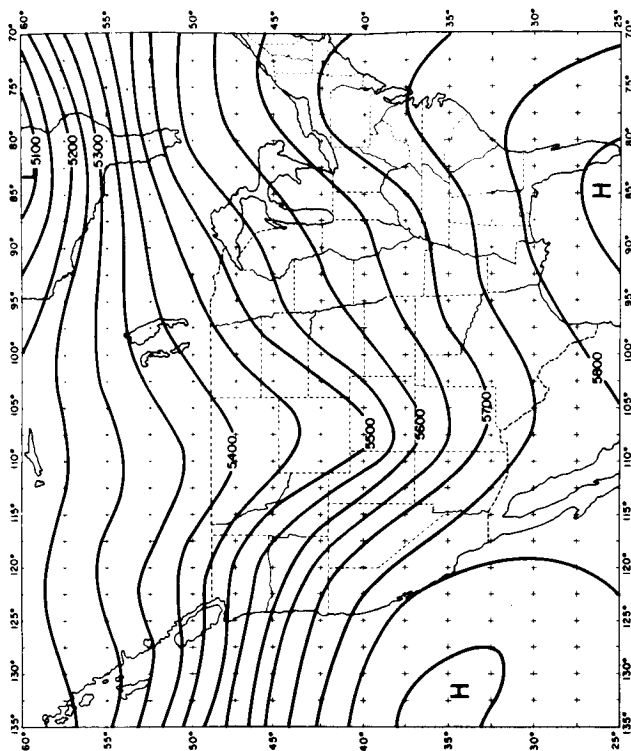
Paegle (1966) has computed three dimensional trajectories from the ψ , χ and ω fields of a balance model, and has discussed some aspects of the development problem. There are still several numerical problems in the interpolation of fields in these three dimensional trajectories, we hope to overcome most of these difficulties in the near future, and thus be able to present a very quantitative assessment of the storm development problem.

Note: This is an extension of a study of the same storm reported by Krishnamurti, Nogues and Baumhefner (1966). The important difference in the two models are inclusion of the effects of terrain, friction, latent and sensible heat. Some minor revisions in the scaling of dynamical equations are also incorporated in this version.

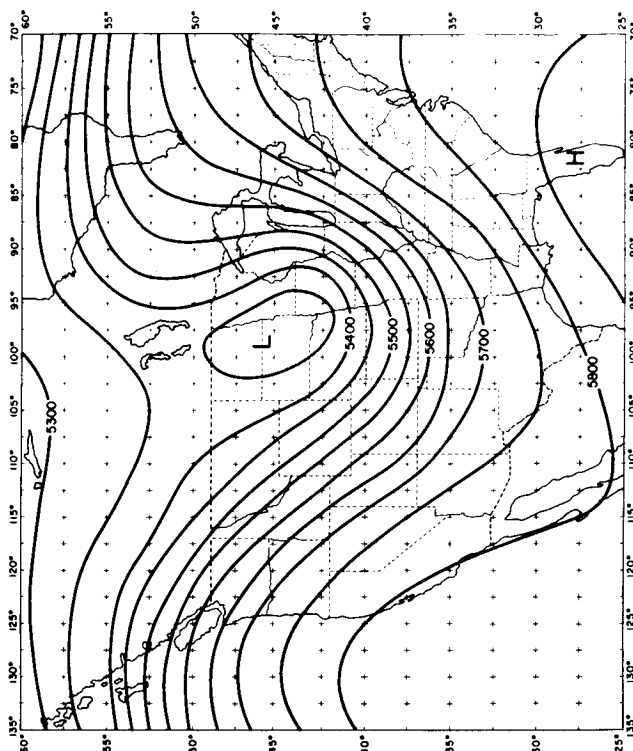
List of References

- Bjerknes, J., 1951: Extratropical Cyclones. Compendium of Meteorology pp. 577-598, American Meteorological Society, Boston, Mass.
- Danielsen, E. F., 1966: Research in Four Dimensional Diagnosis of Cyclonic Storm Cloud Systems. Scientific Report No. 1 to the Air Force Cambridge Laboratories, Pennsylvania State University, University Park, Pennsylvania.
- Krishnamurti, T. N., J. Nogues and D. Baumhefner, 1966: On the Partitioning of Baroclinic Vertical Velocity in a Developing Wave Cyclone. Scientific Report No. 1 to AFCRL, Department of Meteorology, University of California, Los Angeles.
- Newton, C. W., and E. Palmen, 1963: Kinematic and Thermal Properties of a Large-amplitude Wave in the Westerlies. Tellus, Vol. 15, pp. 99-119.
- Paegle, J., 1966: Numerical Calculation of Three Dimensional Trajectories Utilizing the Balanced Horizontal and Vertical Motions. AFCRL Final Report. Department of Meteorology, University of California, Los Angeles. AF 19(628) AFCRL-67-0128.
- Petterssen, S., 1956: Weather Analysis and Forecasting, Vol. 1, Chapter 16, pp. 320-338. The McGraw-Hill Book Company, New York.
- Phillips, N. A., 1963: Geostrophic Motion. Reviews of Geophysics. Vol. 1, pp. 123-176.
- Petterssen, S., 1936: Contribution to the Theory of Frontogenesis. Geofys. Publikasjoner, Norske Videnskaps-Akad. Oslo, Vol. XI, No. 6.

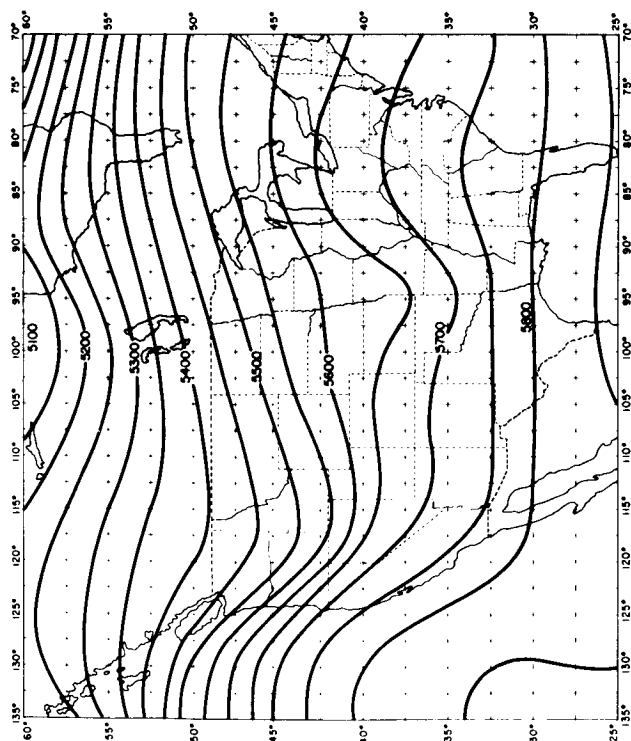
Figure 1. 500 millibar surface heights (meters) for four map times,
April 12, 13 1964.



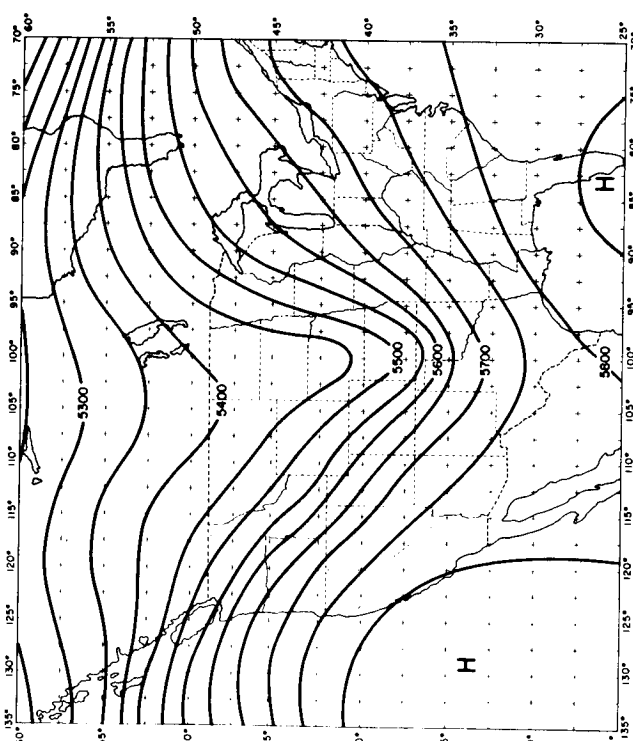
500 MB 12 APRIL 1964 12Z



500 MB 13 APRIL 1964 12Z

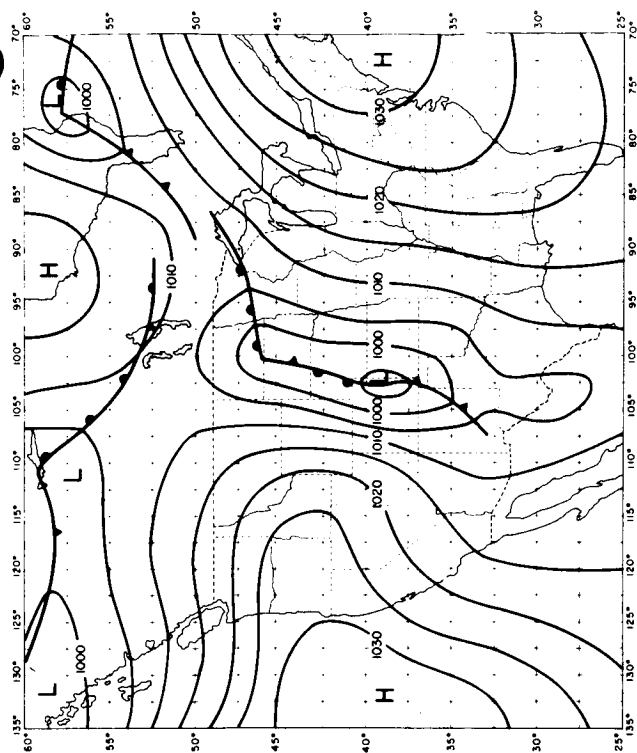


500 MB 12 APRIL 1964 00Z

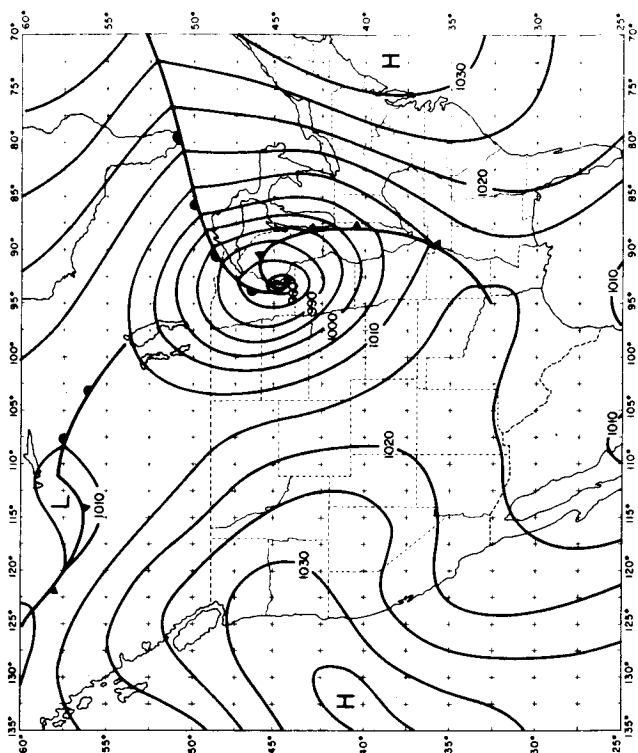


500 MB 13 APRIL 1964 00Z

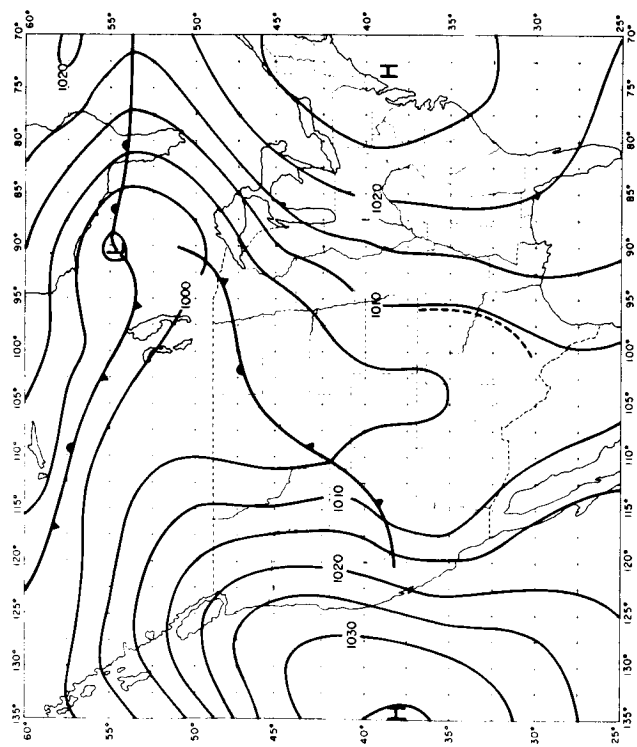
Figure 2. Surface isobars for four map times, April 12, 13 1964.



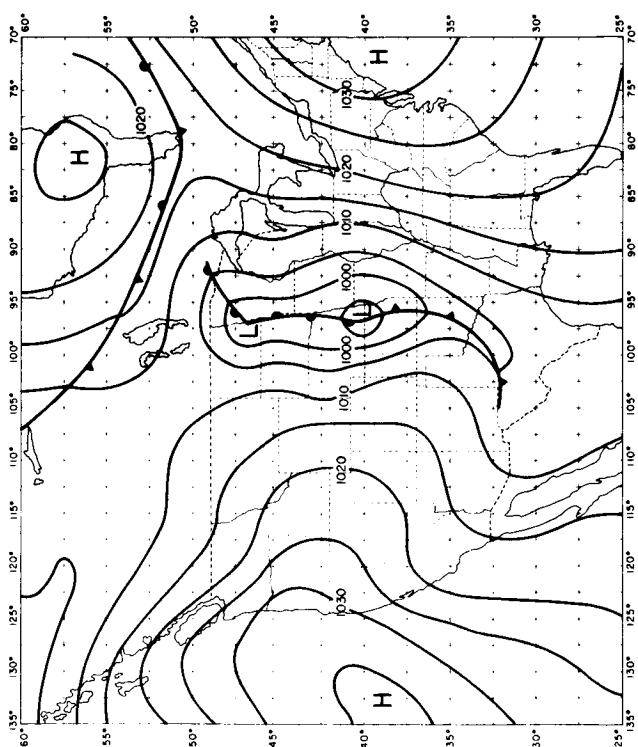
SURFACE MAP 12 APRIL 1964 12Z



SURFACE MAP 13 APRIL 1964 12Z



SURFACE MAP 12 APRIL 1964 00Z

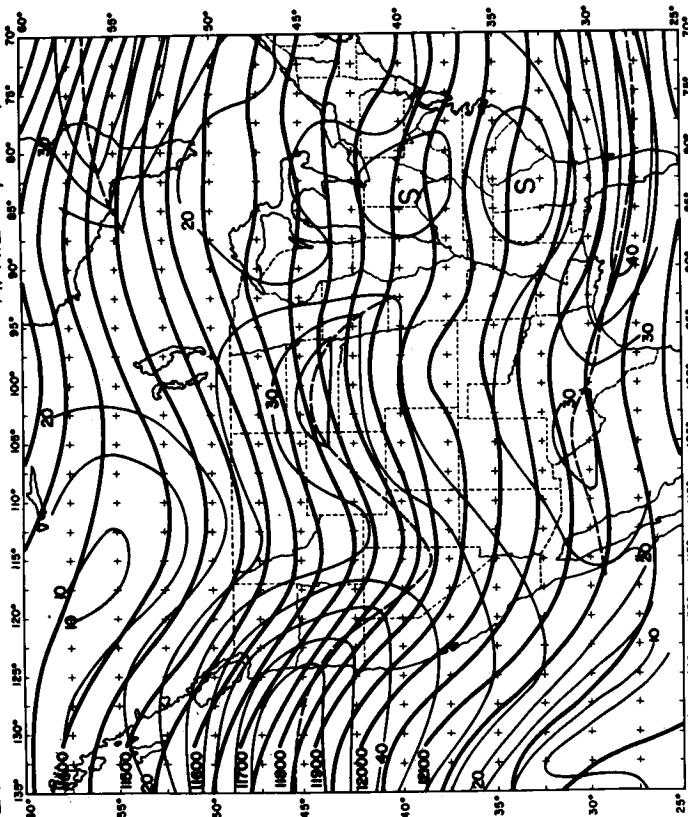


SURFACE MAP 13 APRIL 1964 00Z

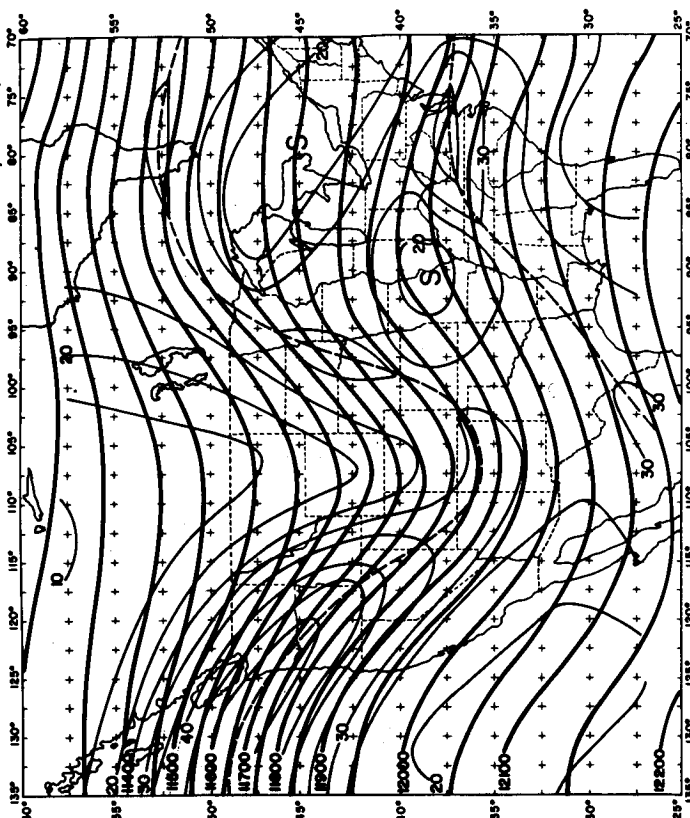
Figure 3. 200 millibar heights (meters) for four map times
(heavy lines) and isotachs of the total wind (thin
lines) meter/sec.

200 mb

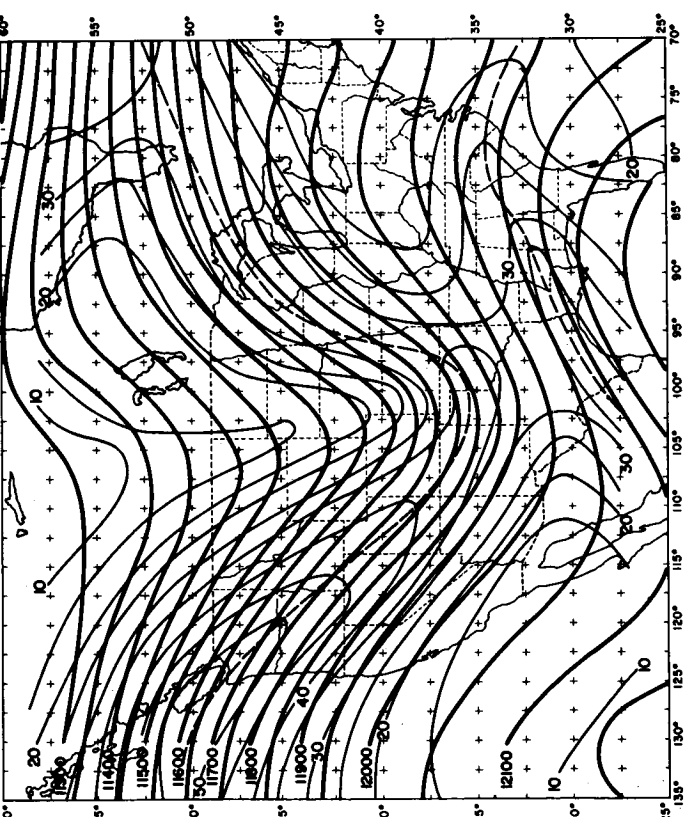
APRIL 12, 00Z, 1964



APRIL 12, 12Z, 1964



APRIL 13, 00Z, 1964



APRIL 13, 12Z, 1964

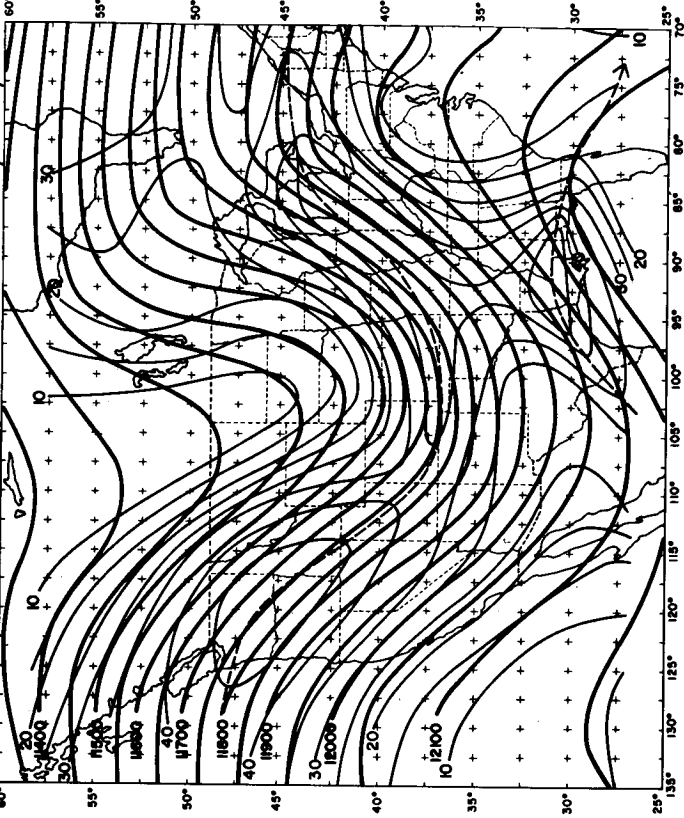


Figure 4. Analysis of total precipitable water (cms) for
four map times.

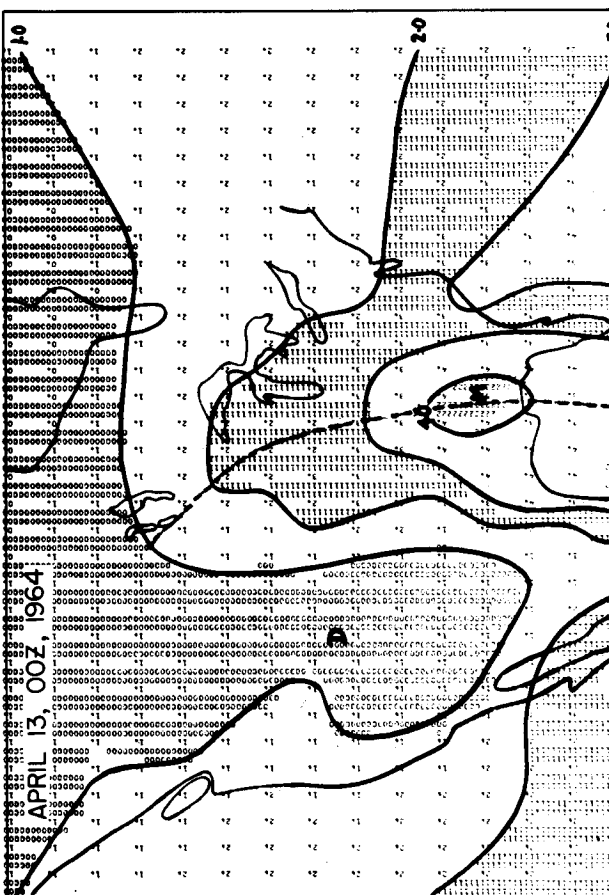
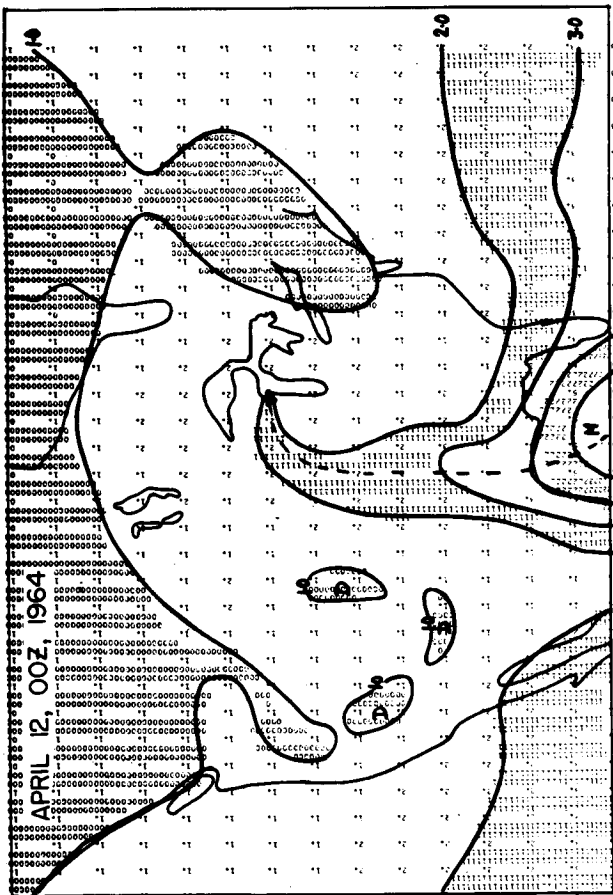
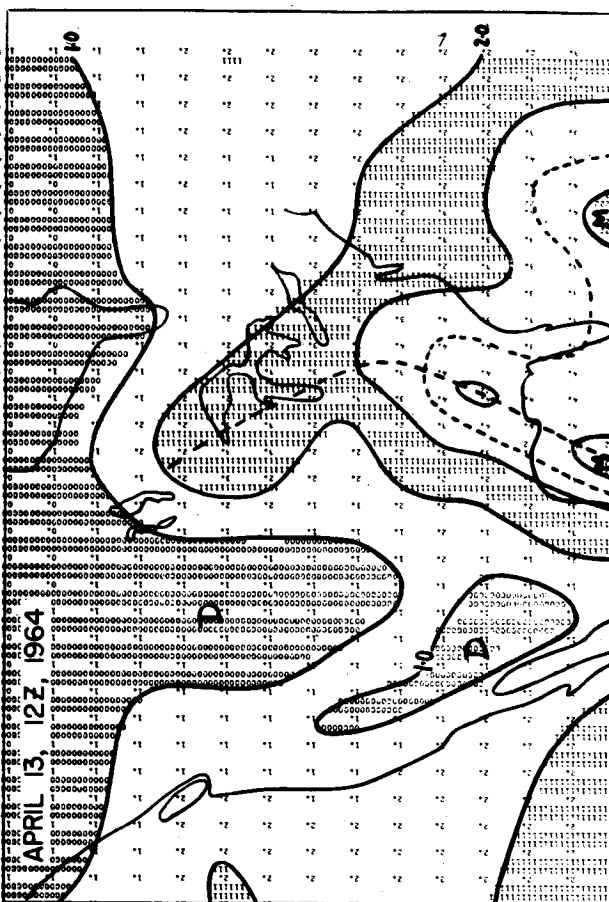
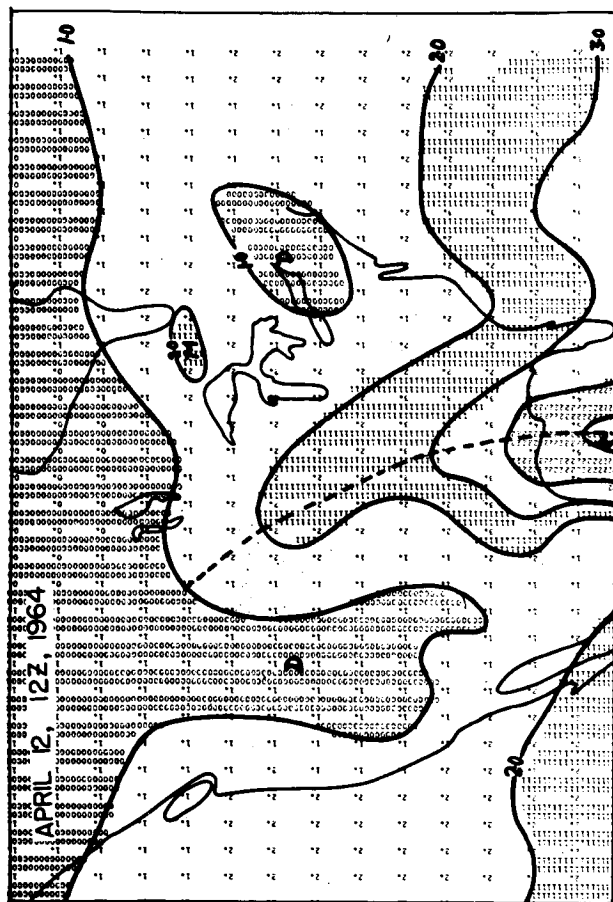
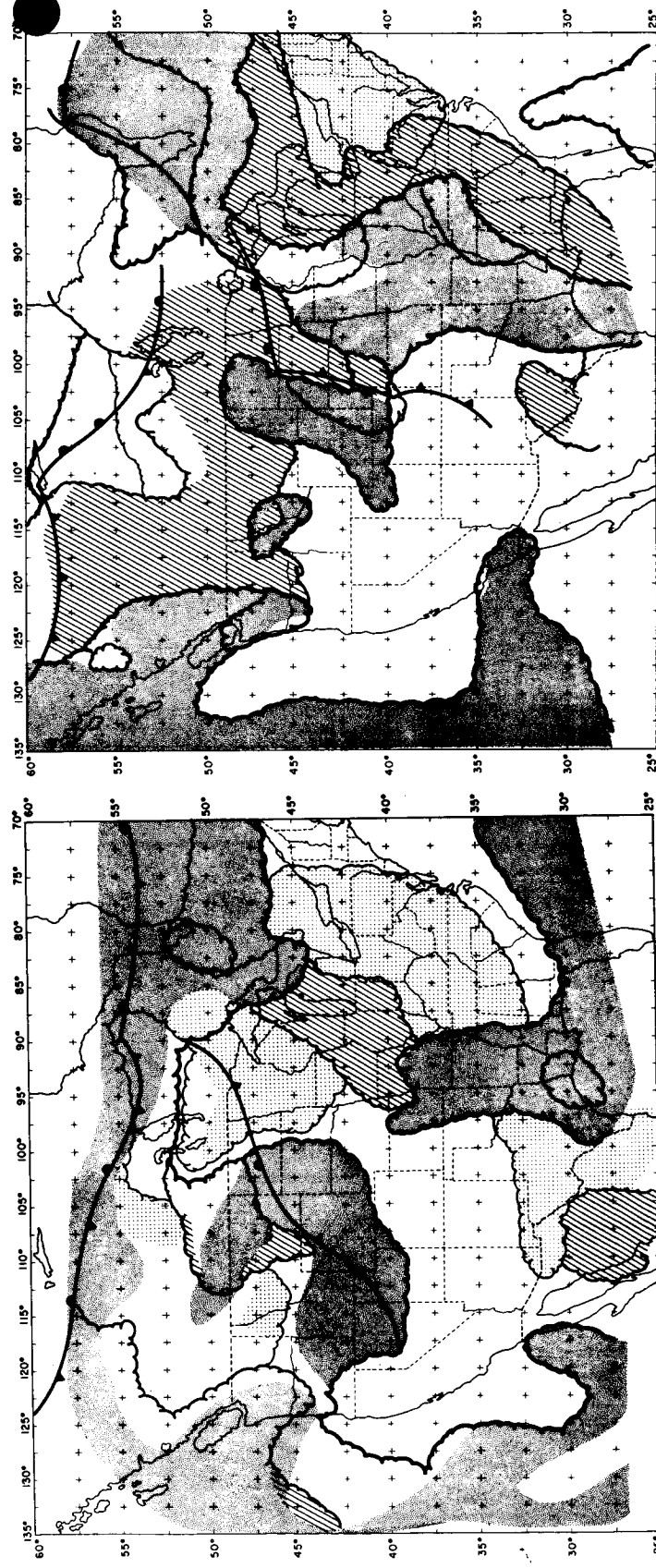
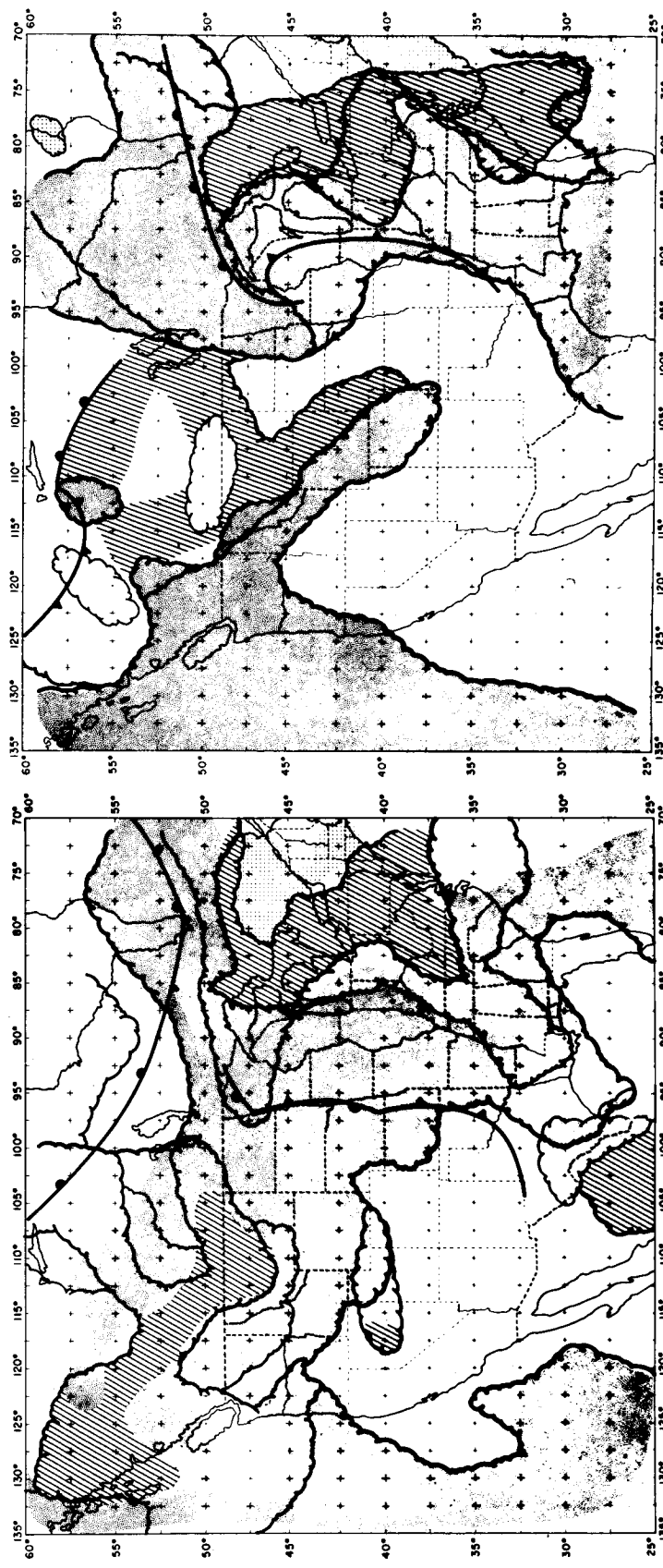


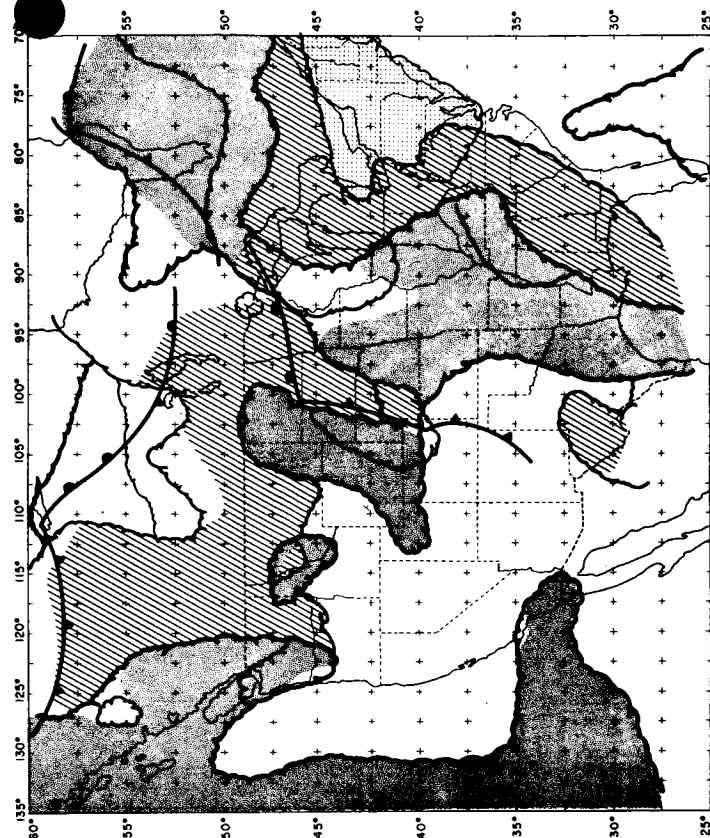
Figure 5. Nephanaalysis for April 12, 13, 1964 for four map
times based on conventional and Tiros data.



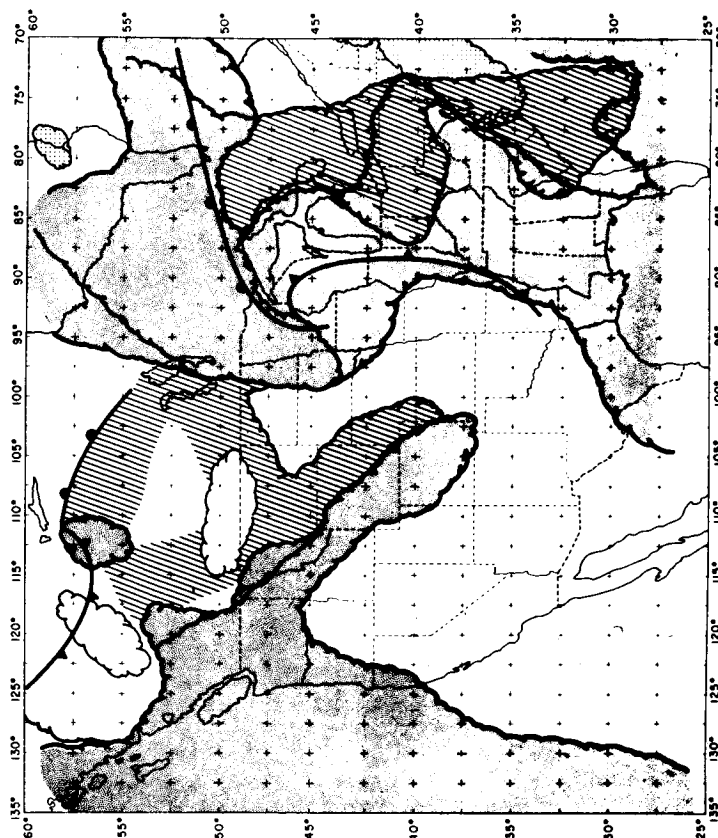
12 APRIL 1964 00Z NEPH ANALYSIS



13 APRIL 1964 00Z NEPH ANALYSIS

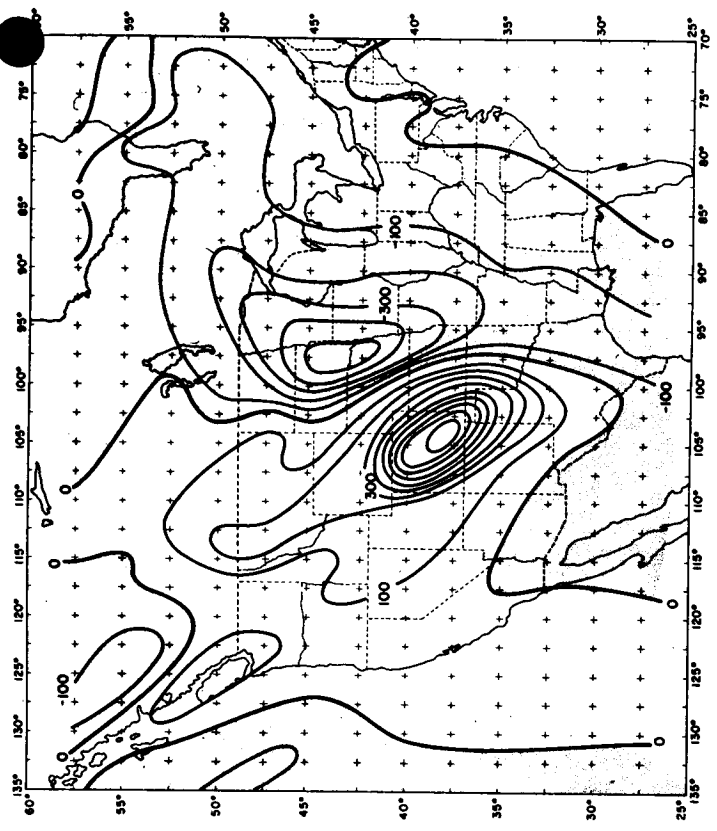


12 APRIL 1964 12Z NEPH ANALYSIS

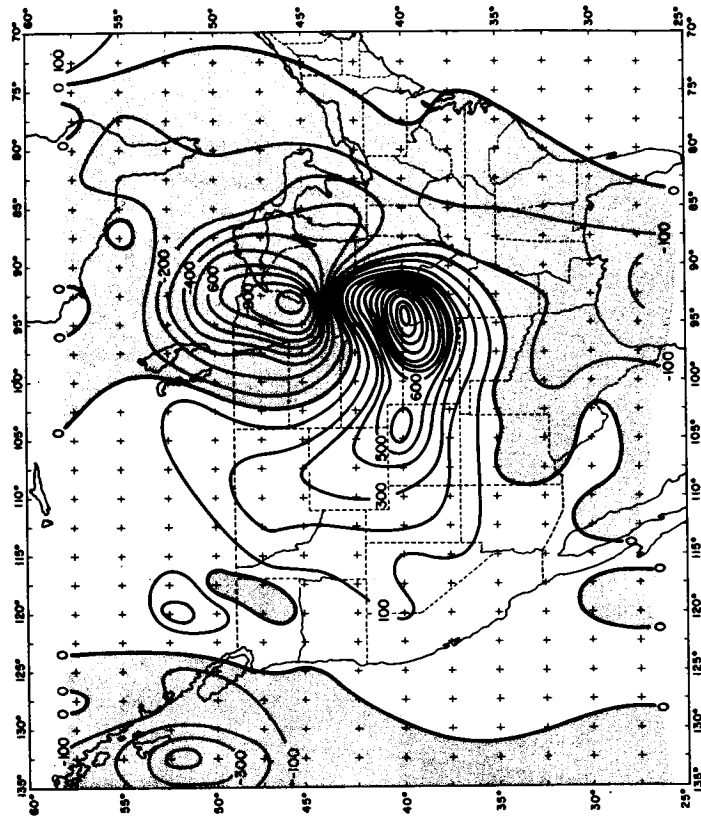


13 APRIL 1964 12Z NEPH ANALYSIS

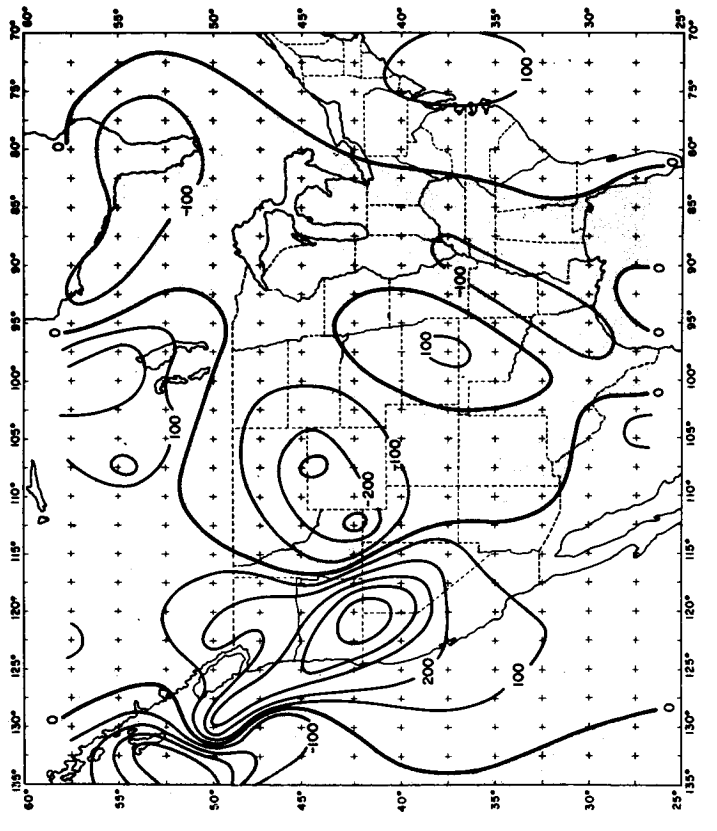
Figure 6. Vertical velocity 10^{-5} mb/sec for April 12, 13, 1964.
(Four map times). The results apply at the 500 mb
surface. Calculations were made using a multi level linear
balance model.



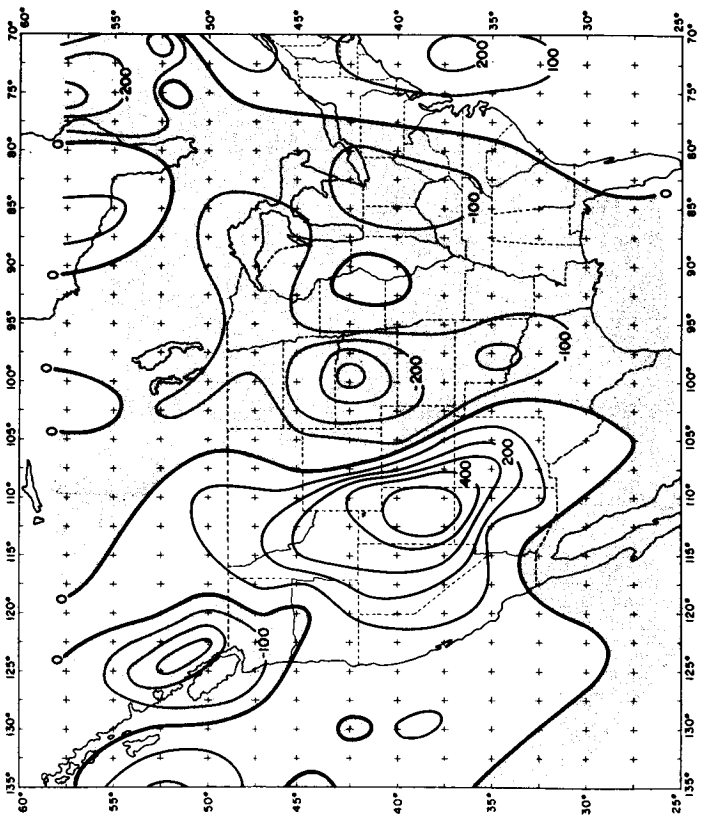
ω_L 500MB 13 APRIL 1964 00Z



ω_L 500MB 13 APRIL 1964 12Z



ω_L 500MB 12 APRIL 1964 00Z

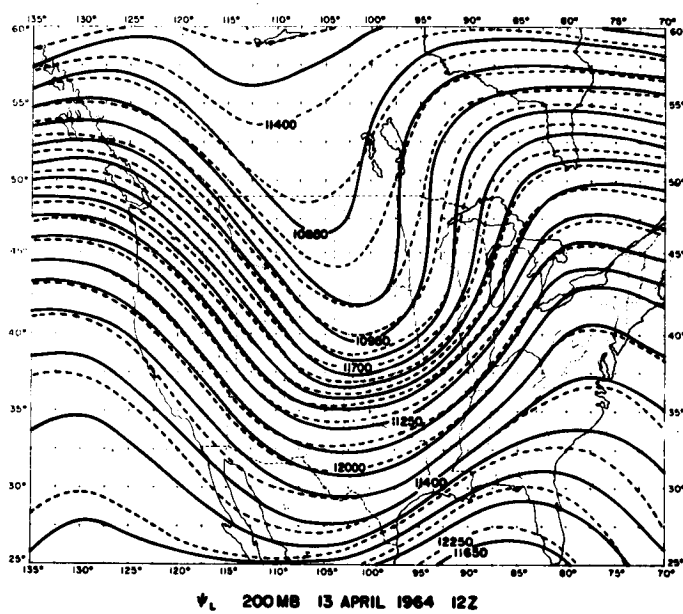


ω_L 500MB 12 APRIL 1964 12Z

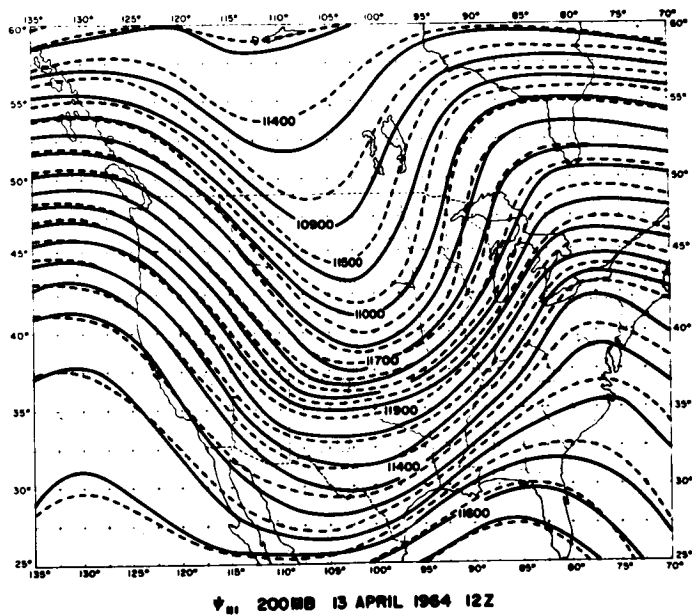
Figure 7. Top: Linear balanced stream function, solid lines
and geopotential heights of the 200 mb surface
shown as dashed lines.

Middle: Semi-geostrophic stream function, solid
lines and geopotential heights of the 200 mb
surface shown as dashed lines.

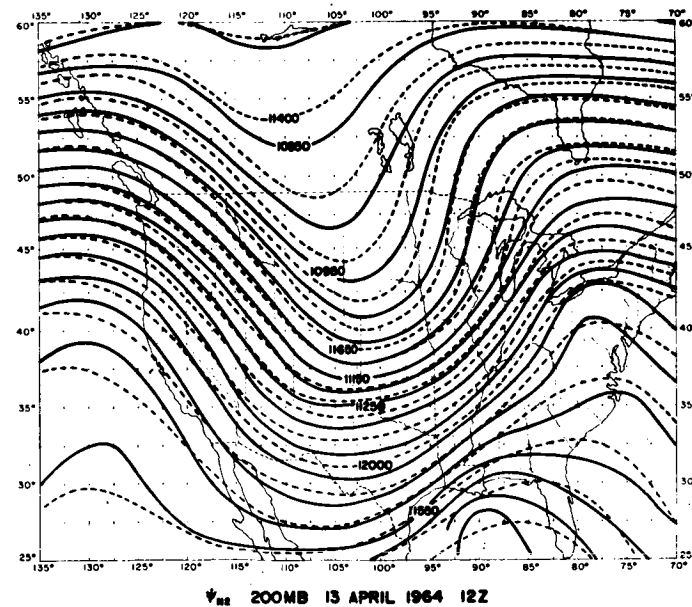
Bottom: Balanced stream function solid lines and
geopotential heights of the 200 mb surface
shown as dashed lines.



ψ_L 200MB 13 APRIL 1964 12Z



ψ_H 200MB 13 APRIL 1964 12Z



ψ_H 200MB 13 APRIL 1964 12Z

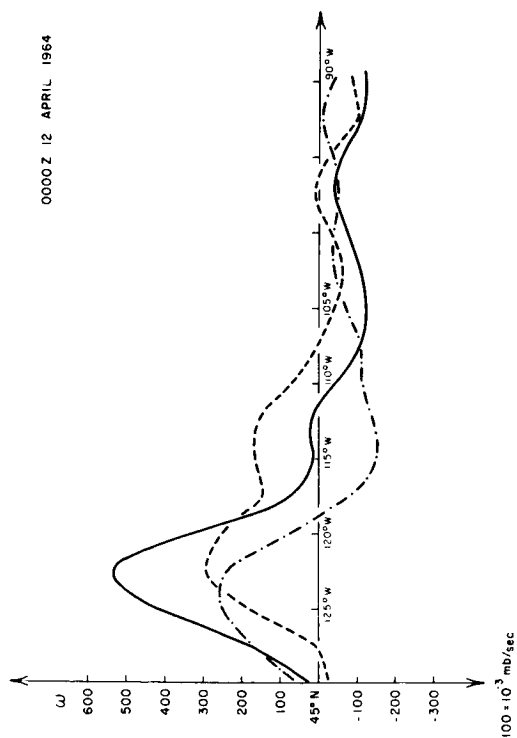
Figure 8. Partitioning of quasi-geostrophic vertical velocity for four map times along a line connecting maximum rising and sinking motions.

Solid line: Total contribution.

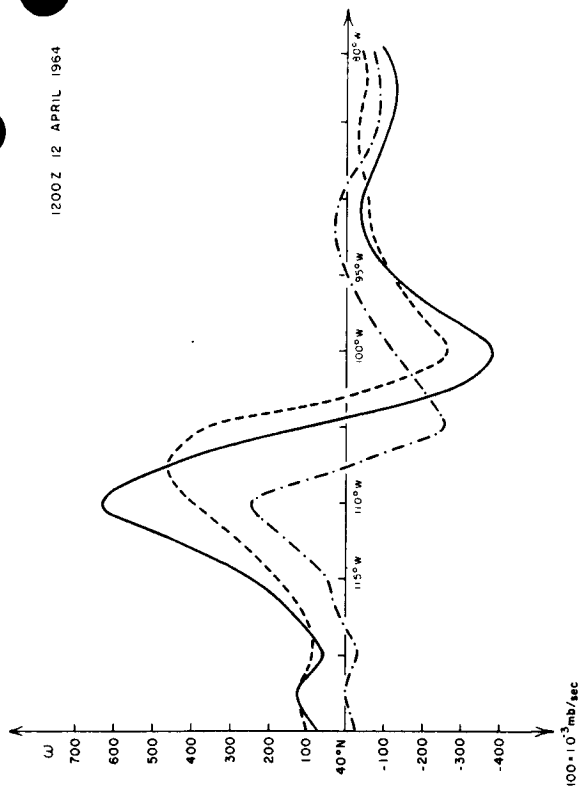
Dash line: Thermal contribution.

Dash Dot line: Vorticity contribution.

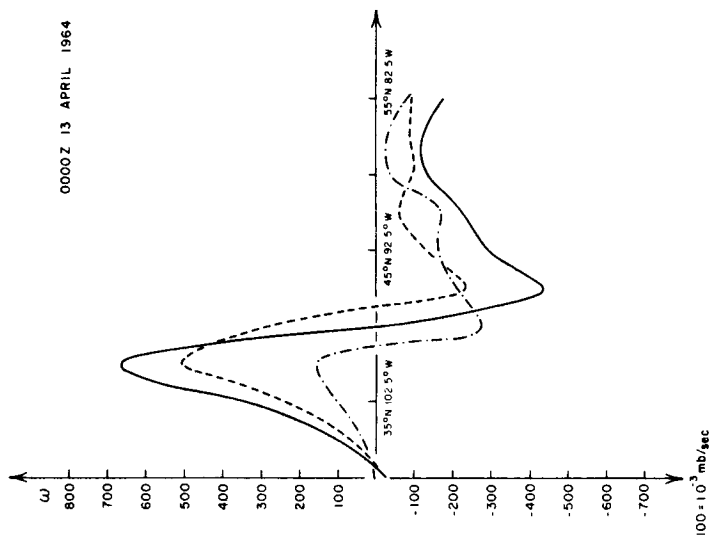
0000 Z 12 APRIL 1964



1200 Z 12 APRIL 1964



0000 Z 13 APRIL 1964



1200 Z 13 APRIL 1964

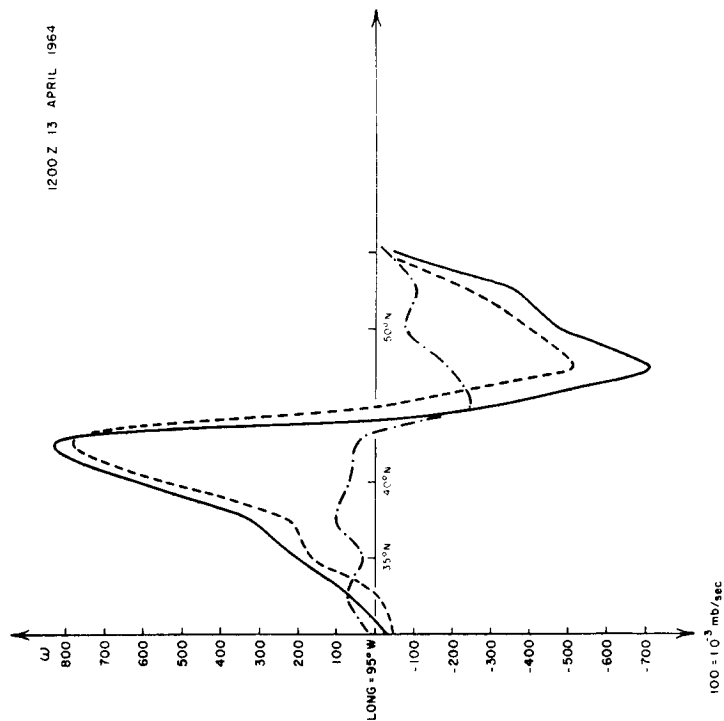


Figure 9. Top left: Total quasi-geostrophic vertical velocity from a 2-level model, at the 500 millibar surface.

Top right: Surface isobars.

Bottom left: Quasi-geostrophic vertical velocity from a 2-level model, at the 500 millibar surface.

(Thermal contribution)

Bottom right: Quasi-geostrophic vertical velocity from a 2-level model, at the 500 millibar surface.

(Vorticity contribution)

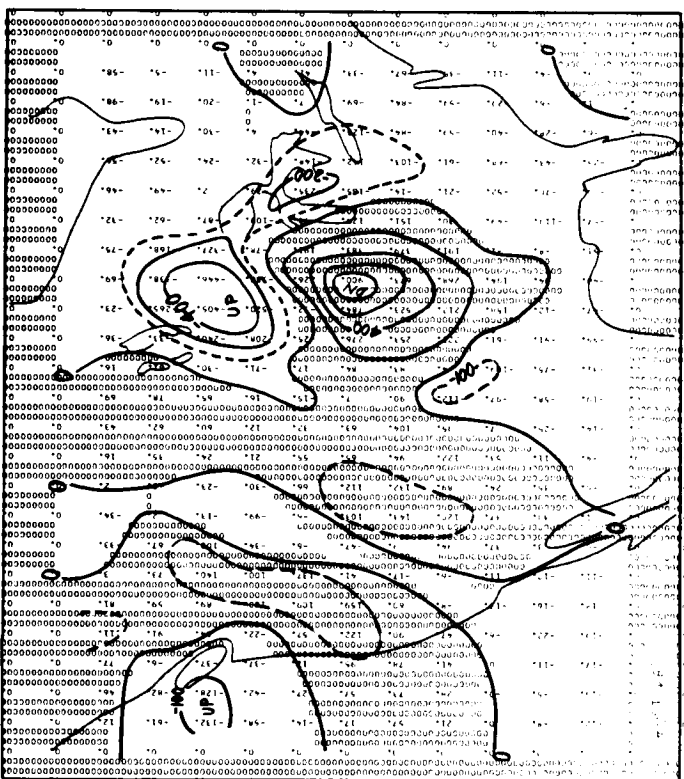
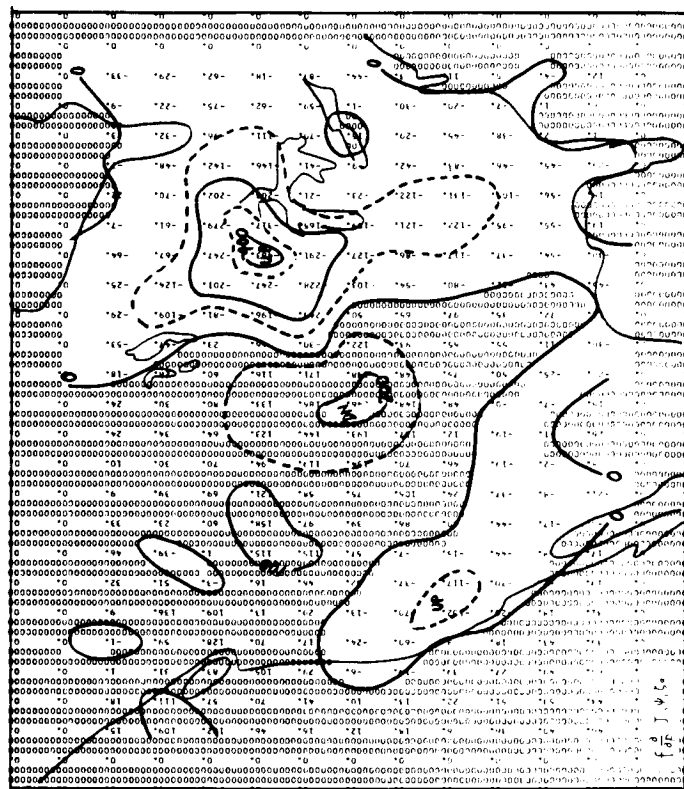
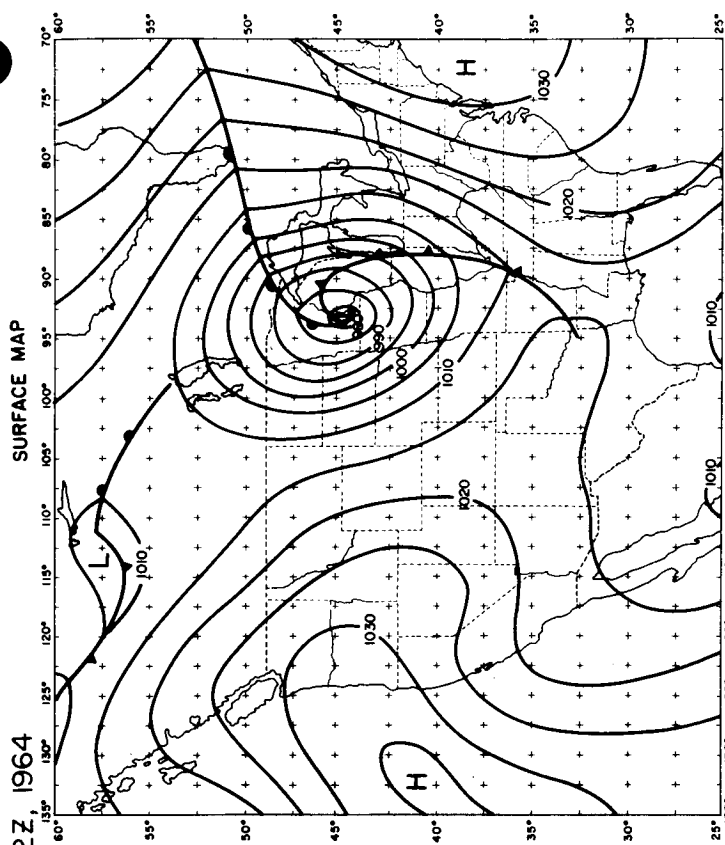


Figure 10. Top: Contribution to balance vertical motion:
differential vorticity advection.

Bottom: Contribution to balance vertical motion:
Laplacian of thermal advection.

APRIL 13, 12Z, 1964

VERTICAL MOTIONS

 10^5 mb/sec

500 mb

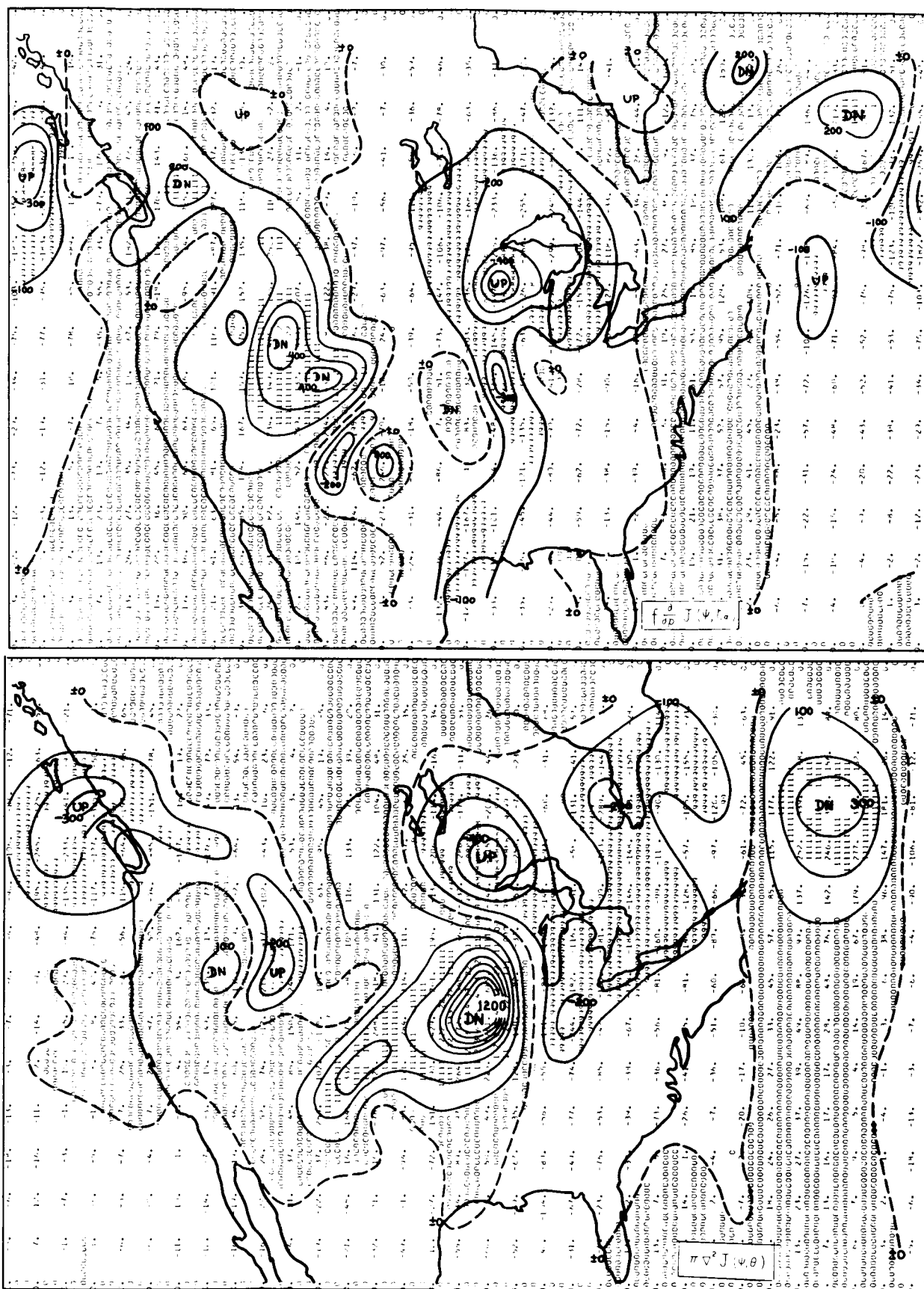


Figure 11. Top: Contribution to balance vertical motion.

Deformation term.

Bottom: Contribution to balance vertical motion.

Divergence term.

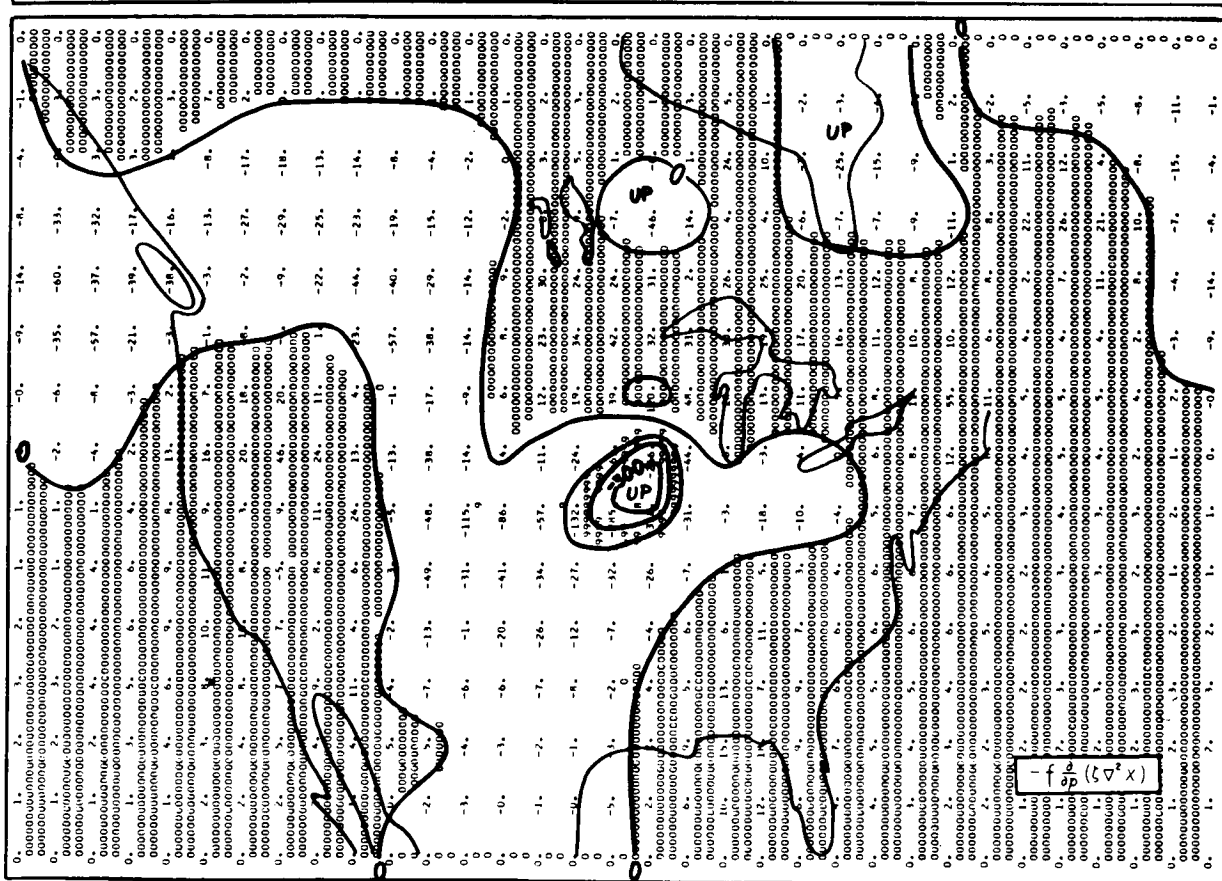
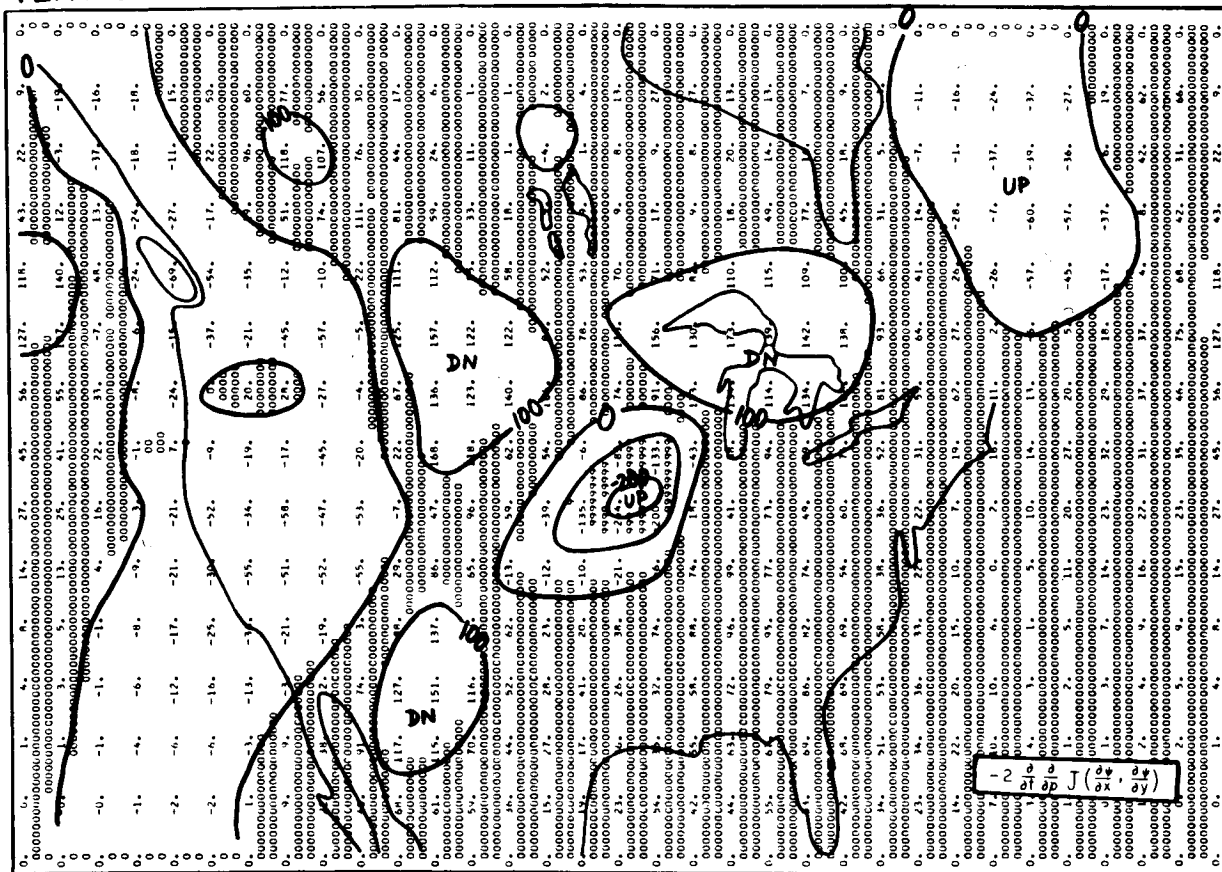


Figure 12. Top: Contribution to balance vertical motion at
1000 millibar surface terrain effect. The dash
lines indicate the surface isobars.

Bottom: Contribution to balance vertical motion by
surface frictional stresses at the 900 millibar
surface.

Figure 13. Decay of frictional vertical velocity plotted against pressure (ordinate) for a selected point from Figure 9 (bottom).

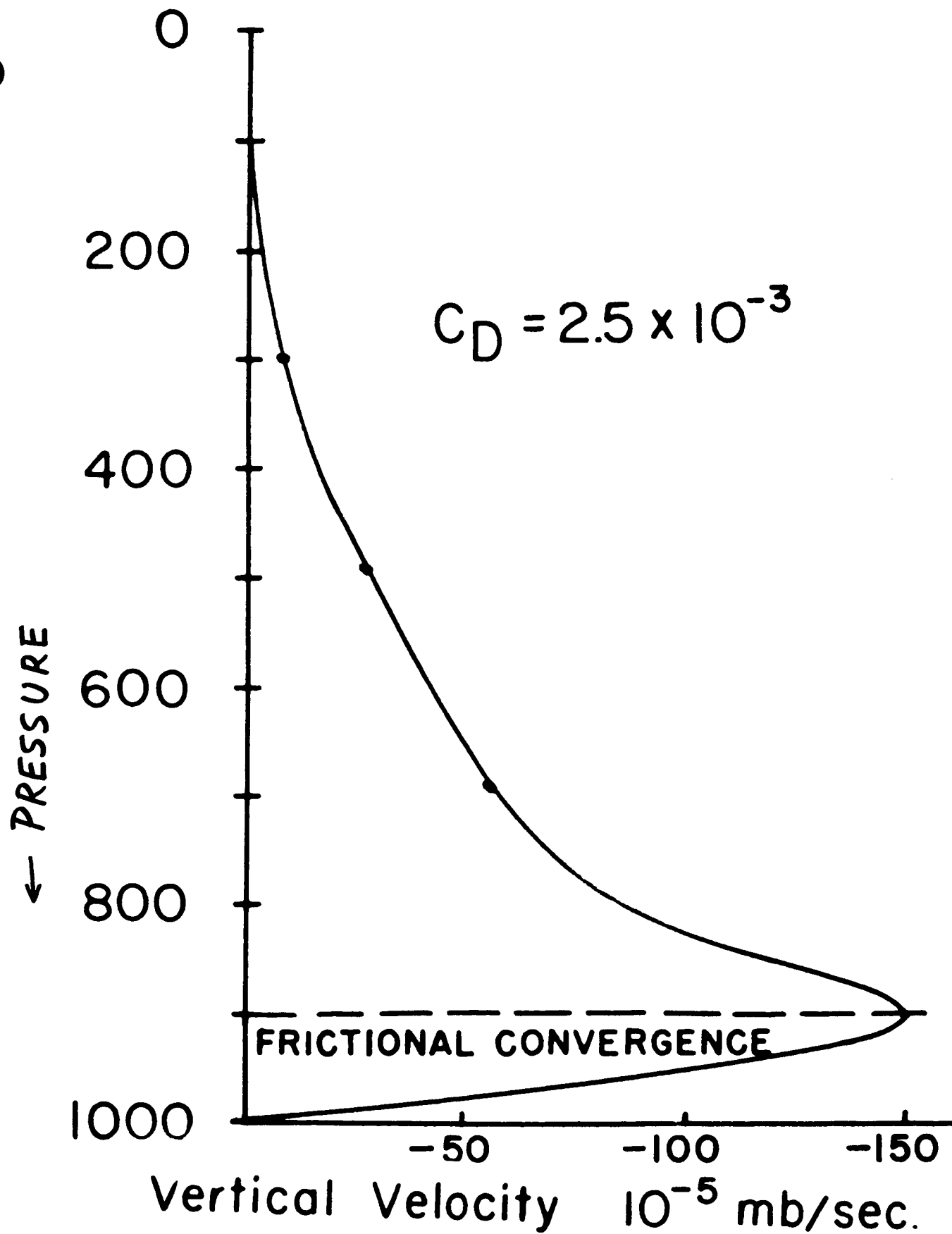


Figure 14. Contribution to the balance vertical motion from latent heat release at the 900, 700, 500 and the 300 millibar surface. Pressure levels and magnitudes are indicated on the maps. (April 13, 12Z 1964)

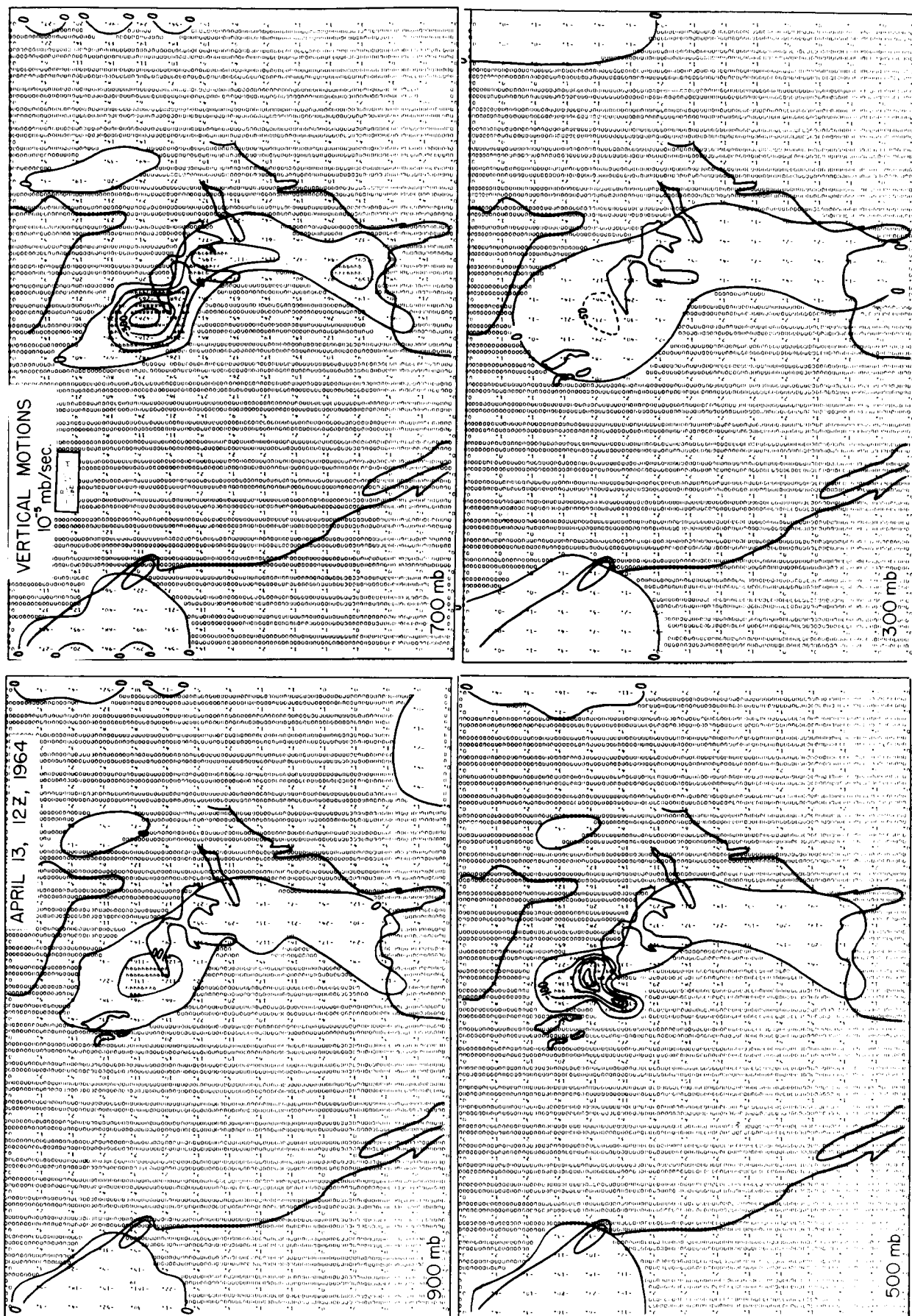


Figure 15. Top: Total balance vertical motion including contributions of 12 forcing functions and terrain.

Bottom: Balance vertical motions, sum of contribution from differential vorticity advection and Laplacian of thermal advection.

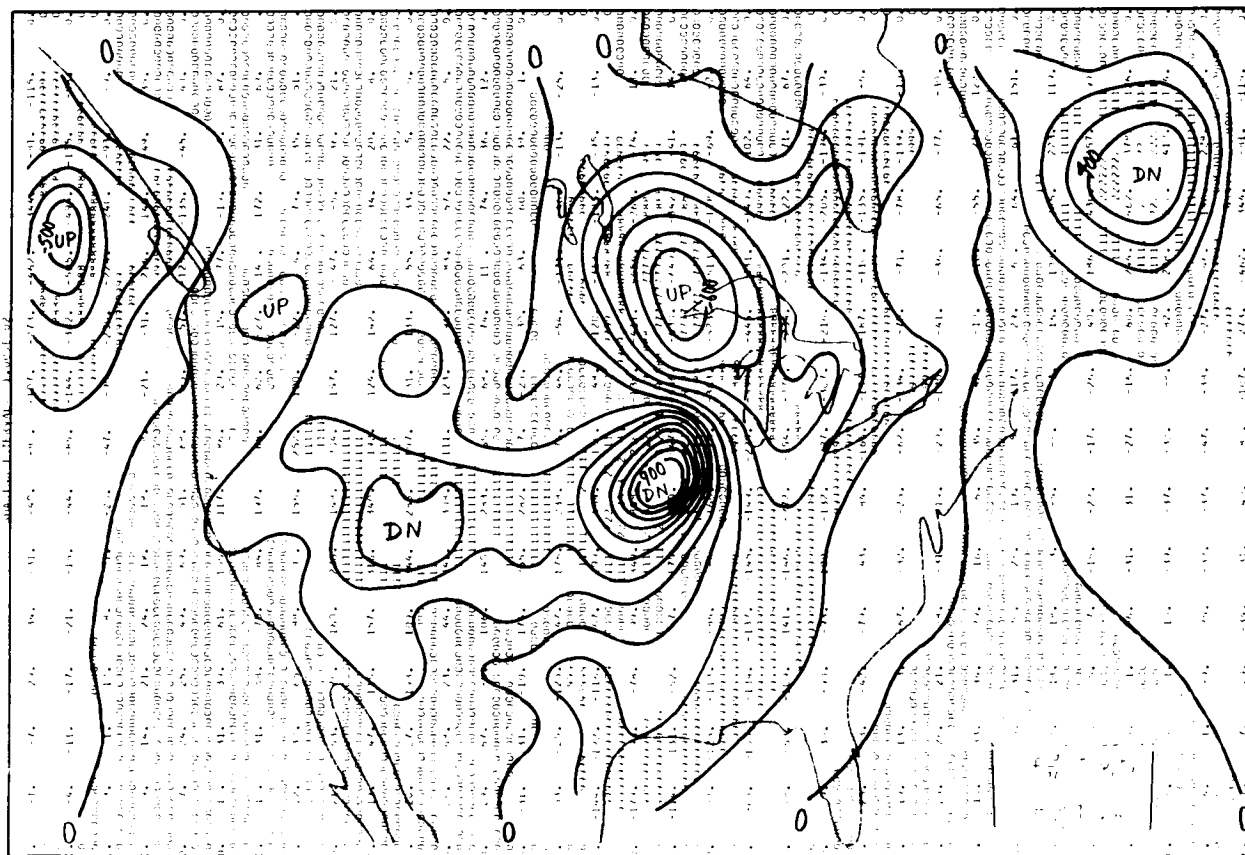
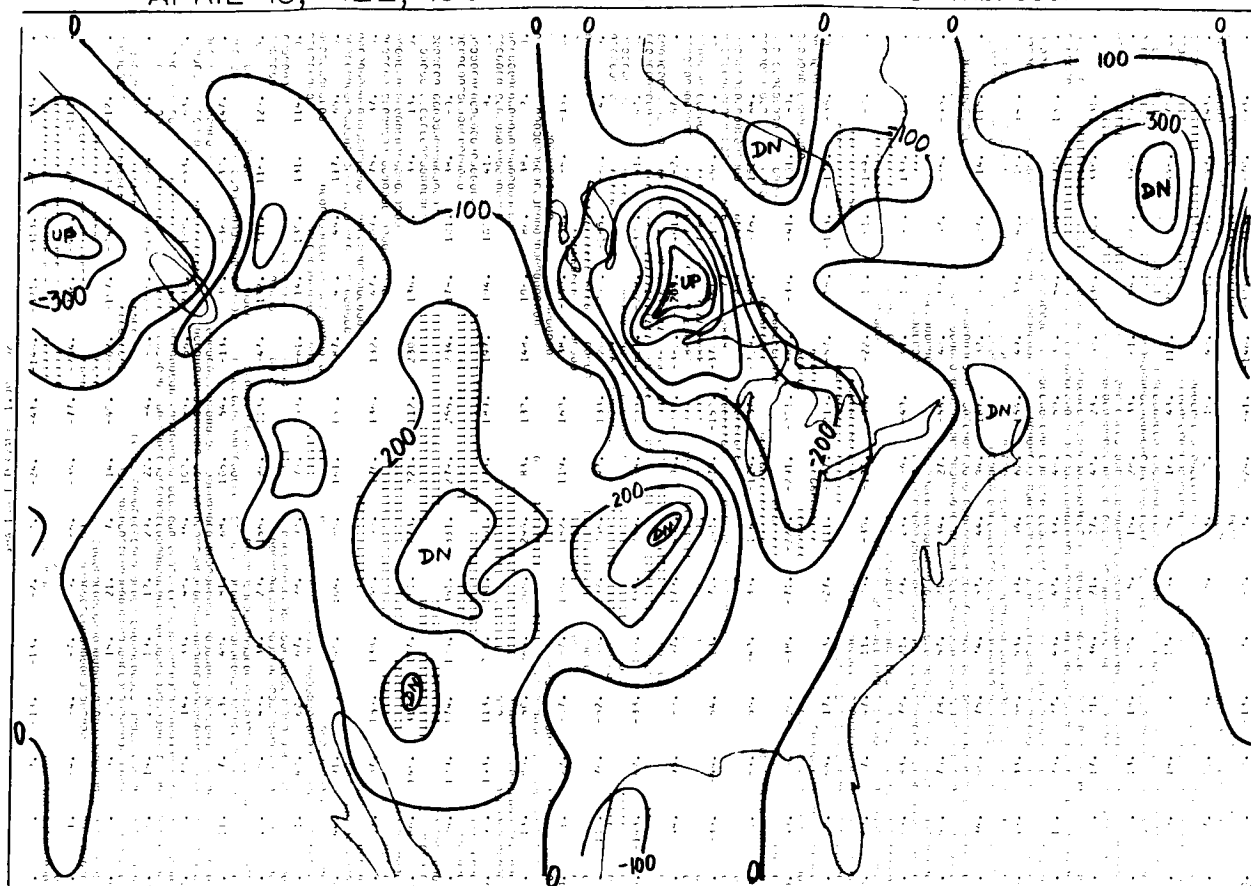


TABLE 1. Contribution to the vertical motion by different forcing functions.

FORCING FUNCTIONS	Vertical motion in units 10^9 m/sec at different points.							
	1	2	3	4	5	6	7	8
1. $f \frac{\partial}{\partial p} J(\psi, \zeta_a)$	-121	-135	-14	-63	-326	-266	-255	-171
2. $\pi \nabla^2 J(\psi, \theta)$	35	128	180	82	-37	-257	-258	-7
3. $-2 \frac{\partial}{\partial t} \frac{\partial}{\partial p} J\left(\frac{\partial \psi}{\partial x}, \frac{\partial \psi}{\partial y}\right)$	88	74	18	-43	173	130	82	9
4. $-f \frac{\partial}{\partial p} (\zeta \nabla^2 x)$	6	-7	-31	-44	48	31	2	-14
5. $f \frac{\partial}{\partial p} g \frac{\partial}{\partial p} \left[\frac{\partial \zeta_y}{\partial x} - \frac{\partial \zeta_x}{\partial y} \right]$	-8	-14	-19	-47	-41	-38	-32	-17
6. $-\frac{R}{C_{pp}} \nabla^2 H_L$	1	6	7	14	-14	-13	-372	-27
7. $-\frac{R}{C_{pp}} \nabla^2 H_s$	0	0	0	0	1	1	1	1
8. $f \frac{\partial}{\partial p} (\omega \frac{\partial}{\partial p} \nabla^2 \psi)$	13	15	10	15	13	16	78	35
9. $f \frac{\partial}{\partial p} (\nabla \omega \cdot \nabla \frac{\partial \psi}{\partial p})$	-14	-23	-21	-26	-19	-10	-8	-18
10. $-f \frac{\partial}{\partial p} (\nabla x \cdot \nabla \zeta_a)$	9	26	25	29	38	15	-9	0
11. $-\pi \nabla^2 (\nabla x \cdot \nabla \theta)$	-6	-7	-15	8	22	29	18	2
12. $-\beta \frac{\partial}{\partial p} \frac{\partial}{\partial y} \frac{\partial \psi}{\partial t}$	10	7	2	-5	-7	-8	-7	-4
TOTAL WITHOUT TERRAIN	13	70	141	-80	-151	-370	-761	-212
TOTAL WITH TERRAIN	13	71	141	-79	-150	-370	-761	-212

N67-30787

Numerical Calculation of Three Dimensional Trajectories

Utilizing the Balanced Horizontal and Vertical Motions

By Jan Paegle

ABSTRACT

Three dimensional trajectories have numerous applications in synoptic studies. In addition to studying the path itself of a parcel, other effects can be investigated such as the total derivatives of parcel parameters.

Three previous trajectory studies are reviewed briefly to illustrate the methods used in their computation and the sort of investigations which are best done with the use of trajectories. Two of these methods use the adiabatic assumption, calculating isentropic trajectories and the third computes constant density trajectories. A method for computing trajectories from a balanced diagnostic model in a pressure coordinate system is presented in more detail. Some specific results of this method are presented and compared with the results from one of the adiabatic methods.

Sensitivity of the results to the computational scheme is discussed and the importance of good time and space interpolation is stressed.

1. Introduction

This discussion of trajectories will be divided into descriptions of their uses, some methods of computing them, and the results of the applications of these methods to particular cases.

Trajectories have a variety of potential uses. In the past they have been used to study scales of motion ranging from the cumulus scale, Murray (1965) to the hemispheric scale, Mesinger (1965). Many such studies have investigated just the motion of the parcels. Mesinger (1965) computed parcel densities, Danielsen (1966) computed vertical motions, and Nagle and Clark (1966) related trajectory histories to cloud patterns.

Trajectories can be used for other applications also. Total derivatives of quantities such as potential temperature and vorticity may be calculated directly by computations along trajectories. Phenomena such as the maintenance of a blocking high, the development of a tropical depression and other inadequately explained occurrences can be more effectively studied by seeing what goes into such systems to develop or maintain them. The relative strength of various effects such as convergence and frictional stresses to modify systems can probably be studied best along trajectories. Thus trajectories are an important tool in studying the processes which go on in the atmosphere.

2. Methods of computing trajectories

Several methods exist for computing trajectories. Some of the more popular of these have used the adiabatic assumption to compute trajectories on isentropic surfaces. Nagle and Clark (1966) used this method to compute trajectories on a single isentropic surface. The method was to allow the wind field to advect the air parcels according to the following scheme:

$$\text{integrate } \frac{dx}{dt} = u \quad \frac{dy}{dt} = v \quad \text{in time}$$

$$\text{using } \mathbf{V} = \frac{1}{f} \mathbf{K} \times \nabla_{\theta} \Psi + S^{-1} \nabla \chi$$

$$\text{where } \Psi = gz + c_p T \quad (\text{Montgomery stream function})$$

$$\text{and } S = \frac{\partial p}{\partial \theta}, \quad \nabla_{\theta}^2 \chi = -\frac{\partial S}{\partial t} - \nabla_{\theta} \cdot \left[\frac{S}{f} \mathbf{K} \times \nabla_{\theta} \Psi \right]$$

The time step used was 1/2 hour and the stream function was computed from the pressure height of the 305 deg. isentropic surface interpolated at half hour intervals between standard map times.

Danielsen (1966) calculated isentropic trajectories graphically. His scheme was to solve the equations:

$$\Psi_f = \Psi_i - \frac{1}{2} (V_f^2 - V_i^2) + \int_{t_i}^{t_f} \frac{\partial \Psi}{\partial t} dt$$

$$D = \frac{1}{2} (V_f + V_i) \Delta t$$

simultaneously by a graphical iterative scheme. The first equation represents the change in the Montgomery stream function with time and the second the distance

traveled in that time. A time step of 12 hours was used and the smoothness of the trajectory was insured by making it tangent to the Ψ_i streamline at the first time and to the Ψ_f streamline at the final time. The computation was carried on at three isentropic surfaces.

Another type of trajectory which can be computed is the constant density (isopycnic) trajectory. This type of trajectory has become of increasing interest recently because of the possibility of setting up a large number of constant density balloons as a data network. Mesinger (1965) computed 30 day trajectories in order to study this at the three constant density surfaces roughly corresponding to 800 mb, 700 mb, and 300 mb. The method was similar to Nagle and Clark's (1966) work. The equations:

$$\frac{dx}{dt} = u, \quad \frac{dy}{dt} = v$$

were integrated in time with steps of about one hour using:

$$\mathbf{V} = \mathbf{k} \times \nabla_p \Psi + \nabla_p \chi$$

$$\text{where } \Psi \text{ is from } \nabla_p^2 \xi - \frac{1}{f} \nabla_p f \cdot \nabla_p \xi - f \nabla_p^2 \Psi = 0$$

$$\text{where } \xi = gz + RT$$

$$\text{and } \nabla_p^2 \chi = \nabla_p \mathbf{V}$$

Isopycnic trajectories are not applicable to an actual parcel of air since the atmospheric processes are not characterized by constant density. The adiabatic assumption is also not always good, and presents some practical problems if the

trajectories to several points in the vertical are needed, since each of the isentropic surfaces which pass through these points must be analyzed. The trajectories which will be presented here are computed by a somewhat different scheme using a diagnostic balanced model in a pressure coordinate system. This method will be discussed in more detail.

Again the equations:

$$\frac{dx}{dt} = u, \quad \frac{dy}{dt} = v, \quad \frac{dp}{dt} = \omega$$

are integrated in time. The wind field is obtained from:

$$\mathbf{V} = \mathbf{k} \times \nabla_p \Psi - \nabla_p \chi$$

where Ψ is from $\nabla \cdot (f \nabla \Psi) = \nabla^2 \phi - 2J(u, v)$

and χ from $\nabla^2 \chi = \frac{\partial \omega}{\partial p}$

The vertical motion is computed through a scheme of successive iterations to obtain ω from the non-linear balanced ω -equation (Krishnamurti, Nogues, Baumhefner (1966)).

Winds are given at five pressure levels (1000, 800, 600, 400 and 200 mb) and vertical motions at four pressure levels (900, 700, 500 and 300 mb) on a 33×15 grid. The winds are smoothed by an eight point averaging in the horizontal and vertical. This results in 27 points being weighted when the velocity of a parcel is linearly interpolated between the nearest eight smoothed data values. The smoothing for the vertical motions is done by a four point averaging, not eight, and only in the horizontal, in order to specify smoothed winds and vertical motions at

the same grid points. The reason for this weighting is to insure smooth trajectories, especially as the parcel passes from one grid cube to the next.

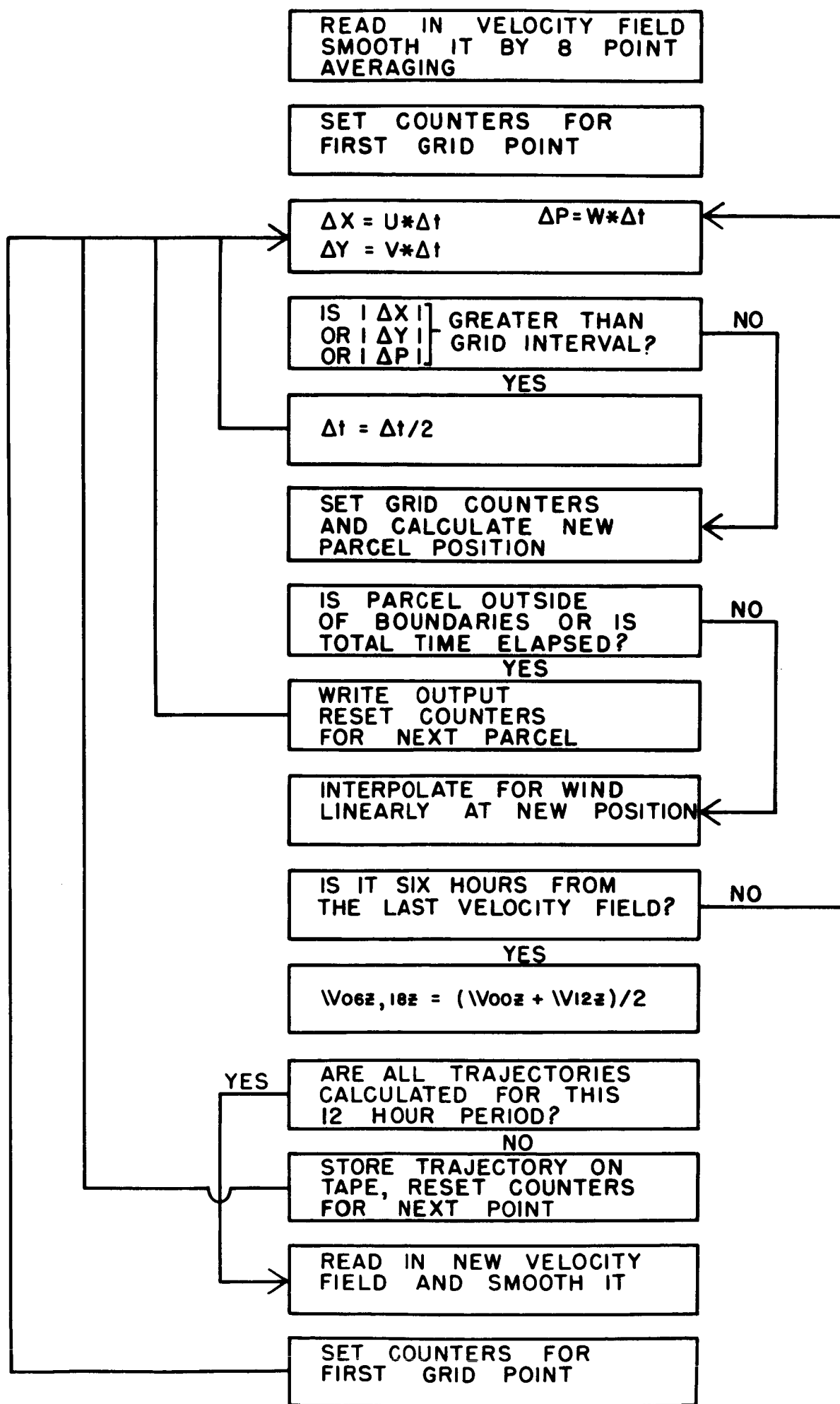
The wind data from one map time is allowed to advect the parcel for six hours before the map time and six hours after--a total of 12 hours. At the time corresponding to six hours between map times a mean wind of both is used and this is the extent of the smoothing done in time. This would seem to be one area of needed refinement but results show that the trajectories are quite smooth even at the time of transition of data from different map times.

A computer program is used to compute the trajectories. Each trajectory ends on a grid point at the final map time. The wind at that point is allowed to advect the air parcel backward in time for some specified time interval (of the order of an hour) to a previous location. The interpolation and smoothing scheme defined above is used to advect the parcel backward in time over the next time interval and this continues backward in time. A new velocity field is read in for each 12 hours. The parcel is followed until the time of the trajectory is over or until it is found to have originated outside the grid network. Then the same procedure is followed for the next parcel.

If only the wind field of one map time is used and the vertical motions are set equal to zero the result is a streamline, which is another useful application of the technique.

A very much simplified flow chart is presented in Figure 1. The major part of the program is calculation of the parcel position by keeping track of the grid

Figure 1: Flow Chart for Computer Program used to Calculate Trajectories.



cube within which the parcel is located. This necessitates checks of distance traveled by a parcel to compare with its distance from the sides of the grid cube within which it is advected. As it passes from one grid cube to the next at least one of three counters changes to correspond to its passage through a grid wall. These counters are constantly checked with values corresponding to boundaries which are at 200 mb, 900 mb and $1/2$ the grid spacing within the horizontal boundaries.

It is also necessary to always know the exact distance of the parcel from the nearest eight grid points in order to correctly interpolate for the velocity field. The problem is complicated by the fact that the north south grid lines are curved. This necessitates the knowledge of the exact latitude of the parcel to correctly interpolate.

The output parameters for each trajectory are parcel position, velocity components, and speed at each time interval. Also it would be easy to output values of moisture, vorticity, or some other field whose conservative properties are of interest.

3. Results

The most apparent trajectory results come from looking at the paths of the parcels. Thus the purpose of Nagle and Clark's (1966) study was to relate cloud observations from satellites to mass motion parameters of the atmosphere. The major finding was that the net vertical parcel displacement along trajectories correlated

better with deep layer cloudiness than did any instantaneous parameter. Mesinger (1965) found that using just the non-divergent part of the wind produced random distributions of the constant density particles. Introducing the divergent part of the wind produced clustering of the parcels with some relatively parcel free regions in the area of the subtropical high. After 30 days this was not felt to be serious enough to impair the effectiveness of such a data network. A main reason for Danielsen's (1966) work was to compute vertical motions. He found maximum values of the order of 200 mb/12 hr, and supported Nagle and Clark's (1966) finding that the cloud pattern depends more upon the history of the parcel than upon any instantaneous parameter such as vertical motion.

Four synoptic scale cases have been studied using the trajectory calculation proposed here. Two of these were intense developments of mid-latitude storms over the United States and two were tropical cases over the Caribbean and Gulf of Mexico regions.

From these studies several immediate conclusions can be drawn. One impression of the results is that the trajectories are quite smooth and apparently representative of the large scale. Maximum lengths for 42 hour trajectories are of the order of 3000 miles and 300 mb for intense mid latitude storms. For the tropical examples maximum distances traveled were about 1000 km in 54 hours and about 50 mb vertical displacement. Figure 2 shows trajectories computed for an April 1964 case studied by Krishnamurti, Nogues, and Baumhefner (1966).

Figure 2. Top: Backward trajectories in time labeled with hourly positions. Final positions correspond to hour zero and are for 12Z 13 April 1964.

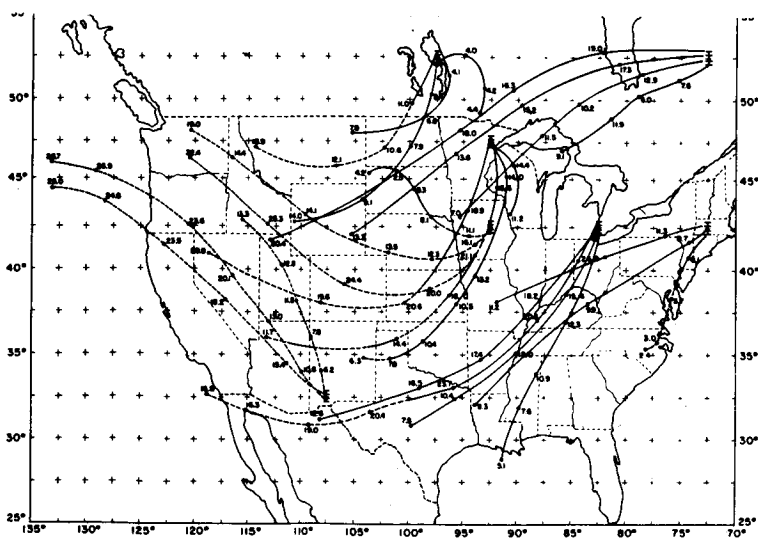
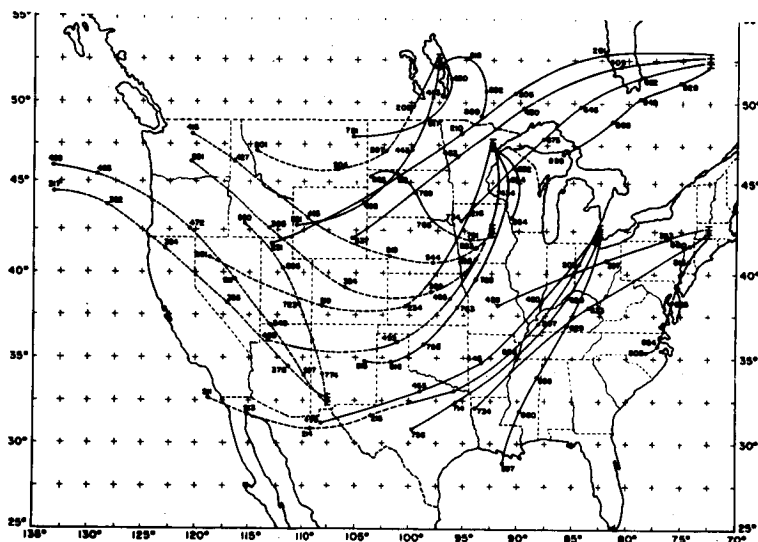
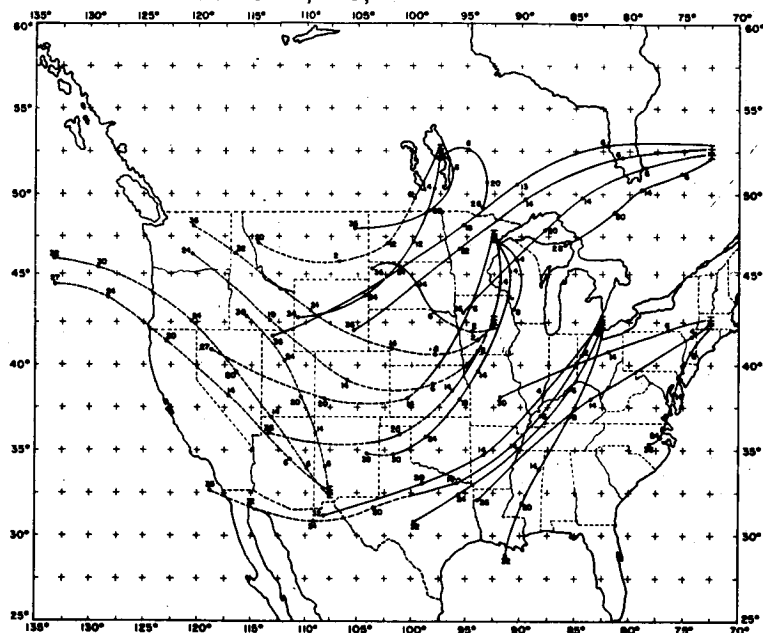
Middle: Same trajectories as above labeled with pressure (mb).

Bottom: Same trajectories as above labeled with a function of total speed. To obtain speed in meters/sec multiply by 1.4142.

Dashed lines represent sinking motion.

Solid lines represent rising motion.

APRIL 12, 13, 1964



It shows sinking decelerating air coming into a rapidly developing cyclone and rising accelerating air parcels moving out of it to the east, and gives a feeling for the extent of differential advection in the vertical above any given point.

The three dimensional motion in this case is shown in Figure 3. The insert at the lower left of this picture shows Danielsen's (1964) model of the flow out of a high pressure center behind a developing cyclone. In this model a rectangle of air particles elongated parallel to the flow at high levels over the anticyclone deforms and becomes elongated perpendicular to the flow in the final state. The northern trajectories undergo rising motion near the cyclone and recurve cyclonically to conserve their potential vorticity. The southern trajectories continue sinking and increase in anticyclonic curvature, forming the low level anticyclone. The major part of this figure shows the situation obtained from numerical computer results on an actual case, and shows some similarity to this model. There are some major differences, however. The computer results showed much weaker sinking in the region of the anticyclone. This is supported by the conservation of moisture in the sinking air. The low level anticyclone could not possibly have been fed by upper tropospheric or lower stratospheric air as is indicated by Danielsen's (1964) results.

Figure 4 shows a comparison of the present method and that used by Danielsen (1966) for another mid-latitude case. Exact comparisons are difficult to make but over most of the map there is good agreement. The only obvious exception is that Danielsen's trajectories show more curvature of the parcels as they move to the south of the trough. The reason for this discrepancy is not quite clear.

Figure 3. Three dimensional trajectories in April 1964 case. Surface analysis corresponds to 12Z 13 April 1964. Insert at lower left shows Danielsen's model for an occluding cyclone.

Dashed lines are sinking trajectories.

Solid lines are rising trajectories.

Three digit numbers correspond to pressures (mb) along trajectories.

Time is plotted backwards (2 digit numbers). Hour zero is final position.

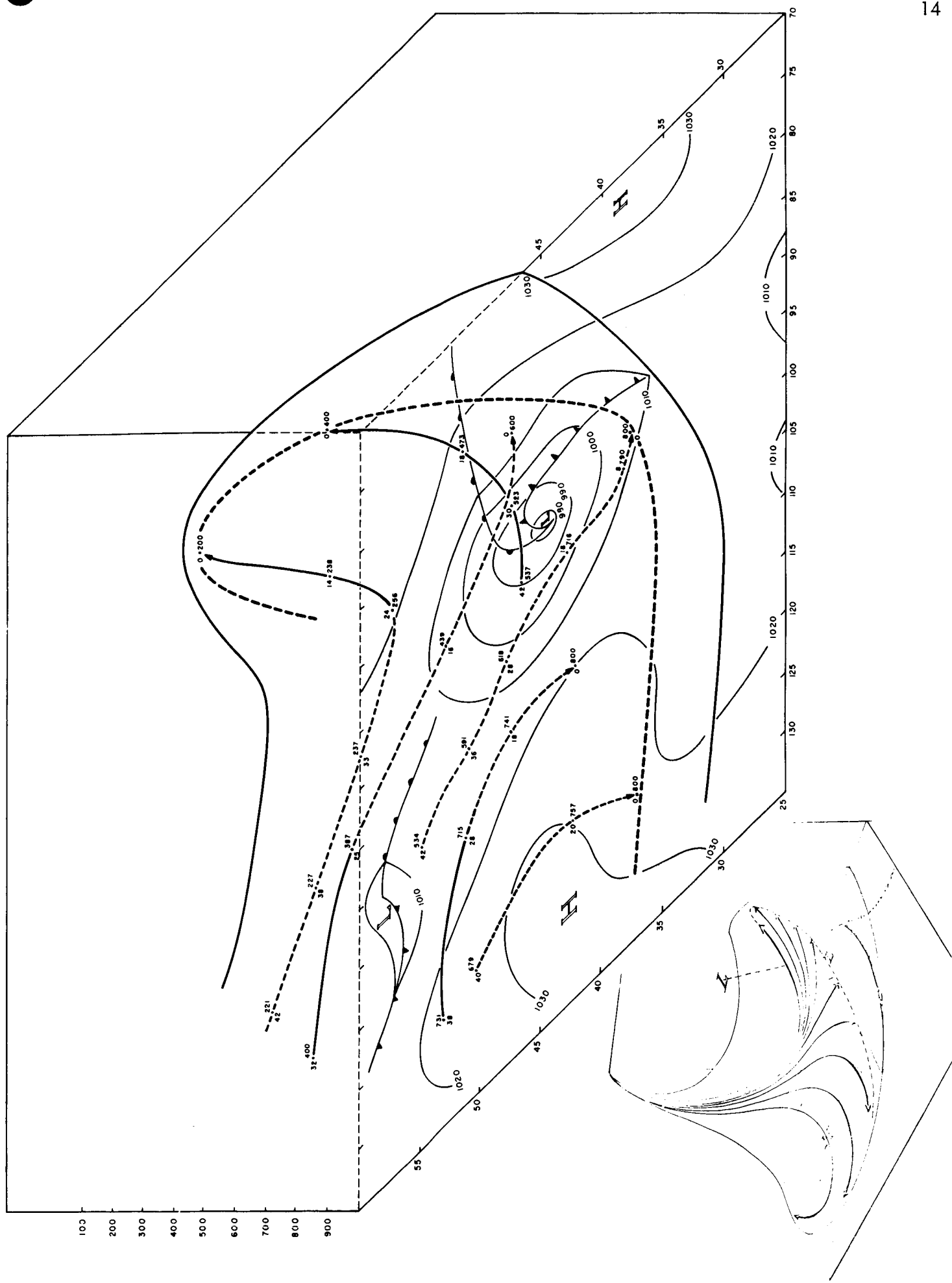
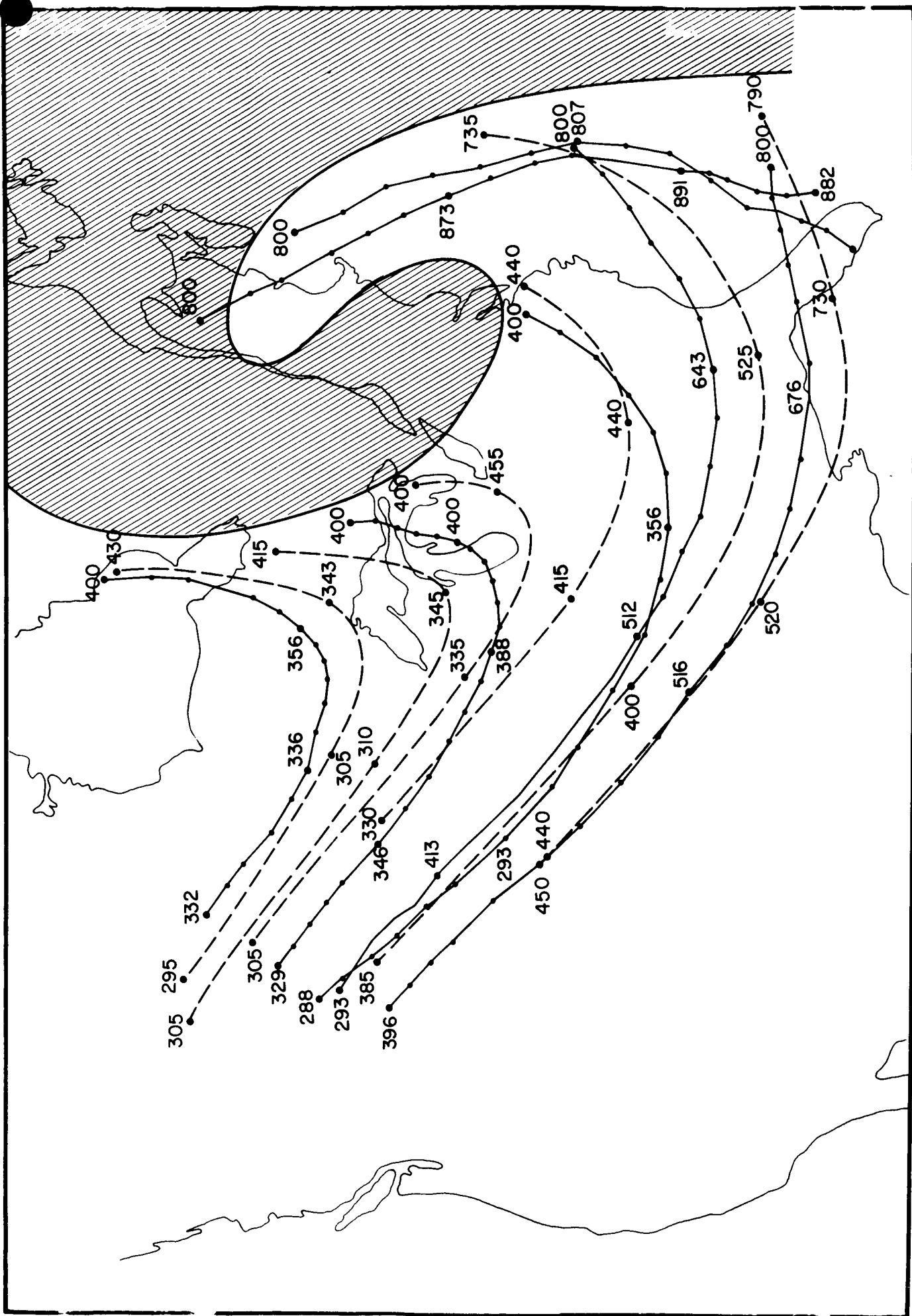


Figure 4. Comparison of Danielsen's (1966) trajectories (solid lines) with computer product (dashed lines) for period ending 12Z 30 Nov. 1963. (The striped area shows the location of the moisture).



The striped area in this figure represents the comma shaped cloud pattern as analyzed by Danielsen (1966). It is interesting to note that all the trajectories in this area of the map which end up in the clear air undergo strong net sinking. The only trajectory which ends up in the cloudy air rises about 80 mb. Danielsen gives the source of the dry tongue as the air associated with the upper tropospheric and lower stratospheric strong northwesterly flow often found to the southwest of a developing cyclone. The computer produced trajectories indicate that at lower levels the source for this dry tongue may be much further south than this jet, and that the air still undergoes sinking to remain cloudless. This is illustrated by the easternmost computer trajectory in this figure, which originates over southwestern Florida, and ends up in the dry air. The trajectory nearest it (the one mentioned above) follows a similar path but rises to end up in a completely different weather regime.

The program is designed to study the variation along the trajectories of potential temperature, vorticity, divergence, moisture, and many other such parameters. In this initial phase of the study these quantities were interpolated linearly between grid points and between pressure surfaces, as was the wind and there was no time interpolation except at the mid-point between map times.

Table 1 shows some results of this initial attempt. This table corresponds to the trajectories leading to the point just west of Lake Superior in Figure 2. These trajectories are in the region where the heaviest rain fell and the general trend of potential temperature and moisture along the trajectories corresponds

fairly well with the amount of rain that fell. The large fluctuations in the potential temperature which are evident in this table are greater than was found over most of the other trajectories, where the potential temperature did not vary more than about 1 or 2 deg C over 42 hours. The large variations here are partly due to their nearness to fronts.

From this table it can be seen that the variation of the potential temperature, vorticity, and divergence are large in time. These discrepancies would undoubtedly become much less with a good time interpolation scheme. Probably a parabolic fit of the variables using two previous map times and the closest one in the future, as was done by Mesinger (1965), would be appropriate. Also for quantities such as potential temperature and moisture the vertical interpolation should perhaps be exponential in pressure rather than linear.

In the case of the trajectory itself the present interpolation scheme was probably not nearly as destructive. A linear interpolation in pressure is probably a fair assumption for the wind. Also the advection of a parcel by a stationary wind field for 12 hours is not too bad since the isotach field is usually elongated along the direction of the flow. However, interpolation of the wind field in time should also be done in the way described above for greater accuracy.

Another way of improving the results is to use solutions for vertical motions which take into account such effects as terrain, condensation and friction. Such vertical motions have been computed by Krishnamurti (1967) and they produced less intense sinking centers and would hence come much closer to conserving the moisture than the adiabatic vertical motions.

4. Conclusions

Three dimensional trajectories can be used in many meteorological investigations. The amount of information which can be derived from them depends upon the accuracy of the scheme used. The general picture obtained about the motion field is not especially sensitive to approximations such as adiabatic flow or to linear space interpolation or limited time interpolation. One can well anticipate areas of cloudiness or even precipitation from such trajectories. However to investigate the variation of properties of the parcel one must use great care in selection of interpolation schemes, and vertical motions and divergent wind components should be computed using non-adiabatic and friction effects.

Table 1

HOUR	Trajectory Leading to 800 mb				Trajectory Leading to 600 mb			
	θ (deg K)	q (gm/kg)	VORT $\times 10^5$ (sec ⁻¹)	DIV $\times 10^6$ (sec ⁻¹)	θ (deg K)	q (gm/kg)	VORT $\times 10^5$ (sec ⁻¹)	DIV $\times 10^6$ (sec ⁻¹)
0	298	6.7	23	-1	308	3.6	16	6
6	293	7.0	17	-3	305	3.8	17	-2
12	299	9.3	10	-9	305	5.7	9	2
18					304	4.9	13	-3
24					305	4.2	12	0
30					306	3.0	12	0
36					307	2.4	8	0

HOUR	Trajectory Leading to 400 mb				Trajectory Leading to 200 mb			
	θ (deg K)	q (gm/kg)	VORT $\times 10^5$ (sec ⁻¹)	DIV $\times 10^6$ (sec ⁻¹)	θ (deg K)	q (gm/kg)	VORT $\times 10^5$ (sec ⁻¹)	DIV $\times 10^6$ (sec ⁻¹)
0	316	.8	9	13	342	.1	11	8
6	315	1.0	14	0	341	.1	10	6
12	314	1.4	10	6	338	.1	19	-1
18	312	1.0	14	-3	338	.1	14	-5
24	311	.8	11	-4	339	0	14	-9
30	313	.7	8	1				
36	314	.8	9	1				

The contents of this table correspond to Figure 2. Hours increase backward in time with hour zero indicating the final point on a trajectory.

List of References

- Danielsen, E. F., 1964: Project Springfield Report. Defense Atomic Support Agency.
- Danielsen, E. F., 1966: Research in Four Dimensional Diagnosis of Cyclonic Storm Cloud Systems. Scientific Report No. 1, Prepared for Air Force Cambridge Research Laboratories, Pennsylvania State University.
- Krishnamurti, T. N., J. Nogues, and D. Baumhefner, 1966a: On the Partitioning of the Baroclinic Vertical Motions in a Developing Wave Cyclone. Scientific Report No. 1, Prepared for Air Force Cambridge Research Laboratories, Dept. of Meteorology, University of California.
- Krishnamurti, T. N., 1967: A Study of a Developing Wave Cyclone. Final Report prepared for Air Force Cambridge Research Laboratories, Dept. of Meteorology, University of California. AF 19(628) AFCRL-67-0128.
- Mesinger, F., 1965: Behavior of a Large Number of Constant-Volume Trajectories. Journal of the Atmospheric Sciences, Vol. 22, No. 5, pp. 479-492.
- Murray, F., 1965: Numerical Simulation of the Evolution of Cumulus Towers. Scientific Report No. S.M. -49230, Douglas Aircraft Company, Santa Monica, California.
- Nagle, R. E. and Clark, 1966: Interpretative Uses of the Diagnostic Cycle Routine. Final Report Prepared for Environmental Science Services Administration under Grant Cwb 11254.

PRECEDING PAGE BLANK NOT FILMED.

N67-30788

A Study of a Non-developing Easterly Wave

David Baumhefner

PRECEDING PAGE BLANK NOT FILMED.

TABLE OF CONTENTS

	<u>Page</u>
List of Illustrations.....	v
Table of Symbols.....	xi
Abstract.....	xiii
Chapter I Introduction.....	1
Chapter II The Diagnostic Model	
A. Data Preparation.....	4
B. Model Structure.....	26
C. Comparisons of Model Structure and Data Variation.....	30
Stream Function.....	30
Temperature.....	45
Friction.....	59
Latent Heat.....	63
Numerical vs. Kinematic.....	69
Chapter III A Tropical Case Study -- 12-14 August 1961	
A. Introduction.....	76
B. Discussion of the Results.....	77
12 August 1961 12Z.....	77
13 August 1961 00Z.....	91
13 August 1961 12Z.....	105
14 August 1961 00Z.....	119

	<u>Page</u>
14 August 1961 12Z.....	134
C. Trajectory Calculations.....	148
D. Concluding Remarks.....	156
References.....	159
Appendix	
Derivation of the Non-linear Balanced Model.....	161
Inclusion of Frictional Effects.....	164

LIST OF ILLUSTRATIONS

<u>Figure</u>	<u>Title</u>	<u>Page</u>
1	Locations of the Radiosonde and Pibal Stations used in the Data Analysis.....	6
2	Vector Representation of the Streamlines and Isotachs at 1000 and 800 mbs, 13 August 1961 00Z.....	9
3	Vector Representation of the Streamlines and Isotachs at 600 and 400 mbs, 13 August 1961 00Z.....	11
4A	Vector Representation of the Streamlines and Isotachs at 200 mbs, 13 August 1961 00Z.....	14
B	Temperature and Moisture at 1000 mbs, 13 August 1961 00Z.....	14
5	Temperature and Moisture at 800 and 600 mbs, 13 August 1961 00Z.....	16
6	Temperature and Moisture at 400 and 200 mbs, 13 August 1961 00Z.....	18
7	Geopotential Heights at 1000 and 800 mbs, 13 August 1961 00Z.....	20
8	Geopotential Heights at 600 and 400 mbs, 13 August 1961 00Z.....	22
9	Geopotential Heights at 200 mbs, 13 August 1961 00Z.....	24
10	Schematic Drawing of the Internal Structure of the Model.....	28
11	Balanced Equation Stream Function at 1000 and 600 mbs, 13 August 1961 00Z.....	33
12A	Balanced Equation Stream Function at 200 mbs, 13 August 1961 00Z.....	35
B	Kinematic Stream Function at 1000 mbs, 13 August 1961 00Z.....	35

<u>Figure</u>	<u>Title</u>	<u>Page</u>
13	Kinematic Stream Function at 600 and 200 mbs, 13 August 1961 00Z.....	37
14	Vertical Motion Obtained from a Balance Stream Function and Geopotential Thickness at 900 and 500 mbs, 13 August 1961 00Z.....	41
15	Vertical Motion Obtained from a Kinematic Stream Function and Geopotential Thickness at 900 and 500 mbs, 13 August 1961 00Z.....	43
16A	Kinematic Stream Function Vertical Motion in Partitioned Form, 13 August 1961 00Z.....	47
B	Balanced Stream Function Vertical Motion in Partitioned Form, 13 August 1961 00Z.....	47
17	Geopotential Thickness Temperature at 900 and 500 mbs, 13 August 1961 00Z.....	50
18	Observed Temperature at 900 and 500 mbs, 13 August 1961 00Z.....	52
19	Vertical Motion Obtained from Observed Temperature and Kinematic Stream Function at 900 and 500 mbs, 13 August 1961 00Z.....	55
20A	Observed Temperature Vertical Motion in Partitioned Form, 13 August 1961 00Z.....	58
B	Thickness Temperature Vertical Motion in Partitioned Form, 13 August 1961 00Z.....	58
21A	Frictional Component of the Vertical Motion at 900 mbs with 1000 mb Wind Vectors, 13 August 1961 00Z.....	62
B	Total Vertical Motion at 900 mb with Friction Added, 13 August 1961 00Z.....	62
22A	Integrated Three-dimensional Moisture Flux, 13 August 1961 00Z.....	67
B	Latent Heat Component of the Vertical Motion at 900 mb, 13 August 1961 00Z.....	67

<u>Figure</u>	<u>Title</u>	<u>Page</u>
23	Final Vertical Motion at 900 and 500 mbs with Friction and Diabatic Heating, 13 August 1961 00Z.....	71
24	Kinematic Vertical Motion at 900 and 500 mbs, 13 August 1961 00Z.....	73
25	Vector Representation of the Velocity Field with the Temperature at 1000 and 800 mbs, 12 August 1961 12Z.....	79
26	Vector Representation of the Velocity Field with the Temperature at 600 and 400 mbs, 12 August 1961 12Z.....	81
27A	Vector Representation of the Velocity Field with the Temperature at 200 mbs, 12 August 1961 12Z.....	83
B	Integrated Moisture Flux, 12 August 1961 12Z.....	83
28	Vertical Motion at 900 and 700 mbs with the Observed Relative Humidity, 12 August 1961 12Z.....	85
29	Vertical Motion at 500 and 300 mbs with the Observed Relative Humidity, 12 August 1961 12Z.....	87
30A	Cross-section of Partitioned Vertical Motion at 20°N, 12 August 1961 12Z.....	89
B	Cross-section of Moisture and Cloudiness at 20°N, 12 August 1961 12Z.....	89
31	Vector Representation of the Velocity Field with the Temperature at 100 and 800 mbs, 13 August 1961 00Z.....	93
32	Vector Representation of the Velocity Field with the Temperature at 600 and 400 mbs, 13 August 1961 00Z.....	95

<u>Figure</u>	<u>Title</u>	<u>Page</u>
33A	Vector Representation of the Velocity Field with the Temperature at 200 mbs, 13 August 1961 00Z.....	97
B	Integrated Moisture Flux, 13 August 1961 00Z.....	97
34	Vertical Motion at 900 and 700 mbs with the Observed Relative Humidity, 13 August 1961 00Z.....	99
35	Vertical Motion at 500 and 300 mbs with the Observed Relative Humidity, 13 August 1961 00Z.....	101
36A	Cross-section of Partitioned Vertical Motion at 20°N, 13 August 1961 00Z.....	103
B	Cross-section of Moisture and Cloudiness at 20°N, 13 August 1961 00Z.....	103
37	Vector Representation of the Velocity Field with the Temperature at 1000 and 800 mbs, 13 August 1961 12Z.....	108
38	Vector Representation of the Velocity Field with the Temperature at 600 and 400 mbs, 13 August 1961 12Z.....	110
39A	Vector Representation of the Velocity Field with the Temperature at 200 mbs, 13 August 1961 12Z.....	112
B	Integrated Moisture Flux, 13 August 1961 12Z.....	112
40	Vertical Motion at 900 and 700 mbs with the Observed Relative Humidity, 13 August 1961 12Z.....	114
41	Vertical Motion at 500 and 300 mbs with the Observed Relative Humidity, 13 August 1961 12Z.....	116
42A	Cross-section of Partitioned Vertical Motion at 20°N, 13 August 1961 12Z.....	118
B	Cross-section of Moisture and Cloudiness at 20°N, 13 August 1961 12Z.....	118
43	Vector Representation of the Velocity Field with the Temperature at 1000 and 800 mbs, 14 August 1961 00Z.....	122

<u>Figure</u>	<u>Title</u>	<u>Page</u>
44	Vector Representation of the Velocity Field with the Temperature at 600 and 400 mbs, 14 August 1961 00Z.....	124
45A	Vector Representation of the Velocity Field with the Temperature at 200 mb, 14 August 1961 00Z.....	126
B	Integrated Moisture Flux, 14 August 1961 00Z.....	126
46	Vertical Motion at 900 and 700 mbs with the Observed Relative Humidity, 14 August 1961 00Z.....	128
47	Vertical Motion at 500 and 300 mbs, 14 August 1961 00Z....	130
48A	Cross-section of Partitioned Vertical Motion at 20°N, 14 August 1961 00Z.....	132
B	Cross-section of Moisture and Cloudiness at 20°N, 14 August 1961 00Z.....	132
49	Vector Representation of the Velocity Field with the Temperature at 1000 and 800 mbs, 14 August 1961 12Z.....	136
50	Vector Representation of the Velocity Field with the Temperature at 600 and 400 mbs, 14 August 1961 12Z.....	138
51A	Vector Representation of the Velocity Field with the Temperature at 200 mbs, 14 August 1961 12Z.....	140
B	Integrated Moisture Flux, 14 August 1961 12Z.....	140
52	Vertical Motion at 900 and 700 mbs with the Observed Relative Humidity, 14 August 1961 12Z.....	142
53	Vertical Motion at 500 and 300 mbs with the Observed Relative Humidity, 14 August 1961 12Z.....	144
54A	Cross-section of Partitioned Vertical Motion at 20°N, 14 August 1961 12Z.....	146
B	Cross-section of Moisture and Cloudiness at 20°N, 14 August 1961 12Z.....	146

<u>Figure</u>	<u>Title</u>	<u>Page</u>
55	Trajectories at 800, 600, and 400 mbs, 12-14 August 1961.....	150
56	Trajectories at 800, 600, and 400 mbs, 12-14 August 1961.....	152
57	Trajectories at 800, 600, and 400 mbs, 12-14 August 1961.....	154

TABLE OF SYMBOLS

C_p	coefficient of specific heat at constant pressure.
f	Coriolis parameter
g	acceleration of gravity
\mathbf{k}	unit vector in the z-direction
P	atmospheric pressure
R	specific gas constant
σ	static stability
T	temperature
\mathbf{V}_H	horizontal velocity vector
Z	height of the isobaric surfaces
α	specific volume
β	northward variation of Coriolis parameter
θ	potential temperature
ϕ	geopotential gZ
χ	velocity potential for the irrotational component of velocity
ψ	stream function for the non-divergent component of velocity
ω	the individual change of pressure dp/dt
∇	isobaric gradient operator
∇^2	Laplacian operator
J	Jacobian operator

u	zonal component of the wind
v	meridional component of the wind
ζ	relative vorticity
ρ	density
C_D	drag coefficient
q	specific humidity
q_s	saturation specific humidity
L	latent heat of condensation
F	frictional force
δ	divergence
H	adiabatic heating per unit time

ABSTRACT OF THE THESIS

The Dynamical Structure of the Tropical Atmosphere
Based on Experiments with a Diagnostic Numerical Model

by

David Paul Baumhefner

Master of Arts in Meteorology

University of California, Los Angeles, 1966

Professor T. N. Krishnamurti, Chairman

A diagnostic, non-linear balanced model is applied in order to numerically simulate the three-dimensional structure of the tropical atmosphere. The processing of the input data for the model is discussed, including the accuracies of each parameter. Numerous comparisons and experiments are made in order to obtain the best result from the model. These include different types of stream functions and temperature analyses, and the addition of frictional effects and latent heat. A comparison between the kinematic vertical motion and the final numerical result is performed.

Using the final form of the balanced model, a case study for 12-14 August 1961 in the Caribbean is presented. The study contains the horizontal velocity and the thermal distribution together with four levels of resulting vertical motion at each map-time. Cross-sections of the vertical motion in partitioned form are contrasted with the vertical moisture distribution. Trajectory calculations from the case study are performed using 2 hour, centered time steps.

The validity of the numerical vertical motion is discussed along with its effect on the tropical weather.

CHAPTER I

INTRODUCTION

The tropical atmosphere has been the object of an intensive research effort by a large number of meteorologists for some time. The basic structure and different scales of motion of the tropical atmosphere has been poorly understood, due largely to the lack of conventional data in the region. The current research on the overall dynamics of the tropics is being incorporated into several global climate-simulation models. These models must have realistic and reliable information on which to base their modelling approximations in order to be successful in simulating the global circulations. Some attempts have been made, which are mostly experimental in nature, to forecast the tropical atmosphere using a numerical model. Here again the initial state of the atmosphere must be accurately defined in order to obtain the best possible forecast from the prognostic model. The problem of hurricane formation and forecasting is becoming increasingly more important because of the destructive nature of these storms on population centers. Very little is known about the precise mechanism of the hurricane formation or the controlling influences on the track of the cyclone. Continued research on the general structure of the tropical atmosphere may possibly lead to some definite answers to the posed problems.

This paper attempts to derive and describe a previously unknown quantity in the tropical atmosphere: the synoptic-scale vertical motion.

Some meteorologists (Charney, 1963) recently have argued that the synoptic scale vertical motions in the tropics are small and may be neglected. However, it appears from this research that, even though small in magnitude, the synoptic scale rising and sinking may play an important part in the dynamics of the tropics. Together with the horizontal components of the wind, the vertical motion completely describes the three-dimensional velocity field of the tropical atmosphere.

In earlier research work, the vertical motion has always been computed by the kinematic, adiabatic or vorticity methods, (Petterssen, 1956). The results from these studies were always open to criticism because the methods employed are very sensitive to data analysis. Therefore, the application of a numerical diagnostic model in the tropics was considered. Previous experience in the middle latitudes with the numerical model has convinced the author of its superiority over the vertical motion calculations mentioned above. However, a comparison is made between the earlier kinematic method and the numerical model to convince the reader as well.

The particular form of the diagnostic model was chosen to be the non-linear balanced set of equations derived by Charney (1962) and used by Shuman (1957) and Miyakoda (1963). This formulation is the most complete in the sense that very few simplifying approximations are made. The effects of variable static stability, frictional influences, and diabatic heating were included in the model.

The original motive governing this research was to create an accurate initial condition upon which a prediction model would operate. The preliminary results (Krishnamurti, 1966) of the diagnostic phase were so encouraging that the author felt more research was needed. The final product of this diagnostic model, the horizontal components plus the vertical motion, are currently being used by Krishnamurti in a primitive equation prediction scheme, which is still in the experimental stage.

CHAPTER II

THE DIAGNOSTIC MODEL

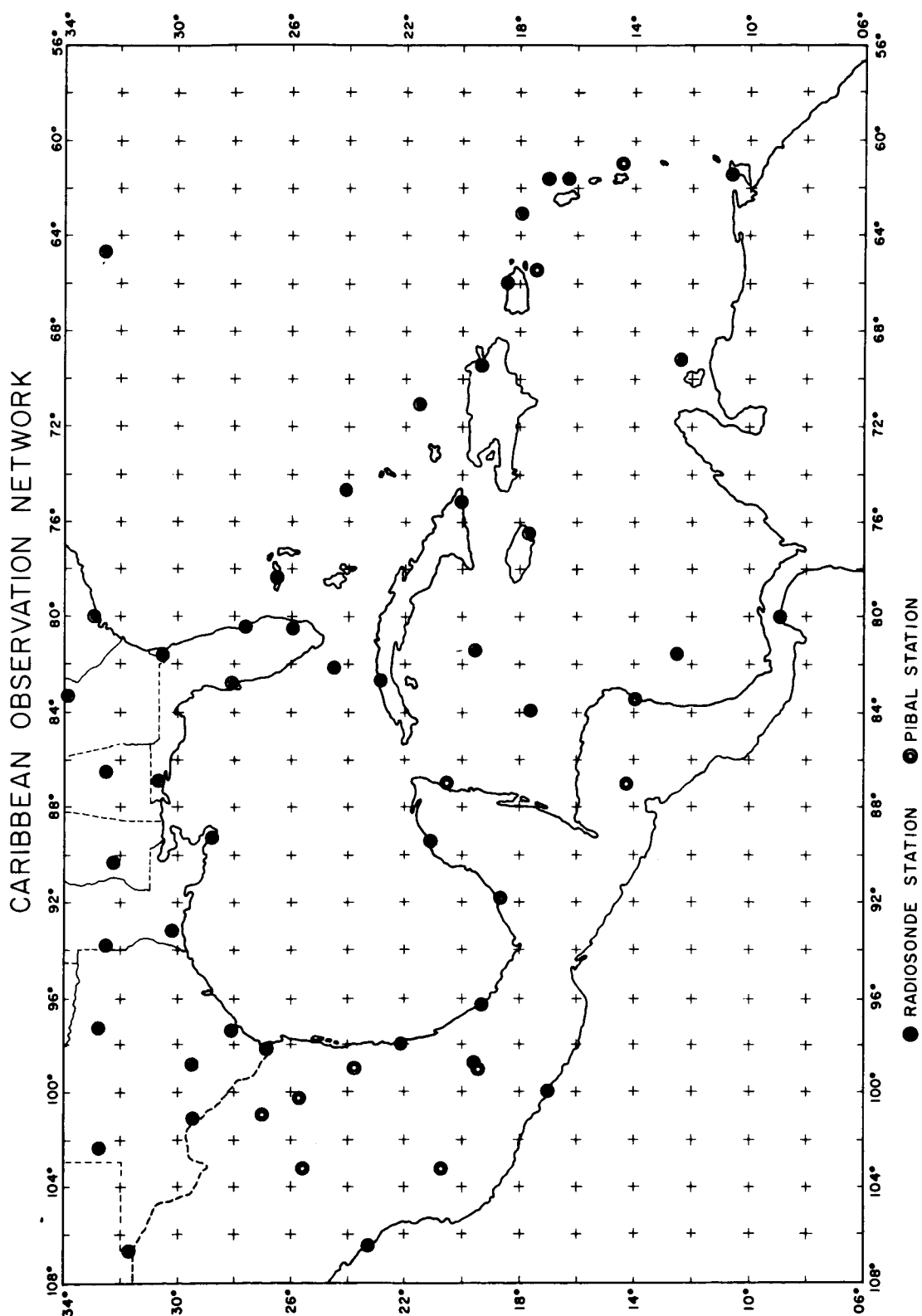
A. Data Preparation

The data analysis problem in the tropics is quite formidable, due to the poor quality of the meteorological observation network. If an accurate three-dimensional picture of the atmosphere and its properties are to be obtained, a region consisting of a sufficient number of well-spaced vertical soundings (radiosondes, rawins, and pibals), must be utilized. Unfortunately the current observation network provides the researcher only one or two good locations. Of these, the Caribbean area was chosen mainly because this region directly effects the weather in the Continental United States and the historical data is readily available.

Figure 1 illustrates the number and density of the reliable stations in the region considered. The horizontal grid network that the numerical model uses, are also displayed in Figure 1. It is evident that two large areas of data void are included in the numerical grid, the northeast and southwest corners. When the analysis was performed, simple extrapolation from the existing data was utilized in these regions. Therefore, the machine products should be considered valid only in the data-dense areas. The majority of the locations depicted, took observations every twelve hours which provides the analysis at different times with equal weighting. The host of surface observations available for the Caribbean were used only as an indirect locator of synoptic scale disturbances

FIGURE 1. Locations of the radiosonde and pibal stations
used in the data analysis.

Small crosses are grid points used by the
numerical model.



and were not employed directly in the analysis.

Since the numerical model accepts data at five levels (1000, 800, 600, 400, 200 mbs.), it was reasoned that the data itself should be vertically averaged to avoid any small-scale perturbations in the vertical as well as the horizontal. These averages were to be centered on the input levels of the model. The first step in the derivation of the mean layer values was to plot the radiosonde data on Skew-T, log P diagrams. The wind data was also plotted on a vertical scale similar to the Skew-T. From these charts the average values for the wind speed and direction were "eyeballed" subjectively and the temperature and mixing ratio were computed directly. Some problems were encountered at the lower boundary, where the averaging could not be taken over 200 mb thickness. Therefore, the input data at 1000 mb is a vertical average from the surface to 900 mb only. The time element restricted the author to simplest methods for computing averages. Figures 2-6 display examples of the analysis of the vertically averaged parameters. These maps are for 13 August 1961 00Z and are part of a case study presented later in this report. Upon examination of the figures, one can see that considerable smoothing was employed to retain just the large-scale flow patterns. Several attempts have been made recently, Yanai (1964) and Holl (1965), to objectively analyze data in the tropics; however, it was felt that these methods were not adequate for this study. In future research of this nature, a good objective analysis would be extremely advantageous.

The streamlines and isotachs, Figures 2-4, are represented at each grid point by a vector whose magnitude is proportioned to the speed of the wind.

FIGURE 2. Vector representation of the streamlines and isotachs.

10 meters per second equals 0.4 centimeters

Solid, labeled isolines are isotachs in meter per second.

Circled X's are closed centers of circulation.

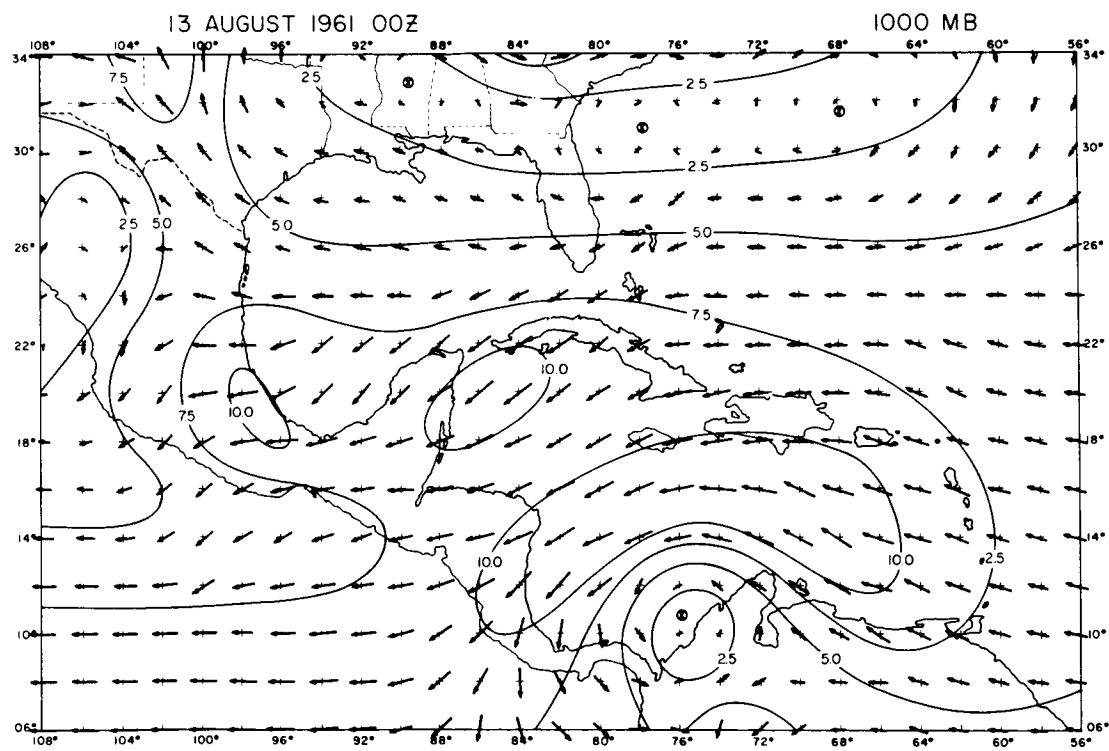
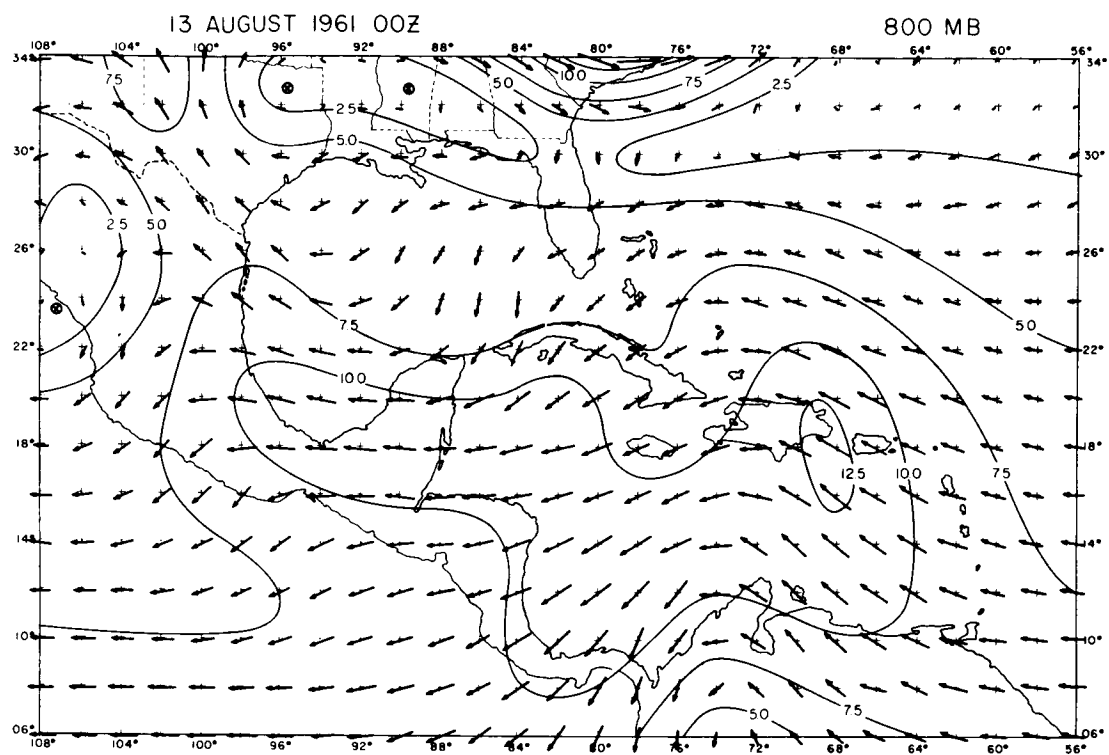
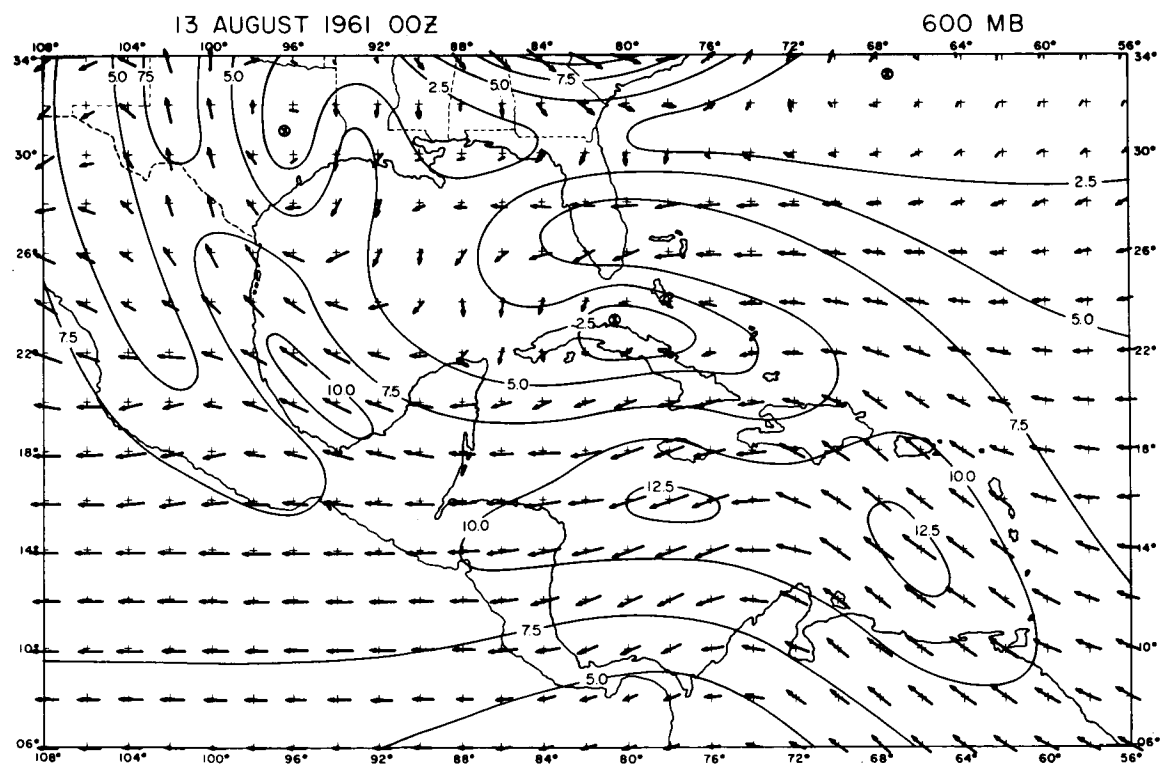
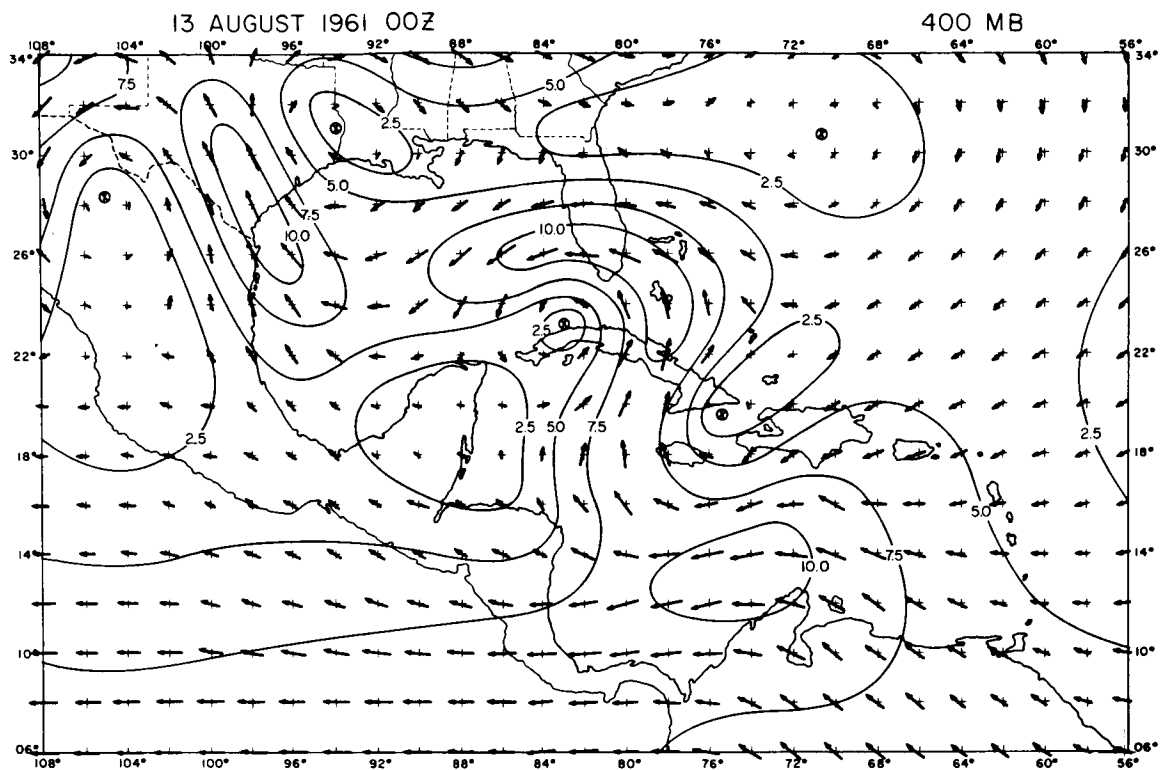


FIGURE 3. Vector representation of the streamlines and isotachs.

10 meters per second equals 0.4 centimeters.

Solid, labeled isolines are isotachs in meter per second.

Circled X's are closed centers of circulation.



They were obtained from the vertically averaged wind data, analyzed in the conventional manner, and were interpolated to the grid points. The vector is drawn to scale so that it roughly approximates a six hour trajectory. This representation allows another scalar field to be super-imposed on the streamline-isotach map. The temperature and moisture maps, Figures 4-6, are analyzed in the normal way. The mixing ratio is read directly from the Skew-T and then averaged; therefore, most of the small-scale noise is removed. It is smoothed further in the horizontal analysis to obtain the illustrated patterns. The moisture analysis is probably the least trust-worthy of the direct parameters being used by the model. The wind and temperature fields are defined with considerable accuracy in the regions of good data coverage, however the synoptic-scale moisture distribution is difficult to derive from the conventional radiosonde data.

The final parameter to be used as input for the numerical model is the geopotential, which is illustrated in Figures 7-9. If one analyses the geopotential height values without the aid of the wind field, the result is a chaotic map bearing no resemblance to the flow patterns. Since the primary objective of the diagnostic model is to represent the flow in an accurate manner, the analysis of the geopotential was adjusted to loosely fit the calculated geostrophic wind from the observed velocity field. At first thought, this might be considered a poor approximation in the tropics. However, after performing the adjustment on the analysis, it appeared that the changes were of the order

FIGURE 4A. Vector representation of the streamlines and isotachs.

10 meters per second equals 0.4 centimeters.

Solid, labeled isolines are isotachs in meter per second.

Circled X's are closed centers of circulation.

FIGURE 4B. Temperature and Moisture

Solid lines are temperature in degrees Centigrade.

Dashed lines are mixing ratio in grams per kilogram.

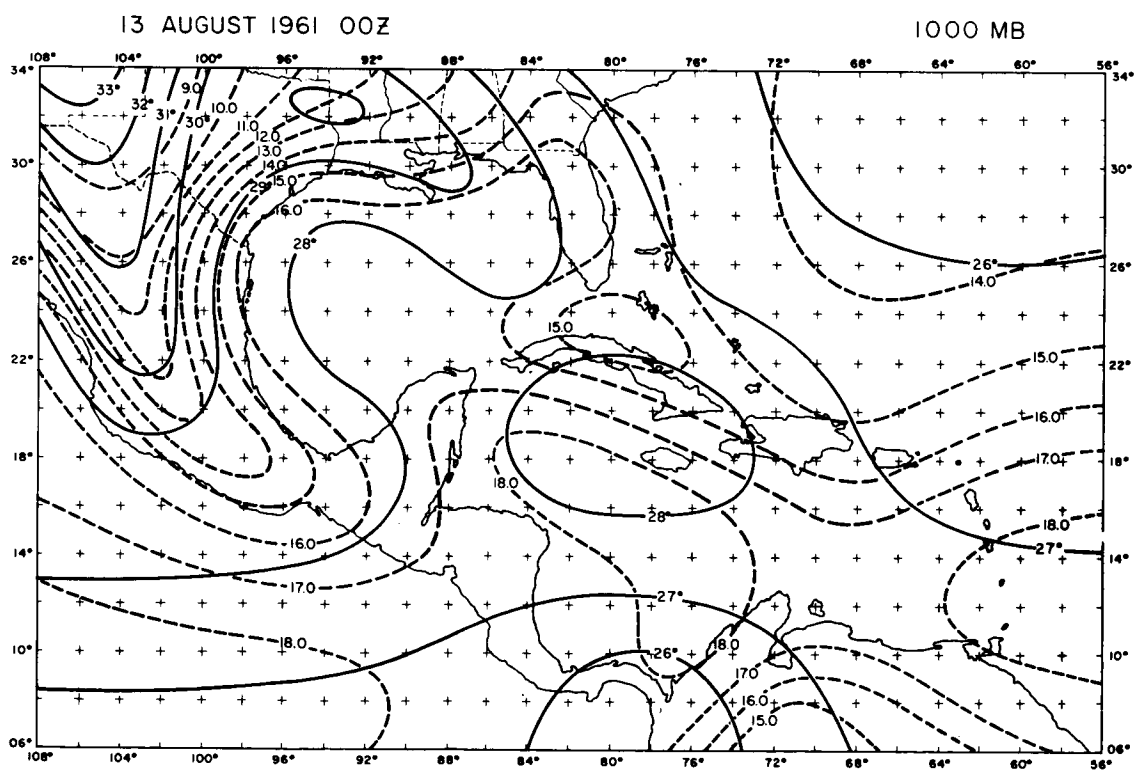
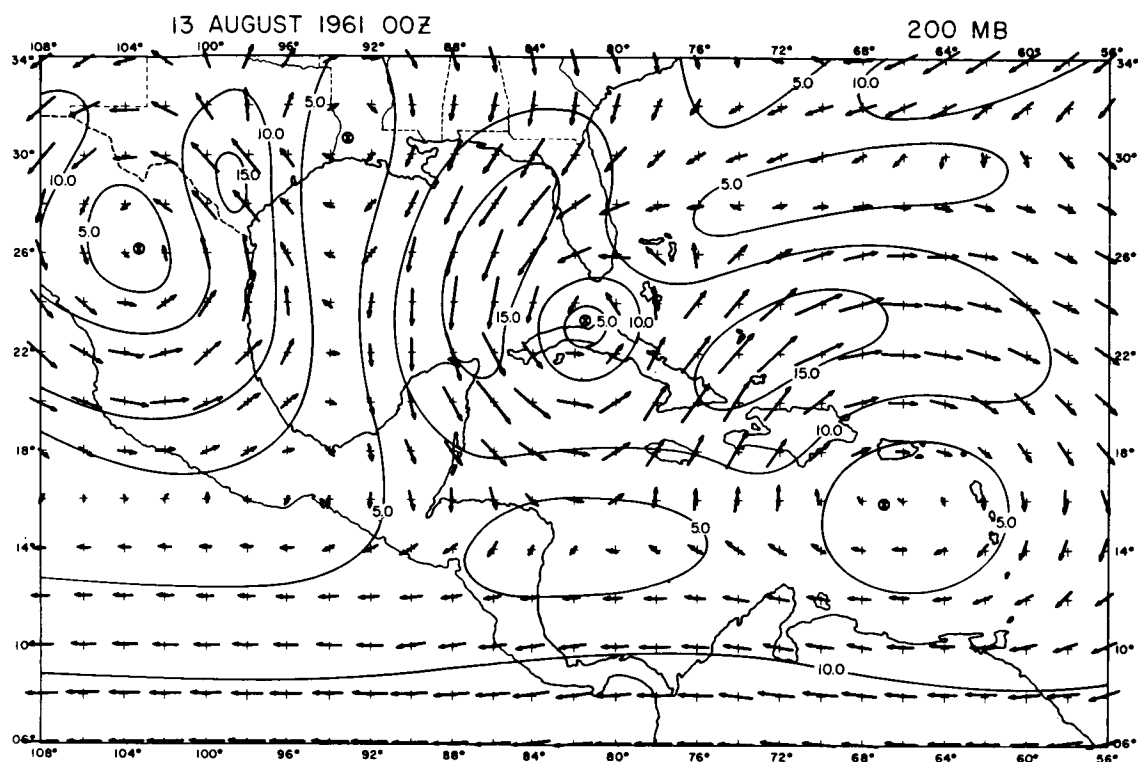


FIGURE 5. Temperature and Moisture

Solid lines are temperature in degrees Centigrade.

Dashed lines are mixing ratio in grams per kilogram.

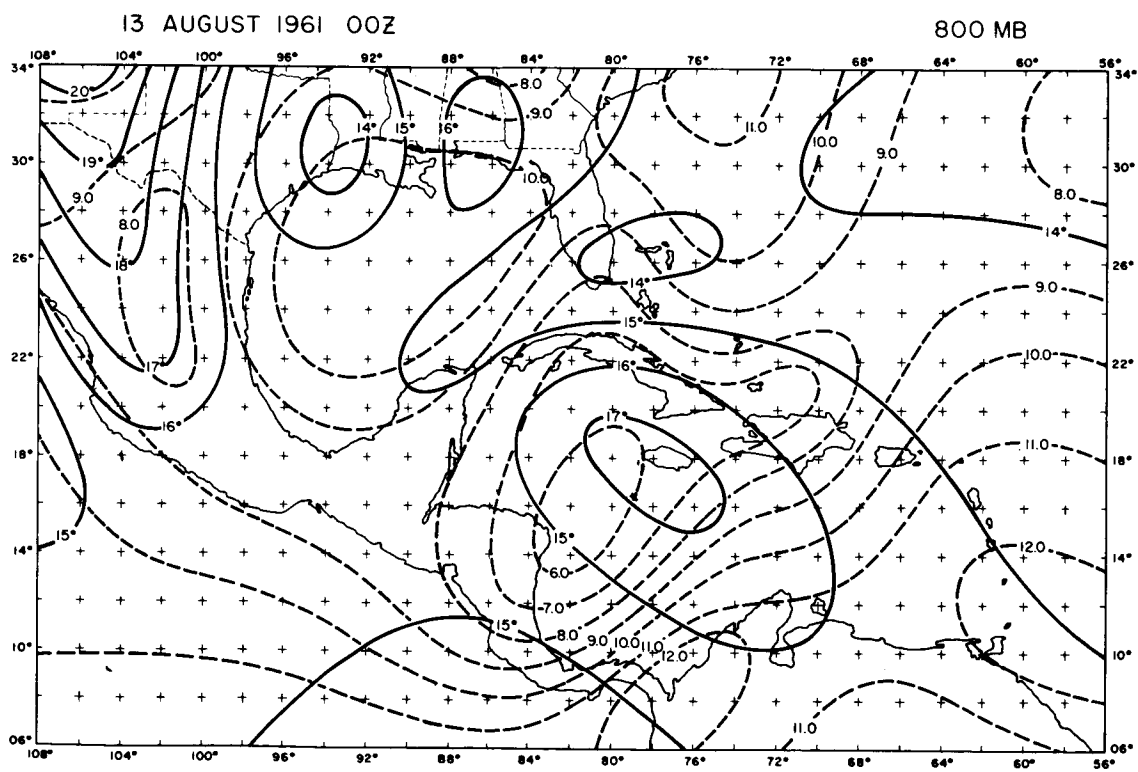
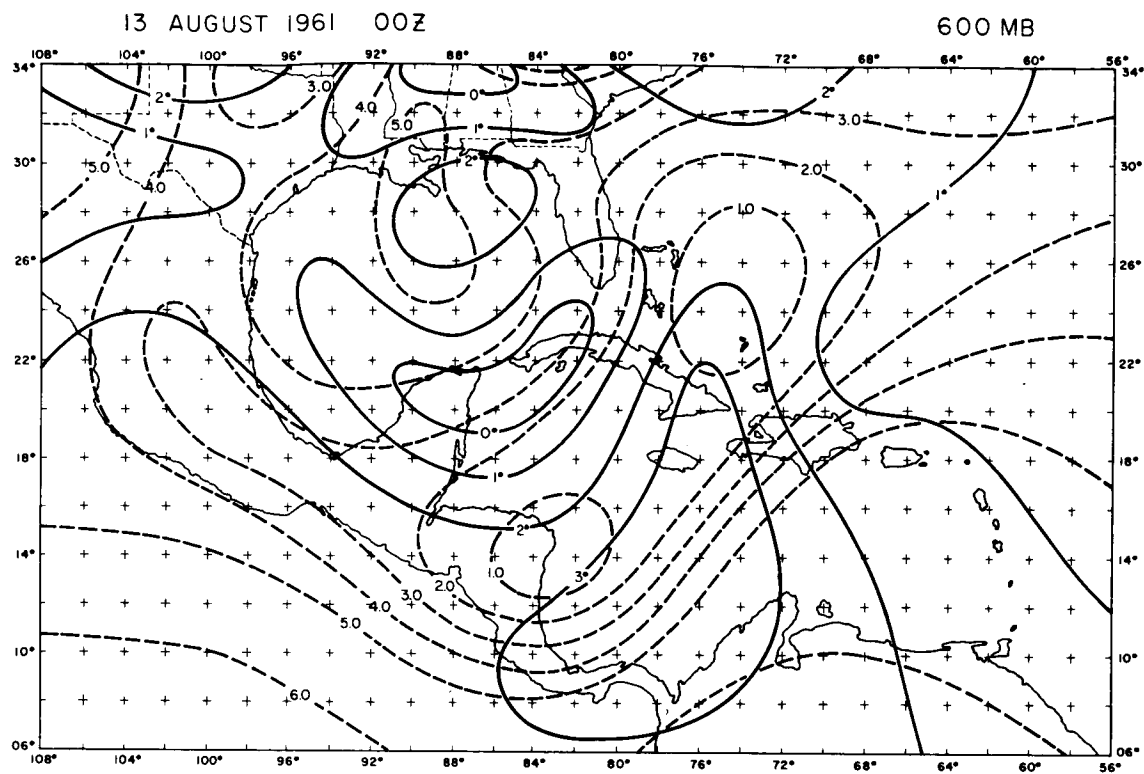


FIGURE 6. Temperature and Moisture

Solid lines are temperature in degrees Centigrade

Dashed lines are mixing ratio in grams per kilogram.

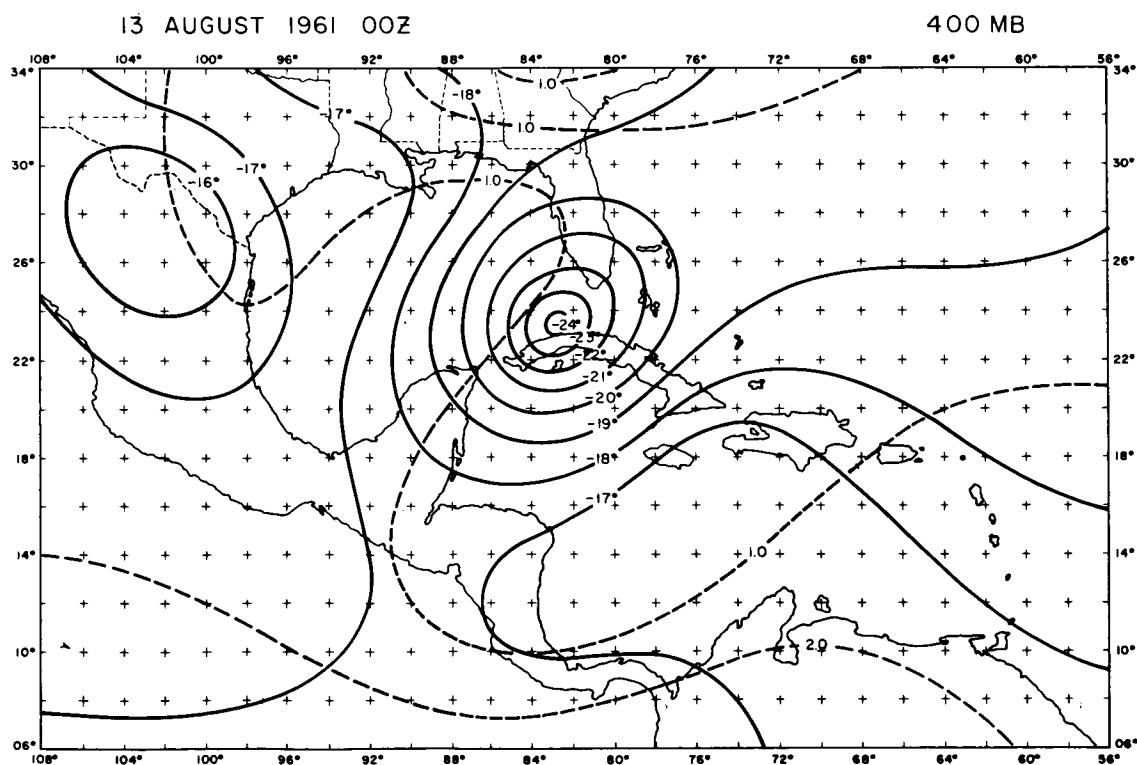
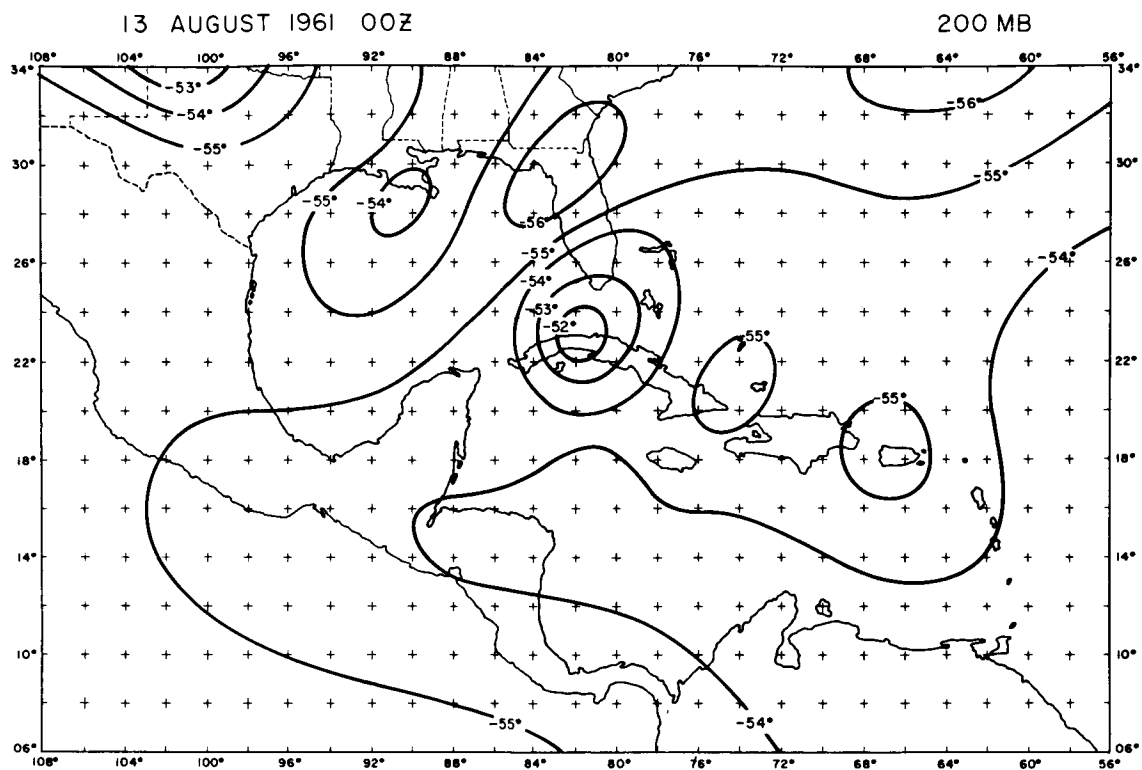


FIGURE 7. Geoptential Heights

Heights are in meters.

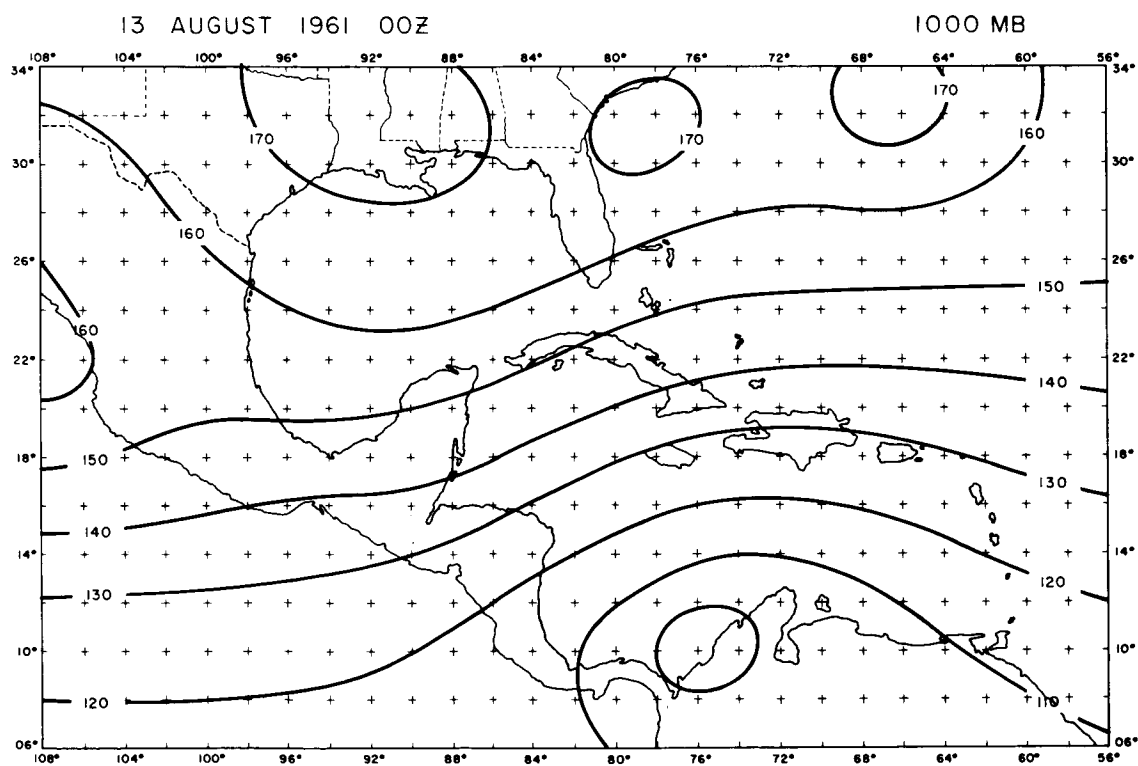
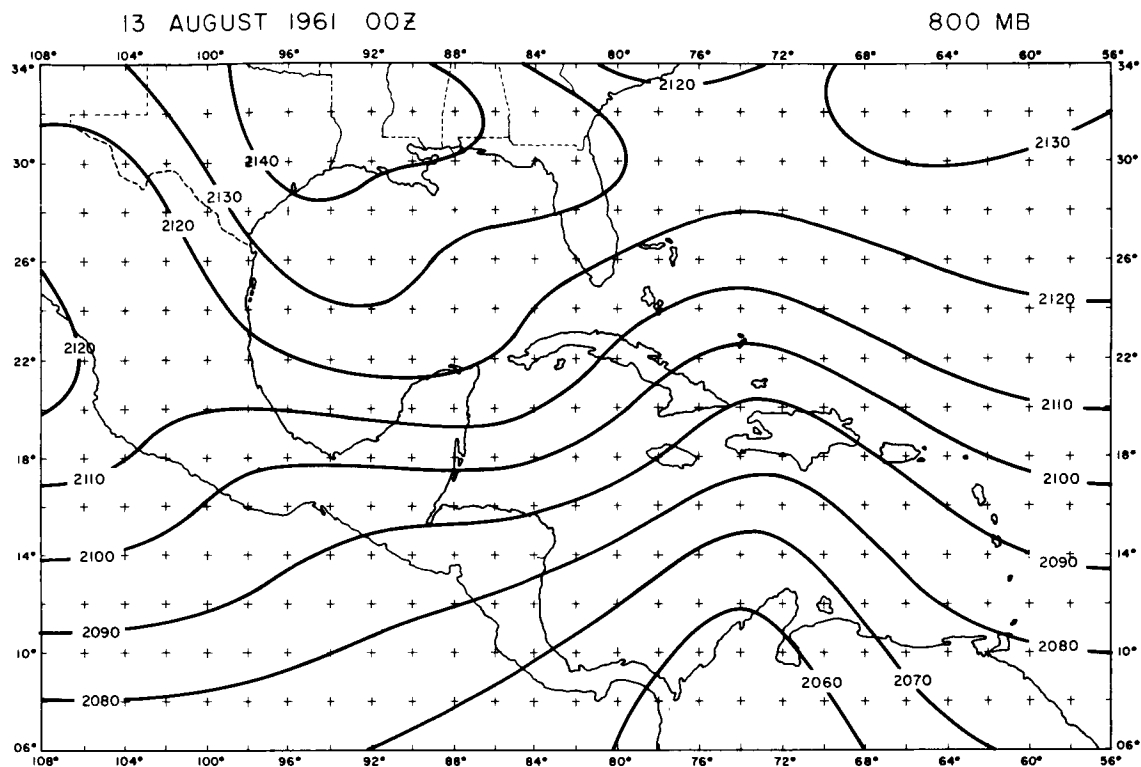


FIGURE 8. Geopotential Heights

Heights are in meters.

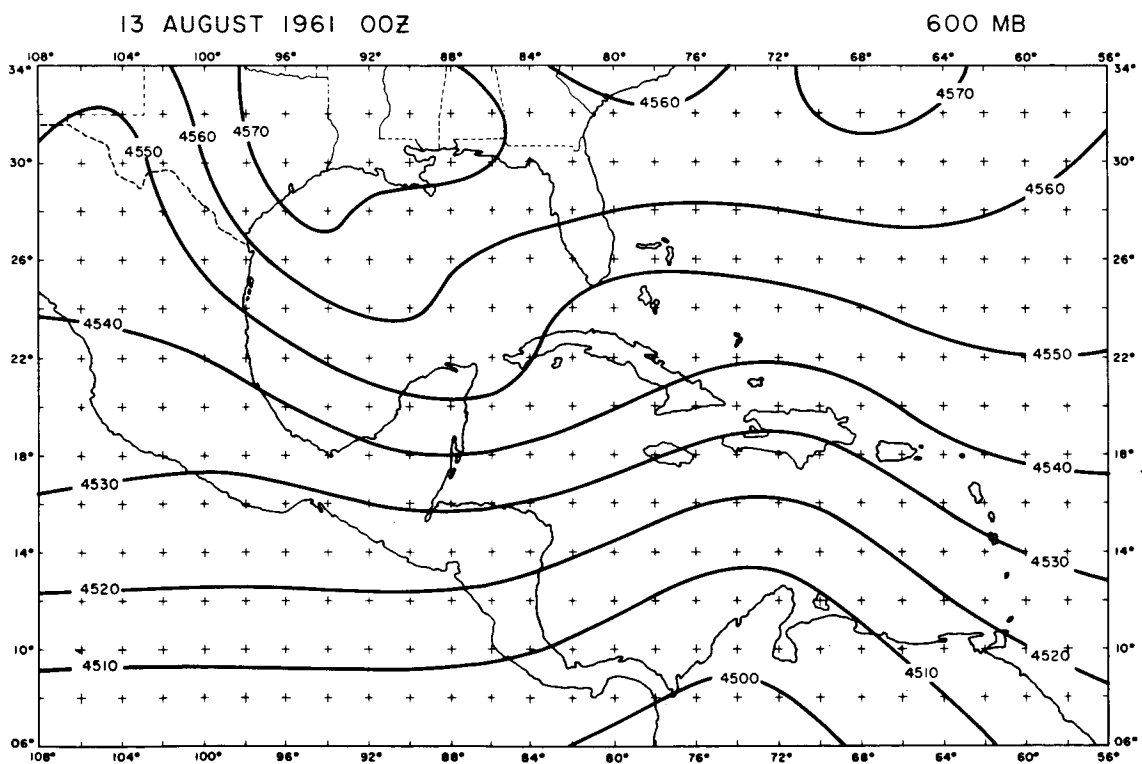
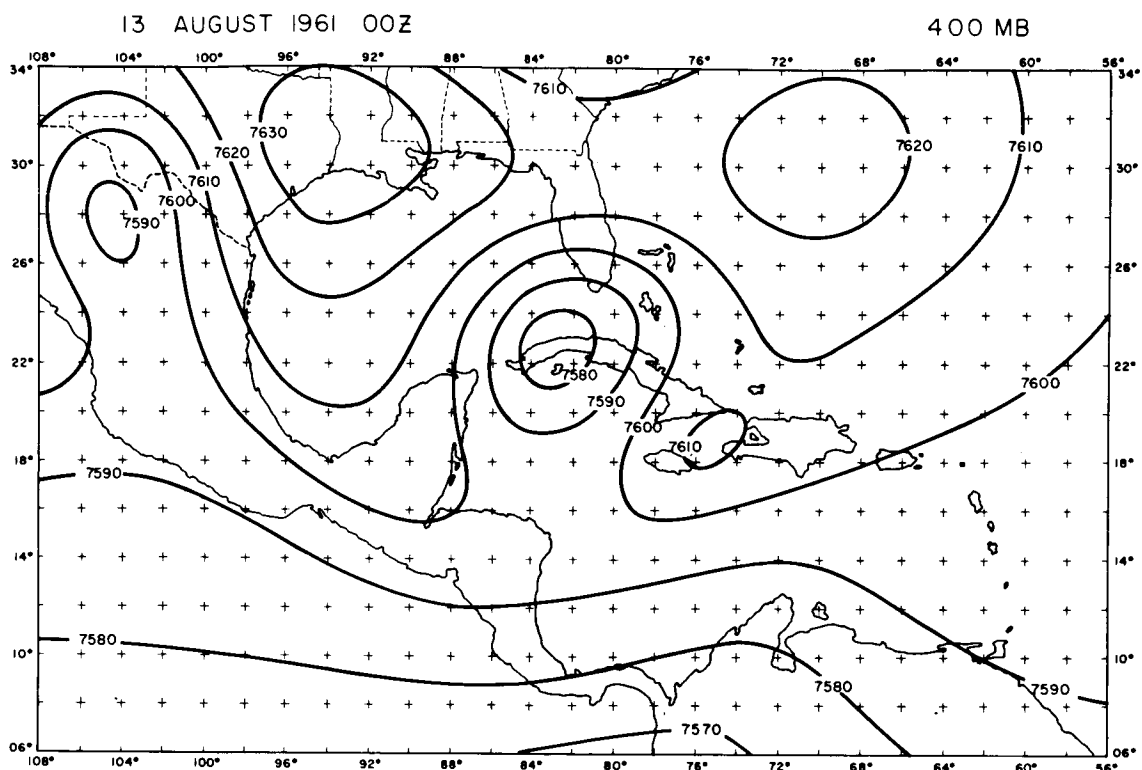
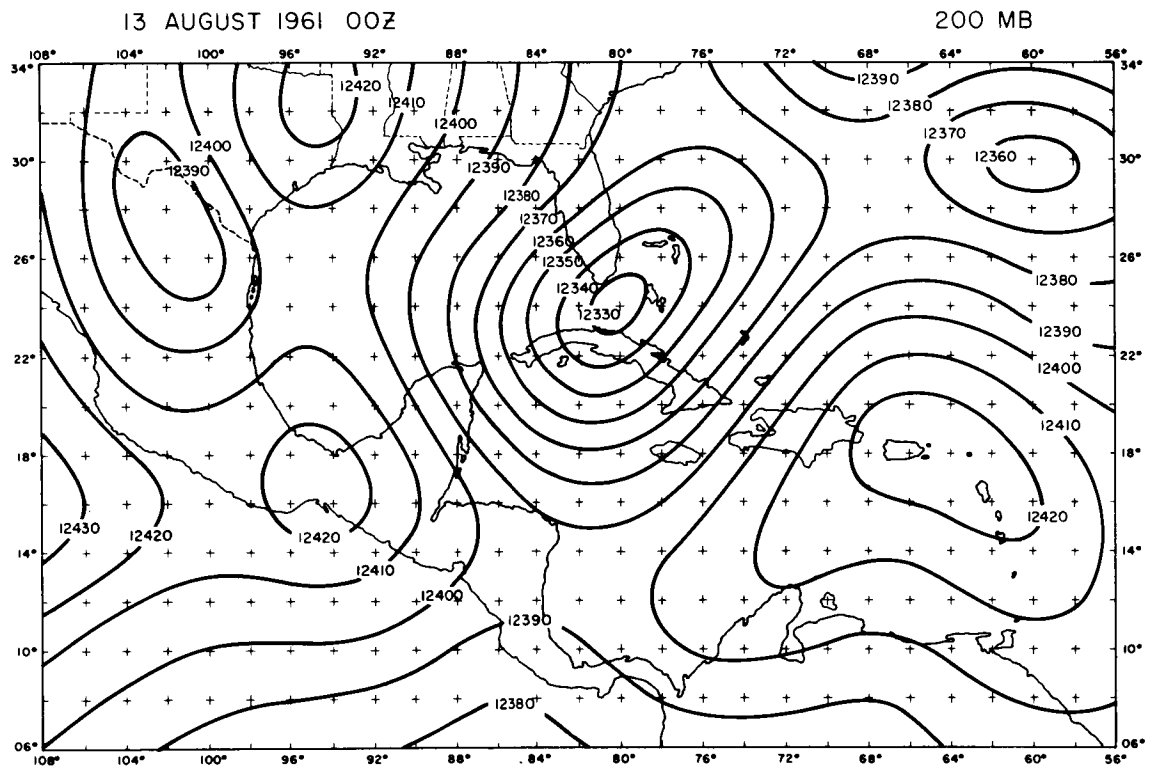


FIGURE 9. Geopotential Heights

Heights are in meters.



of 20 meters or less in the majority of the observations. The final analysis was subjectively smoothed to exclude any small-scale effects in the geopotential data.

It is possible to derive the temperature field with the hydrostatic equation from the geopotential analysis. This calculation was performed to compare the observed temperature patterns from the radiosonde data with the geopotential thickness temperatures. Some difficulty was encountered in the manipulation of the thickness, since the geopotential had been adjusted to the geostrophic approximation. The vertical derivative of the temperature, which is a parameter used by the numerical model, was erratic, giving high values at one level and low values at the next level, or vice versa. Upon examination of a typical tropical sounding, it can be seen that the vertical derivative of temperature increases slightly with height and is continuous. This was, indeed, the case with the observed temperature analysis. Therefore a complicated scheme was introduced to insure the smoothness of the vertical derivative of the thickness. The range of temperature difference between the maximum and the minimum was computed at each level. The central value of the range was then changed to a typical tropical temperature for that particular level. The difference was added or subtracted from all the temperatures resulting in a continuous vertical derivative. The horizontal gradients of thickness at each level are not destroyed during this process. This is important because the numerical model considers only the gradients of the temperature field, not the

absolute magnitude. Since the thickness analysis is a computed function, it will be presented in the section dealing with comparisons, Figure 17.

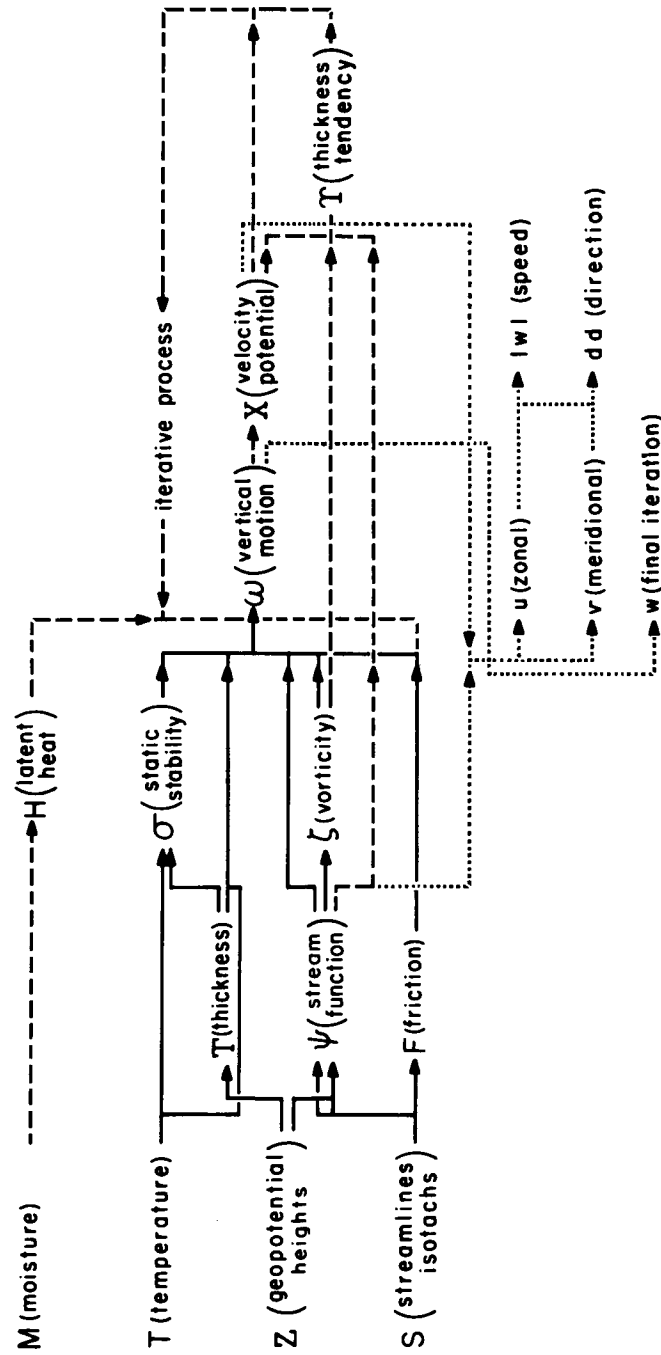
B. Structure of the Model

The numerical model selected to describe the three-dimensional structure of the tropics is commonly called the non-linear or multi-level balanced model (Charney, 1962). A formal derivation of this model is presented in the Appendix. The particular version that is used in this report may be divided into three basic parts: the derivation of the non-divergent part of the horizontal wind, the solution of the vertical motion (ω) equation, and the combination of the above results to form the complete three-dimensional field of motion. This structure is illustrated with more detail in schematic form in Figure 10.

Several different variations are possible within the framework of this model. The original data may be inserted into the model in two different ways, each being a complete specification of the initial state. If the geopotential heights are used, no other parameter is necessary except the moisture, since the non-divergent wind (stream function) and the thickness may be calculated directly. If the geopotential is ignored, the streamlines, isotachs, and temperature must be substituted. From the stream function the vorticity is derived and from the temperature or thickness, the static stability is calculated. These terms, together with a frictional effect from the streamlines or geopotential, will yield the first approximation of the vertical motion. The ω equation, used for the first approximation, does not contain any terms

FIGURE 10. Schematic drawing of the internal structure of the numerical model.

MULTI-LEVEL BALANCED MODEL



— First Approximation of Omega
 --- Iteration Scheme
 Final Results

that are a function of ω . The first guess of the vertical motion is then used to calculate the non-linear terms containing ω . The latent heating term is added at this point, since it is nonlinear in nature. An iterative process is performed until the difference between successive approximations is considered small. The final approximation of the vertical motion, the divergent part of the wind, which is a product of ω , and the stream function, define the complete three-dimensional structure of the atmosphere.

The model utilizes the X, Y, P, co-ordinate system with five levels of input data at 1000, 800, 600, 400 and 200 mbs. Several parameters are linearly interpolated to the intermediate levels, (900, 700, 500, 300 mbs) where the vertical motion is solved. The horizontal grid distance employed was two degrees latitude by two degrees longitude beginning at 108°W and extending to 56°W . The lowest latitude was 6°N and the highest, 34°N . This region contains approximately 500 grid points, which are shown in Figure 1 as crosses. The grid mesh is small enough to resolve wave lengths the order of 800 km, which is still consistent with the theory of the numerical model. This particular system of equations is not adequate for wavelengths smaller than mentioned above.

The simple centered finite-difference method was used to calculate the various terms in the equations of the model. In a diagnostic model, in which all time derivatives are eliminated, it is not necessary to worry about the differencing methods conserving certain properties as in the prognostic model. Therefore, the simplest difference method was taken. Several second-order partial differential equations must be solved to obtain the final results from

the model. A conventional method of relaxation as described by Thompson (1961), is used to obtain the solutions. The boundary conditions were zero at the top (100 mb) and bottom (1000 mb) for the omega equation, including a zero condition at the northern and southern edges. The stream function, velocity potential, and thickness tendency equations need only a two dimensional relaxation, requiring a zero condition at the northern and southern boundaries. The east-west boundaries were eliminated by adding six extra lines of grid points to the existing mesh. The last line of real data was parabolically interpolated over the six extra grid points to fit the real data at the other edge of the mesh, providing a cyclical continuity. Aside from the boundary problem, this area is of no interest when considering the diagnostic phase, however it becomes important in the prognostic application.

The entire model was programmed and solved on the IBM 7094. Each major calculation was transformed into a sub-program and processed individually, storing the results. At the conclusion of the computer operation for each map-time, a tape was generated containing over 400 two-dimensional fields. The tape was then available for any possible calculation from the information derived from the model.

C. Comparisons of model structure and data input variation

Stream Function. - There are two completely different approaches to the problem of obtaining the non-divergent component of the wind. The conventional method involves the use of the so-called balance equation, which

is a simplification of the divergence equation. It is written in the following vector notation (consult table of symbols for definitions),

$$\nabla \cdot f \nabla \Psi = \nabla^2 \phi - 2J\left(\frac{\partial \Psi}{\partial x}, \frac{\partial \Psi}{\partial y}\right) \quad (1)$$

This equation has certain nasty properties in that a solution is not always possible from a given geopotential field, especially in the tropics. The problem may be hurdled if some known quantity is substituted into the Jacobian term for the stream function (Ψ). Since the real wind was available, together with the geopotential, it was decided to insert u and v in place of $\frac{\partial \Psi}{\partial x}$ and $\frac{\partial \Psi}{\partial y}$. At first glance this substitution does not appear to be on firm ground; however, after obtaining solutions of the balance equation, 90% of the wind component in the tropics is non-divergent, substantiating the approximation.

Illustrations of the solution of the balance equation are presented in Figures 11-12. The 800 and 400 mb levels yielded similar results but are not shown. The stream function patterns are remarkably similar to the original geopotential fields, Figures 7-9. In fact the geostrophic wind is very closely approximated by the stream function in the majority of the cases. Some smoothing is evident, probably due to numerical truncation and finite difference errors, in the stream function fields. At 200 mbs the stream function speeds are slightly over-estimated, compared to the geostrophic wind, but still well within the range of observational error.

The alternate method, used to calculate the stream function, is described by Hawkins and Rosenthal (1965). The Helmholtz equation is

FIGURE 11. Balanced Equation Stream Function

Heavy lines are stream function.

Heavy dashed are intermediate isolines.

Light, labeled lines are speed of stream function
in meters per second.

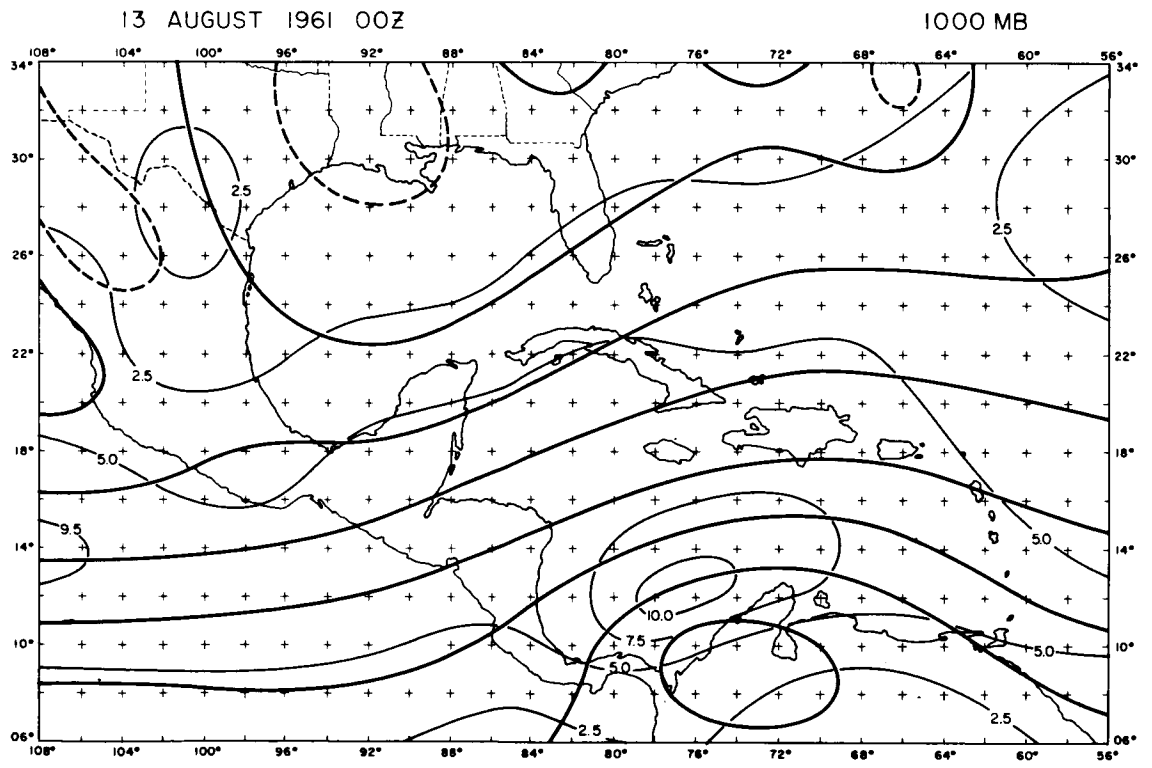
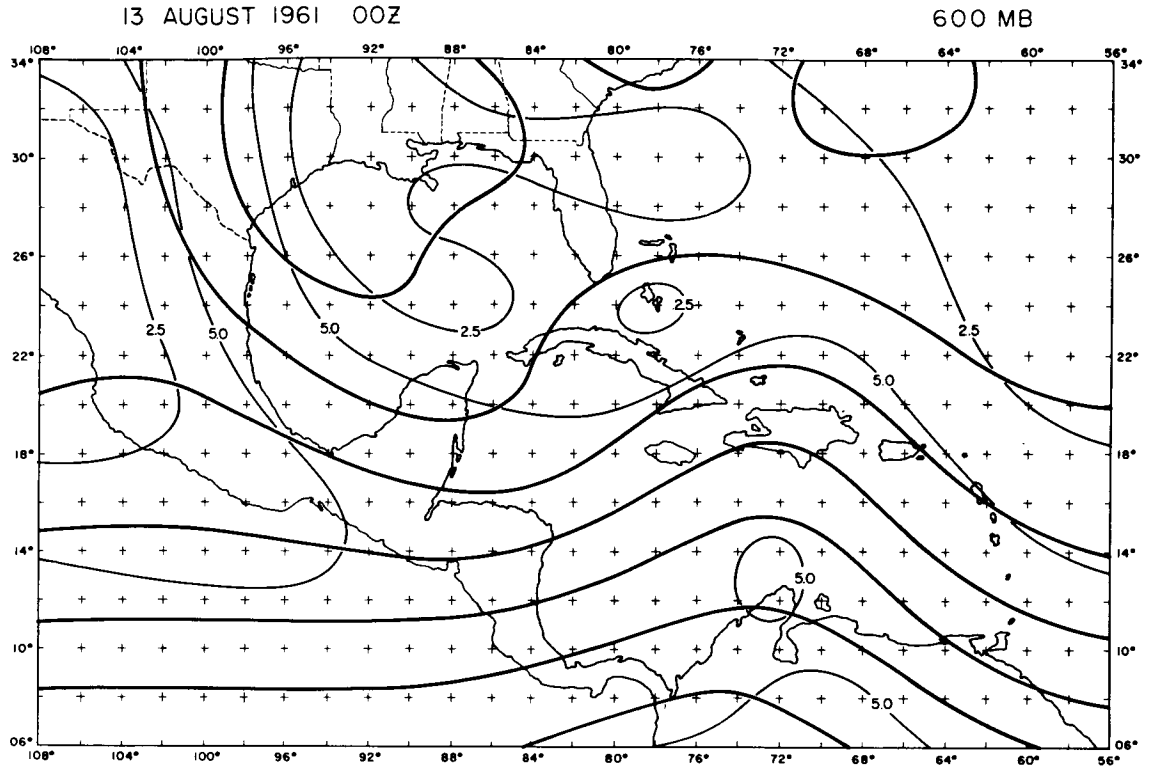


FIGURE 12A. Balanced Equation Stream Function

Heavy lines are stream function.

Light, labeled lines are speed of stream function
in meters per second.

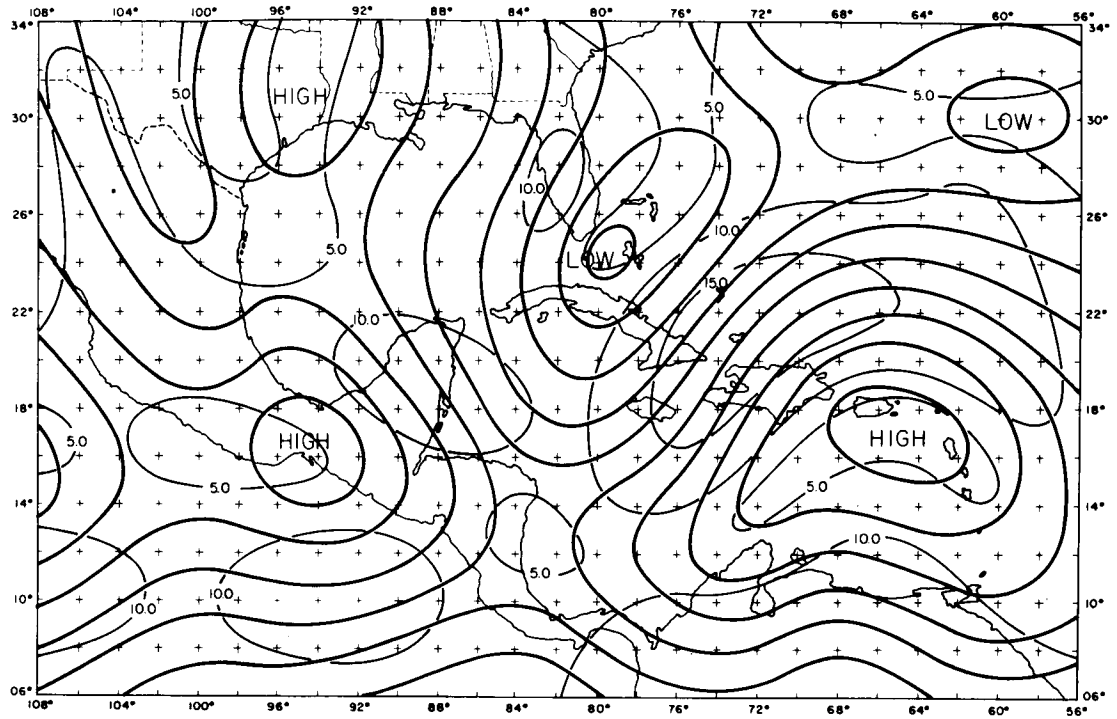
FIGURE 12B. Kinematic Stream Function

Heavy lines are stream function.

Light, labeled lines are speed of stream function
in meters per second.

13 AUGUST 1961 00Z

200 MB



13 AUGUST 1961 00Z

1000 MB

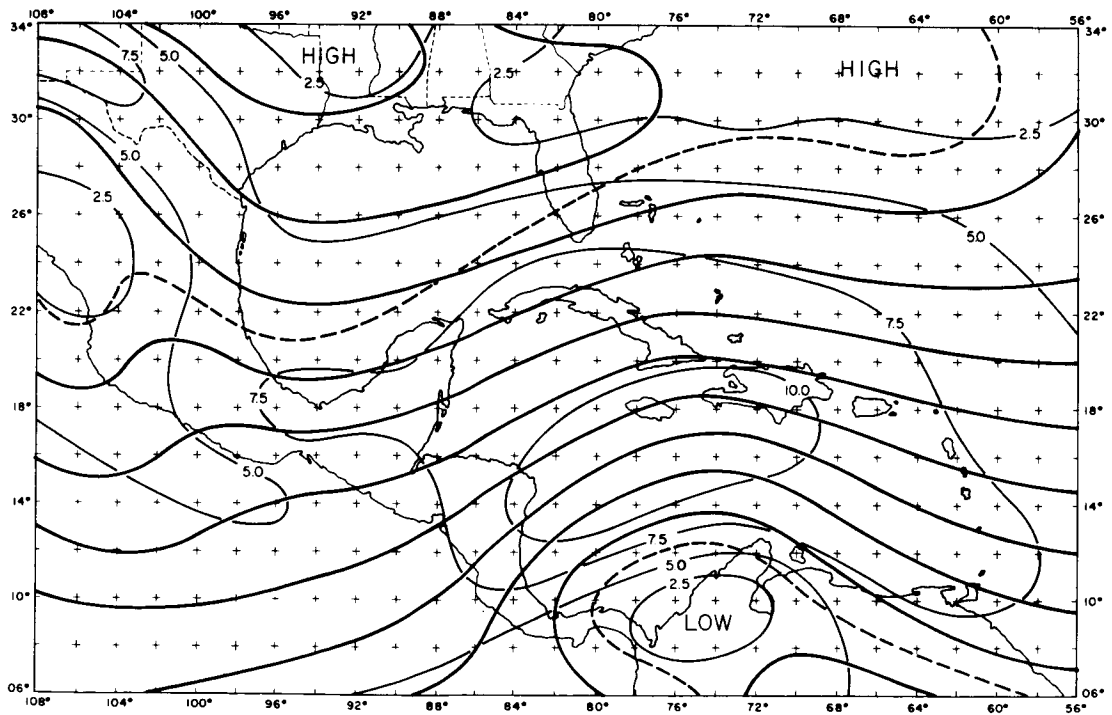
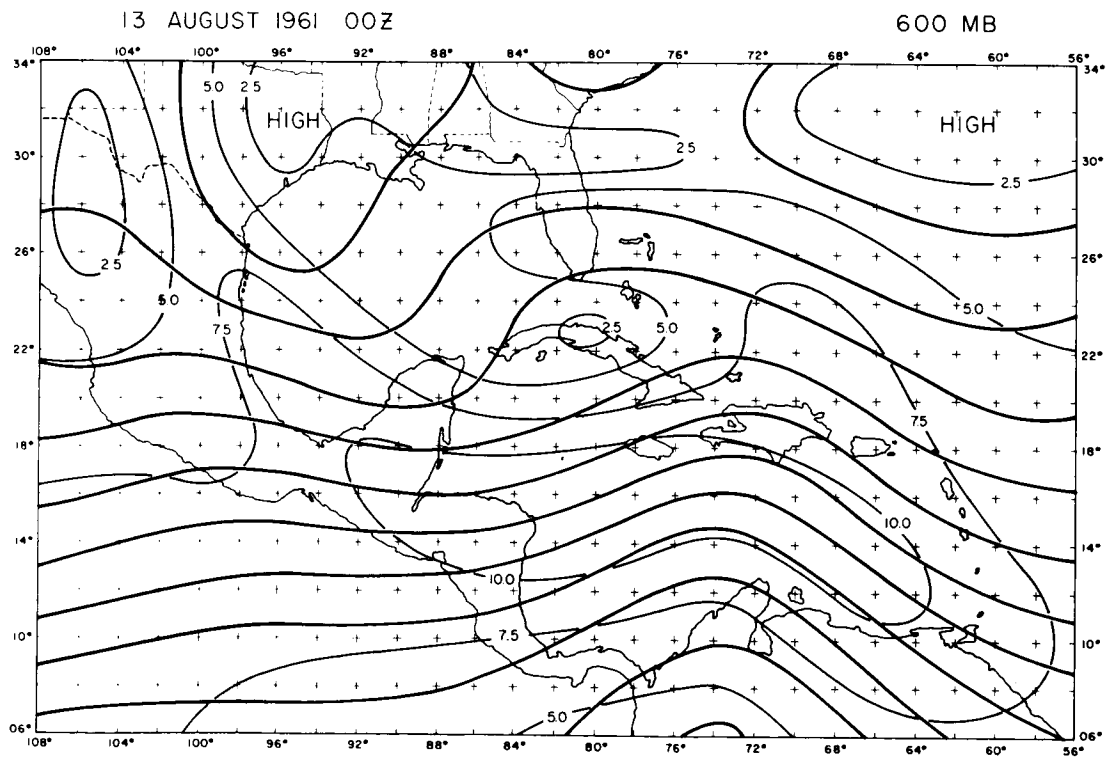
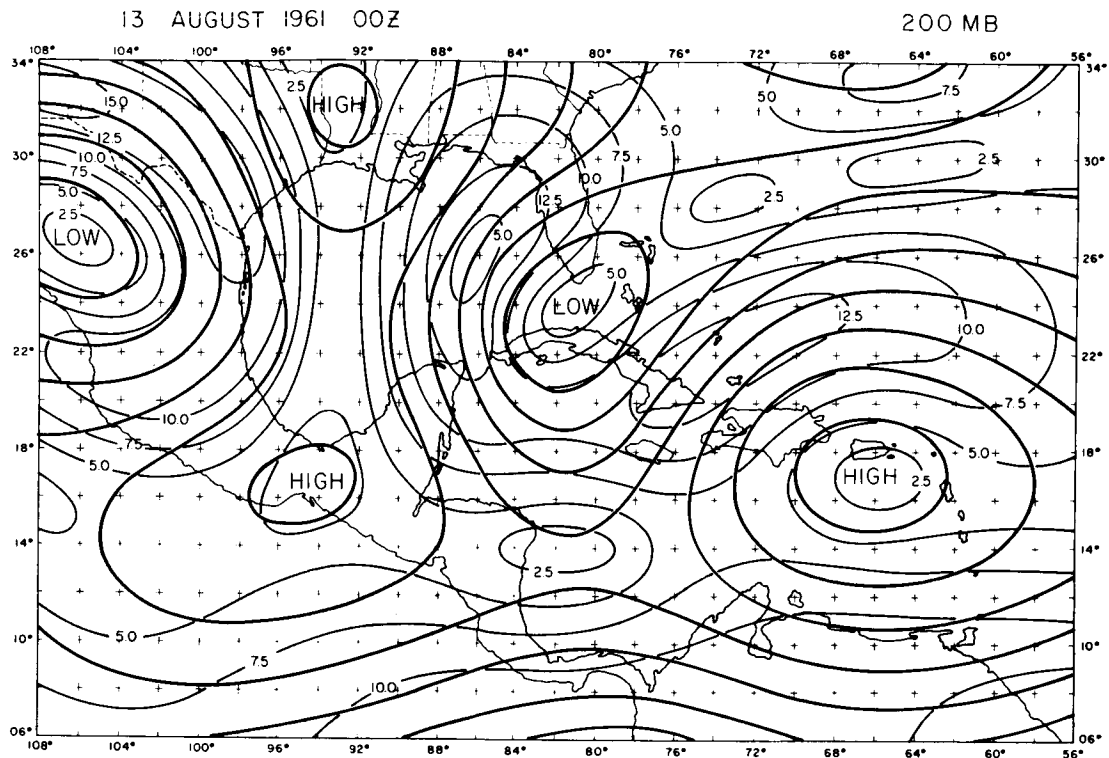


FIGURE 13. Kinematic Stream Function

Heavy lines are stream function.

Light, labeled lines are speed of stream function
in meters per second.



manipulated to form the following equation,

$$\nabla^2 \Psi = \zeta \quad (2)$$

where the relative vorticity is derived directly from the observed wind field.

The boundary values are made a function of the divergence of the wind, instead of the zero condition imposed in the solution of the balance equation. Aside from being a simpler equation, mathematically, several advantages are apparent in this formulation. No geopotential maps along with their accompanying approximations are necessary. Also the possible error in the Jacobian term of the balance equation is eliminated. Actually no approximations are considered when equation (2) is applied, whereas the balance equation involves certain simplifications of the divergence equation. This fact makes, what the author prefers to call the kinematic method, equation (2), more accurate overall.

In Figures 12-13, the kinematic method stream function is represented with the non-divergent wind speeds. Generally speaking the patterns exhibited by the kinematic method compare favorably with the balance equation results, Figures 11-12. One should expect a positive correlation between the two methods since the geostrophic approximation is implied in the height fields. Increased detail in the flow configuration is evident in the kinematic stream function. The non-divergent wind speeds have increased somewhat in magnitude also. The reverse is true at 200 mbs where wind speeds have decreased and the pattern appears to be smoother.

To compare the different stream function products in a more interesting way, each was submitted as the non-divergent wind into the omega equation of the balanced model. All other input parameters were held constant and only the stream function was permitted to vary. The thickness temperature was arbitrarily utilized as the thermal parameter. In order to show the effects of friction and latent heat separately, they were omitted from the vertical motion equation and will be discussed later. The comparison omegas are then essentially adiabatic and frictionless. They are presented in Figure 14 (balanced stream function) and Figure 15 (kinematic stream function).

Perhaps the most surprising result from this comparison, is the difference in the patterns of the vertical motion fields. From a mere visual examination of the stream functions, the differences do not appear as dramatic as displayed in the computed vertical motion. There appears to be numerous areas where the omega has even changed sign. The kinematic stream function technique produces a new center or di-pole of vertical motion just south of Hispanola. Most of the large-scale features are present in both maps, however the orientation and magnitudes are slightly different. The discrepancies at 500 mbs are not nearly as great as 900 mbs, possibly indicating that the geostrophic geopotential is a better approximation at higher levels in the atmosphere.

Since a decision is necessary regarding the choice of stream function for future work, the kinematic method was selected for the non-divergent wind. This process appears to be at least as good as the balance formulation, when the resulting vertical motion fields are considered. The kinematic method also has

FIGURE 14. Vertical Motion obtained from a Balance Equation

Stream Function and Geopotential Thickness.

Isolines are every 20×10^{-5} mb per second (approximately 0.2 centimeters per second).

Solid lines are sinking, dotted lines are neutral, and dashed lines are rising.

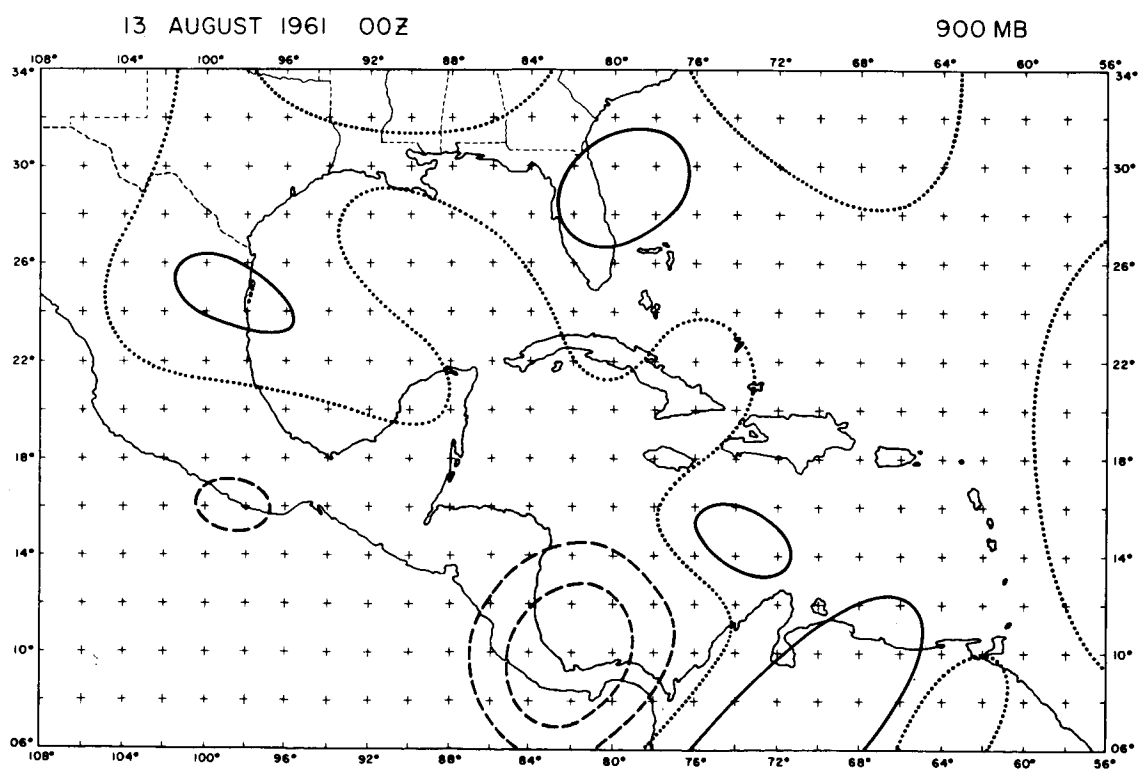
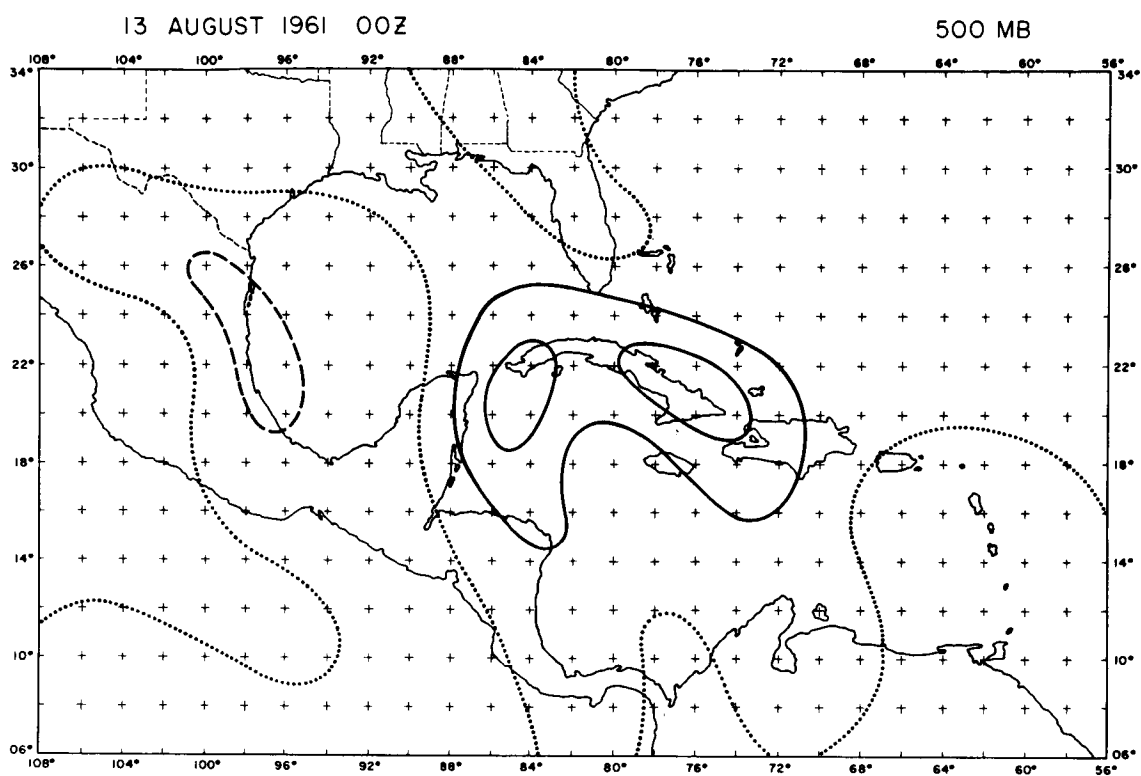
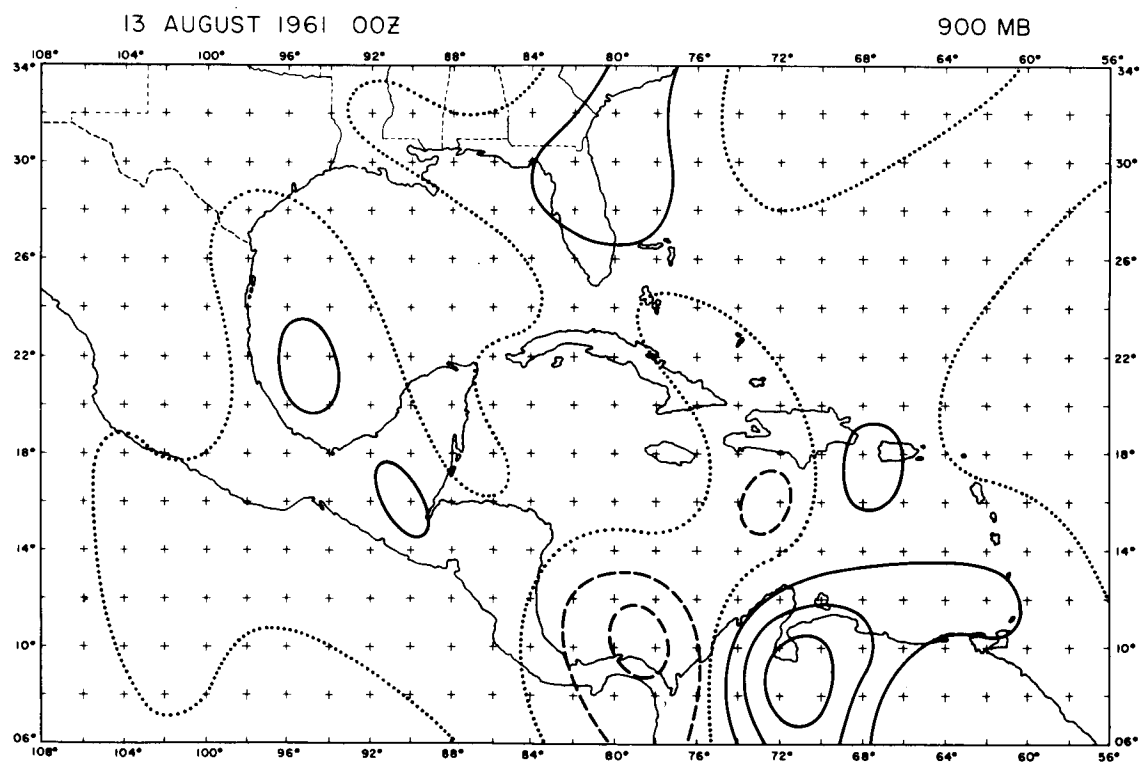
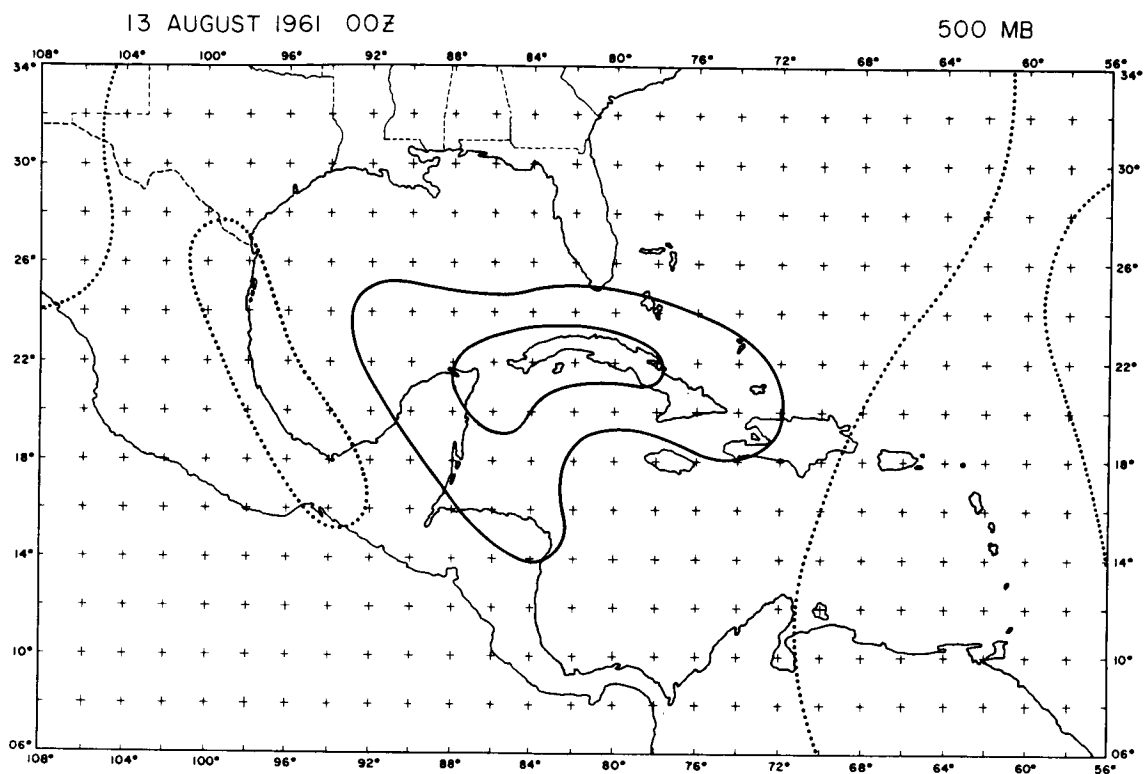


FIGURE 15. Vertical Motion obtained from a Kinematic Stream

Function and Geopotential Thickness.

Isolines are every 20×10^{-5} mb per second (approximately 0.2 centimeters per second).

Solid lines are sinking, dotted lines are neutral, and dashed lines are rising.



the added advantage of completely ignoring the geopotential as mentioned before. Further justification of the kinematic stream function can be obtained by partitioning the vertical motion into its various components or mathematical terms. (Krishnamurti, 1966). This is accomplished by solving the omega equation with only one term at a time. The process insures that the total sum of the components will equal the complete omega value. An illustration of such a partitioning is shown in Figure 16.

Some explanation is necessary to fully understand these cross-sections. Each individual grid point is made up of a vector and several lines. The vector is the total vertical motion pointing in the appropriate direction, (up equals rising air, down equals sinking) and the lines adjacent to the vector are the various components again with their direction indicating sinking or rising. The components are given below in mathematical form and English description in the order that they appear from left to right at each grid point in Figure 16.

$$f \frac{\partial}{\partial p} J(\psi, \nabla^2 \psi + f) \quad ; \text{ differential vorticity advection.}$$

$$\pi \nabla^2 J(\psi, \theta) \quad ; \text{ laplacian of thermal advection.}$$

$$-2 \frac{\partial}{\partial p} \frac{\partial}{\partial t} \left[J \left(\frac{\partial \psi}{\partial x}, \frac{\partial \psi}{\partial y} \right) \right] \quad ; \text{ differential time dependent deformation of the stream function.}$$

$$-f \frac{\partial}{\partial p} (\nabla^2 \psi \nabla^2 \chi) \quad ; \text{ differential divergence-vorticity effect.}$$

(see appendix for derivation of terms).

Actually there are nine terms in the omega equation excluding friction and heating, however the magnitudes of five terms were too small to be represented.

The four terms listed above will henceforth be referred to as the vorticity, thermal, deformation, and divergence terms respectively.

From careful examination of Figure 16, especially at 500 mbs, it appears that the vorticity term of the kinematic method is considerably stronger in most cases, increasing the magnitude of the total omega. This may be related to the more detailed nature of the kinematic stream function and the associated higher non-divergent wind speeds. The thermal term also increases in size in the kinematic case even though the temperature field remained constant. This is primarily due to the advective property in the thermal term being influenced by the stream function. The nonlinear terms do not appear to be important in this particular case. From the previous discussion and comparisons it is reasonable to conclude that the kinematic stream function is superior to the balanced equation formulation.

An interesting side light of this comparison is the illustrated opposition of the vorticity and thermal terms. This effect is most pronounced at 900 mbs, where magnitudes of nearly a half a centimeter per second rising produced by the vorticity, are counteracted with equal magnitudes of sinking from the thermal term. The opposition is reflected in both cross-sections indicating that it is not an effect of a particular choice of stream function. Perhaps the different types of temperature input that will be discussed next, may shed some light on this problem.

Temperature. - The temperature distribution that is to be operated on by the numerical model may be obtained in two different ways. The most

FIGURE 16A Kinematic Stream Function Vertical Motion in
Partitioned Form

Heavy vector is total vertical motion.

Light lines are components of vertical motion.

The order at each grid point from left to right:

Total, vorticity thermal deformation, and divergence.

Thickness temperature used for thermal term.

FIGURE 16B Balanced Stream Function Vertical Motion in
Partitioned Form.

Heavy vector is total vertical motion.

Light lines are components of vertical motion.

The order at each grid point from left to right:

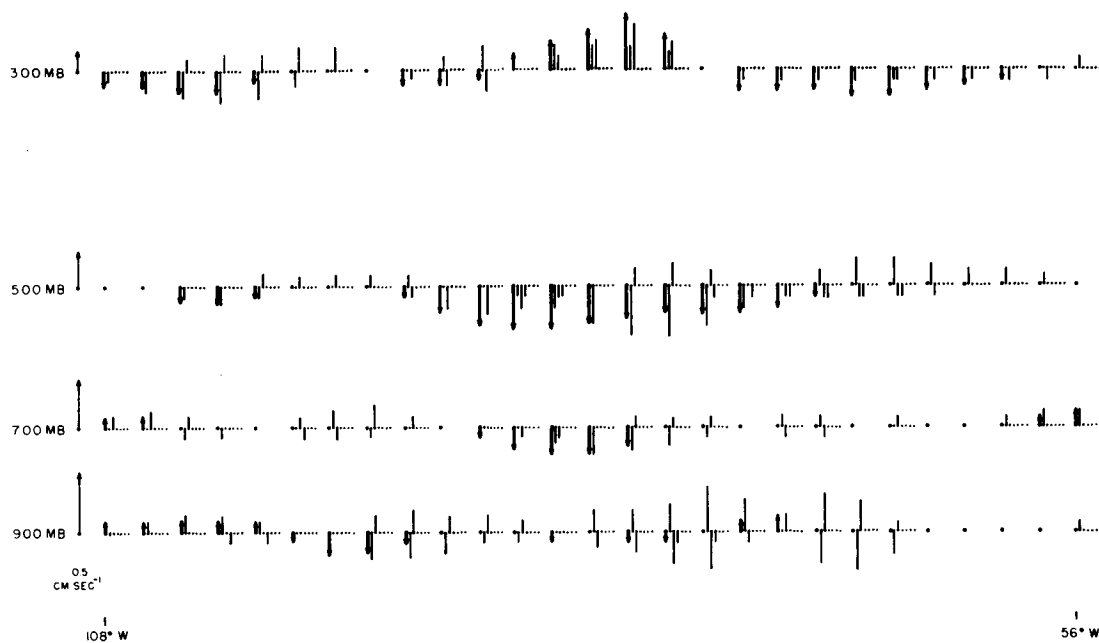
Total, vorticity thermal deformation, and divergence.

Thickness temperature used for thermal term.

OMEGA CROSS SECTION
13 AUGUST 1961 00Z

0 100 100 • 10³ MB SEC⁻¹

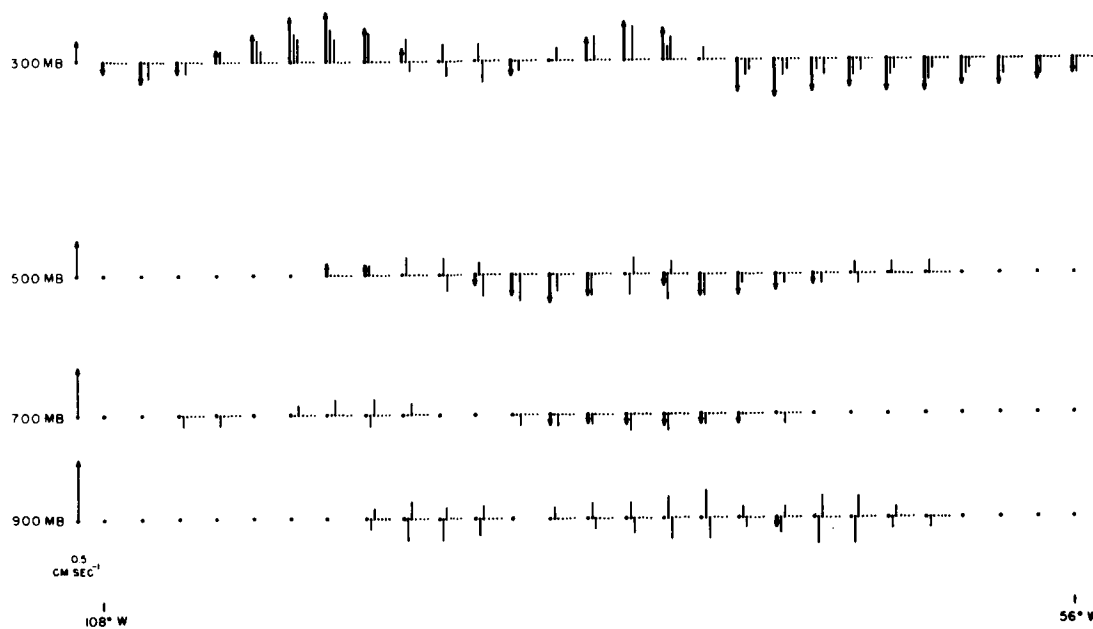
20° N



OMEGA CROSS SECTION
13 AUGUST 1961 00Z

0 100 100 • 10³ MB SEC⁻¹

20° N



obvious method is to analyze, directly, the observed temperatures from the radiosonde. The only computation necessary, before the analysis is performed, is the vertical averaging mentioned previously in the Data Preparation section. If the data network is dense enough, it becomes a fairly easy task to analyze the synoptic-scale temperature patterns directly from the observations even though the gradients are small in magnitude.

The alternate method of obtaining a temperature analysis is a thickness computation from the geopotential field. Since the geopotential is not a well-defined quantity in the tropics, the temperature derived from such a parameter is subject to similar errors. In this particular research, the geopotential was adjusted to geostrophically fit the observed winds for the stream function calculation. Therefore, the thickness temperature contains the geostrophic approximation implicitly. This may not be in the best interest, concerning an accurate analysis, due to the relatively weak gradients of temperature being altered significantly by the adjustment. No experiment was performed, using the observed, unadjusted geopotential heights directly to calculate thickness. Perhaps this might lead to a more reliable calculation of temperature.

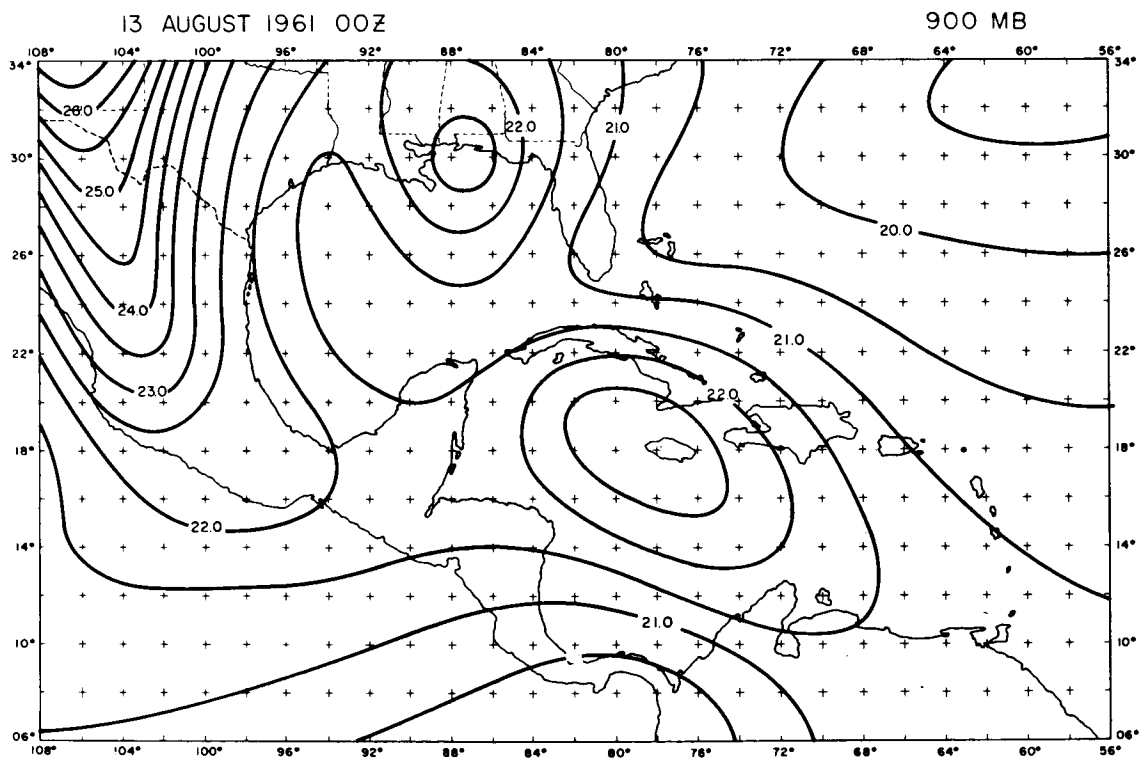
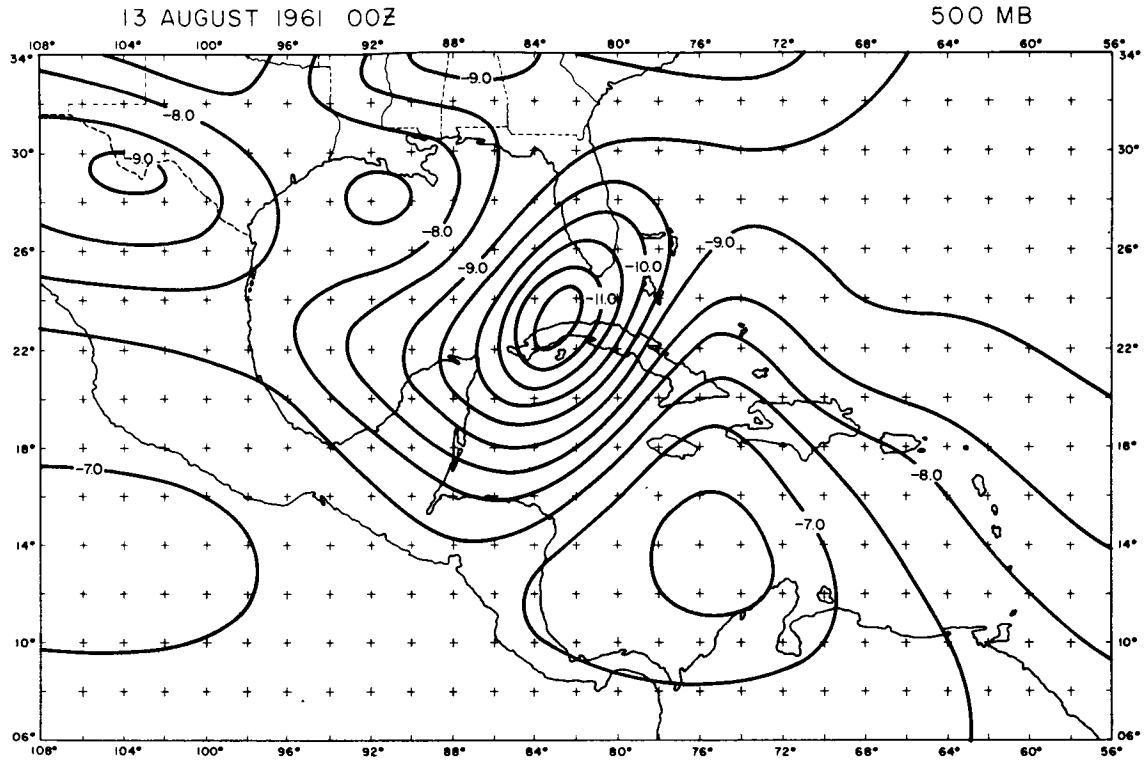
The two types of temperature analysis are illustrated in Figures 17-18. The observed temperature was linearly interpolated from the original input levels to the intermediate levels presented. The thickness temperatures at 900 mbs in Figure 17 appear to be more disorganized than their observed counterparts in Figure 18. There is also considerable discrepancy in the location of gradients

FIGURE 17. Geopotential Thickness Temperature.

Isolines are drawn every 0.5 degrees Centigrade.

FIGURE 18. Observed Temperature

Isolines are drawn every 0.5 degrees Centigrade.



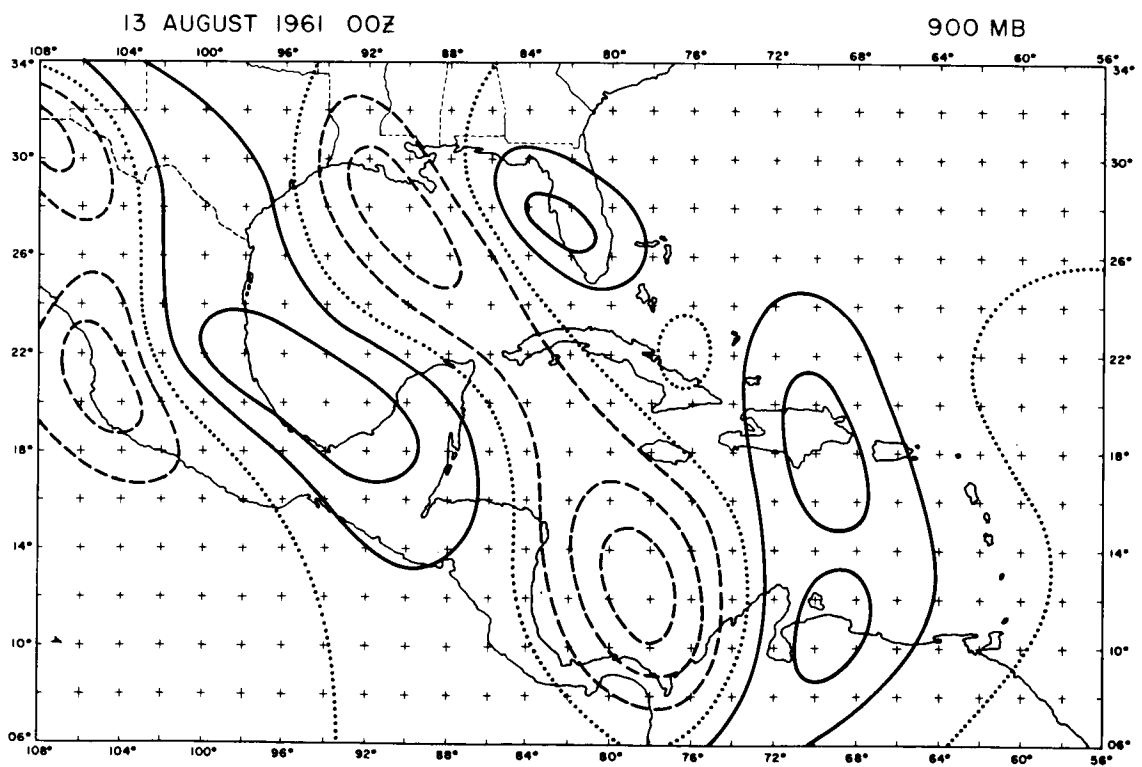
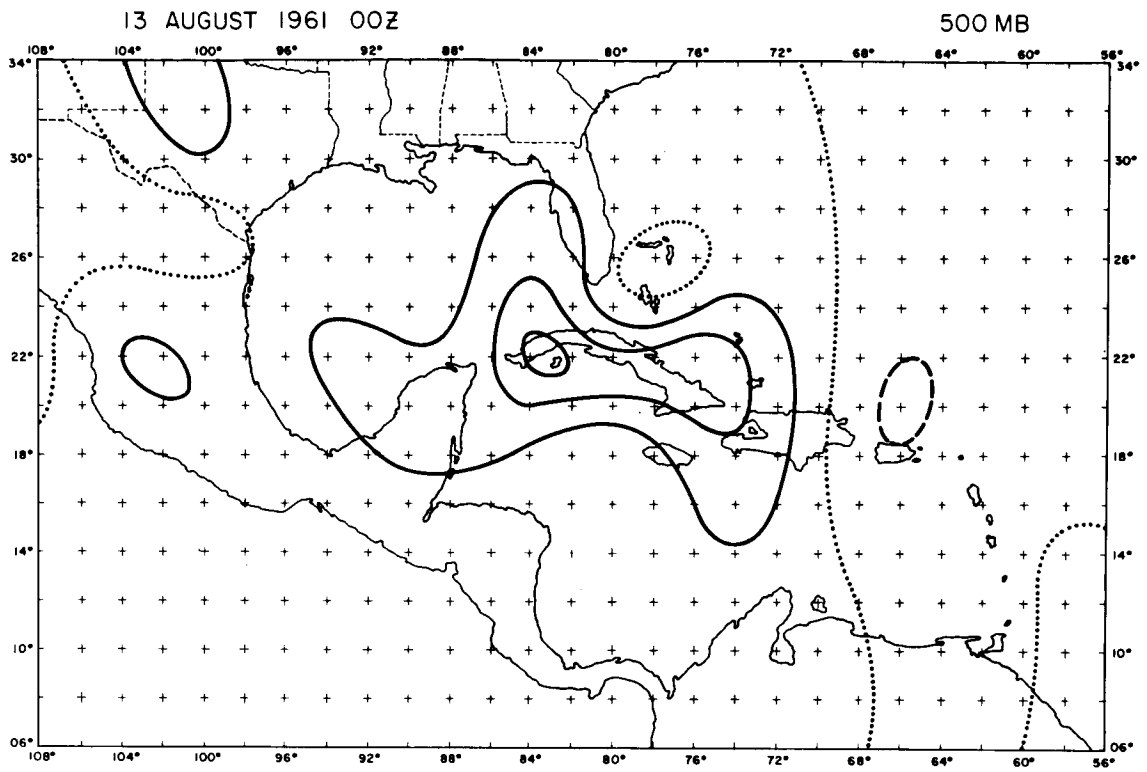
of temperature even in regions of dense data coverage. It must be remembered that the computer model considers gradients of temperature, rather than numerical values. Therefore, large differences in the solution of the omega equation can be expected. The two areas of relatively warm air at 900 mbs are seen on both maps; however, the terrain heating effect, shown on the observed temperature analysis over Mexico, is not picked up on the thickness analysis. At 500 mb, the general patterns are in much better agreement than at 900 mb. Once again, this illustrates that the geostrophic adjustment error is greatest near the surface. The centers of temperature maximum or minimum remain stationary between the two types of analysis. Some smoothing is evident in the thickness temperature, as the observed fields reveal tighter gradients in many locations.

As in the case of the stream function comparison, the two variations of temperature input were submitted to the omega equation. The kinematic stream function was used as the non-divergent wind in both cases. The model structure was kept exactly the same as described in the stream function comparison. Since the thickness temperature was utilized during the previous comparison, it is only necessary to refer to Figure 15. The observed temperature analysis omegas are shown in Figure 19. The relatively large differences in the gradients of temperature, shown on the analyses, becomes quite distinct in the omega patterns. At 900 mbs both the rising and sinking motion increased in magnitude in the case of the observed temperature. The patterns of vertical

FIGURE 19. Vertical Motion obtained from Observed Temperature
and Kinematic Stream Function.

Isolines are every 20×10^{-5} mb per second,
(approximately 0.2 centimeters per second).

Solid lines are sinking, dotted lines are neutral,
and dashed lines are rising.



motion appear to be more organized when the observed temperature is used. Recalling the irregular nature of the thickness temperature at 900 mb, these patterns are probably reflected in the omega field as well. Generally speaking, the vertical motion centers have not translated a great deal between the two types of analysis, however the shape and amplitude of the pattern has changed considerably. At 500 mb the previous statement is true as well, with less overall change.

In order to gain further insight on which temperature representation to use, the omega partitioning was again utilized. In Figure 20 the lower cross-section is a duplication from Figure 16 so that a contrast may easily be drawn from the two different methods. As in the case of the horizontal illustrations of omega, the larger magnitudes of vertical motion are evident with the observed temperature. This is most striking at 900 mb, where the rising has doubled and tripled in size. The reason for this phenomena is explained by examining the components of the vertical motion. The thickness temperature term displays a remarkable opposition to the vorticity term, whereas the observed temperature produces a component in phase with the vorticity. The actual magnitude of the thermal term has not increased, but has reversed its sign, yielding a larger total omega. This effect is also quite noticeable at 700 mb, where approximately 0.5 centimeters per second sinking was generated by the observed temperature, thermal term. The changes at 500 and 300 mbs are less spectacular with 500 mb exhibiting the smallest adjustment.

7

FIGURE 20A. Observed Temperature Vertical Motion in
Partitioned Form.

Heavy vector is total vertical motion.

Light lines are components of vertical motion.

The order at each grid point from left to right: Total,
vorticity thermal deformation, and divergence.

Kinematic stream function used as non-divergent
wind.

FIGURE 20B. Thickness Temperature Vertical Motion in
Partitioned Form.

Heavy vector is total vertical motion.

Light lines are components of vertical motion.

The order at each grid point from left to right:

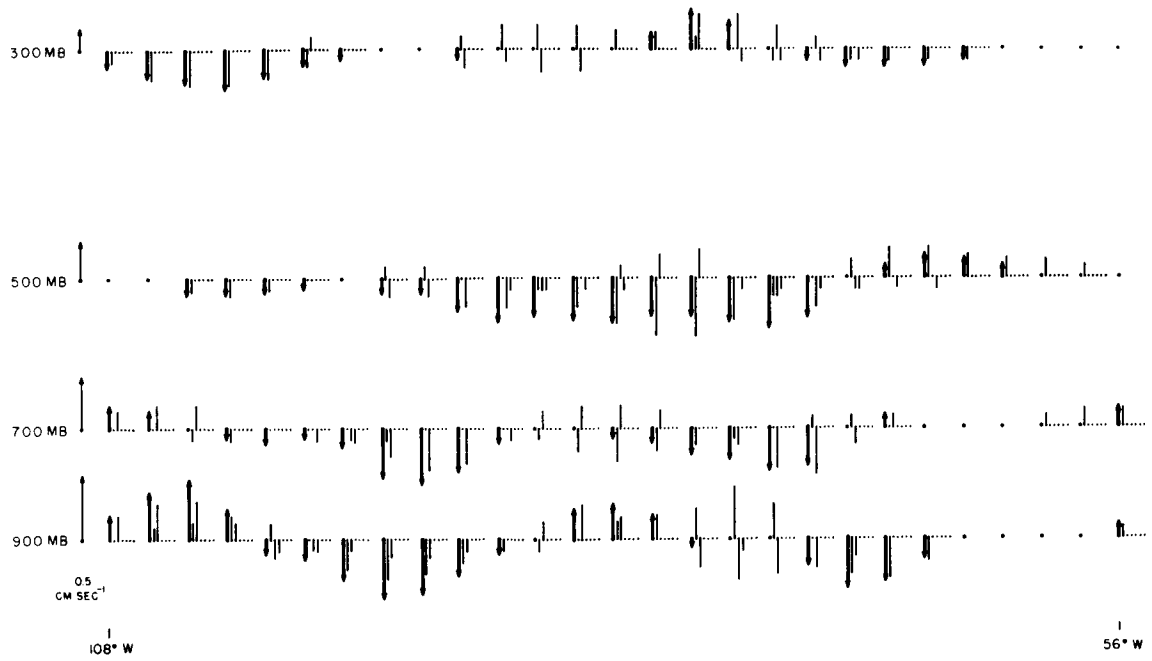
Total, vorticity thermal deformation, and divergence.

Kinematic stream function used as non-divergent wind.

OMEGA CROSS SECTION
13 AUGUST 1961 00Z

0 100 100 $\times 10^3$ MB SEC⁻¹

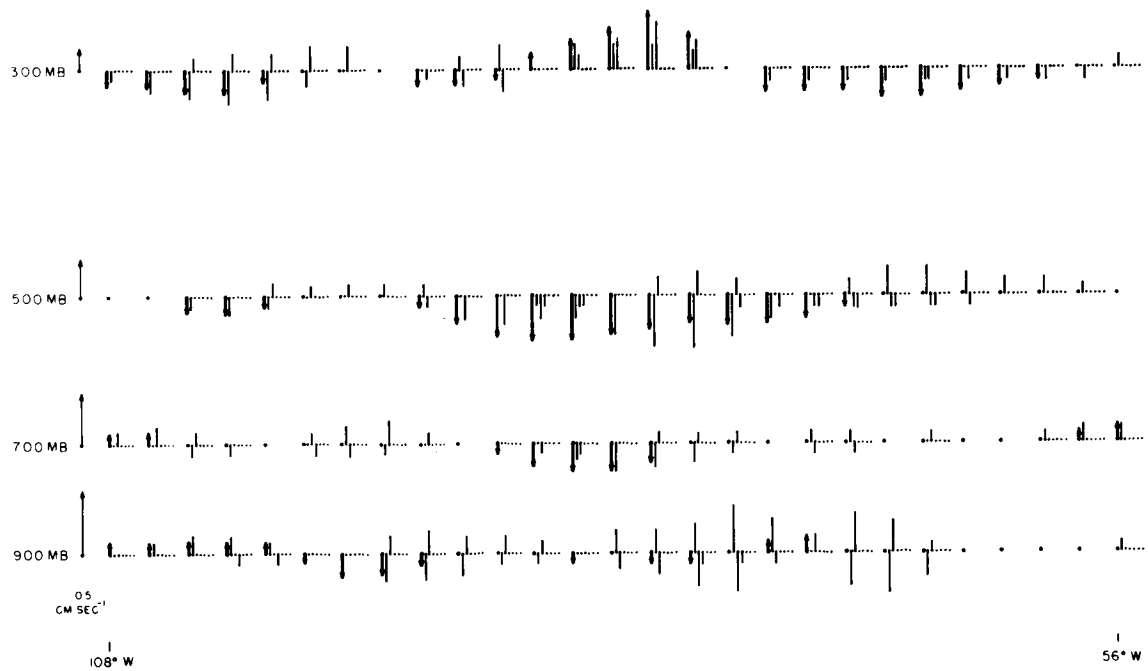
20° N



OMEGA CROSS SECTION
13 AUGUST 1961 00Z

0 100 100 $\times 10^3$ MB SEC⁻¹

20° N



Sifting the evidence presented above, a logical choice for the temperature field would be the observed values. The omega patterns appear to be more reasonable and larger in magnitude using the observed thermal distribution. Several other advantages are present using the observed temperature. The fields are relatively easy to obtain and analyze, and no approximations are necessary in the evaluation of the thermal parameter; which is not the case with the thickness temperature.

It now appears that the kinematic stream function together with the observed temperature distribution gives the better result when applied to an adiabatic, frictionless, numerical model. Since the comparisons offer no absolute proof of the validity of either method, the previous conclusion is based on subjective as well as objective reasoning. In all further work in this paper, the basic input to the diagnostic model will consist of the observed velocity and thermal patterns. This involves the analysis of one extra scalar field, but the various comparisons indicate that it may be worth the additional work.

Friction. - The effect of the surface drag or frictional stress on the atmosphere may be included in the formulation of the balanced numerical model. Such an effect is usually some function of the surface wind speed and is included in the boundary conditions for the solution of the vertical motion (Cressman, 1963). The author chose instead, to derive the frictional term as an internal forcing function (known quantity) in the omega equation. This enables the partitioning process to separate the frictional part of the rising and sinking from the rest of

the vertical motion. The results from both methods are essentially the same.

The frictional term was obtained using the theory presented in Petterssen (1956). A mathematical derivation can be found in the Appendix. Allowing the frictional effect only at 1000 mb and using the empirical approximation of the stress, the final form of the forcing function may be written;

$$+ f_e g C_D \left[\frac{\partial}{\partial x} \frac{\partial^2}{\partial p^2} (|\mathbf{V}|v) - \frac{\partial}{\partial y} \frac{\partial^2}{\partial p^2} (|\mathbf{V}|u) \right] \quad (3)$$

the drag coefficient was held constant in the horizontal and its numerical value assumed to be 2.0×10^{-3} . Term (3) appears in the 900 mb omega equation only with the rest of the levels having no frictional effects in their equations. Since the observed wind field was available at 1000 mb, as a by-product from the stream-function calculation, a direct substitution was made into term (3).

However, it is possible to write the u and v components in terms of the non-divergent and irrotational parts of the wind. Term (3) may then be evaluated internally in the model without the aid of the observed surface velocities.

The resulting omega distribution from this formulation is illustrated in Figure 21. The partitioned frictional component is shown with the 1000 mb wind vectors in order to point out the relations between the wind field and the vertical motion. From this representation it is easily seen that the sinking motion corresponds with diffluent regions in the velocity field and rising correlates well with confluent area. One apparent contradiction to this rule is located in the northeast corner of the map where weak sinking is taking place over an area of confluence. The maximum intensity of the vertical motion field induced by the

FIGURE 21A. Frictional Component of the Vertical Motion
with the 1000 mb Wind Vectors.

Heavy lines are sinking, dotted lines are neutral
and dashed lines are rising.

Isolines are drawn every 10×10^{-5} mb per second.

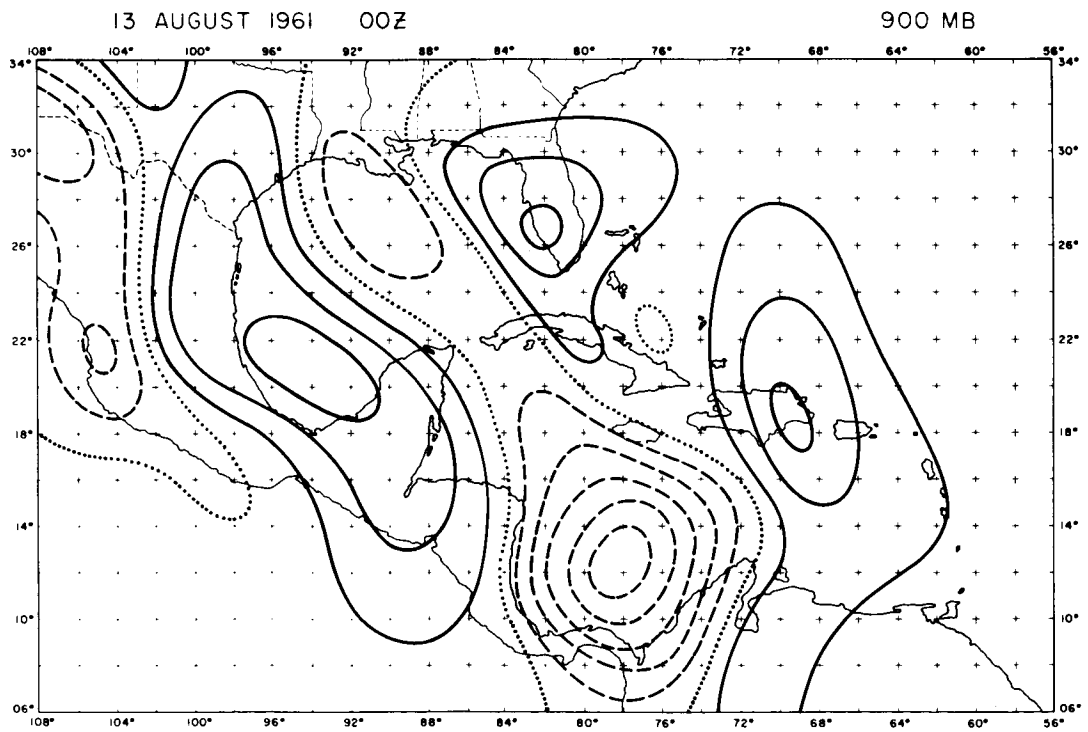
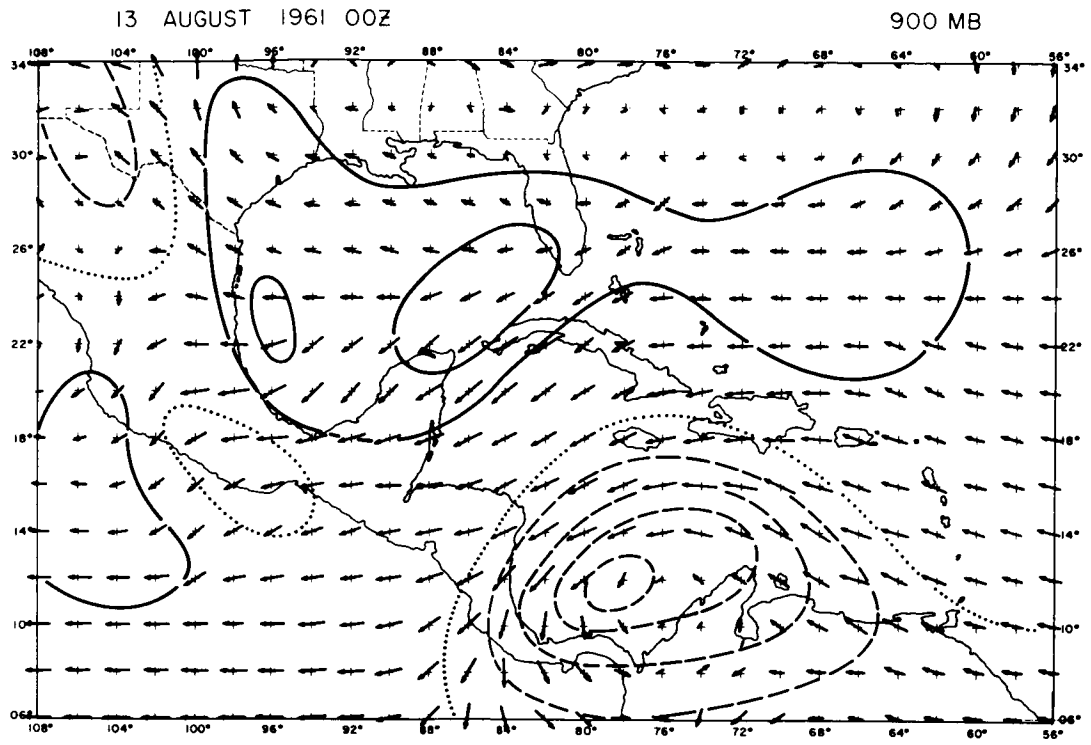
Wind vectors are proportional to wind speed.

(10 meters per second equals 0.4 centimeters).

FIGURE 21B. Total Vertical Motion with Friction added.

Heavy lines are sinking, dotted lines are neutral
and dashed lines are rising.

Isolines are drawn every 20×10^{-5} mb per second.



frictional term is approximately 0.5 centimeters per second. This appears to be reasonable in the tropics since the wind speeds are weaker than extra-tropical storm velocities. From the partitioning it is shown that the frictional term is the same order of magnitude as the adiabatic terms in the omega equation. Therefore, it is important to include frictional effects in the tropics.

If the resulting frictional component of omega were converted into the divergent portion of the wind, the circulation centers at the surface would exhibit a characteristic inflow or outflow. This is exactly the effect that is desired, when friction is included in a numerical model. Therefore the formulation of term (3) proved to be quite adequate for use in the diagnostic model. The magnitude of the total vertical motion with friction, as shown in Figure 21, has increased considerably when compared with the frictionless omega in Figure 19. The shape of the pattern has remained more or less constant however, almost every center has increased in intensity. The maximum rising motion is now nearly 1.0 centimeters per second in the vicinity of the closed circulation. It appears that friction is an important contributor in the generation of the vertical motion fields in the tropics.

Latent Heat. - According to some recent theoretical and numerical studies of Charney (1964), Kuo (1965) and various others, the contribution of latent heat in the development of synoptic-scale tropical storms is of major importance. It was therefore reasoned that the inclusion of some latent heat effects in the diagnostic-model was necessary. In the middle latitudes, the

addition of latent heat is relatively simple, because the diabatic heating usually takes place in stable regions where the large-scale motions are dominant. Several authors, Danard (1964) and Petterssen (1961) have, indeed, accomplished various types of latent heat inclusion with considerable success. However, this is not such an easy task in the tropics, since the greatest amount of latent heat being produced is on a much smaller scale than is considered by the numerical model. The cumulus scale "hot towers" are very effective in the generation of latent heat as mentioned by Riehl (1958). Therefore a parameterization of the cumulus-scale latent heat is needed to incorporate this effect into the numerical model.

Both Charney (1964) and Kuo (1965) have derived a method by which the cumulus-scale latent heat contribution is estimated. Of the two methods, Kuo's formulation is the most complicated involving actual calculations of the area covered by cumulo-imbus towers. However, Charney's method, which resembles the stable region formulations, was considered suitable for the needs of the diagnostic model. He uses the three-dimensional moisture flux of a column above the boundary layer as the parameter that is proportional to the amount of latent heat being released. In the case of the five level model, the convergence of moisture flux may be written;

$$I = \left[\frac{1}{g} \int_{q_{00}}^0 \nabla \cdot \mathbf{V} q \, dp \right] - \frac{\omega_{q_{00}} q_{q_{00}}}{g} \quad (4)$$

The first term is the horizontal flux above the boundary layer and the second is the moisture leaving or entering the top of the boundary layer. In this

particular model, 900 mb was selected as the top of the boundary layer effects.

The quantity (I) is calculated in the iterative process of the omega equation, since it is necessary to have the vertical motion at 900 mb and the divergent wind with the stream function at the other levels. The specific humidity is taken directly from the analyzed mixing ratio shown in the Data Preparation section. An example of the moisture convergence (4) is shown in Figure 22. Each isoline of moisture convergence is equivalent to approximately 2.5° of warming a day if all the moisture coming into the column is precipitated. The patterns of moisture flux are quite smooth and are consistent with the three-dimensional velocity field.

The latent heat effect may be incorporated into the vertical motion equation at each level by forming the following heating term;

$$-\frac{RLg}{C_p P} \nabla^2 \left[\frac{1}{q_{s900}} \frac{\partial q_s}{\partial p} A I \right] \quad (5)$$

where A is a coefficient of the moisture flux. Since (I) is constant with height, the only vertical variation allowed is the change of the saturation specific humidity. This parameter controls the decrease of the latent heat release with height. Before the heating term is activated in the omega equation at each grid point, it must pass three rigid requirements. First, the moisture flux should be positive; obviously, clouds are not likely to form in a column where moisture divergence is taking place. Second, the synoptic scale vertical motion at the level in question should be rising; this is analogous to the first requirement. And third, the relative humidity at the particular level be greater than or equal

FIGURE 22A. Integrated Three-dimensional Moisture Flux.

Solid lines are convergence, dotted lines are neutral,
and dashed lines are divergence.

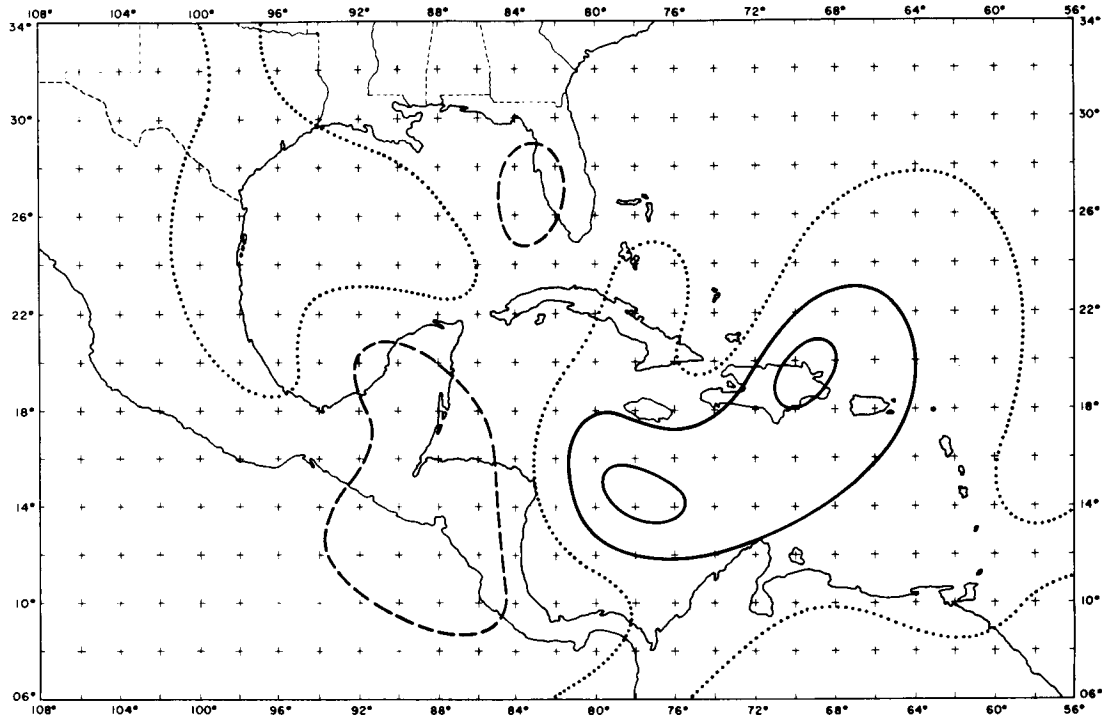
Isolines are drawn every 100×10^{-8} second mb
per meter.

FIGURE 22B. Latent Heat Component of the Vertical Motion.

Dashed lines are rising motion drawn every
 20×10^{-5} mb per second.

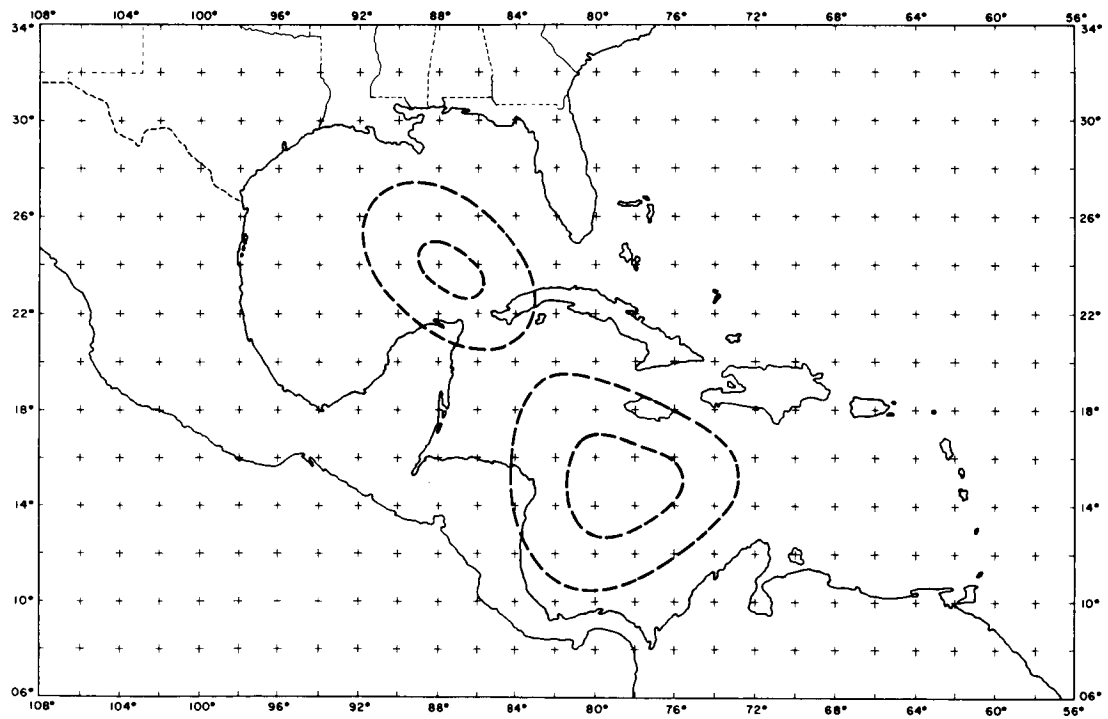
13 AUGUST 1961 00Z

MOISTURE CONVERGENCE



13 AUGUST 1961 00Z

900 MB



to 60 per cent. The latter prerequisite is imposed to eliminate the regions of relatively dry air in which clouds are probably not forming.

When the omega equation was solved, with the entire amount of moisture flux converted to latent heat, the magnitude of the vertical motion was very large masking the effect of the other terms in the equation. Therefore the coefficient A was adjusted to allow only a fraction of the moisture to be transformed. This is, in fact, consistent with Kuo's findings, where he lets a portion of the moisture in his model raise the humidity and form the cloudiness in the column. Kuo's theory predicts that about $1/4$ of the moisture converging into the column actually falls out as rain. Several experiments were run in order to determine a suitable value for the coefficient as well as varying the restrictions mentioned previously. The experiments consisted of observing the computed omegas in partitioned form to see if the latent heat addition was the same magnitude as the vorticity and thermal terms. The value finally chosen for the coefficient of the moisture flux was 0.2, which agrees with Kuo's work and works fairly well in the balanced numerical model.

The latent heating component of the final solution of the omega equation is also illustrated in Figure 22. Even when one-fifth of the moisture convergence is used, the rising motion is of the order of 0.5 centimeters per second. The magnitude of this term places it alongside the adiabatic and frictional terms in importance. Upon careful examination of the drawing it is evident that some vertical motion is being produced in regions of moisture divergence. This effect is due to the forcing function being specified at only

a few, select grid points. Over the rest of the grid, the heating term is zero allowing the relaxation technique to solve for a solution of the differential equation to the zero condition at the boundaries. No method has yet been found to correct the existing problem. Baring this disturbing result, the latent heat solutions are very encouraging and will be used throughout the case study presented later.

Numerical vs. Kinematic. - The final version of the vertical motion together with latent heat and friction is illustrated in Figure 23. As before, the addition of another term did not alter the shape of the vertical motion patterns. However, the magnitude of the rising centers has increased giving a maximum of 1.5 centimeters per second. The typical value of omega in the tropics, as found by the balanced model numerical techniques, is approximately 0.5 to 1.0 centimeters per second. Contrasting the vertical motion at 500 mb with 900 mb, the usual parabolic profile of omega is not found. Instead, many levels of non-divergence are present in the tropics giving a much more complicated structure to the vertical motion distribution.

Since Figure 23 represents the final product from the numerical model, the author felt that a contrast between the numerical results and a kinematic vertical motion calculation would be enlightening. The same observed wind fields (Figures 1-3), that were used in the derivation of the stream function, were employed in the kinematic omega calculation. The continuity equation was integrated with the observed divergences and a zero boundary condition at

FIGURE 23. Final Vertical Motion with Friction and Diabatic Heating.

Isolines are drawn every 20×10^{-5} mbs per second.

Solid lines are sinking, dotted lines are neutral, and dashed lines are rising.

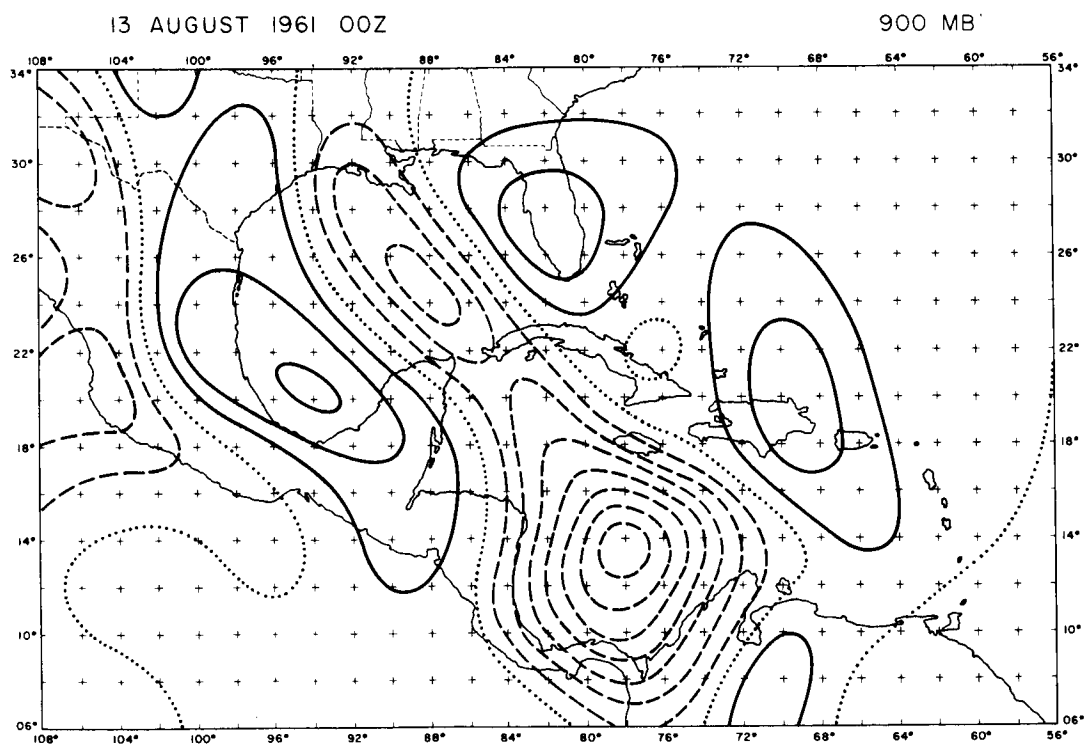
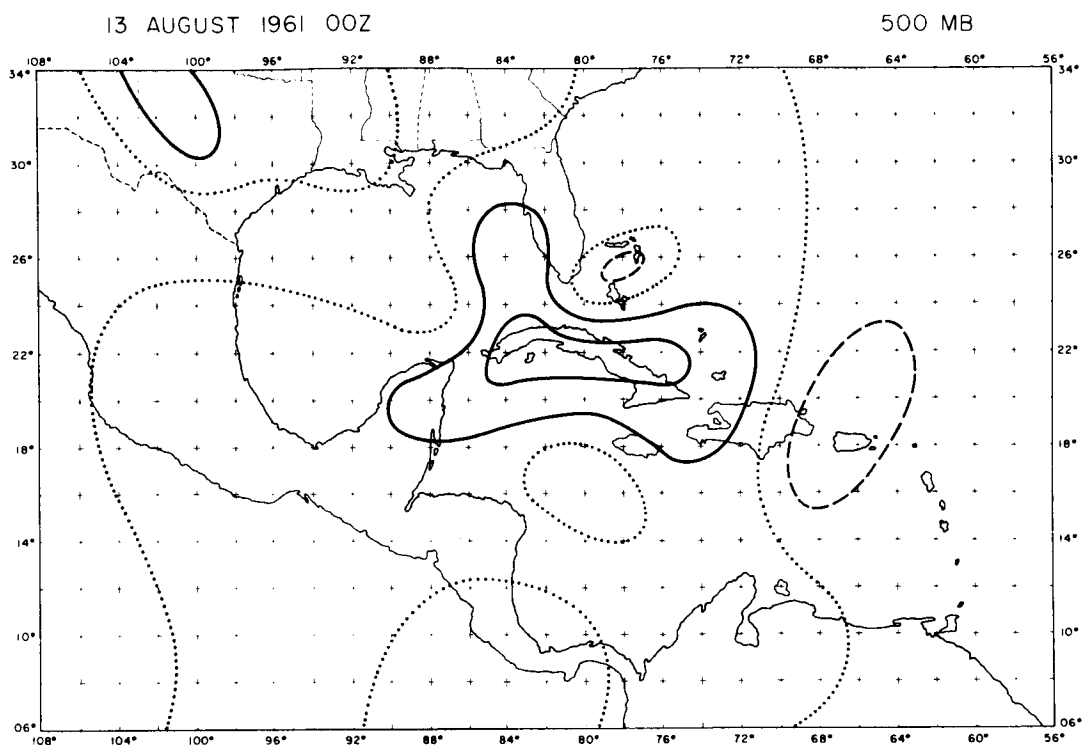
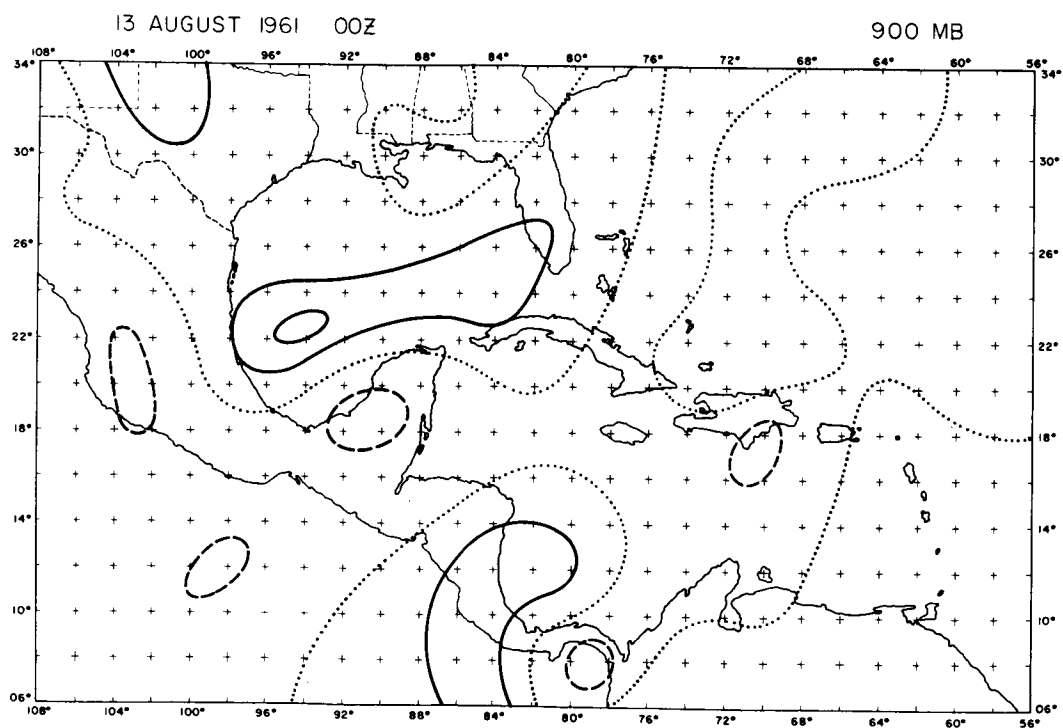
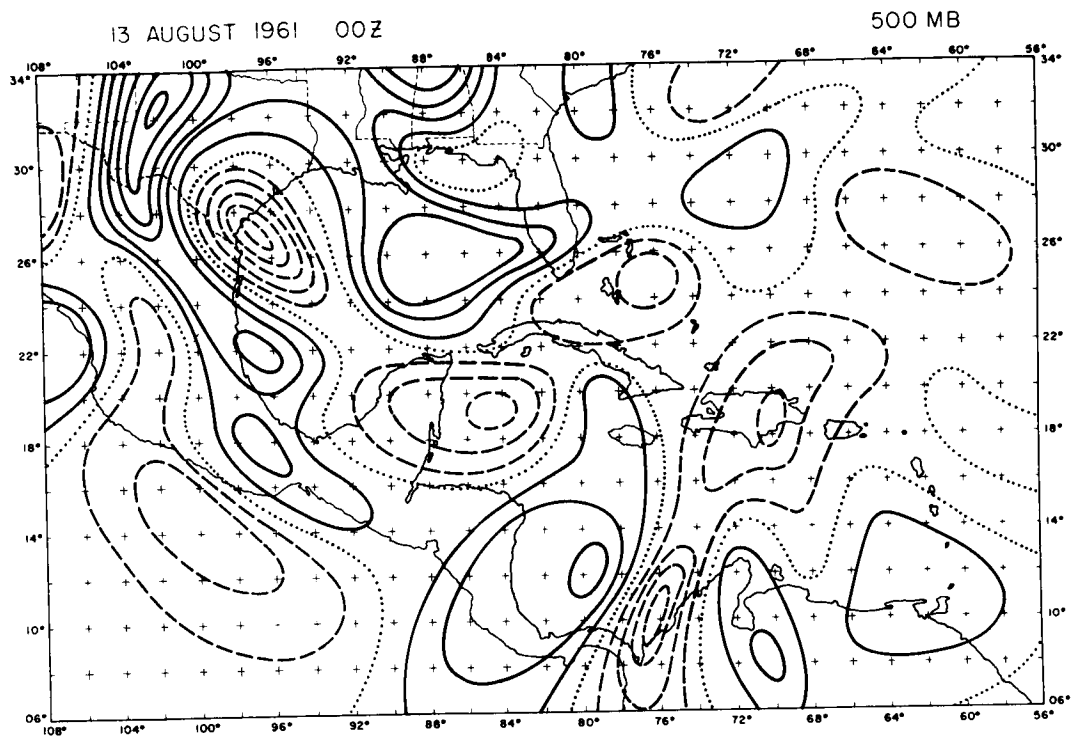


FIGURE 24. Kinematic Vertical Motion

Isolines are drawn every 100×10^{-5} mb per second.

(approximately 1 centimeter per second).

Solid lines are sinking, dotted lines are neutral, and dashed lines are rising.



the surface. The results are shown in Figure 24. It may be noted that the isolines of vertical velocity are 100×10^{-5} mbs per second instead of 20×10^{-5} .

The comparison between the two methods is quite remarkable. The kinematic omegas bear little or no resemblance to the numerical product although they are both derived from the same initial data. The 900 mb kinematic pattern, which is a product of only one divergence field, appears to be somewhat smoother than the result at 500 mb indicating the divergence fields are poorly calculated. Other reasons for the poor correlation between the different methods seem to be obscure; however, the lack of a sufficient number of observations to adequately describe the velocity field is probably the largest contributor to the poor kinematic result. The smooth omega patterns obtained by the balance model contain, implicitly, a well-defined stream function at each grid point, whereas the kinematic vertical motion is derived directly from the data analysis. The observed velocity distribution in the tropics is probably known within ± 2 meters per second in regions of good data, which may be contrasted with the eight significant figure accuracy of the smooth stream function in the computer. Even though the non-divergent wind is derived from the observed velocity it is not nearly as sensitive to data inaccuracies as the divergence. This fact alone gives the numerical approach a superior result in areas of relatively sparse data.

Another argument against the kinematic vertical motion can be found by examining the magnitude produced by the two methods. The average vertical velocity in the numerical model is about 0.5-1.0 centimeters per second, while

the kinematic method yields 2.0-5.0 centimeters per second in the same regions. Such large synoptic scale rising motion seems unreasonable to the author for the following reason. Since the lower half of the tropical atmosphere is potentially unstable due to the large amount of moisture present, any large-scale lifting of the magnitude described above would saturate the air over a wide region in a very short time. Severe convection would then be present over a large synoptic-scale area. While isolated instances of this phenomena probably do occur, they certainly do not happen as often as the kinematic vertical motion indicates. Using the vertical velocity as derived by the balance equations, the air would rise over a longer time-scale allowing the convection time to create meso-scale sinking to counteract the synoptic-scale system. Such a balance would be more typical of the everyday weather in the tropics. At any rate, the main purpose of this research is to carefully examine the numerical product which appears to be superior over the other methods of calculating vertical motion.

CHAPTER III

A TROPICAL CASE STUDY -- 12-14 AUGUST 1961

A. Introduction

The five-level balanced numerical model, which was described in the last chapter, is now applied to a series of five map-times, in which some typical weather configurations of the tropics are found. The case study was selected more or less at random, however several interesting features should be watched throughout the period. In the lower levels, an open wave in the easterly flow translates toward the west; while the upper troposphere contains a closed vortex, which drifts slowly to the southwest. The lower wave, which is moving faster, becomes involved with the upper closed low in the latter part of the case study. These two systems will receive most of the attention in the following discussions, since they are located in regions of good data coverage.

The input data for each map-time will be displayed in the velocity vector representation with the temperature fields superimposed. The velocity distribution together with the thermal patterns constitute a complete data package for the first approximation of the vertical motion. Some difficulty in discerning the characteristics of the flow may bother the reader; however, the vector method is quite useful to indicate advective properties. The integrated moisture flux is illustrated including the number of grid points that released latent heat. The calculated vertical motion is then shown together with the

observed relative humidity. And finally, two cross-sections are compared, one containing the omegas in partitioned form, and the other illustrating the observed relative humidity and the cloudiness patterns. From the illustrations previously mentioned, it is possible to obtain a complete picture of the three-dimensional structure of the tropics as well as the relationship between the synoptic-scale vertical motion and the moisture distribution.

B. Discussion of the Results

12 August 1961 12Z. - The wind and temperature fields for the first map-time are displayed in Figures 25-27. Upon examination of these figures, the two weather systems mentioned in the introduction are quite noticeable. The wave in the easterly current is most intense at 600 mbs over Hispanola with a westward tilt from the surface. At 400 mbs, a small, amplitude of the wave is observed, indicating severe damping of the perturbation with height. A weak closed vortex at 1000 mbs is also associated with the easterly wave. The upper low is found at 600 mbs just south of Florida. It becomes very well organized at 200 mbs with a strong meridional circulation.

The thermal distribution is weak and poorly defined in the lower troposphere. The warmest air seems to be located in the northeasterly flow of the wave, while colder temperatures are noted to the east. At 600 mbs a hint of the upper tropospheric vortex can be found in the thermal field. This cold dome of air is most intense at 400 mbs, reversing at 200 mbs with relatively warmer air being present in the center.

FIGURE 25. Vector Representation of the Velocity Field with
the Temperature.

Vector length proportional to speed

(0.4 centimeters equals 10 meters per second)

Circled X's are closed centers of circulation.

Temperature analyzed every 1° Centigrade.

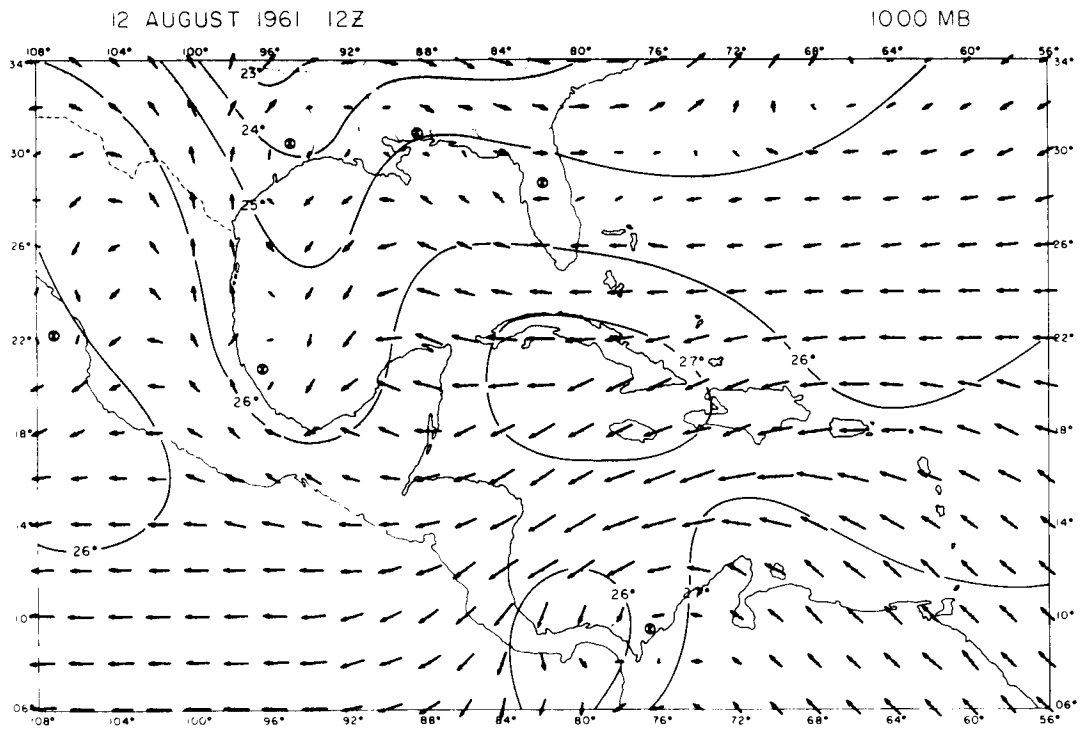
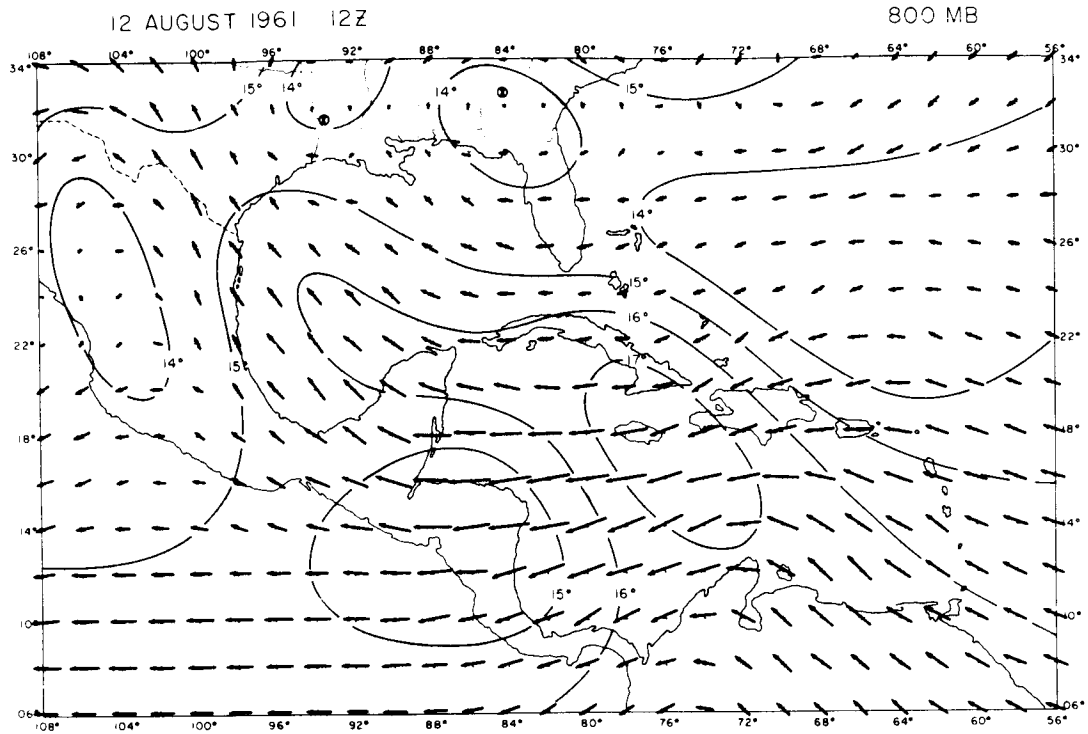


FIGURE 26. Vector Representation of the Velocity Field with

the Temperature.

Vector length proportional to speed

(0.4 centimeters equals 10 meters per second)

Circled X's are closed centers of circulation.

Temperature analyzed every 1° Centigrade.

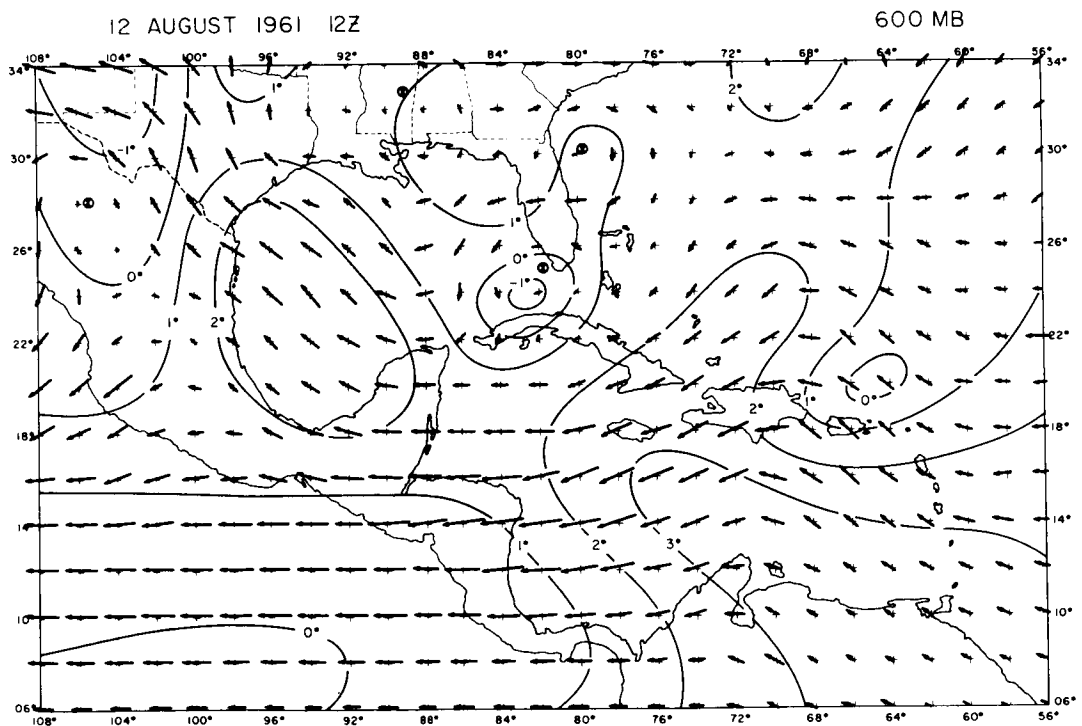
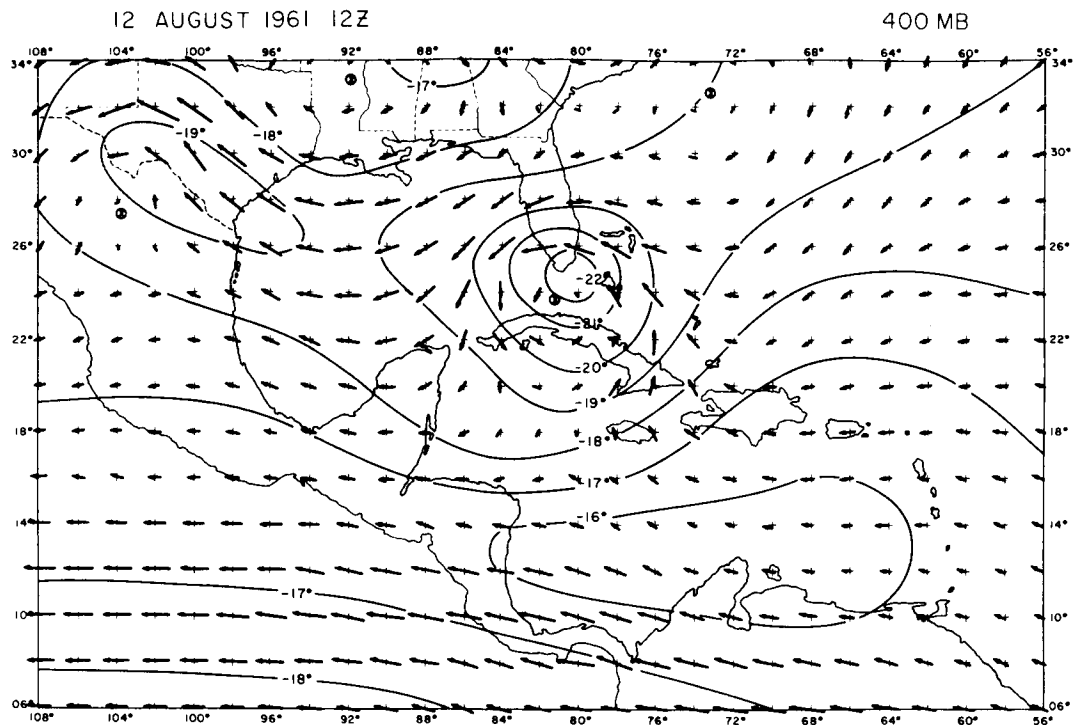


FIGURE 27A. Vector Representation of the Velocity Field with
the Temperature.

Vector length proportional to speed

(0.4 centimeters equals 10 meters per second).

Circled X's are closed centers of circulation.

Temperature analyzed every 1° Centigrade.

FIGURE 27B. Integrated Moisture Flux

Isolines are every $100 \times 10^{-6} \text{ mb sec m}^{-1}$

Solid lines are convergence, dotted lines are neutral,
and dashed lines are divergence.

Circled cross's are grid points of latent heat addition.

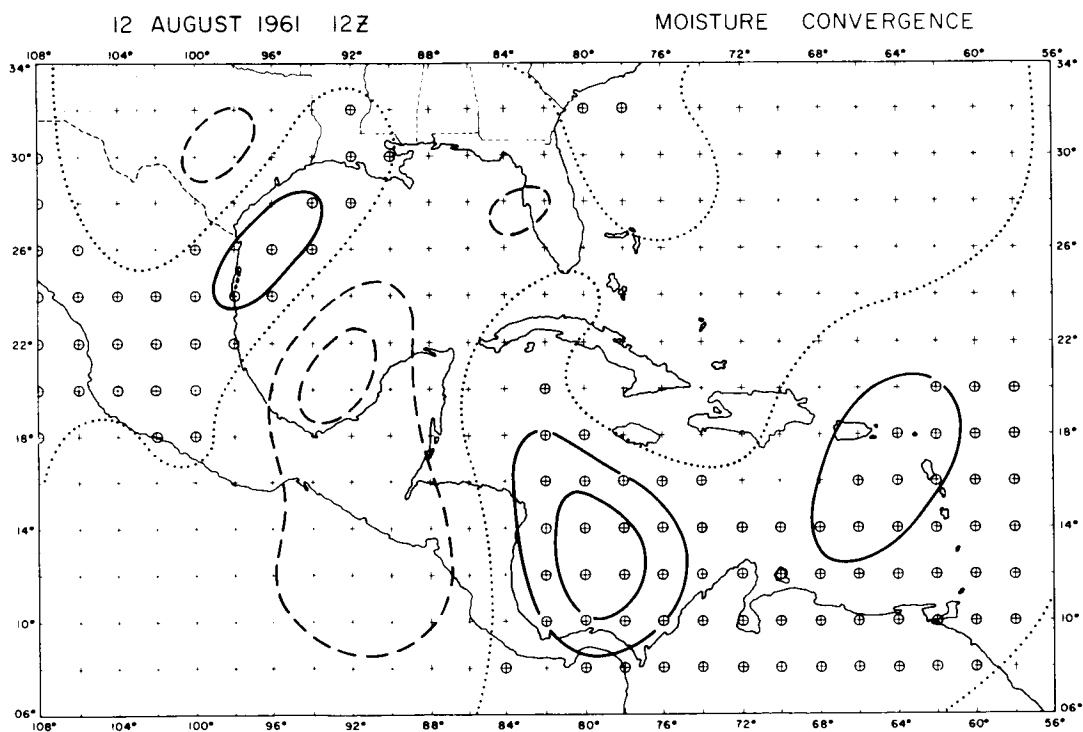
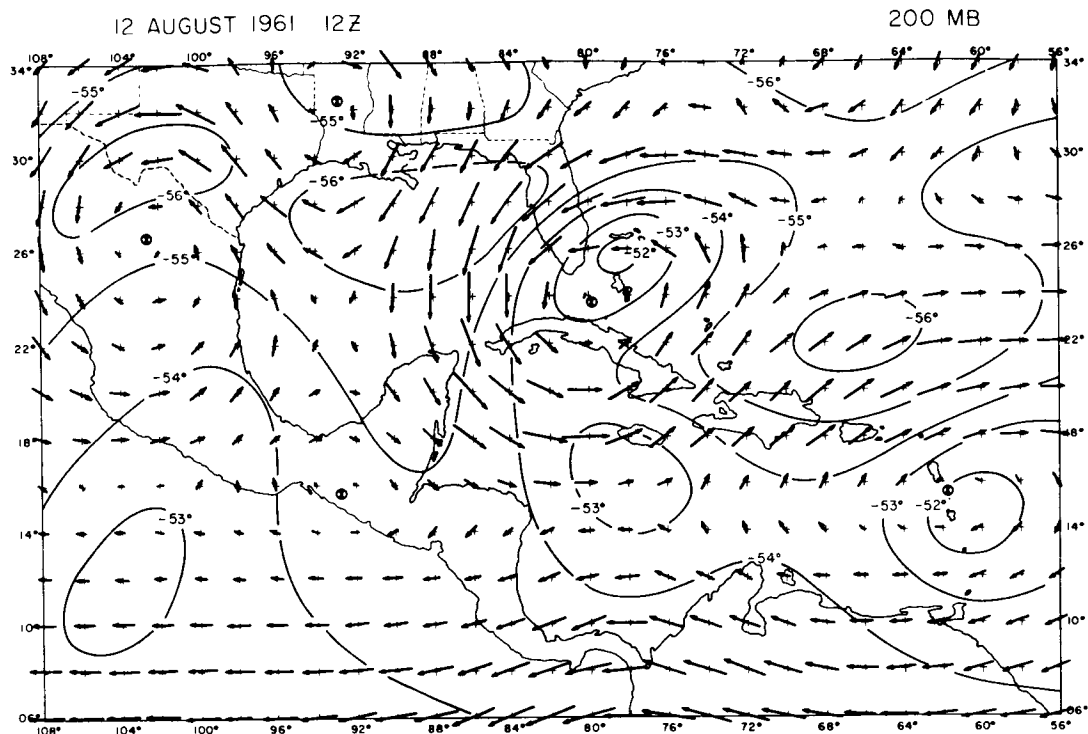


FIGURE 28. Vertical Motion with the Observed Relative Humidity.

Isolines of vertical motion are $20 \times 10^{-5} \text{ mb sec}^{-1}$.

Heavy solid lines are sinking, dotted lines are neutral, and dashed lines are rising.

Light solid lines are relative humidity analyzed every 10 per cent.

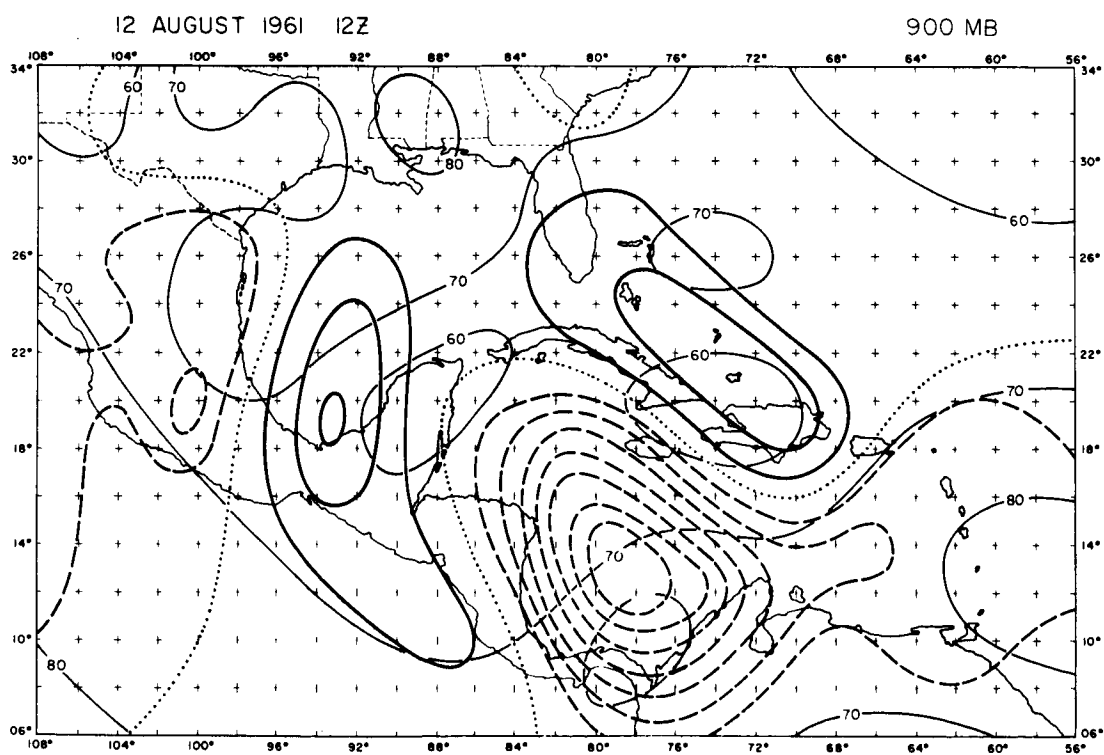
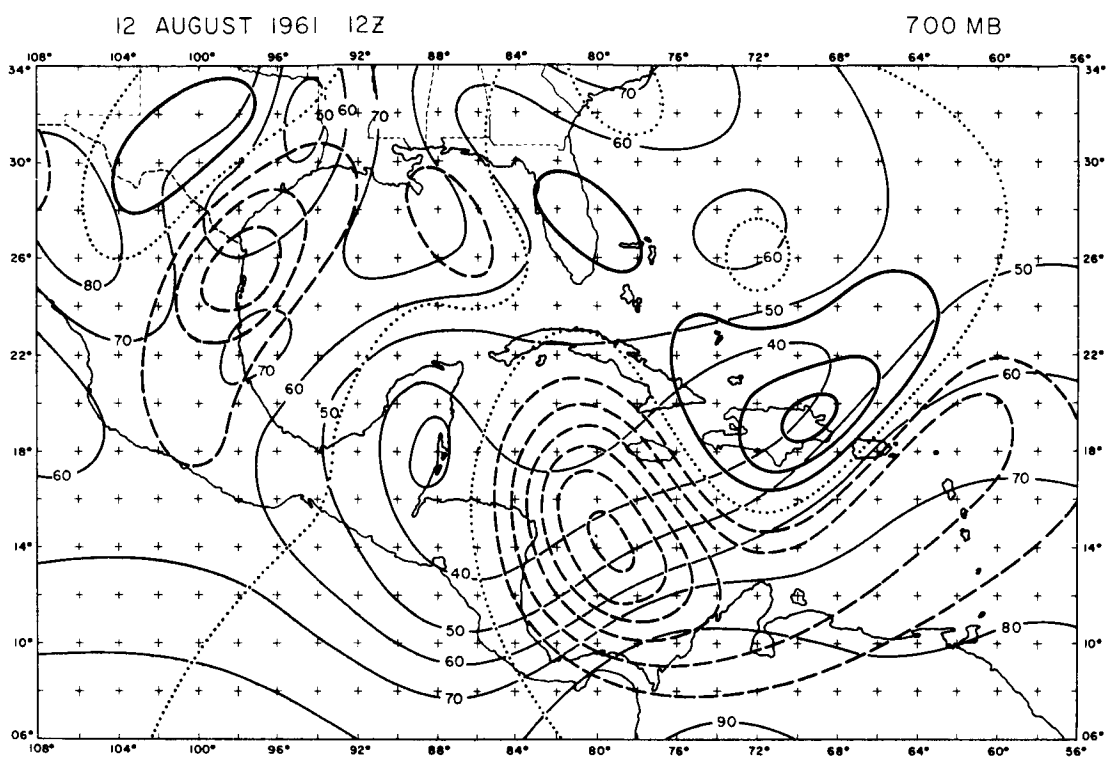


FIGURE 29. Vertical Motion with the Observed Relative Humidity.

Isolines of vertical motion are $20 \times 10^{-5} \text{ mb sec}^{-1}$.

Heavy solid lines are sinking, dotted lines are neutral, and dashed lines are rising.

Light solid lines are relative humidity analyzed every 10 per cent.

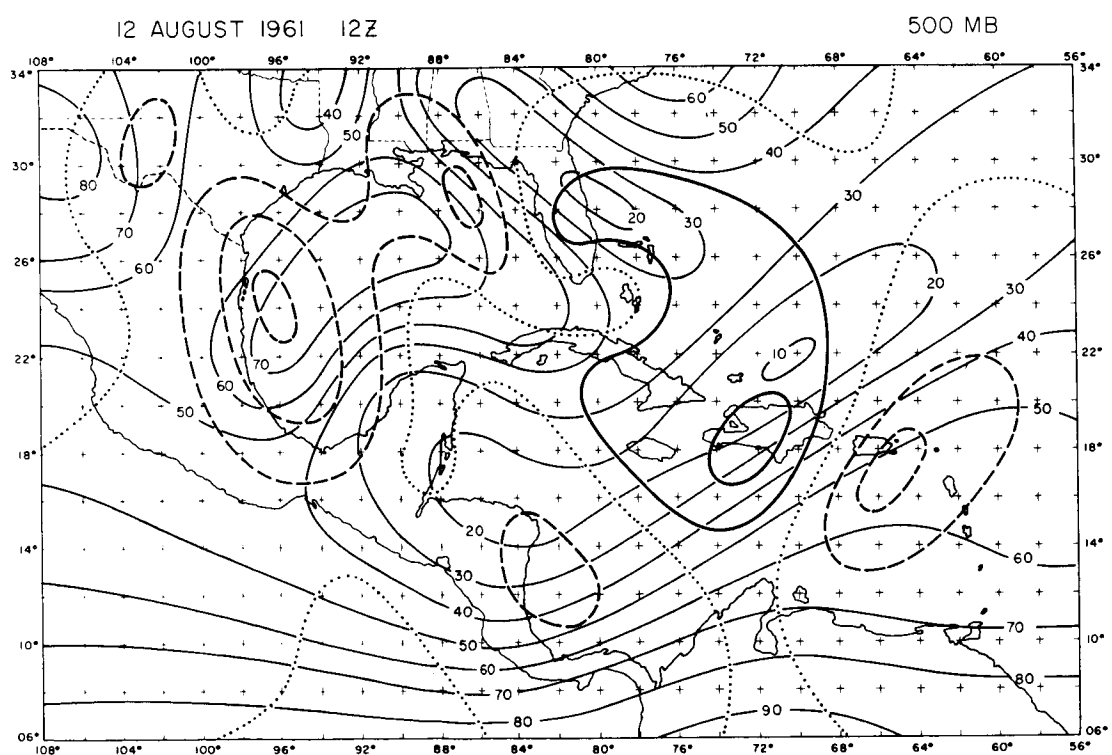
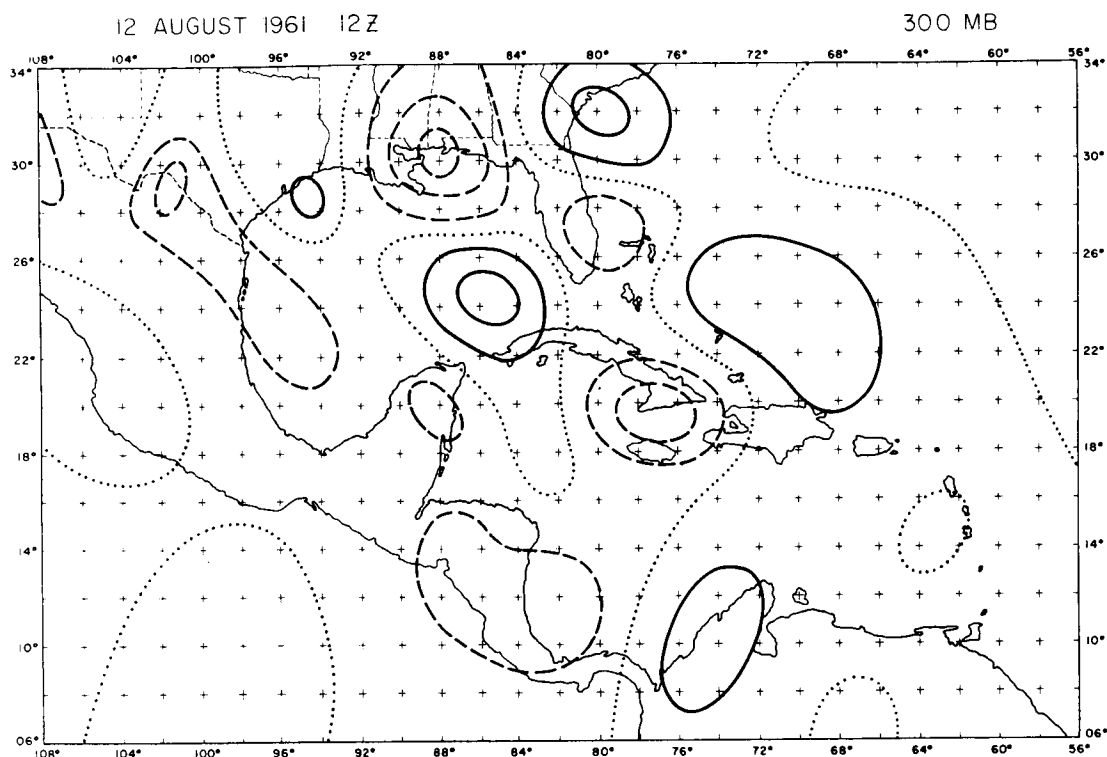


FIGURE 30A. Partitioned Vertical Motion

Heavy vector is the total, light lines are the components.

Order at each grid point from left to right: Total, vorticity, thermal, deformation, divergence, friction, and latent heat.

FIGURE 30B. Moisture and Cloudiness

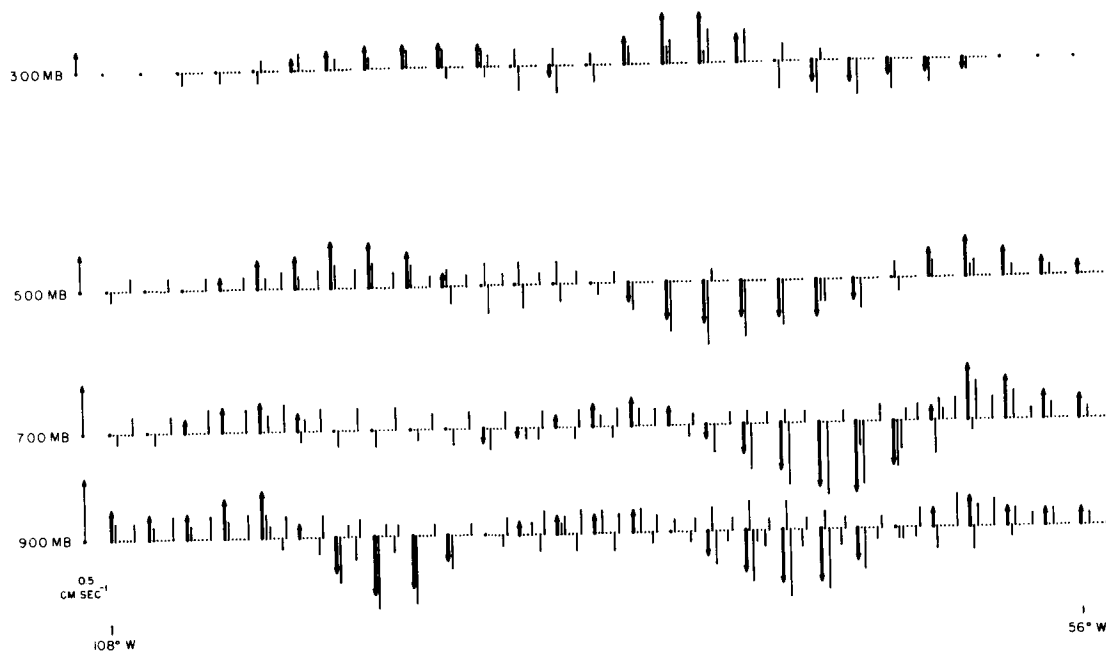
Solid lines are relative humidity every 10 per cent.

Clouds represented in schematic form.

OMEGA CROSS SECTION
12 AUGUST 1961 12Z

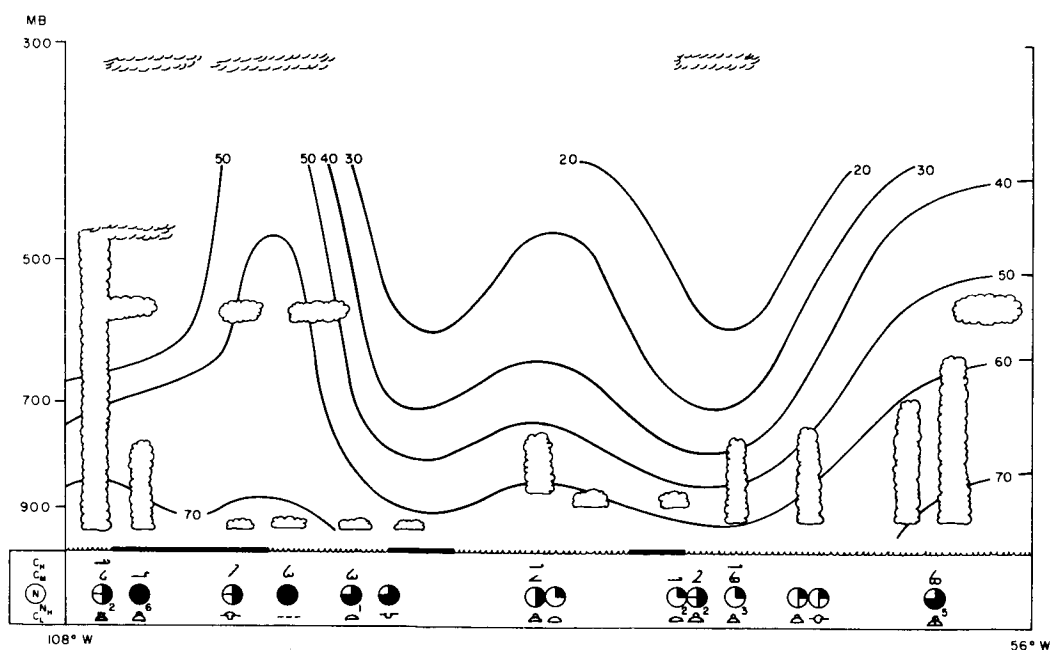
0 100 $100 \cdot 10^{-3} \text{ MB SEC}^{-1}$

20° N



MOISTURE CROSS SECTION
12 AUGUST 1961 12Z

20° N



The vertical motion associated with the previous velocity and thermal patterns is illustrated in Figures 28-29. At first glance the rising and sinking does not appear to be connected with any observable system in the initial data. This is basically true at 900 mb, however, at 700 and 500 mbs the customary dipole of vertical motion with a magnitude of 0.5 centimeters per second may be seen over the easterly wave. The 300 mb vertical motion is composed of numerous cells of alternate rising and sinking around the closed vortex. There is some positive correlation between sinking and drier air as shown by the relative humidity isolines. The correlation is even poorer when rising is compared with moist air. The vertical motion should not be expected to agree very well with the moisture patterns, since it is the mechanism that alters the distribution of moisture. However, some correlation should be present to verify the accuracy of the omegas.

A possible reason for the large rising center south of Cuba can be obtained from the moisture flux in Figure 27. The resulting moisture convergence in this area is responsible for a large contribution by the latent heating term. In order to answer further questions regarding the omega distribution, a cross-section of the partitioned vertical motion together with the moisture is displayed in Figure 30, (refer to stream function section for partitioning explanation). The addition of friction and latent heat as the fifth and sixth components is accomplished. From the cross-section one can see that the sinking air is basically produced by the thermal term, while the rising is augmented by the

latent heating term. At 500 and 300 mbs, the vorticity term plays a more important role.

A comparison between the two cross-sections in Figure 30 shows a much higher correlation between the moisture distribution and the vertical motion than in Figures 28-29. This is probably due to the choice of the cross-section, which stretches over the best data coverage on the grid. The structure of the easterly wave on the right side of the cross-section is brought out clearly, with sinking in the dry air and rising in the moist air. An older system to the left is in the process of being destroyed by sinking at the surface. Overall, the vertical velocity-moisture correlation is very encouraging, which indicates a high reliability may be placed on the machine product of vertical motion.

13 August 1961 00Z. This is the map-time in the case study upon which all the comparisons were based in Chapter II. After a lapse of 12 hours, the open wave in the easterlies has translated about 4 degrees of longitude, Figures 31-33. Little change in the structure of the easterly wave is noticed except for a slight increase in amplitude at 800 mbs. The associated closed vortex is still present at the lowest level. At 400 mbs a small center of outflow has appeared just west of the lower perturbation. This effect has intensified the southerly flow around the upper tropospheric low. The 200 mb speeds have also increased in the circulation of the upper vortex.

The thermal patterns in the lower troposphere have remained more or less constant with relatively strong cold air advection into the warm center on

FIGURE 31. Vector Representation of the Velocity Field with
the Temperature.

Vector length proportional to speed

(0.4 centimeters equals 10 meters per second).

Circled X's are closed centers of circulation.

Temperature analyzed every 1° Centigrade.

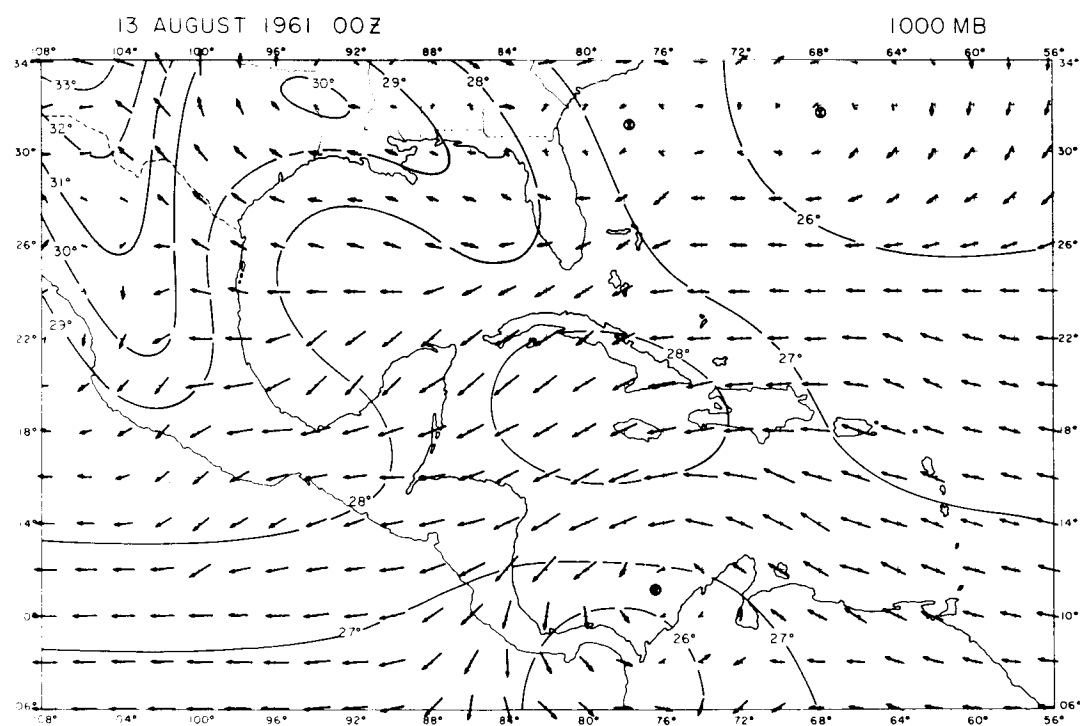
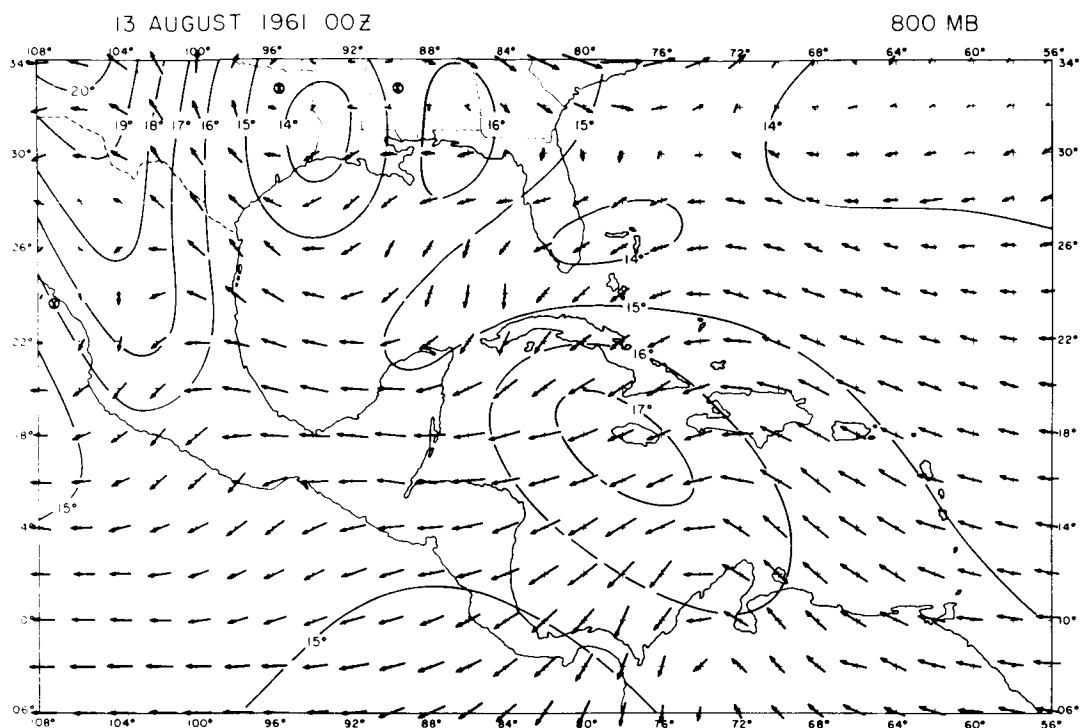


FIGURE 32. Vector Representation of the Velocity Field with
the Temperature.

Vector length proportional to speed

(0.4 centimeters equals 10 meters per second).

Circled X's are closed centers of circulation.

Temperature analyzed every 1° Centigrade.

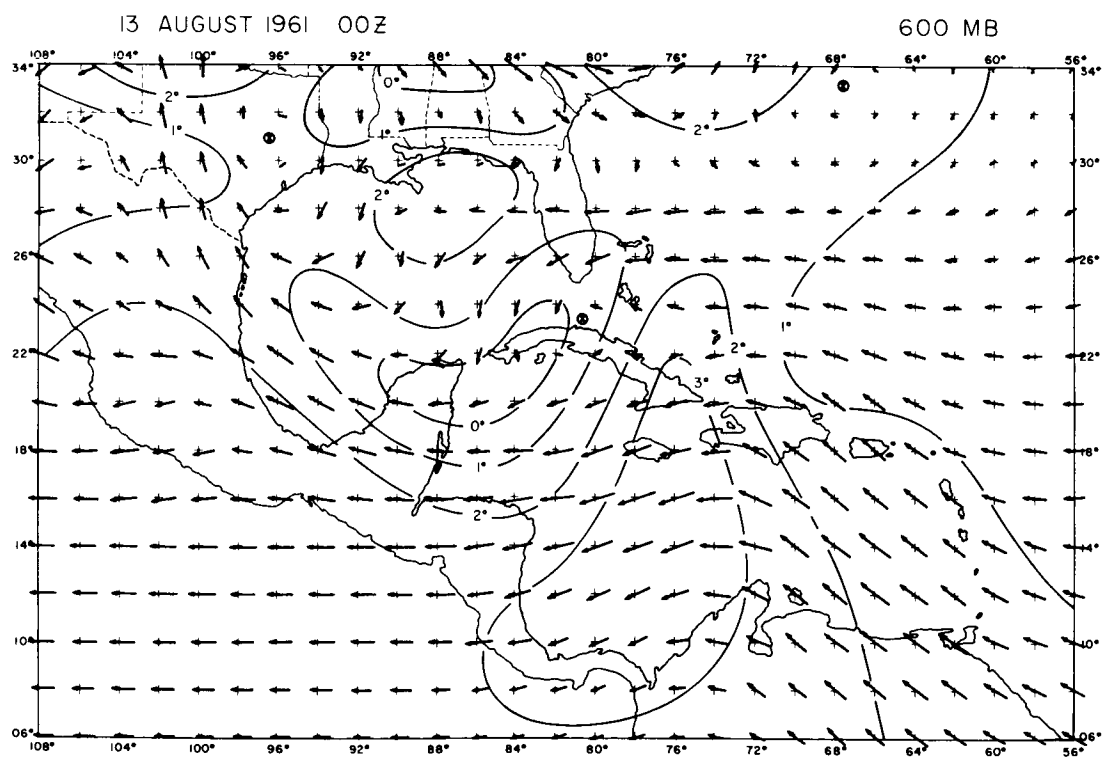
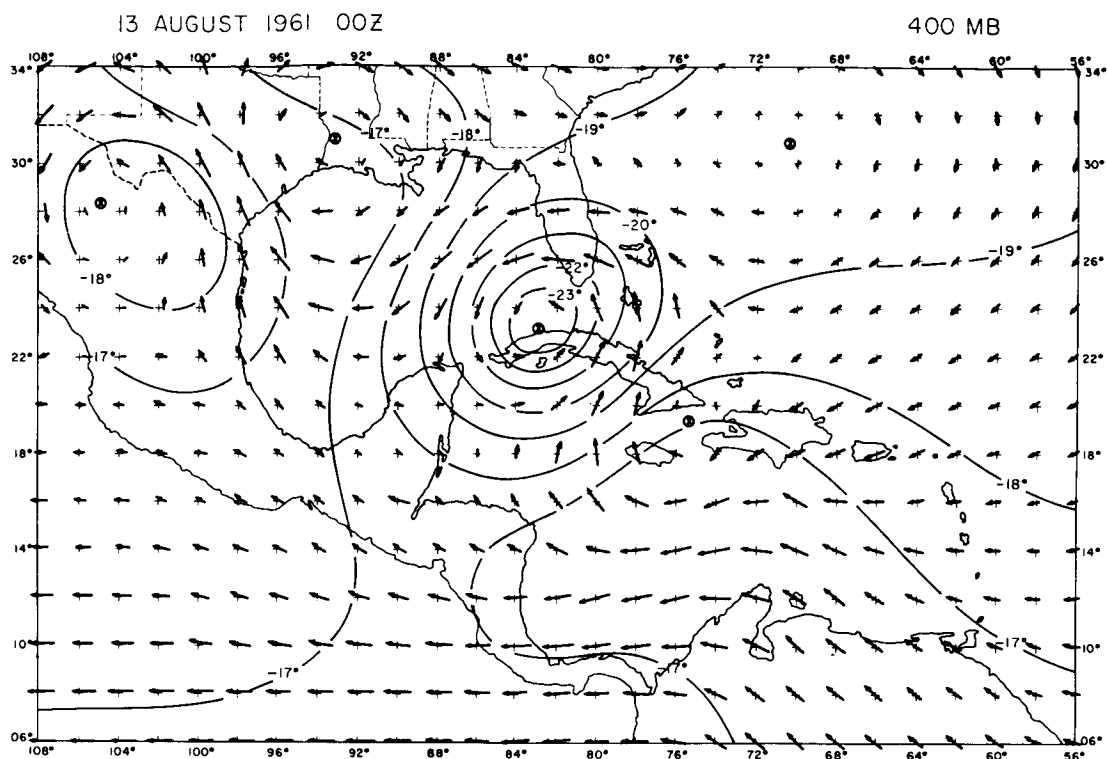


FIGURE 33A. Vector Representation of the Velocity Field with
the Temperature.

Vector length proportional to speed

(0.4 centimeters equals 10 meters per second).

Circled X's are closed centers of circulation.

Temperature analyzed every 1° Centigrade.

FIGURE 33B. Integrated Moisture Flux

Isolines are every $100 \times 10^{-6} \text{ mb sec m}^{-1}$.

Solid lines are convergence, dotted lines are neutral,
and dashed lines are divergence.

Circled crosses are grid points of latent heat addition.

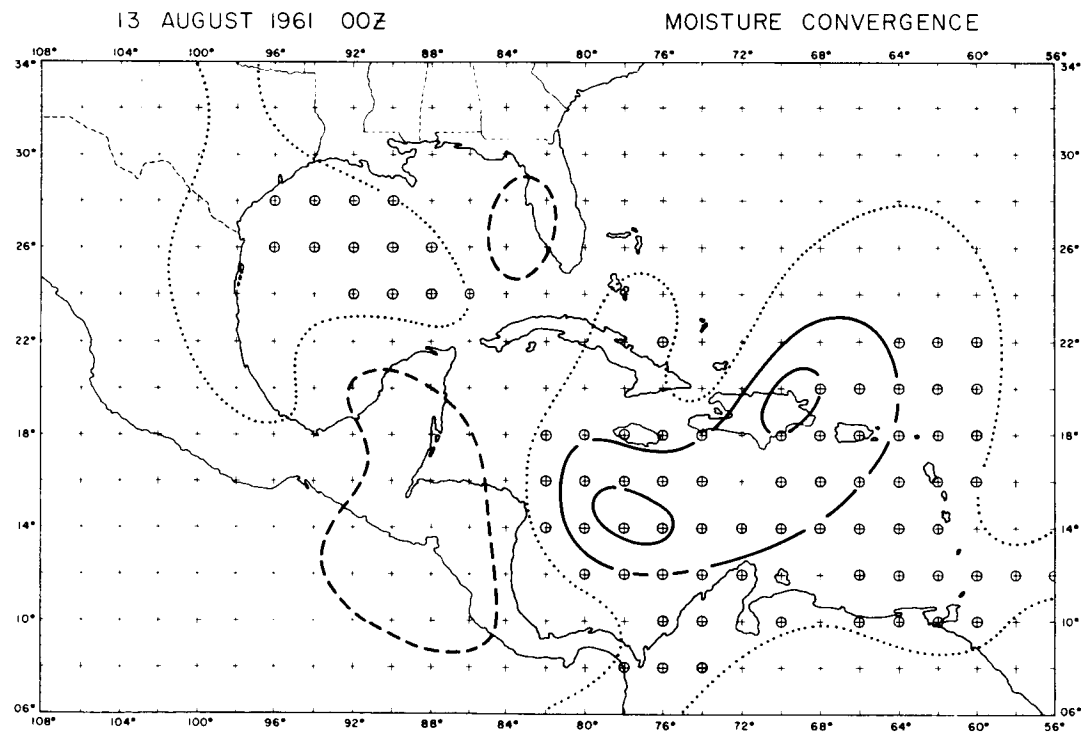
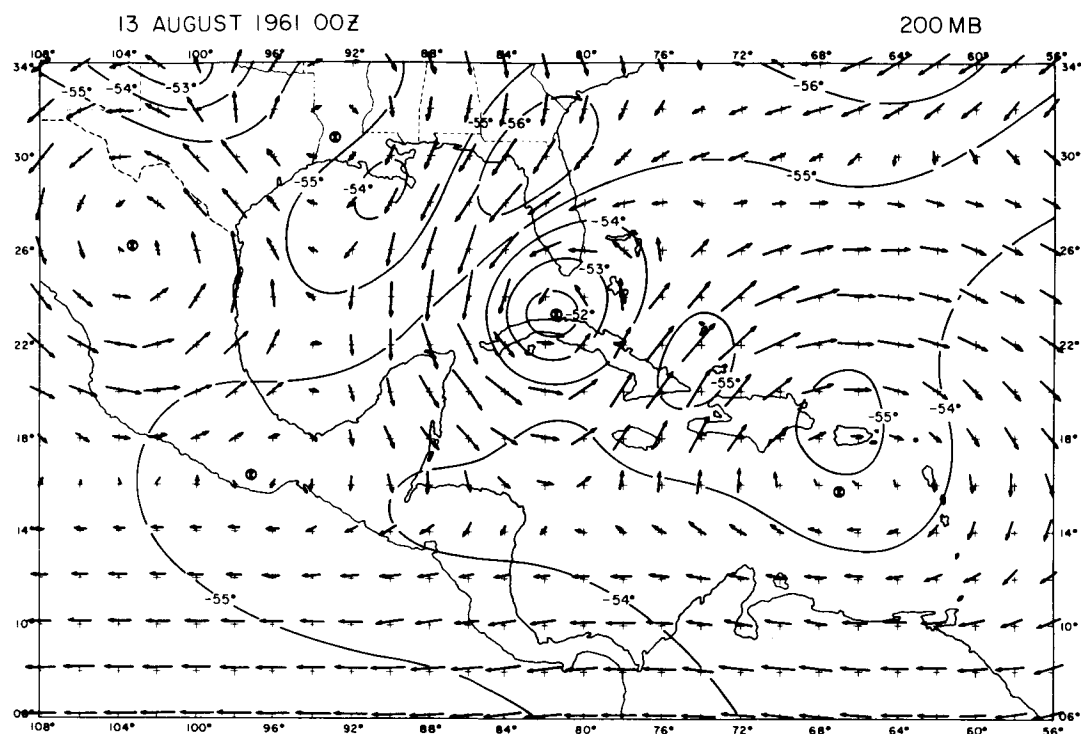


FIGURE 34. Vertical motion with the Observed Relative Humidity.

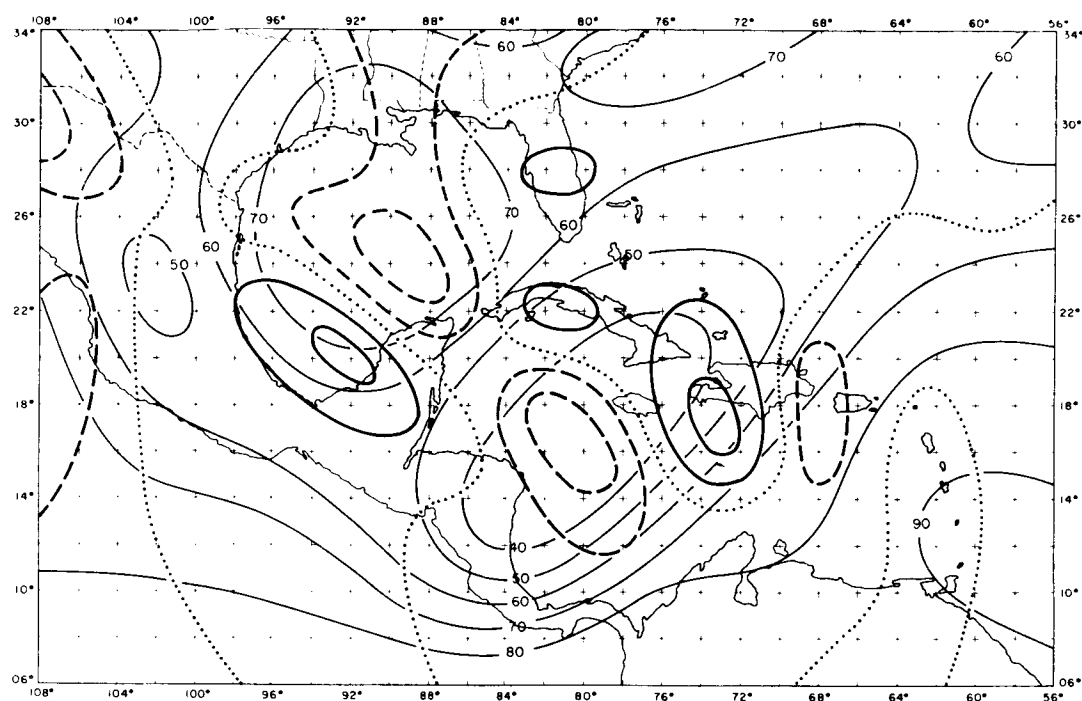
Isolines of vertical motion are $20 \times 10^{-5} \text{ mb sec}^{-1}$.

Heavy solid lines are sinking, dotted lines are neutral, and dashed lines are rising.

Light solid lines are relative humidity analyzed every 10 per cent.

13 AUGUST 1961 00Z

700 MB



13 AUGUST 1961 00Z

900 MB

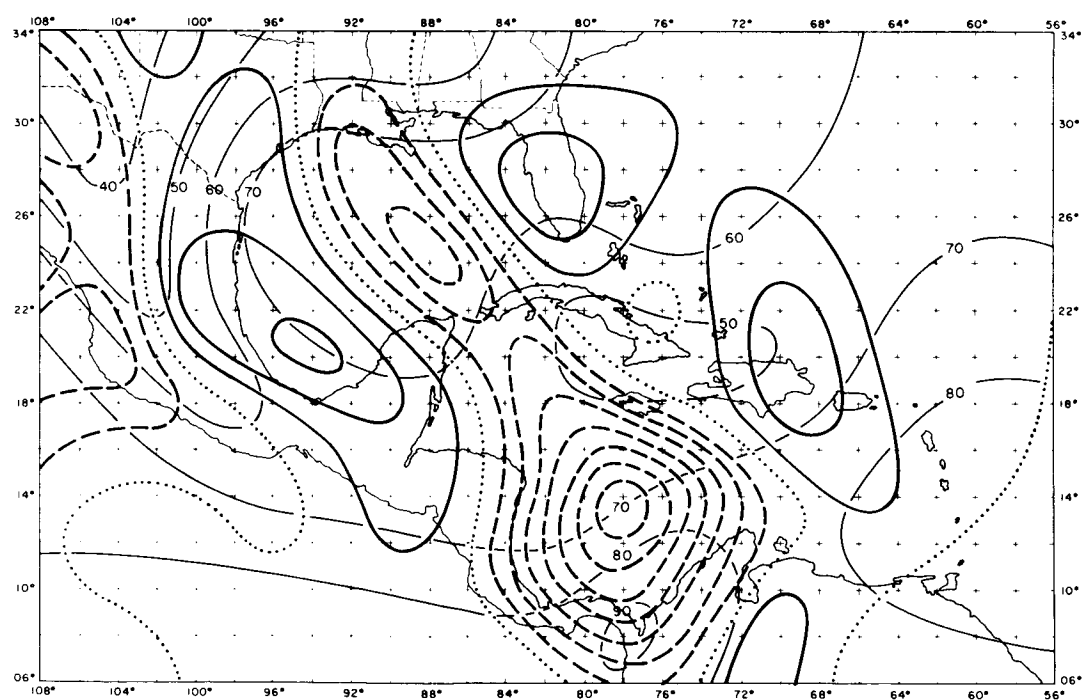


FIGURE 35. Vertical Motion with the Observed Relative Humidity.

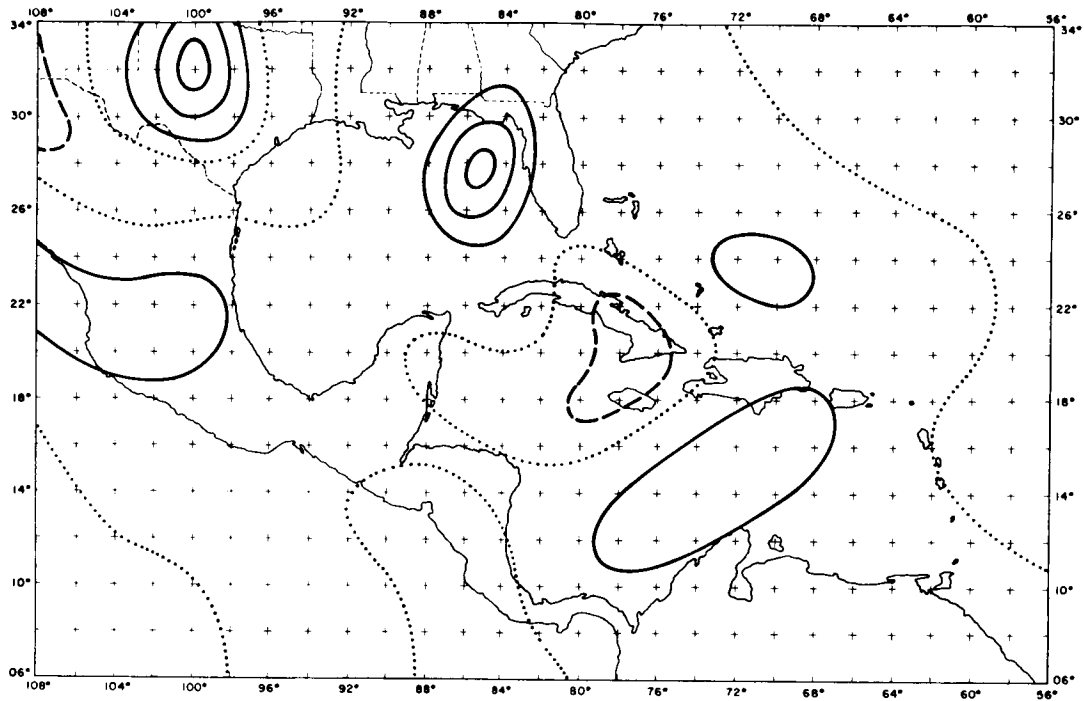
Isolines of vertical motion are $20 \times 10^{-5} \text{ mb sec}^{-1}$.

Heavy solid lines are sinking, dotted lines are neutral, and dashed lines are rising.

Light solid lines are relative humidity analyzed every 10 per cent.

13 AUGUST 1961 00Z

300 MB



13 AUGUST 1961 00Z

500 MB

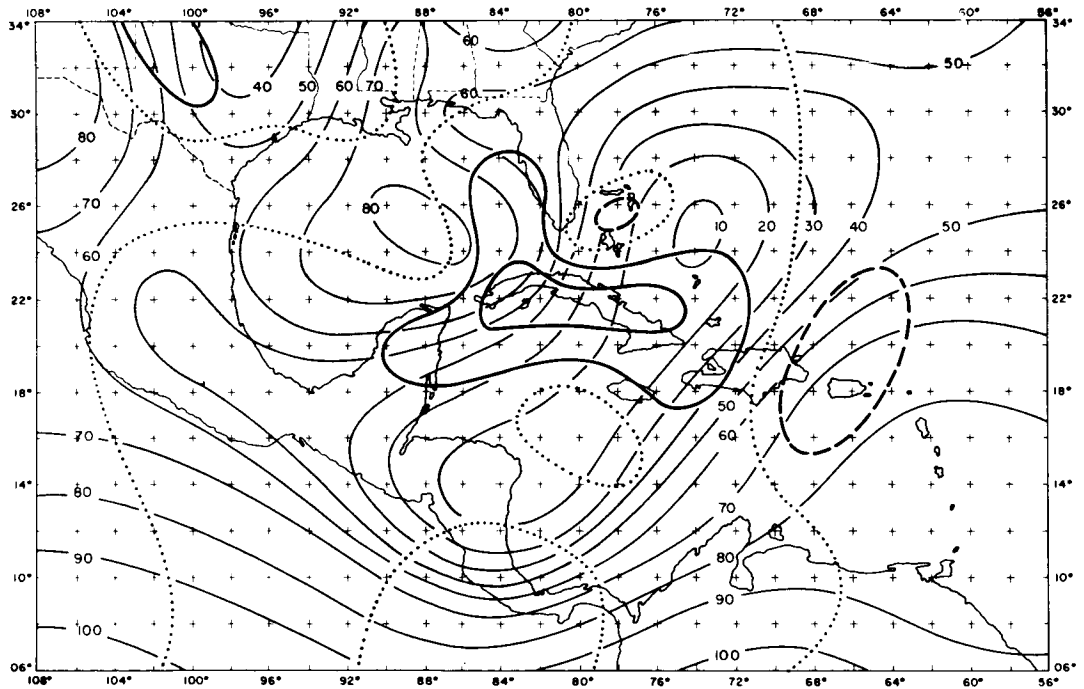


FIGURE 36A. Partitioned Vertical Motion

Heavy vector is the total, light lines are the components.

Order at each grid point from left to right: Total, vorticity, thermal, deformation, divergence, friction, and latent heat.

FIGURE 36B. Moisture and Cloudiness

Solid lines are relative humidity every 10 per cent.

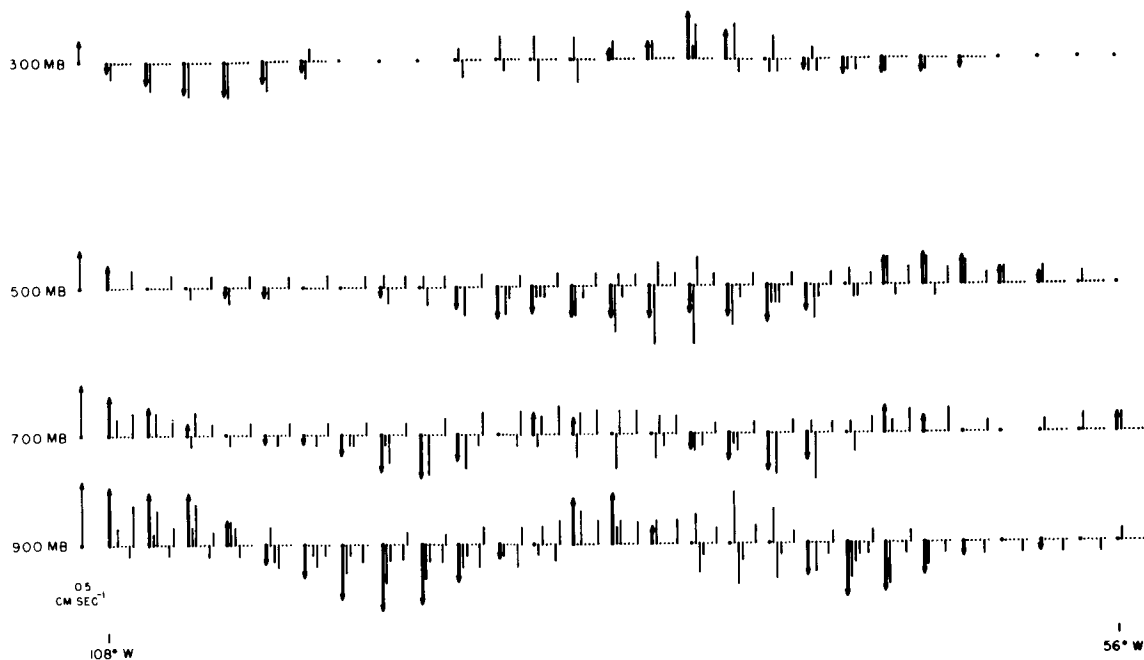
Clouds represented in schematic form.

OMEGA CROSS SECTION

13 AUGUST 1961 00Z

0 100 100 • 10³ MB SEC⁻¹

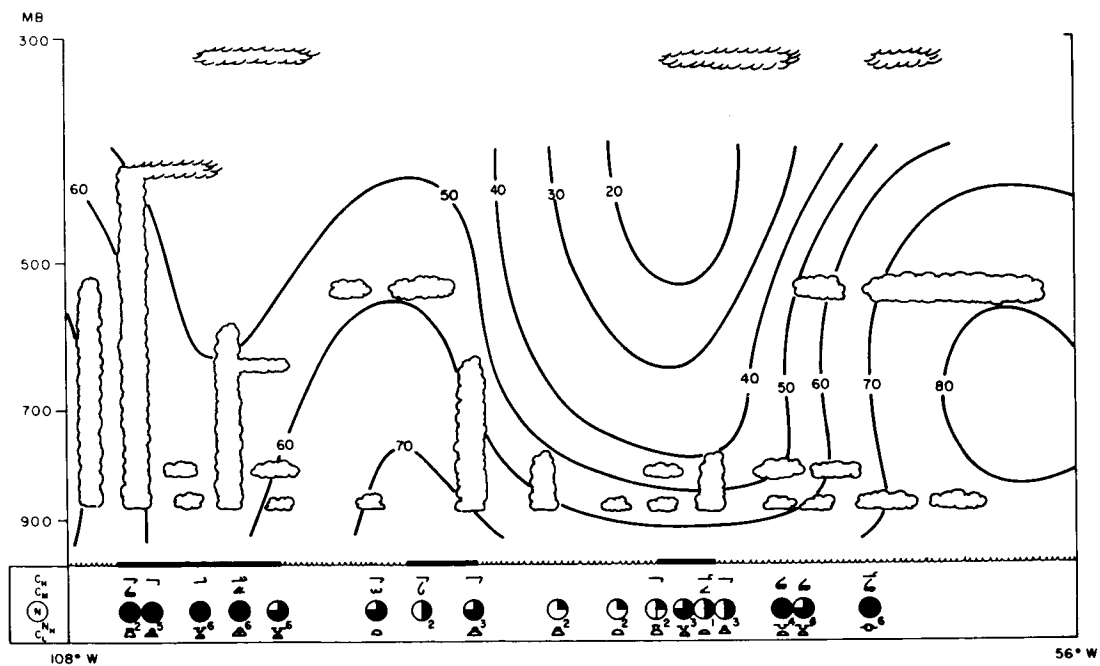
20° N



MOISTURE CROSS SECTION

13 AUGUST 1961 00Z

20° N



the western side of the wave. The warm tongue of air at 600 mbs has become more aligned with the axis of the disturbance in the easterlies. The cold pocket associated with the upper low has expanded and moved towards the southwest. The gradients of temperature have increased in magnitude at 400 mbs as well as shifting southwestward around the closed center of circulation. This is in agreement with the increase in speeds observed at the highest level considering the thermal wind. Observing the 200 mb thermal field, it can be seen that the warm air in the center of the vortex has moved rapidly toward the southwest, with the cold centers still located on the periphery of the circulation.

The resulting vertical velocities and the integrated moisture flux may be seen in Figures 33-35. Again the strongest vertical motion is observed at the lowest level where a magnitude of 1.5 centimeters per second is obtained. The center of this rising motion has moved little in 12 hours; but its vertical extent has been reduced considerably with 700 mbs showing only 0.5 centimeters per second. The moisture flux, latent heat contribution is still quite large in this area. A secondary center of moisture convergence has intensified to the east of the open wave.

Examining the structure of the vertical motion in the easterly perturbation, the dipole at 700 and 500 mbs is positioned to the east of the trough axis. Also, the 900 mb omegas indicate 0.5 centimeters per second of sinking behind the wave. This would tend to destroy any low-level convergence pattern already present. The isolines of relative humidity show a gradual increase in moisture

from the east with extremely dry air located ahead of the easterly wave. Again the correlation between moisture and vertical motion is fair to poor. The rising and sinking associated with the upper vortex has shown signs of some organization. A broad area of sinking at 300 mb is present over the wave in the lower troposphere.

The cross-section comparison is found in Figure 36. The partitioned omegas point out more vividly the disorganization of the vertical motion in the easterly wave. All of the components contribute to the sinking at the lowest level. The opposition of the vorticity and thermal terms in some areas is quite noticeable. The latent heat term appears to be most significant at 700 and 500 mbs in the rising motion of the perturbation. The overlap of the diabatic term is in evidence in the sinking air, however, the other terms are strong enough to counteract the spurious rising.

The vertical moisture distribution has translated toward the west in the vicinity of the easterly perturbation. The sinking at the lowest level corresponds with the lack of towering cumulus in the area. High clouds are still present in the rising motion at 500 mbs. The moisture wave in the west is slowly drying with little convective activity which agrees with the sinking over the region. The moisture during this map-time continues to have some relationship with the vertical motion when examined on a cross-section.

13 August 1961 12Z. A major change in the wave patterns can be seen on the velocity field maps, Figures 37-39. The perturbation in the easterly

current has accelerated toward the northwest with an increase in amplitude. Because of the extremely rapid movement, it seems probable that a new wave might have developed ahead of the original disturbance. At any rate, the trajectory of the first system is somewhat in doubt. The amplitude is still most intense at 600 mbs, with the strongest winds appearing at 800 mbs. The vortex in the lowest level has disappeared and the associated cyclonic curvature has decreased in the area. The upper tropospheric closed low has continued to drift toward the southwest. The velocity configuration around the vortex has changed little except at 600 mbs, where it is no longer visible.

The temperature pattern has remained constant at the lowest level, however, at 800 and 600 mbs, the warmest air has shifted to a location behind the easterly wave. This orientation changes the sense of the thermal advection from cold to warm in the region behind the trough axis. The cold dome in the upper atmosphere has exhibited little change in 12 hours, including the warmer air immediately above the system at 200 mb.

The vertical motions, Figures 40-41, obtained at this map-time, illustrate the observed changes in the velocity and thermal fields. The rising air behind the perturbation is becoming the dominant feature on the map, reaching a magnitude of 1.0 centimeters per second at 500 mbs. As mentioned before, it seems unlikely that the original dipole 12 hours ago, would have translated at the speed indicated by simple extrapolation. The region of sinking air at 900 mbs. east of the rising center has been stationary, with an increase in the

FIGURE 37. Vector Representation of the Velocity Field with
the Temperature.

Vector length proportional to speed

(0.4 centimeters equals 10 meters per second).

Circled X's are closed centers of circulation.

Temperature analyzed every 1° Centigrade.

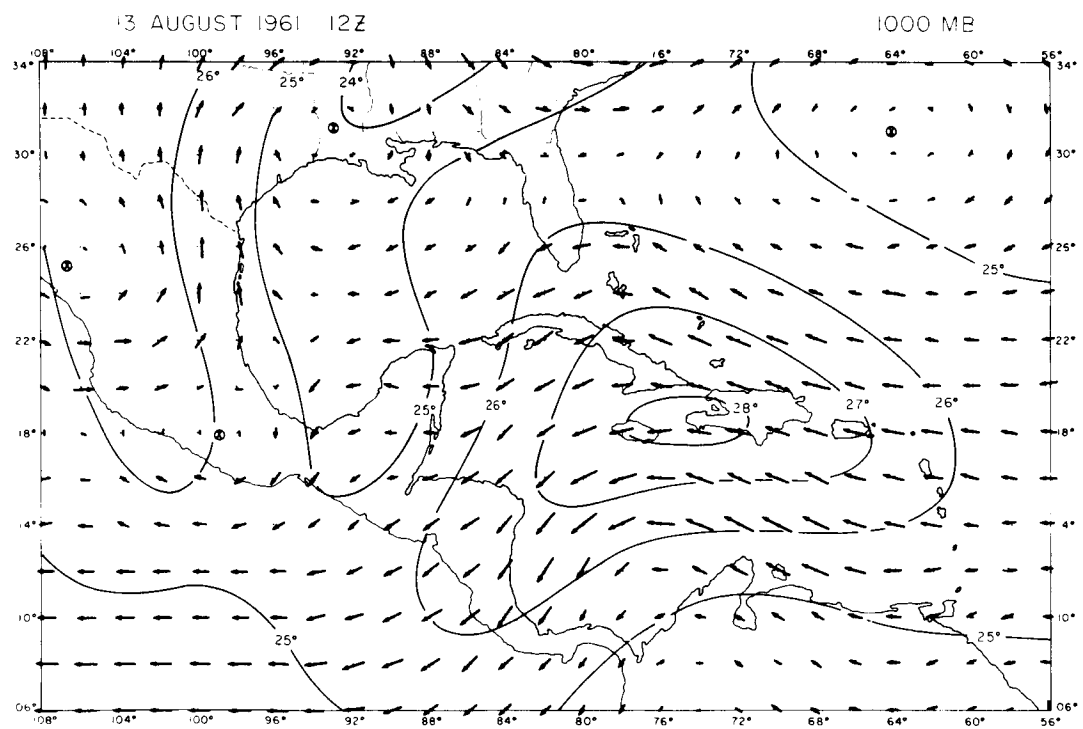
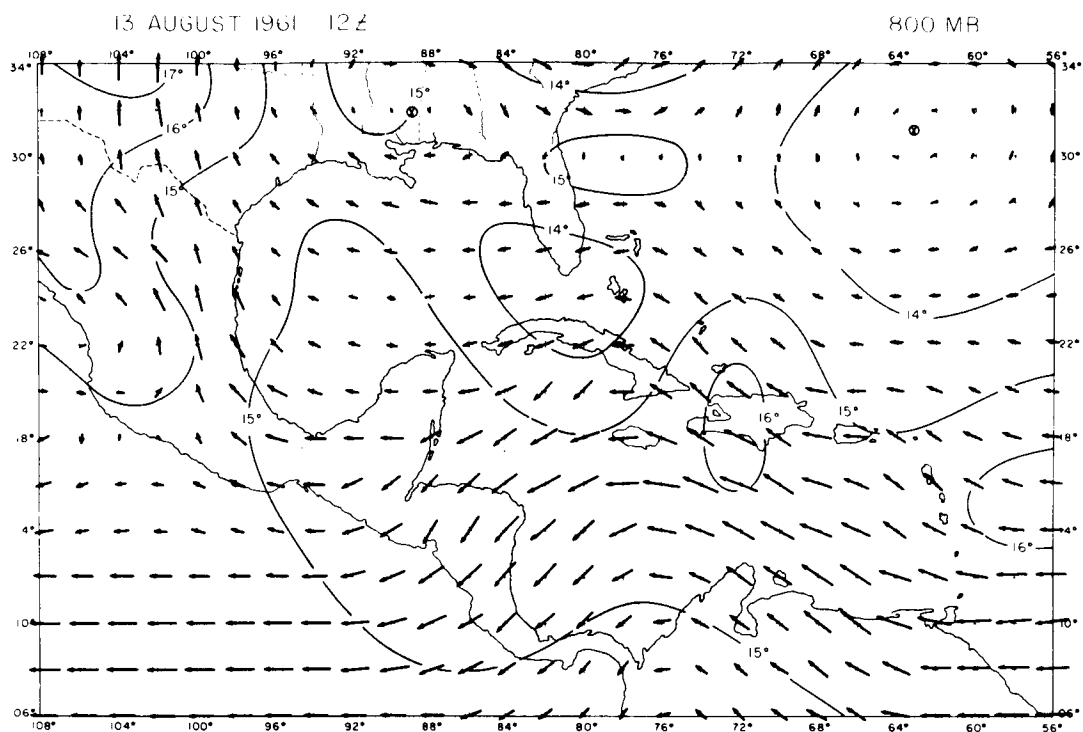


FIGURE 38. Vector Representation of the Velocity Field with
the Temperature.

Vector length proportional to speed

(0.4 centimeters equals 10 meters per second).

Circled X's are closed centers of circulation.

Temperature analyzed every 1° Centigrade.

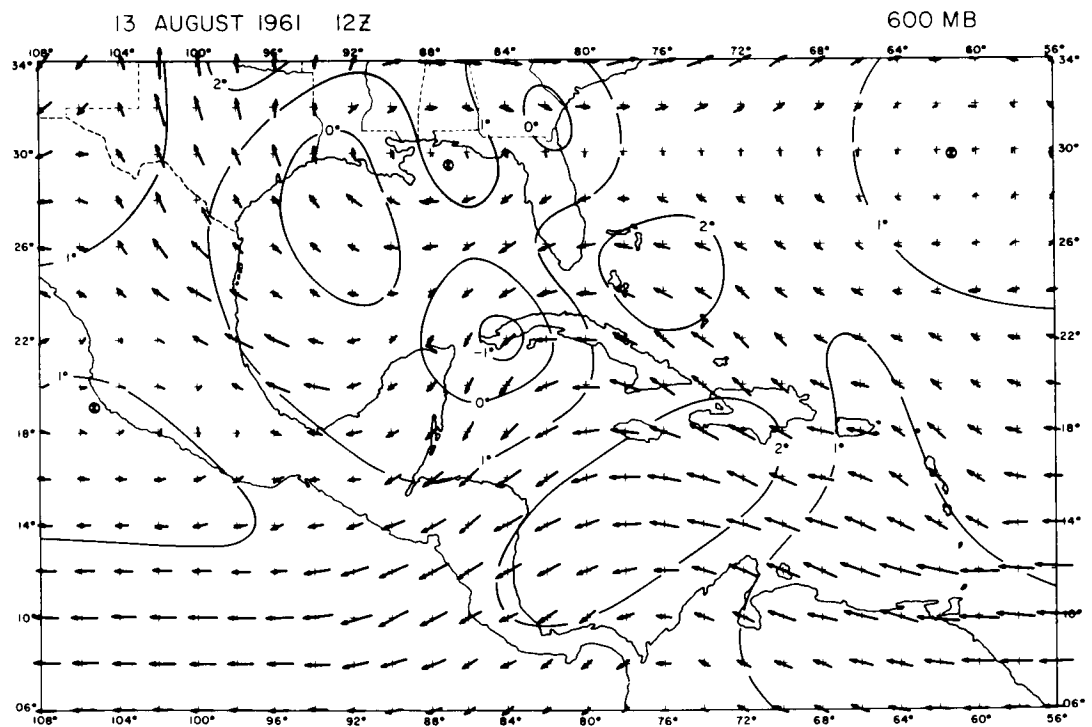
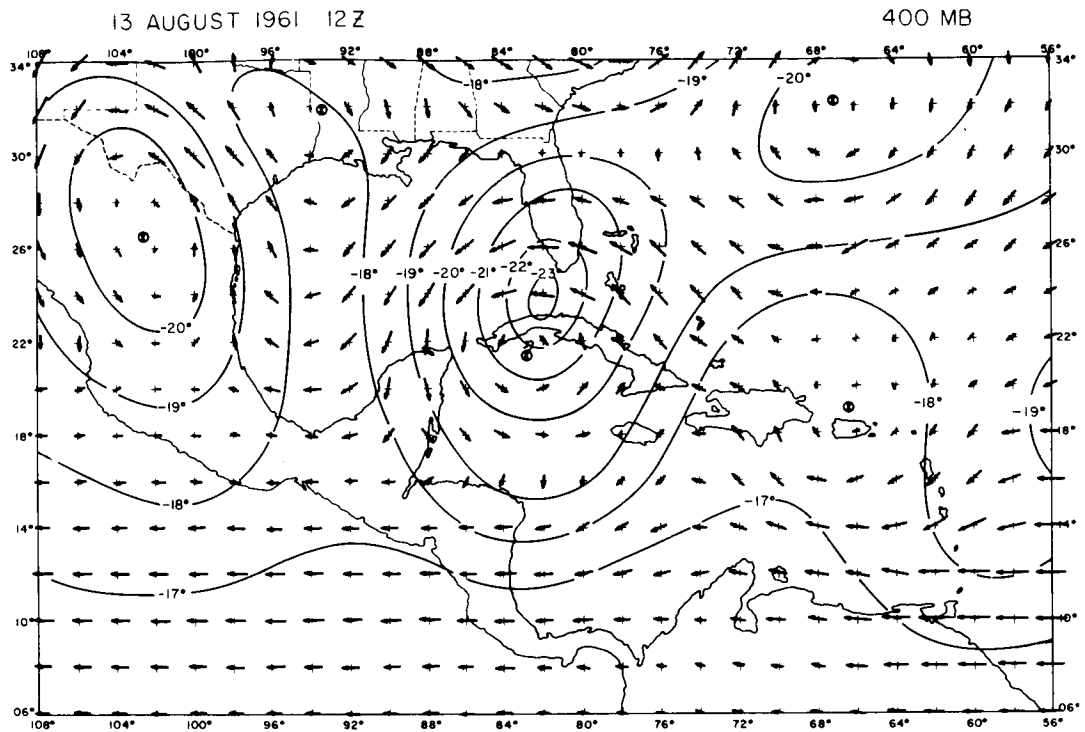


FIGURE 39A. Vector Representation of the Velocity Field with
the Temperature.

Vector length proportional to speed

(0.4 centimeters equals 10 meters per second).

Circled X's are closed centers of circulation.

Temperature analyzed every 1° Centigrade.

FIGURE 39B. Integrated Moisture Flux

Isolines are every 100×10^{-6} mb sec m^{-1} .

Solid lines are convergence, dotted lines are neutral,
and dashed lines are divergence.

Circled crosses are grid points of latent heat addition.

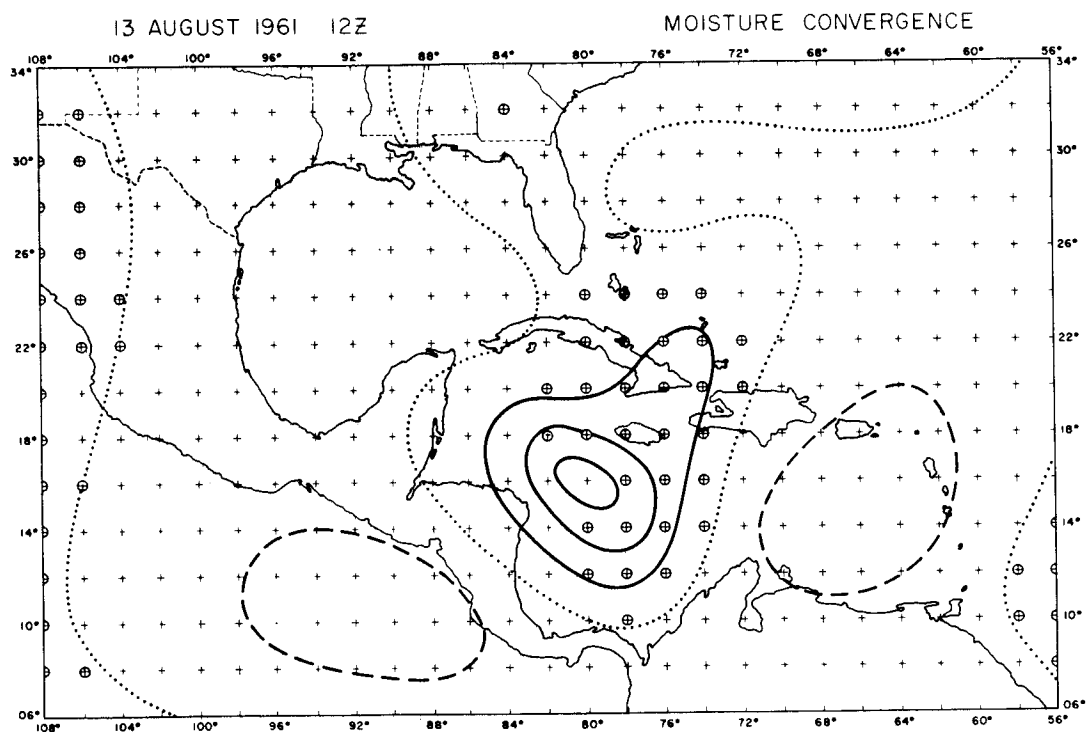
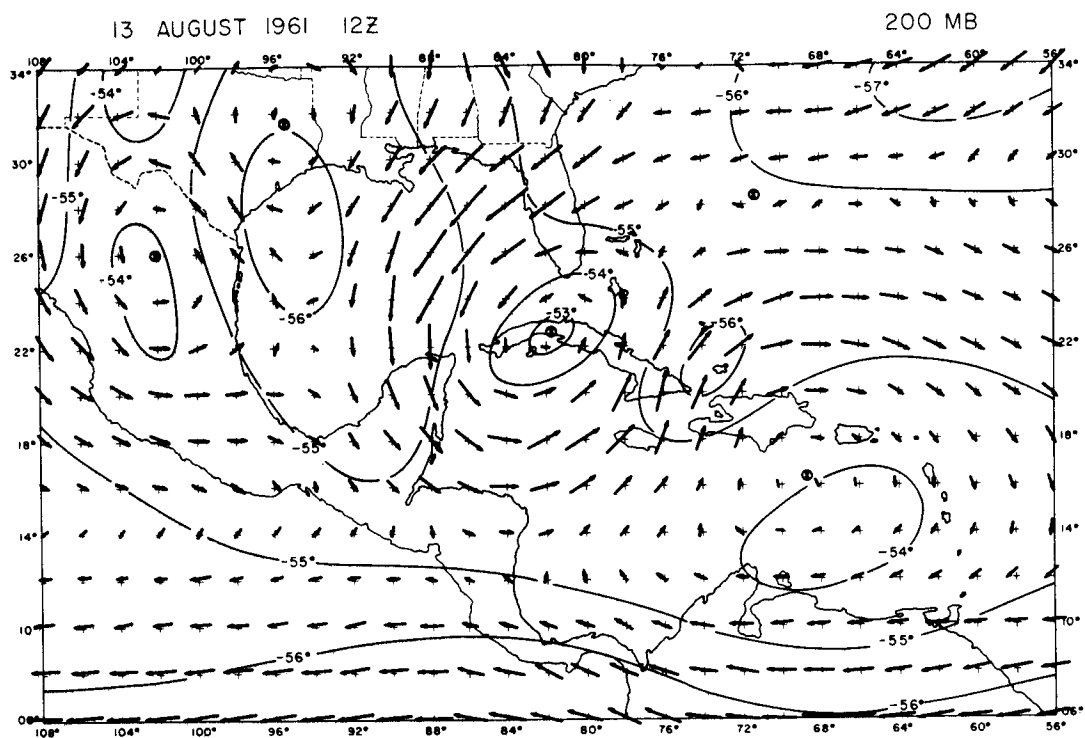


FIGURE 40. Vertical Motion with the Observed Relative Humidity.

Isolines of vertical motion are $20 \times 10^{-5} \text{ mb sec}^{-1}$

Heavy solid lines are sinking, dotted lines are neutral,
and dashed lines are rising.

Light solid lines are relative humidity analyzed every
10 per cent.

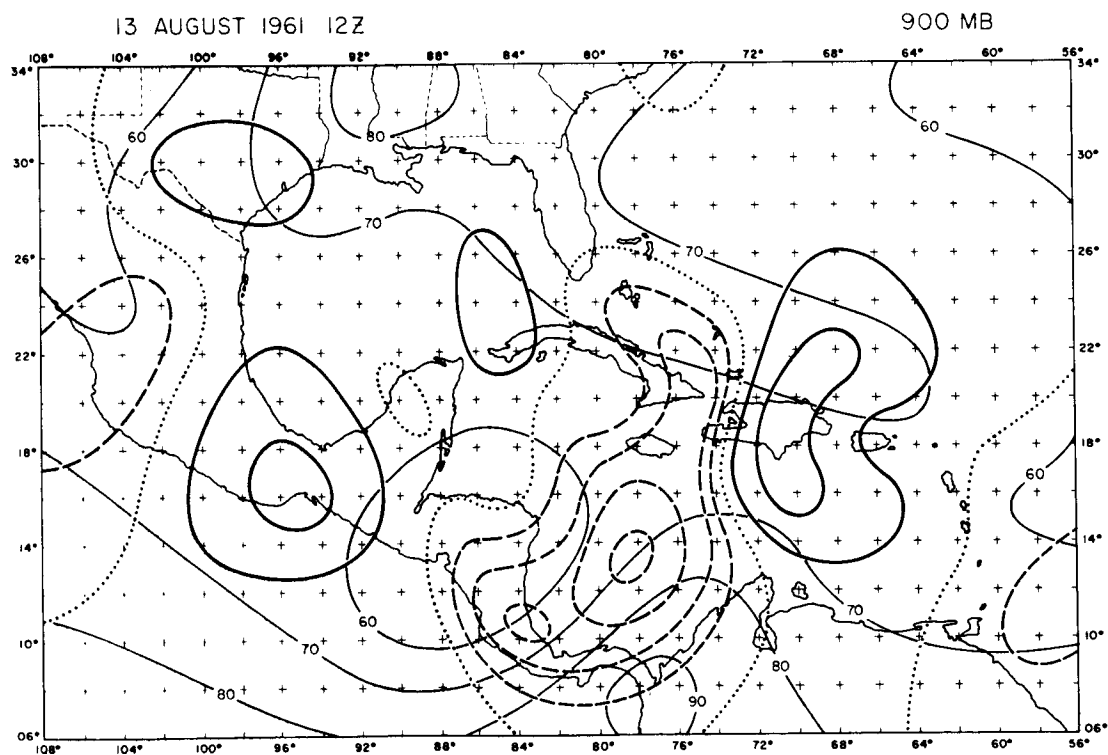
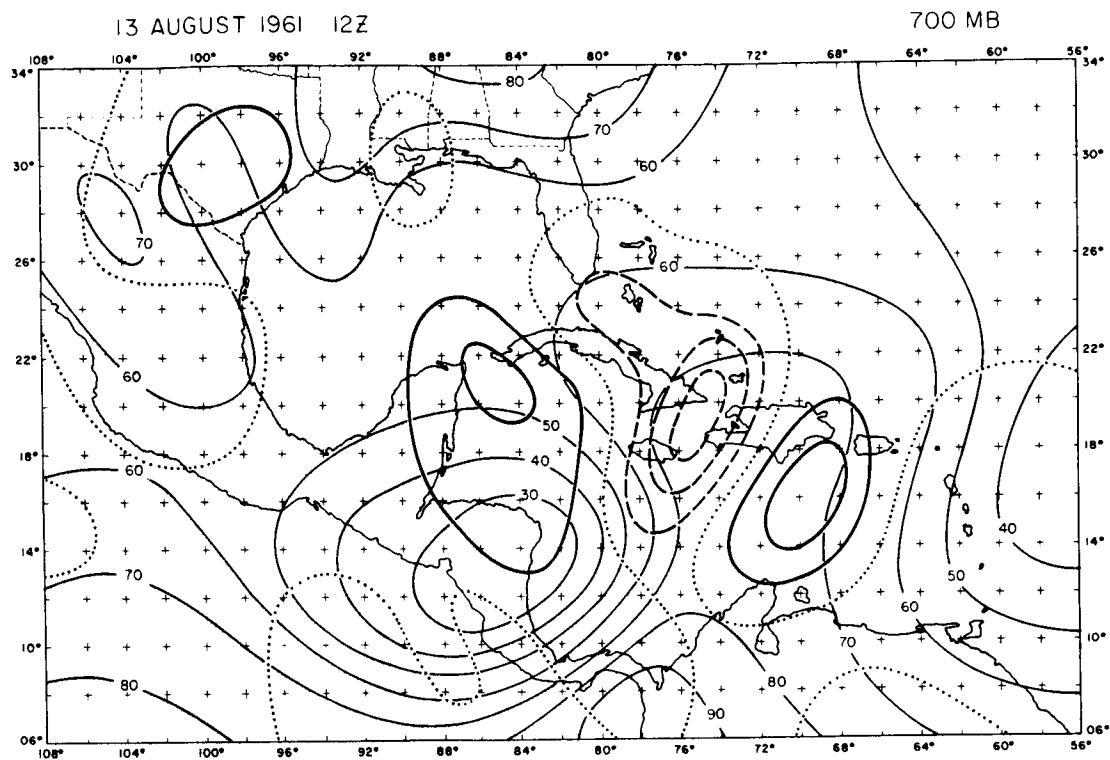


FIGURE 41. Vertical Motion with the Observed Relative Humidity.

Isolines of vertical motion are $20 \times 10^{-5} \text{ mb sec}^{-1}$.

Heavy solid lines are sinking, dotted lines are neutral, and dashed lines are rising.

Light solid lines are relative humidity analyzed every 10 per cent.

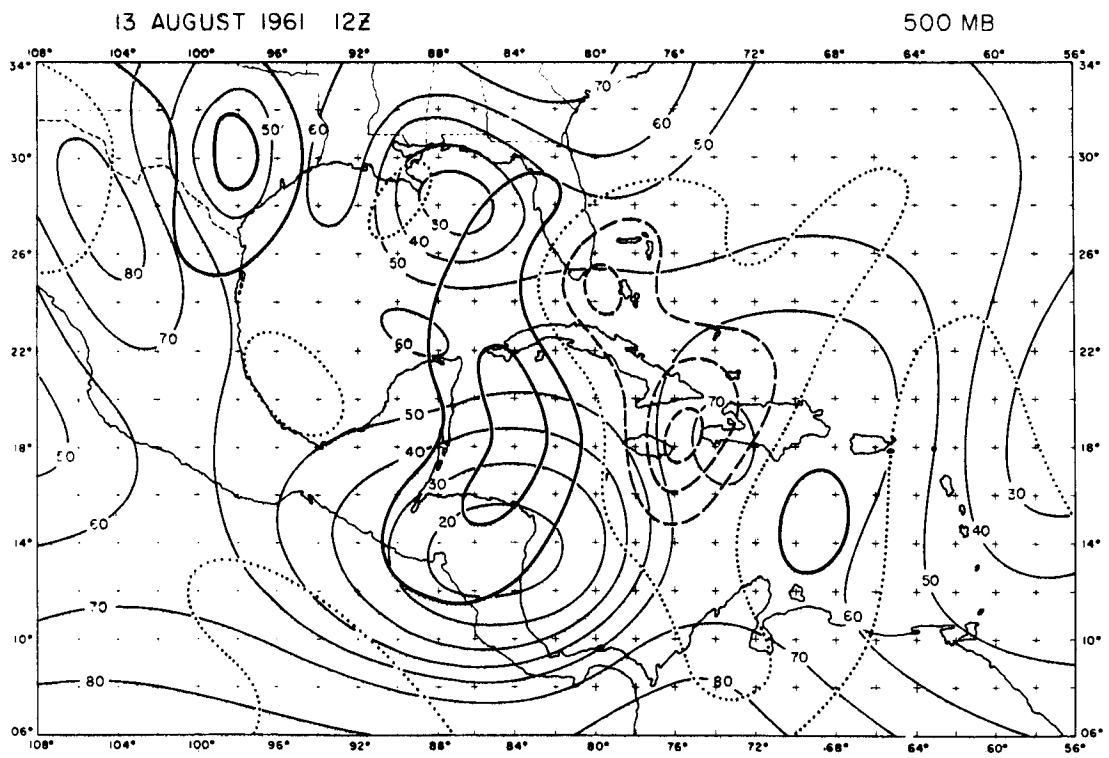
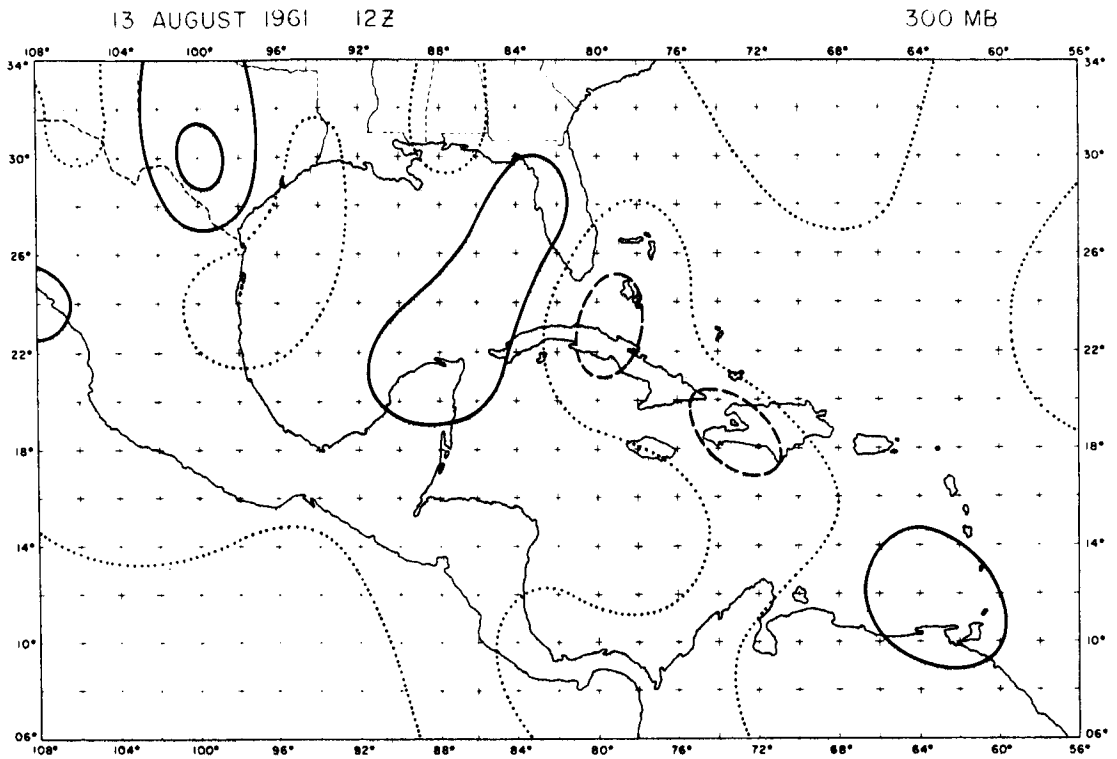


FIGURE 42A. Partitioned Vertical Motion

Heavy vector is the total, light lines are the components.

Order at each grid point from left to right: Total,
vorticity, thermal, deformation, divergence, friction,
and latent heat.

FIGURE 42B. Moisture and Cloudiness

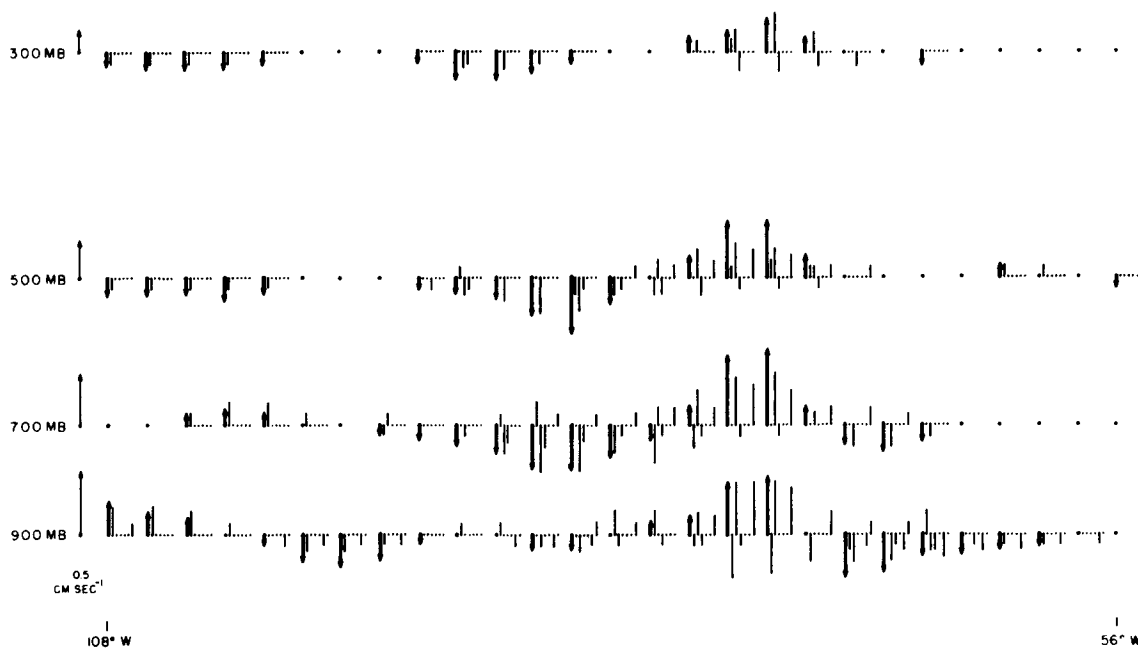
Solid lines are relative humidity every 10 per cent.

Clouds represented in schematic form.

OMEGA CROSS SECTION
13 AUGUST 1961 12Z

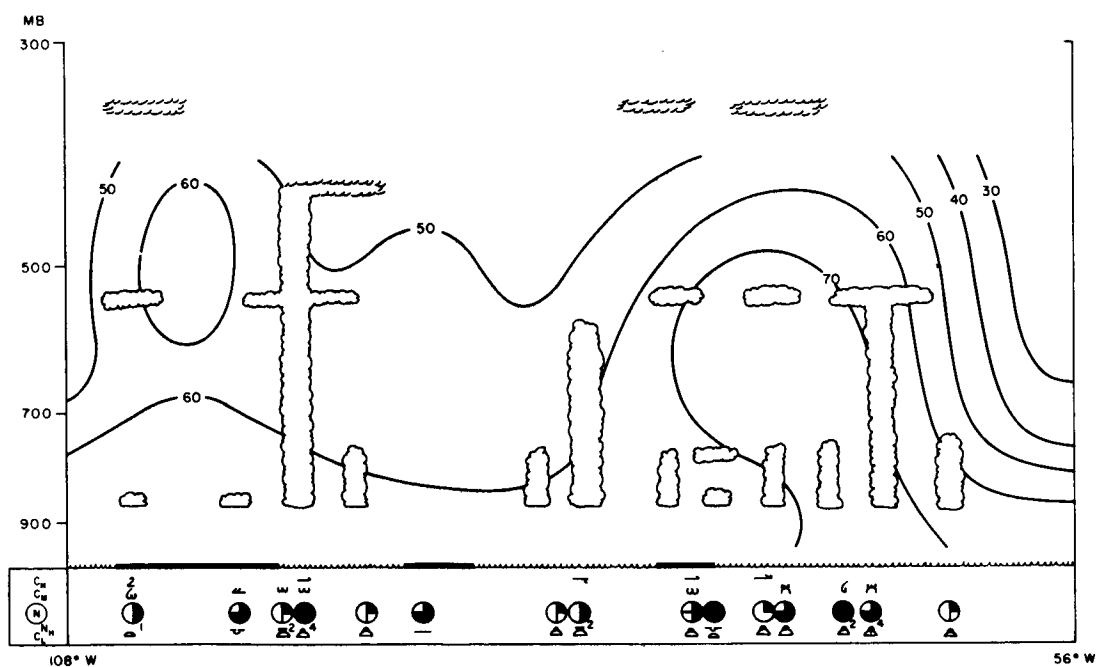
0 100 100 • 10³ MB SEC⁻¹

20° N



MOISTURE CROSS SECTION
13 AUGUST 1961 12Z

20° N



vertical extent in evidence at 700 mbs. The influence of the upper low can be seen at 500 mbs, where two distinct centers of rising motion are present. The vertical velocities of the upper system are now beginning to coincide with the lower disturbance.

The new center of rising air behind the easterly wave is aligned with the moisture tongue appearing in the area. The relatively small size of the vertical motion places a limit on the amount of moisture increase that can directly be product of the rising air. However, the synoptic-scale rising may induce considerable convective activity in the region. The moisture flux, Figure 39, indicates an area of convergence located in the same region, substantiating this argument.

Upon examination of the omega and moisture cross-section in Figure 42, the strong rising behind the wave is due to the thermal and latent heat terms. The effect of the change between cold and warm advection discussed before can be seen quite clearly. The sinking air is still a product of many terms with no particular one dominating. From the moisture and cloudiness display it appears that the model is releasing latent heat in an area of damped convective activity. This is due to the coarse formulation used for the parameterization, and also the time of the observation. The moisture wave associated with the perturbation continues its westward propagation with drier air following. The dry tongue ahead of the wave has disappeared from the cross-section.

14 August 1961 00Z. The wind circulations have again shown remarkable displacements for 12 hours as illustrated in Figures 43-45.

The wave has continued to develop at all levels in the lower troposphere. Very little translation has occurred during the amplification of the system. The reappearance of the closed vortex is noted at 1000 and 800 mbs, with marked increase in the cyclonic curvature at both levels. The speeds at 800 and 600 mbs behind the wave are approaching 15 meters per second, which is the highest observed from the case study in the lower levels of the atmosphere. The upper level system is showing signs of change as it continues its slow southwestward drift. The winds on the eastern side of the circulation are now becoming stronger than the opposite, northerly flow. The speed maximum at 200 mbs is located directly over the lower level perturbation.

The temperature gradients, in general, have increased in magnitude during the last 12 hours, with the most noticeable change occurring at 1000 mbs. The easterly wave and closed vortex are definitely cold-core at this map-time. The relatively warm air to the west at 1000 mbs may be due to subsidence and lack of convection in the region. Warm air advection continues behind the easterly wave at 800 and 600 mbs and a new region of cold air advection is seen to the east. The upper-level temperature configurations have been altered as well. The cold air appears to be splitting into two centers, while the warmer air above has moved from the center of circulation to a position over the easterly wave.

The numerical results are presented in Figures 46-47. The vertical velocities in the easterly wave are quite large (1.0-1.5 centimeters per second)

FIGURE 43. Vector Representation of the Velocity Field with
the Temperature.

Vector length proportional to speed

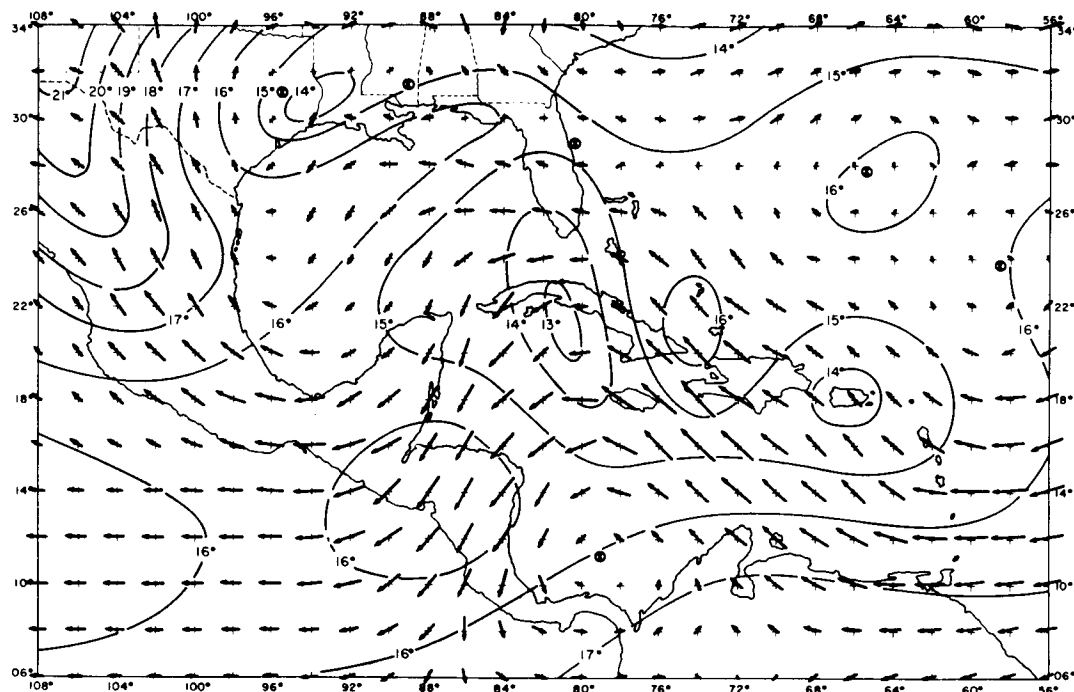
(0.4 centimeters equals 10 meters per second).

Circled X's are closed centers of circulation.

Temperature analyzed every 1° Centigrade.

14 AUGUST 1961 00Z

800 MB



14 AUGUST 1961 00Z

1000 MB

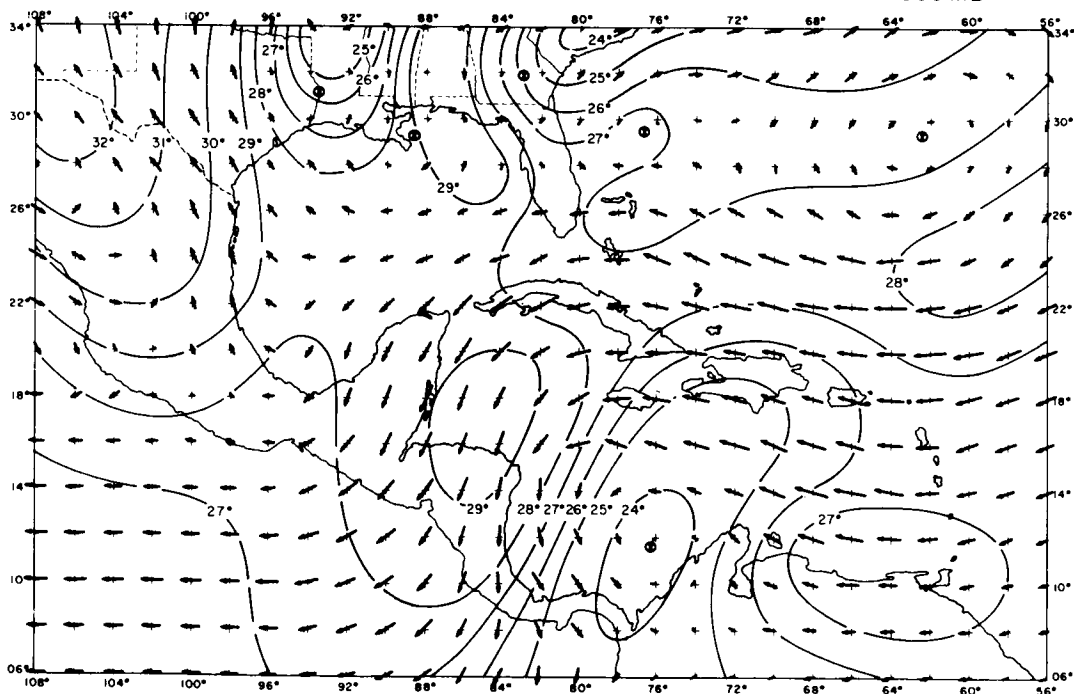


FIGURE 44. Vector Representation of the Velocity Field with
the Temperature.

Vector length proportional to speed

(0.4 centimeters equals 10 meters per second).

Circled X's are closed centers of circulation.

Temperature analyzed every 1° Centigrade.

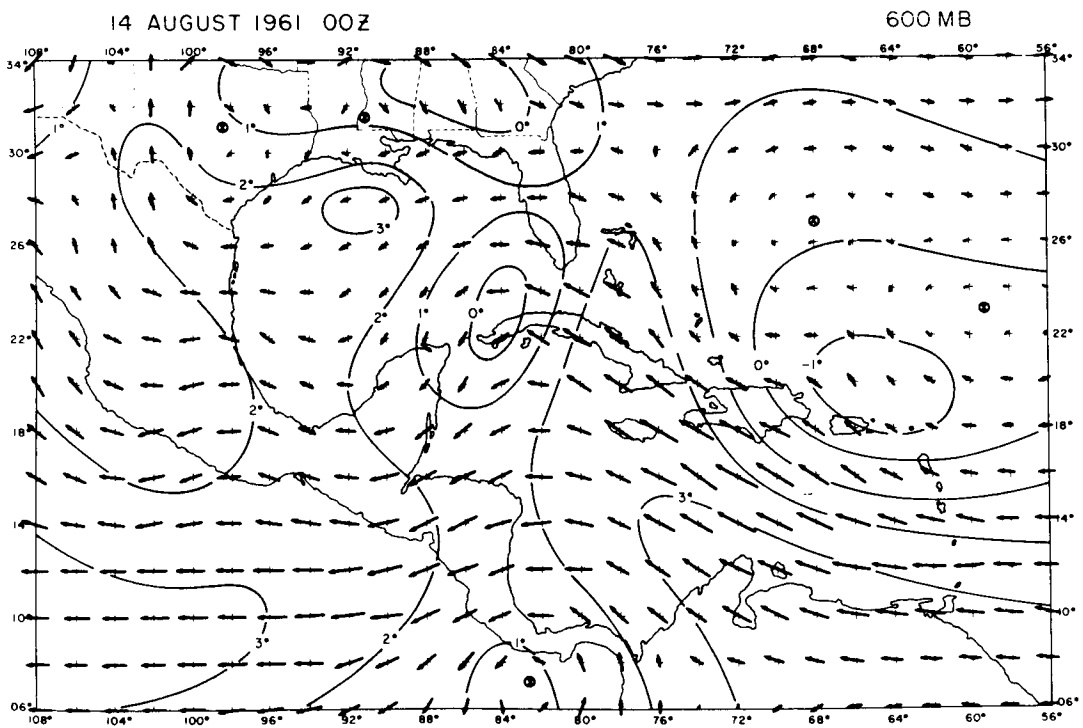
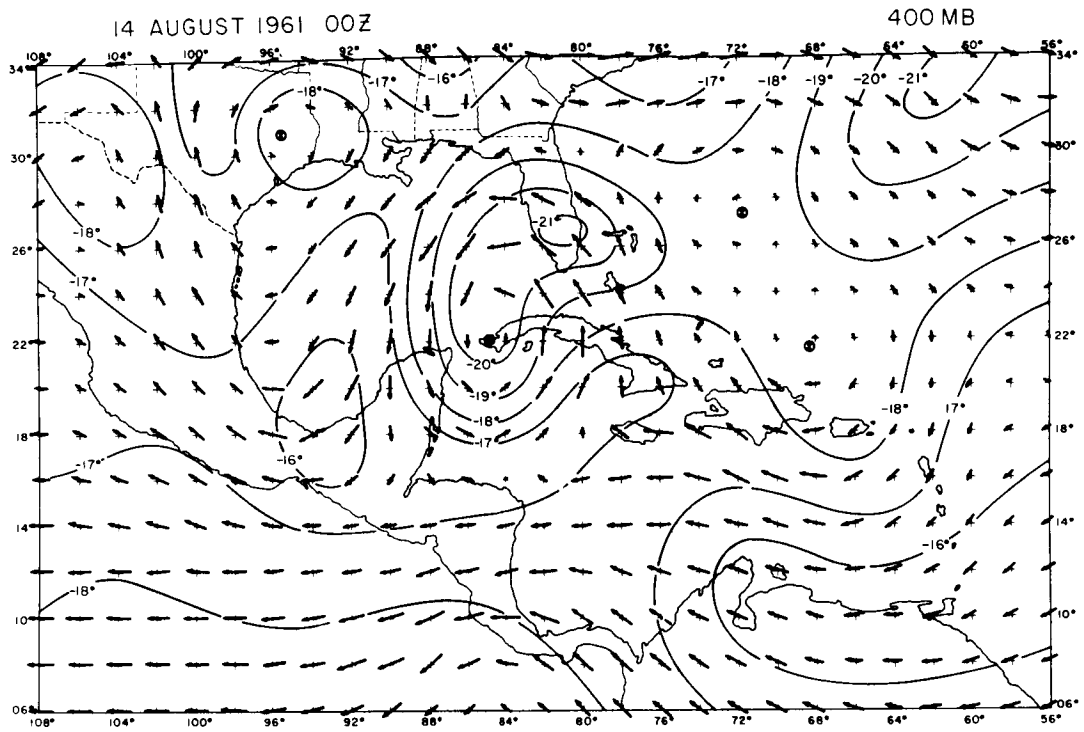


FIGURE 45A. Vector Representation of the Velocity Field with
the Temperature.

Vector length proportional to speed

(0.4 centimeters equals 10 meters per second).

Circled X's are closed centers of circulation.

Temperature analyzed every 1° Centigrade.

FIGURE 45B. Integrated Moisture Flux

Isolines are every $100 \times 10^{-6} \text{ mb sec m}^{-1}$.

Solid lines are convergence, dotted lines are neutral,
and dashed lines are divergence.

Circled crosses are grid points of latent heat addition.

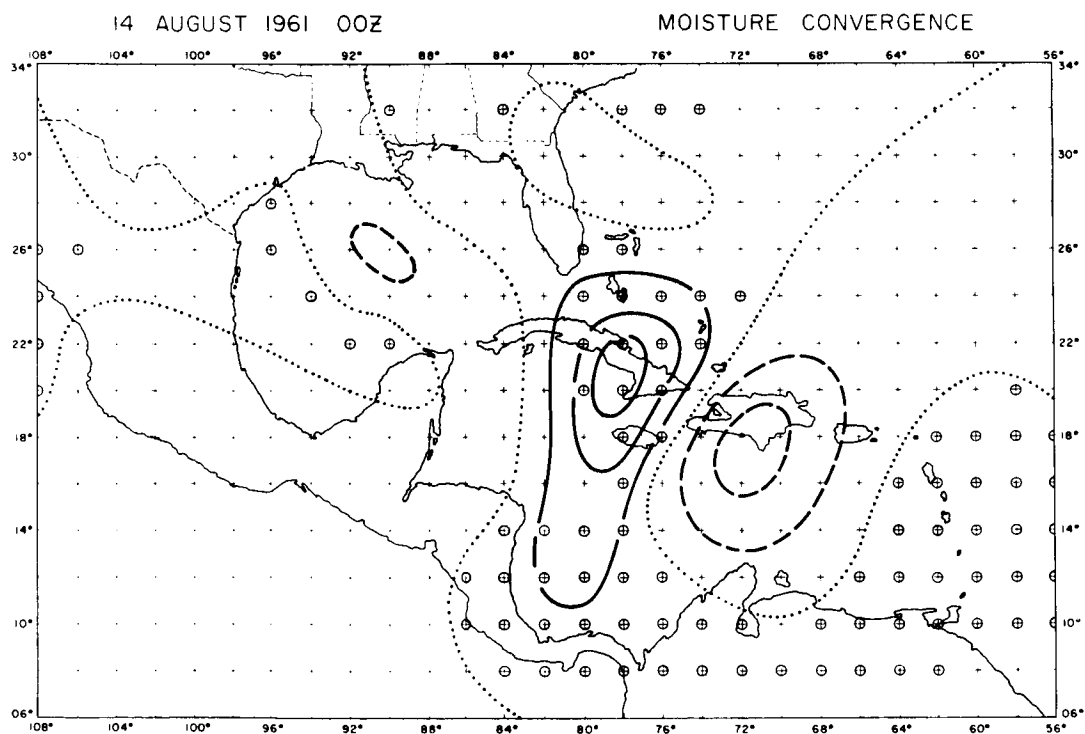
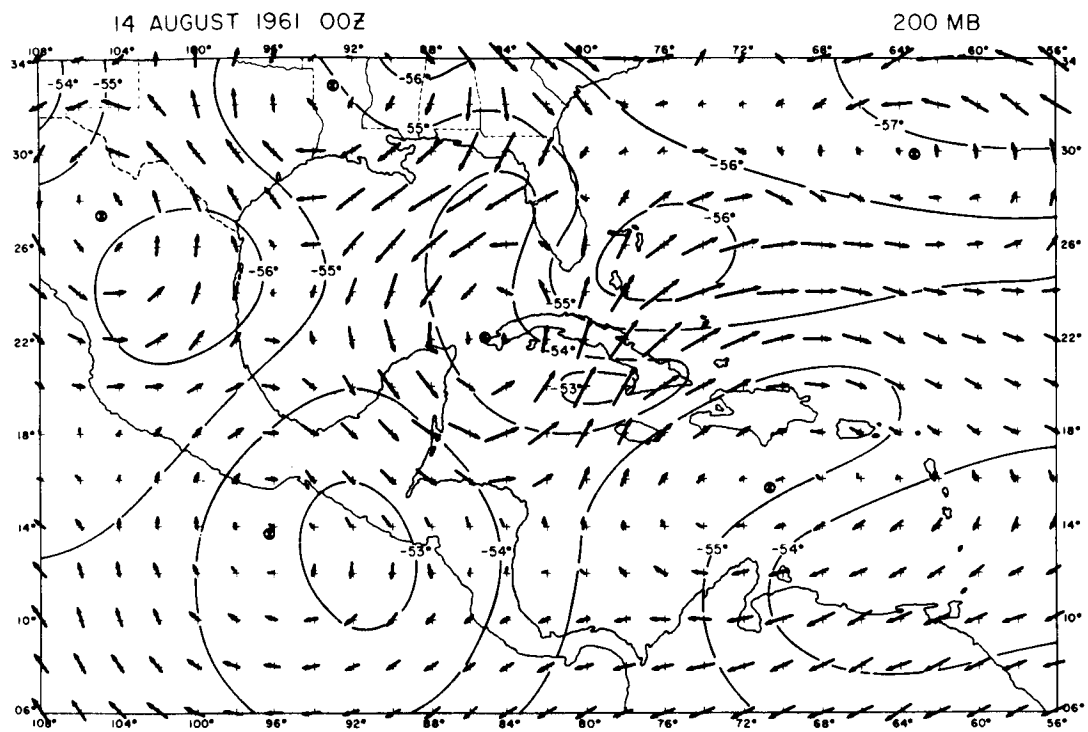


FIGURE 46. Vertical Motion with the Observed Relative Humidity.

Isolines of vertical motion are $20 \times 10^{-5} \text{ mb sec}^{-1}$.

Heavy solid lines are sinking, dotted lines are neutral, and dashed lines are rising.

Light solid lines are relative humidity analyzed every 10 per cent.

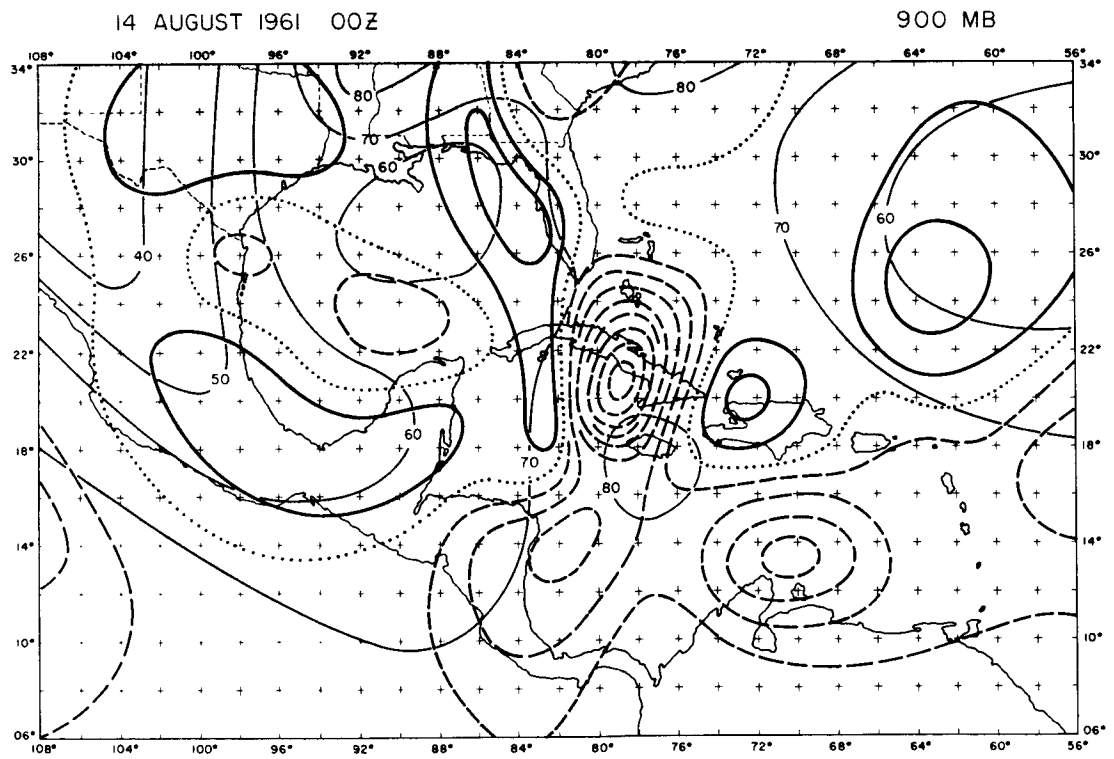
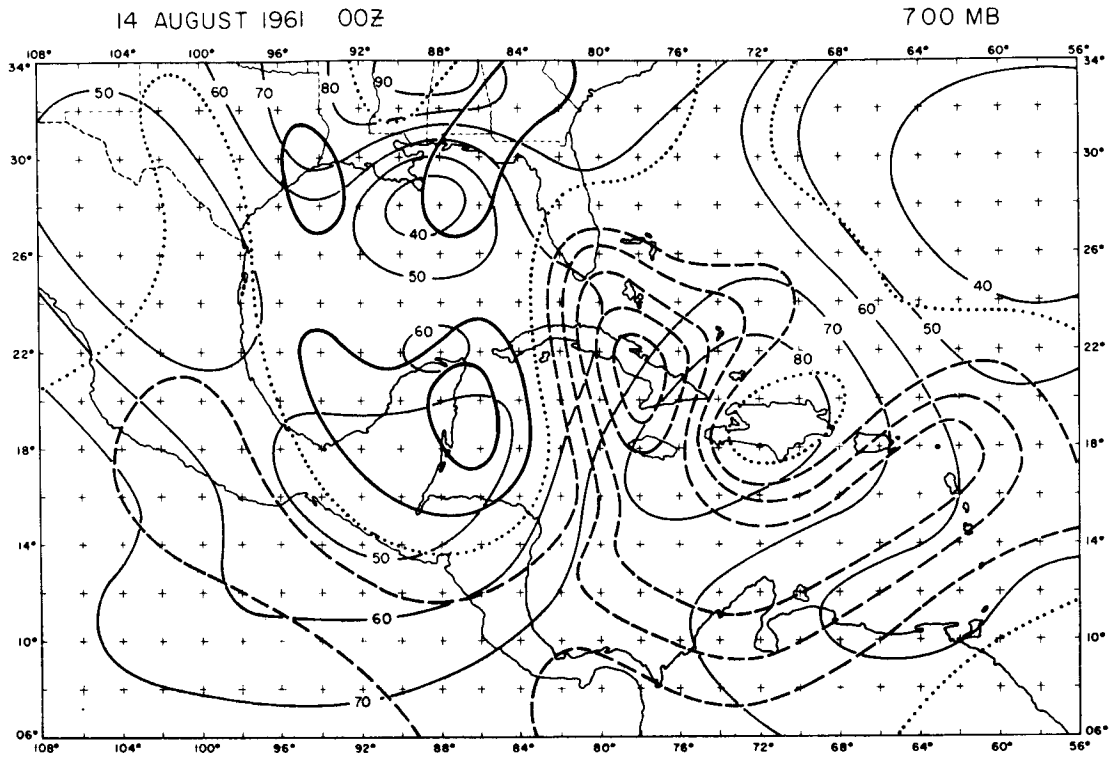


FIGURE 47. Vertical Motion with the Observed Relative Humidity.

Isolines of vertical motion are $20 \times 10^{-5} \text{ mb sec}^{-1}$.

Heavy solid lines are sinking, dotted lines are neutral, and dashed lines are rising.

Light solid lines are relative humidity analyzed every 10 per cent.

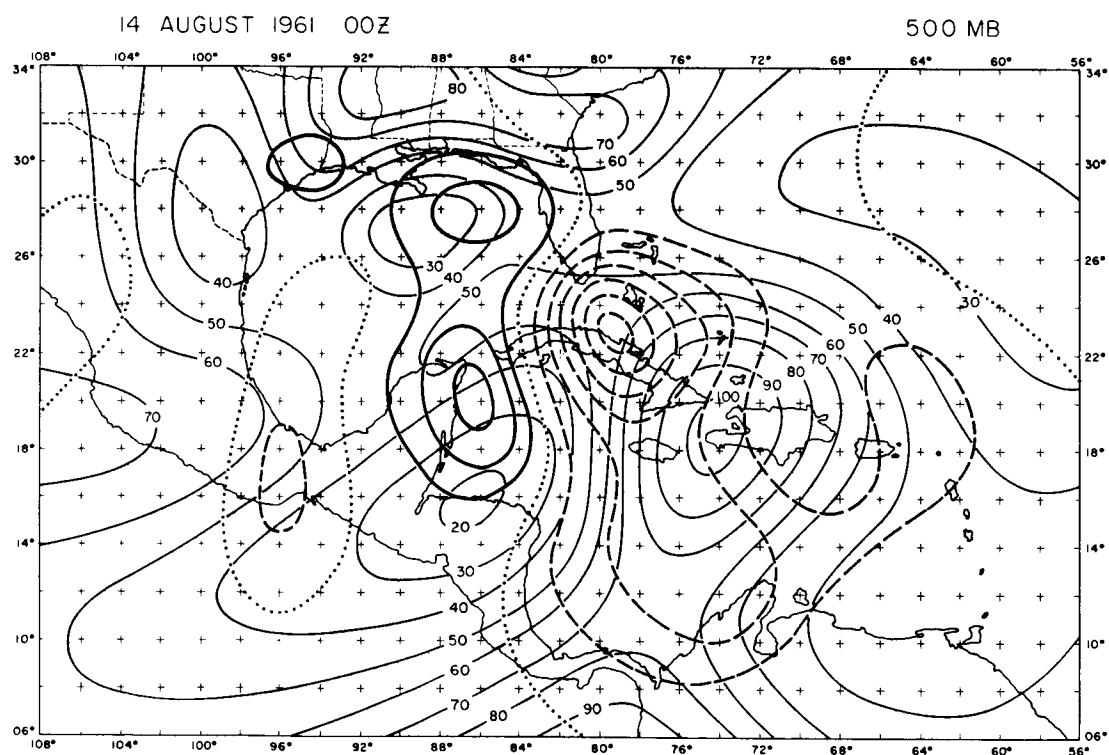
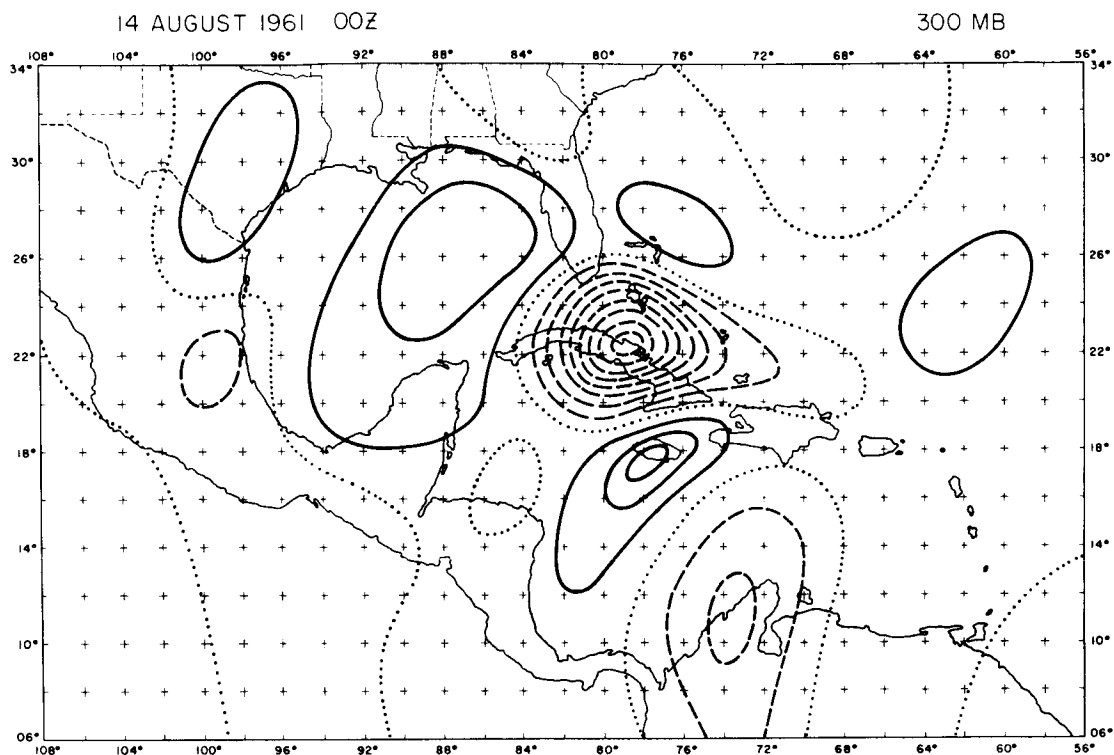


FIGURE 48A. Partitioned Vertical Motion

Heavy vector is the total, light lines are the components.

Order at each grid point from left to right: Total, vorticity, thermal, deformation, divergence, friction, and latent heat.

FIGURE 48B. Moisture and Cloudiness

Solid lines are relative humidity every 10 per cent.

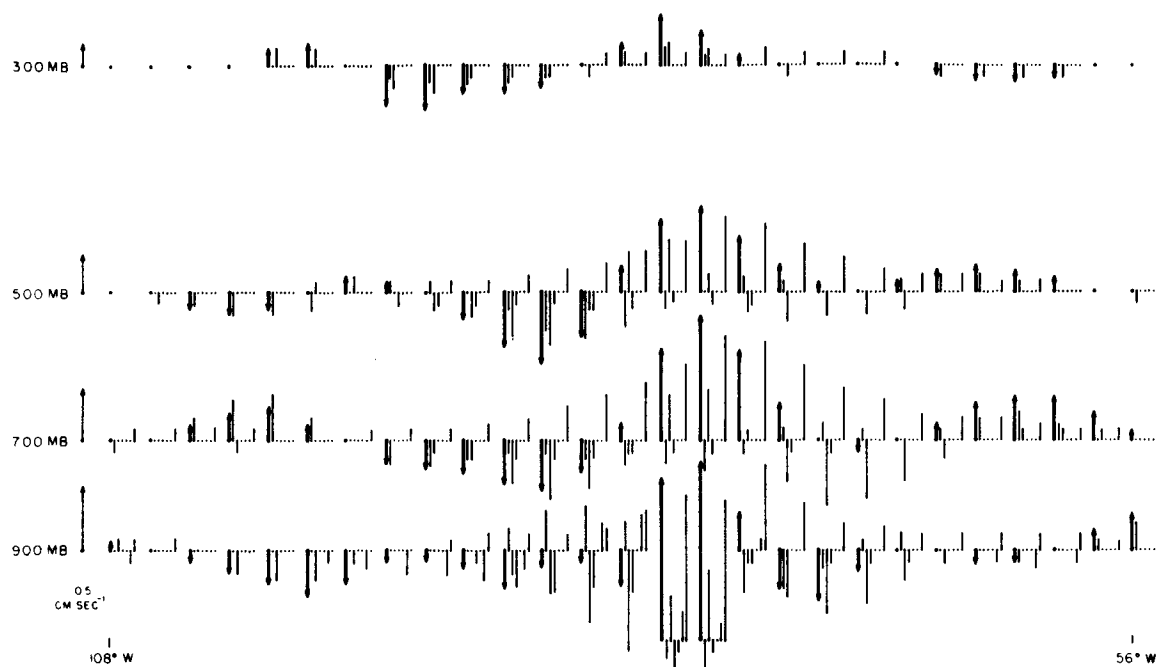
Clouds represented in schematic form.

OMEGA CROSS SECTION

0 100 100 • 10³ MB SEC⁻¹

20° N

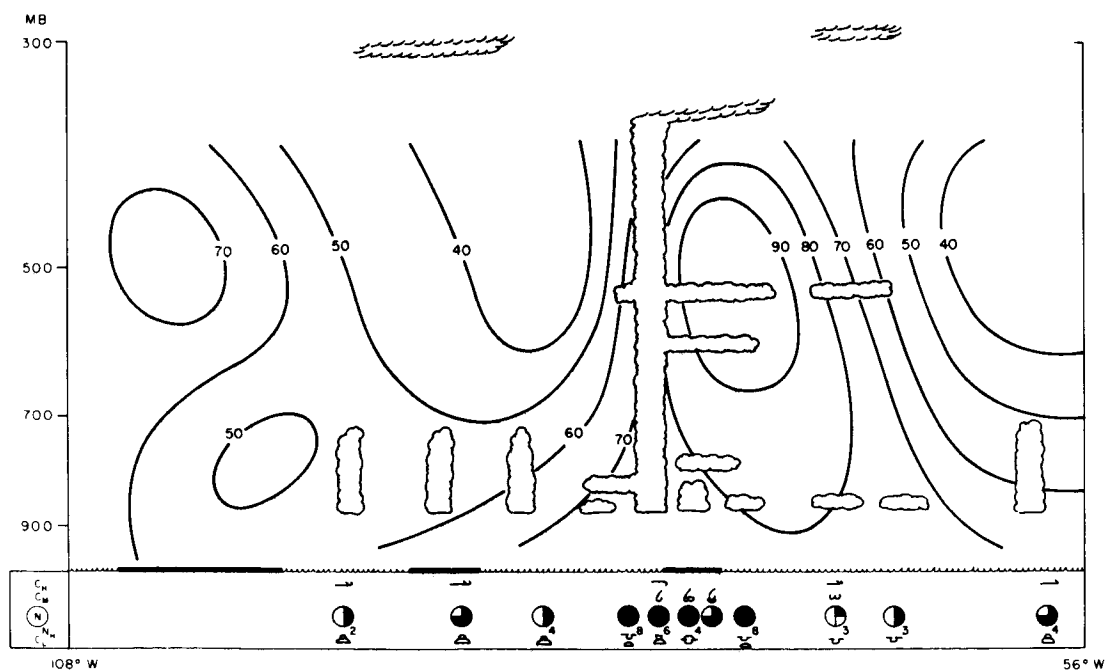
14 AUGUST 1961 00Z



MOISTURE CROSS SECTION

20° N

14 AUGUST 1961 00Z



at this map-time. The rising centers appear to dominate the patterns, with only weak sinking present. A glance at the integrated moisture flux (Figure 45) in the region of the intense rising motion will help explain the large magnitudes observed. The latent heat contribution produced by the extreme convergence in this area will, indeed, be very great. Again, the overlap of the latent heat term has the effect of reducing the magnitude of the sinking centers as seen in Figure 48A. The sinking behind the easterly wave has been masked by this mechanism. Ahead of the perturbation, the downward motion is quite strong in the northerly flow.

The center of maximum rising is positioned over the region of strong moisture advection, again reflecting the dominance of the latent heat parameterization. The sinking air corresponds nicely with the drier air ahead of the disturbance. A remarkable change is noted at 300 mbs where the vertical motion has become very strong. This may be associated with the movement of the temperature gradients at 400 and 200 mbs. The upward motion at the higher level is exactly in phase with the vertical motion produced by the easterly wave. This coupling may have had an effect on the development of the two systems.

The comparison between the vertical motion and the moisture, (Figure 48) shows very good agreement, in spite of the problems in the latent heat parameterization. The convective activity and the middle clouds are located in the region of maximum rising motion, while the sinking air ahead of the system corresponds to lower humidities as seen on the horizontal maps. The air behind the trough axis has become nearly saturated, probably due to

convective mixing, and has continued its movement toward the west.

14 August 1961 12Z. At the final map-time being considered, the easterly wave has begun to move toward the west again (Figures 49-51). The amplitude of the trough has remained constant, however, the southern vortex circulation has weakened somewhat and has disappeared at 800 mbs. The trough at 600 mbs has become quite disorganized with a closed center of outflow situated on the wave axis. The southerly flow behind the wave remained strong, on the order of 15 meters per second. The upper-tropospheric vortex is again reflected in the 600 mb circulation, creating a chaotic flow pattern over the lower trough. The maximum energy of the upper flow around the closed vortex is clearly on the eastern side, with very little northerly component to the west.

The thermal distribution has been altered radically during the past 12 hours in the lower troposphere. The intense baroclinic zone at 1000 mbs, near the wave vortex has changed sign and weakened considerably. Warmer air has replaced the cold-core structure (that was previously observed) in the perturbation. As a result, the warm advection behind the wave at lower levels has ceased to exist. At 600 and 400 mbs a tongue of warm air is still present in the strong southerly flow, producing considerable advection. The colder temperatures associated with the upper vortex have decreased in horizontal extent at 400 mbs, while the sharp temperature gradient in the low at 200 mbs has remained constant.

FIGURE 49. Vector Representation of the Velocity Field with
the Temperature.

Vector length proportional to speed

(0.4 centimeters equals 10 meters per second).

Circled X's are closed centers of circulation.

Temperature analyzed every 1° Centigrade.

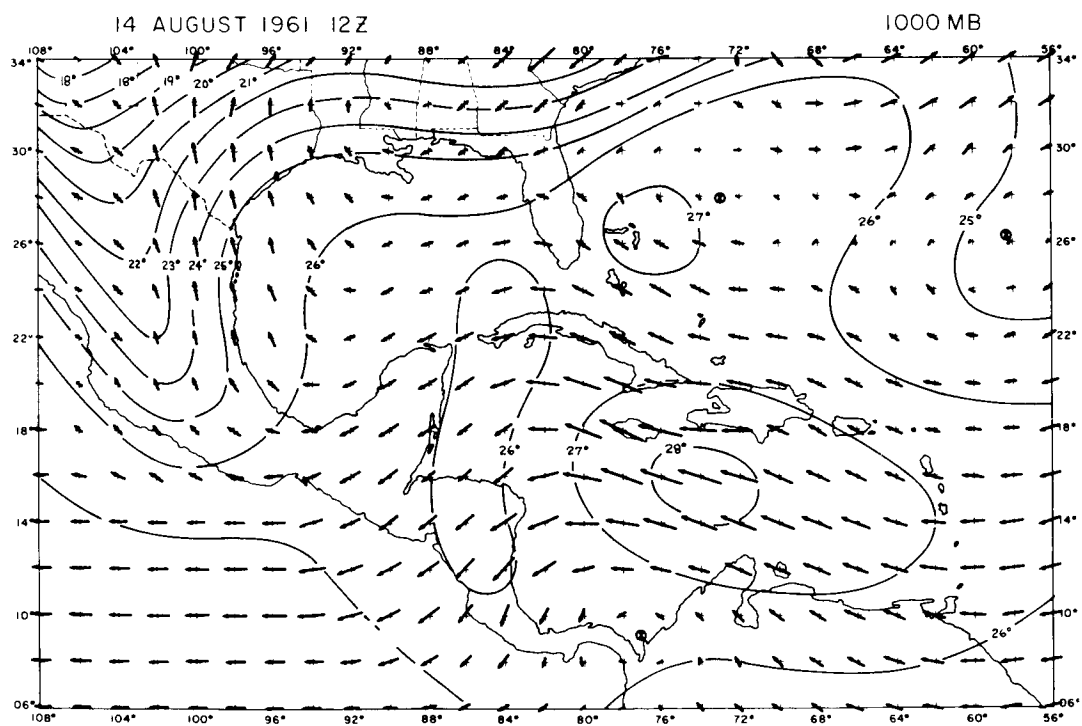
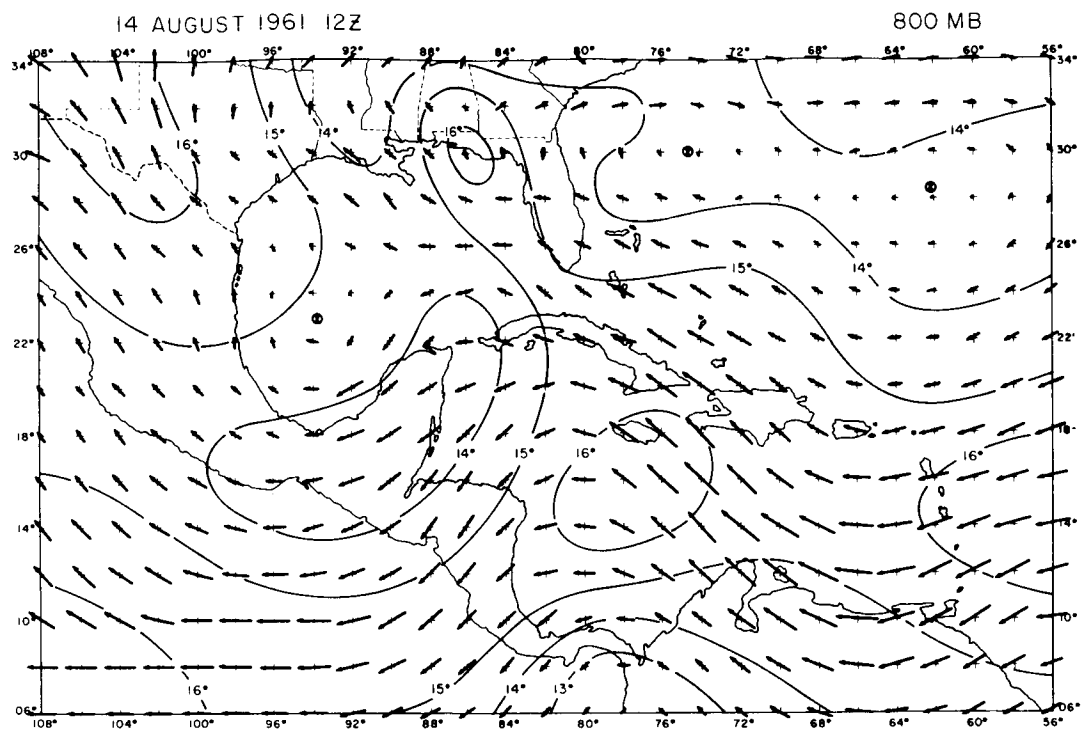


FIGURE 50. Vector Representation of the Velocity Field with
the Temperature.

Vector length proportional to speed

(0.4 centimeters equals 10 meters per second).

Circled X's are closed centers of circulation.

Temperature analyzed every 1° Centigrade.

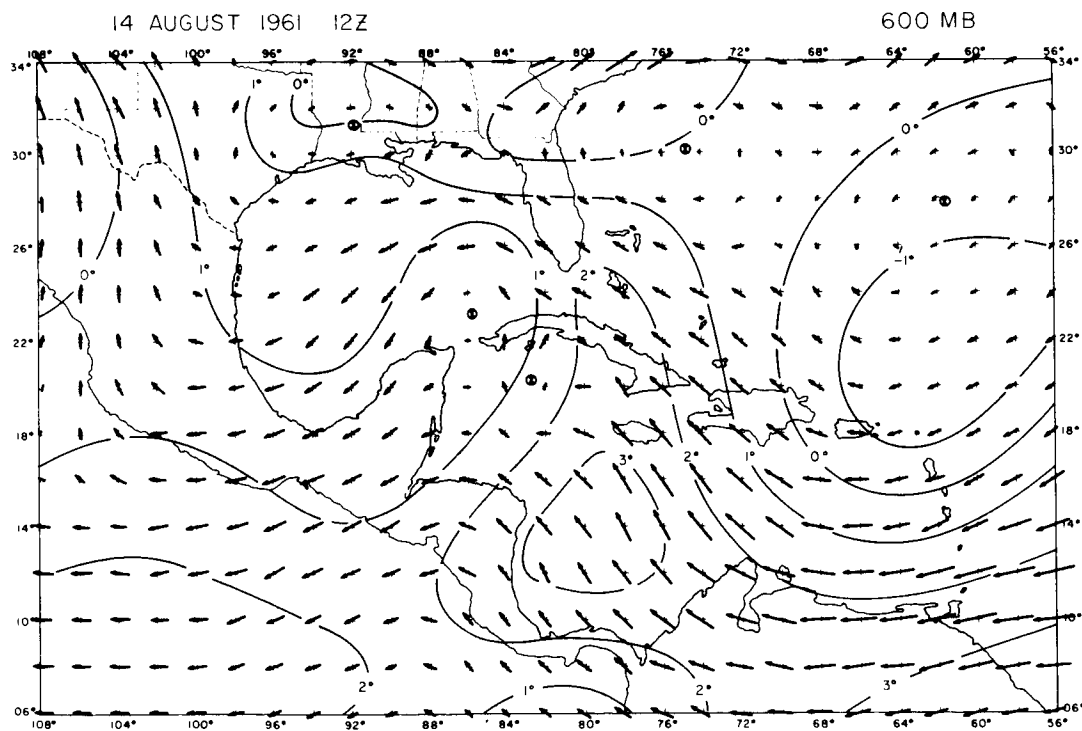
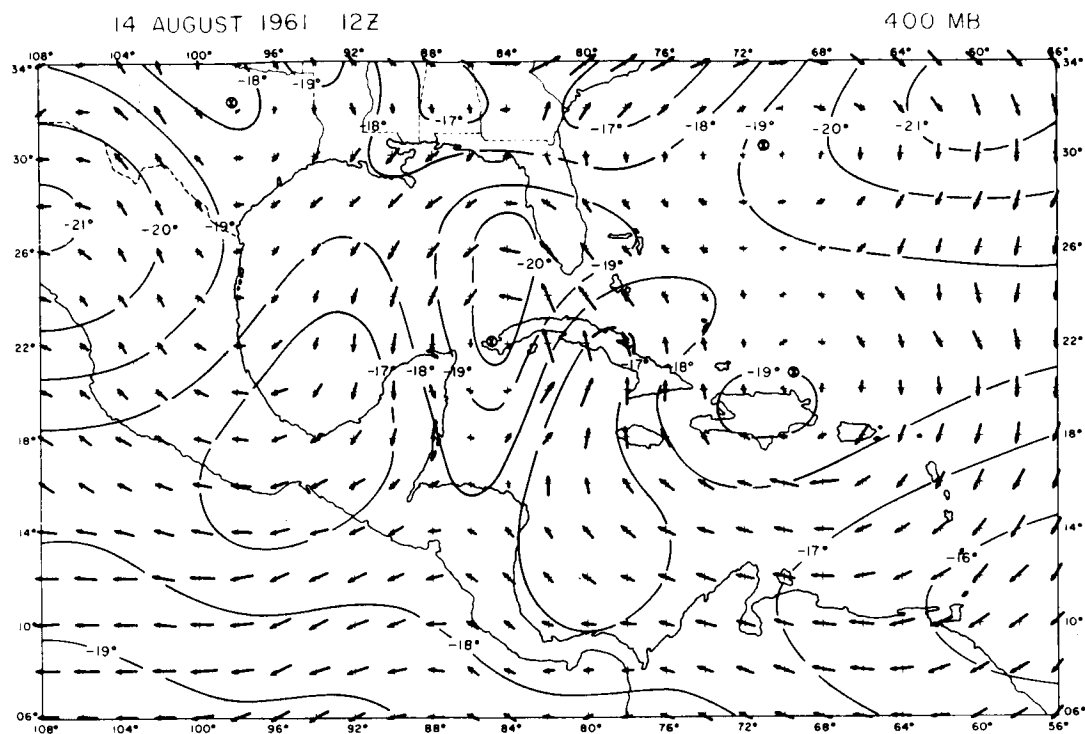


FIGURE 51A. Vector Representation of the Velocity Field with
the Temperature.

Vector length proportional to speed

(0.4 centimeters equals 10 meters per second).

Circled X's are closed centers of circulation.

Temperature analyzed every 1° Centigrade.

FIGURE 51B. Integrated Moisture Flux

Isolines are every 100×10^{-6} mb sec m^{-1} .

Solid lines are convergence, dotted lines are neutral,
and dashed lines are divergence.

Circled crosses are grid points of latent heat addition.

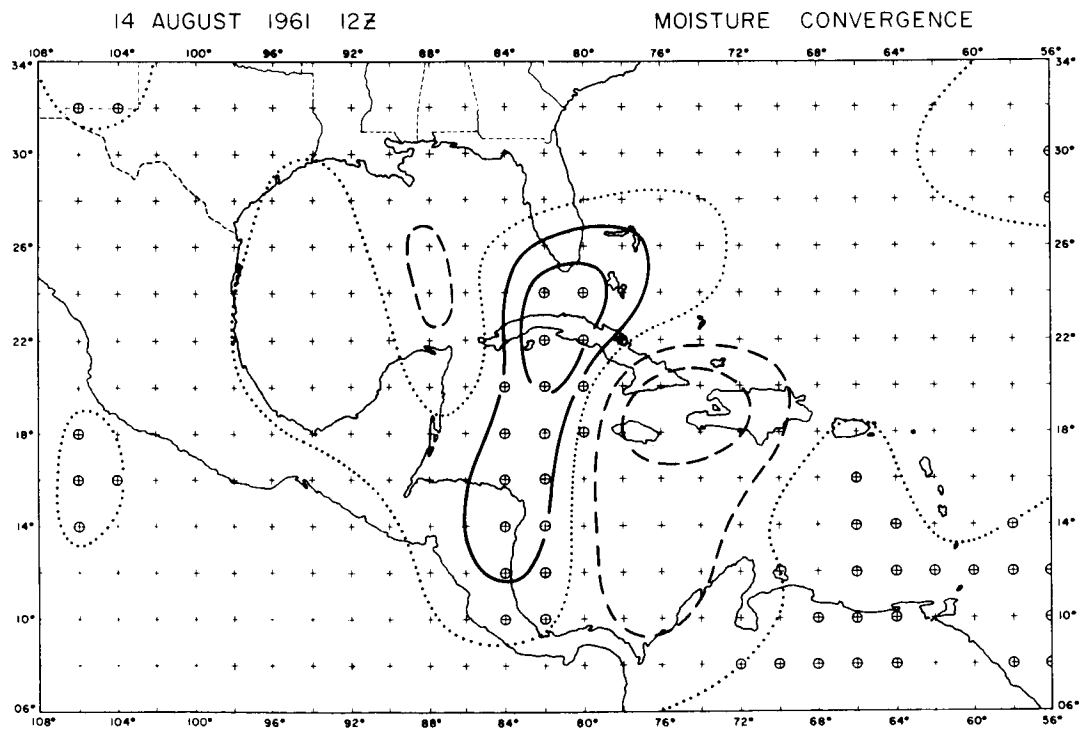
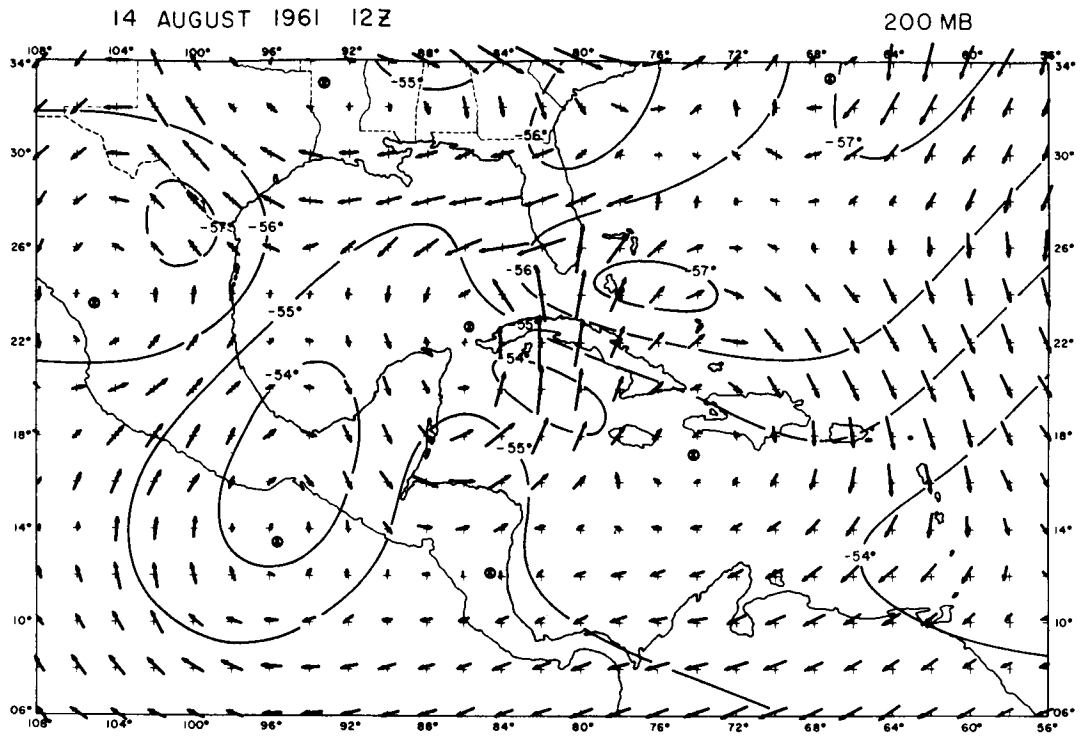


FIGURE 52. Vertical Motion with the Observed Relative Humidity.

Isolines of vertical motion are $20 \times 10^{-5} \text{ mb sec}^{-1}$.

Heavy solid lines are sinking, dotted lines are neutral, and dashed lines are rising.

Light solid lines are relative humidity analyzed every 10 per cent.

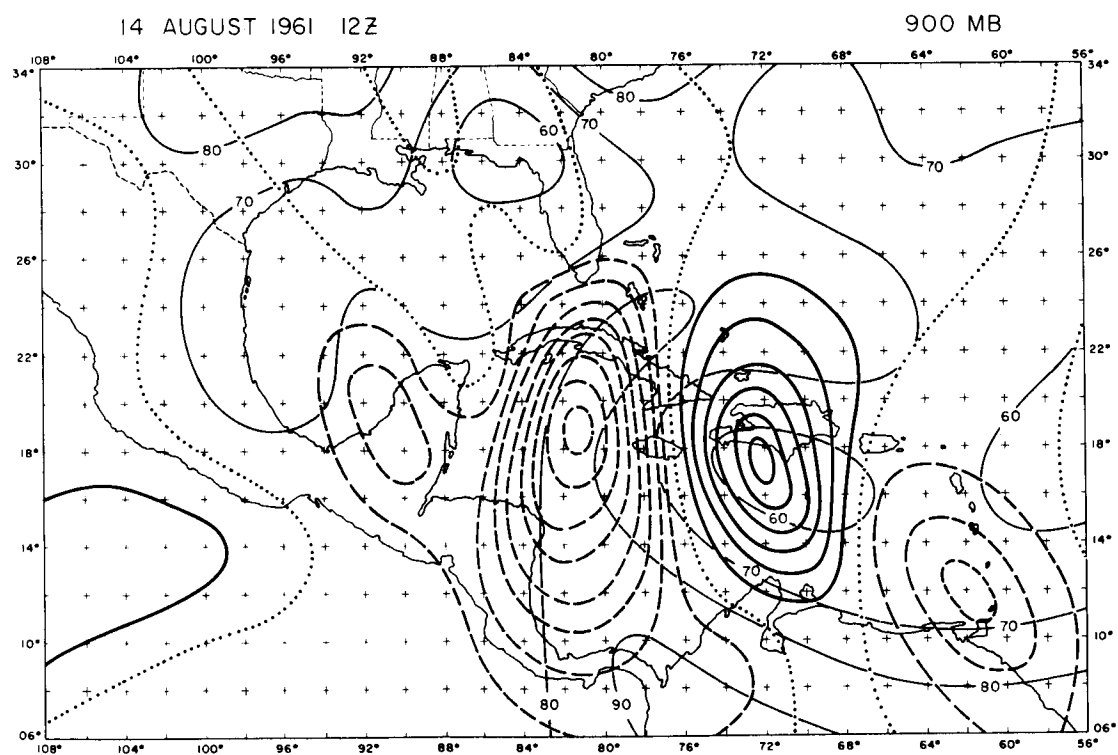
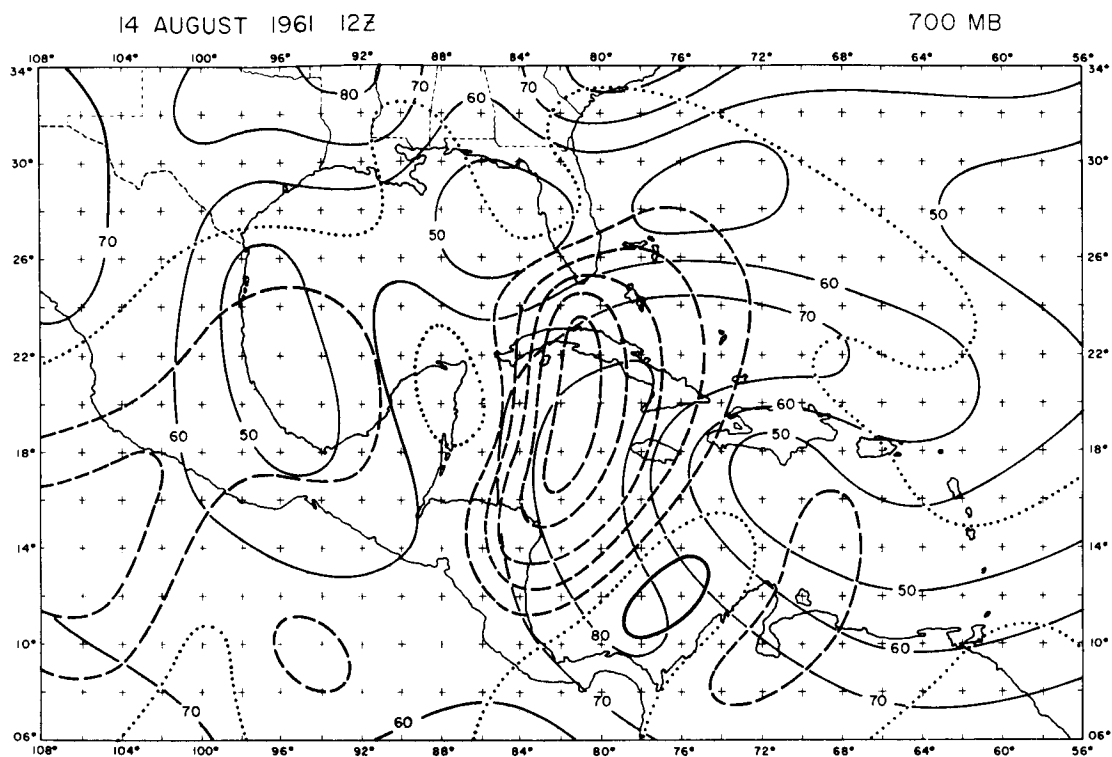


FIGURE 53. Vertical Motion with the Observed Relative Humidity.

Isolines of vertical motion are $20 \times 10^{-5} \text{ mb sec}^{-1}$.

Heavy solid lines are sinking, dotted lines are neutral, and dashed lines are rising.

Light solid lines are relative humidity analyzed every 10 per cent.

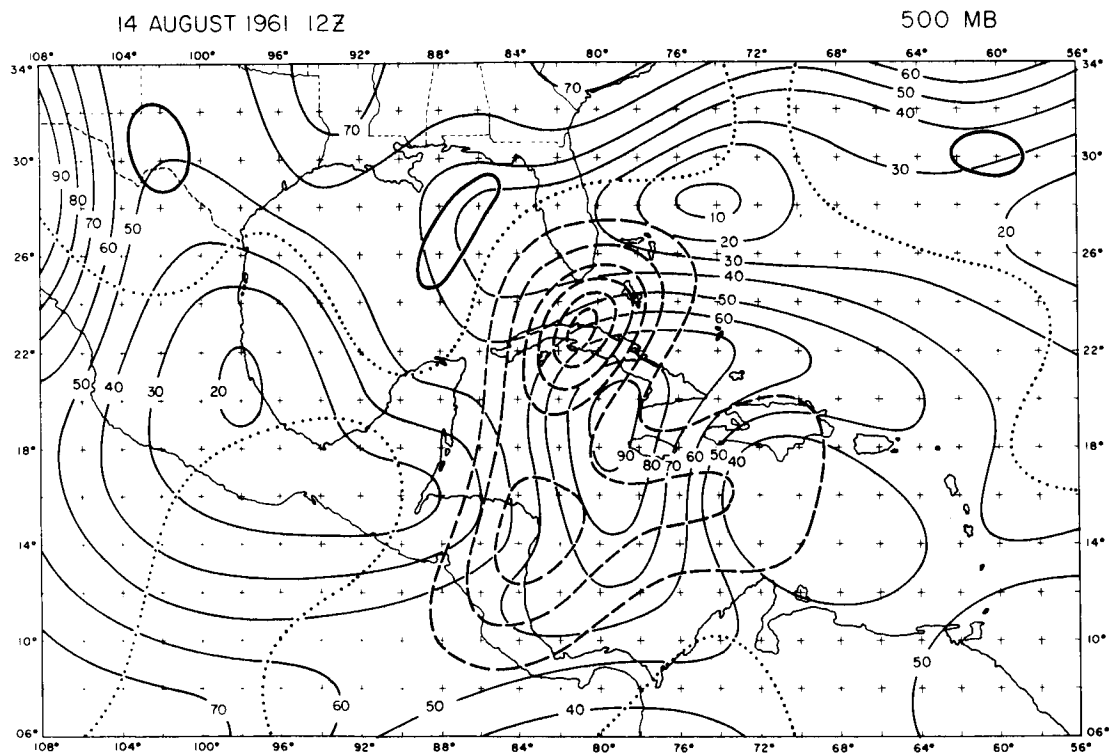
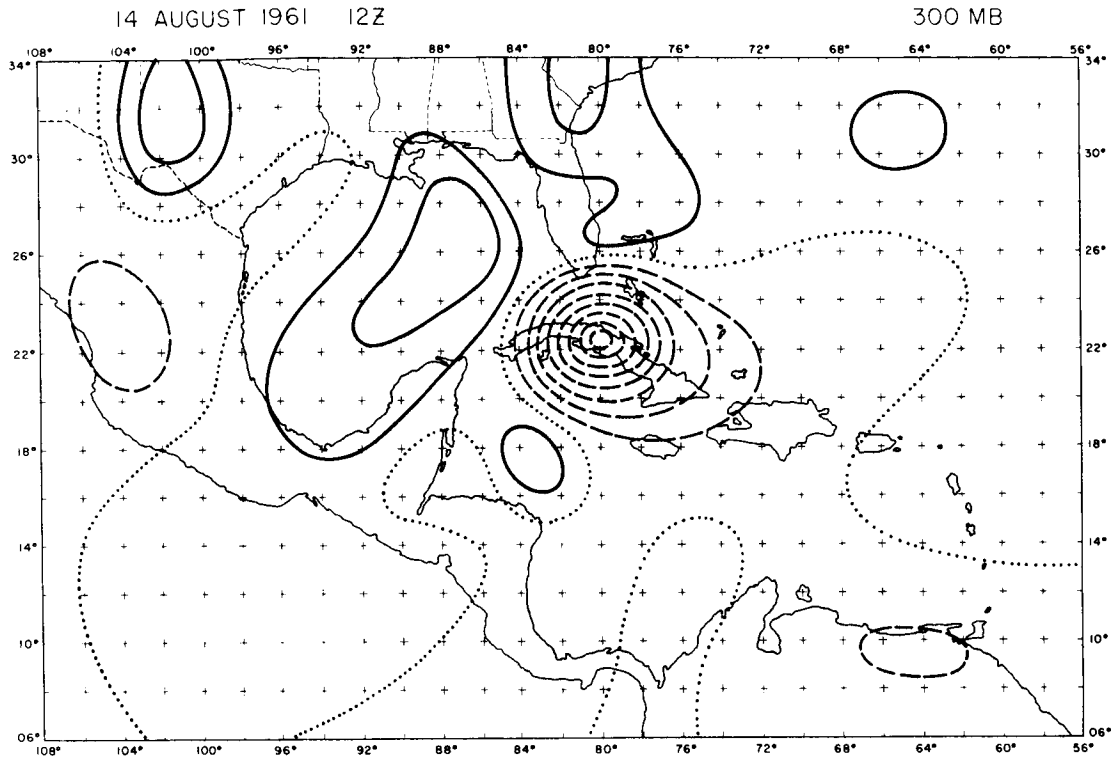


FIGURE 54A. Partitioned Vertical Motion

Heavy vector is the total, light lines are the components.

Order at each grid point from left to right: Total,
vorticity, thermal, deformation, divergence, friction,
and latent heat.

FIGURE 54B. Moisture and Cloudiness

Solid lines are relative humidity every 10 per cent.

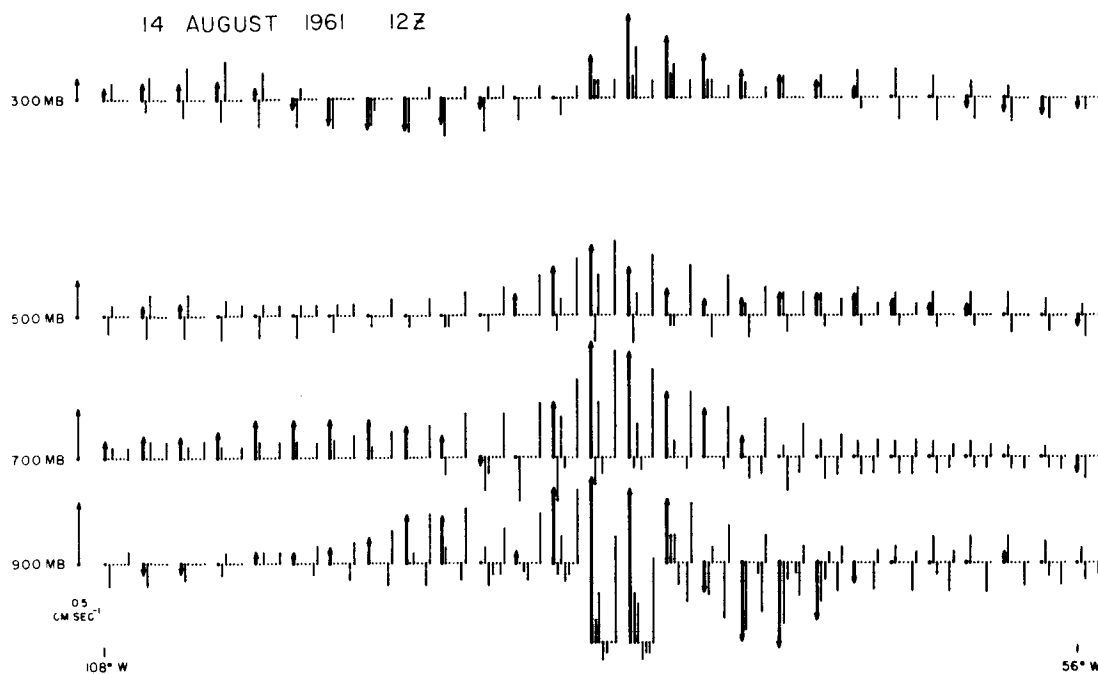
Clouds represented in schematic form.

OMEGA CROSS SECTION

14 AUGUST 1961 12Z

0 100 100 • 10³ MB SEC⁻¹

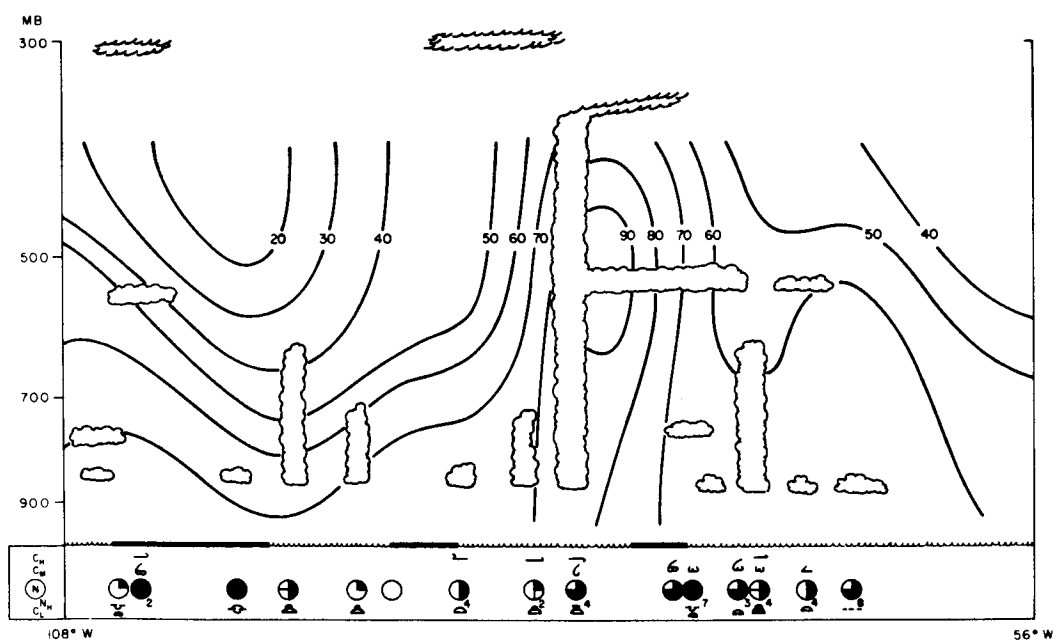
20° N



MOISTURE CROSS SECTION

14 AUGUST 1961 12Z

20° N



In Figures 52-54, the derived vertical motion is displayed. The rising center behind the easterly perturbation has continued in its dominance of the vertical motion field. The integrated moisture flux, (Figure 51) still shows strong convergence in this area, which in turn means a large component of latent heat. Figure 54, the partitioned vertical motion, verifies this conclusion with considerable spill-over of the latent heat term in evidence. The appearance of a center of strong sinking to the east of the wave at 900 mbs can be partially attributed to the increased magnitude of the frictional term. The sinking that was present ahead of the trough has now disappeared at all levels. Consulting the partitioning, the lack of downward motion in this area is not a direct result of latent heat overlap. The extremely strong rising at 300 mbs is a product of both thermal and vorticity terms acting in the same sense.

The agreement between the moisture distribution and the vertical motion has improved at this map-time. The correlation at 900 mbs, in particular, is quite striking. The cross-section vertical motion also verifies the moisture relationship, however, the lower humidities associated with the sinking air behind the wave do not appear on the cross-section. The entire moisture surge has translated toward the west with the corresponding movement of the trough. The drier air ahead of the wave has become more moist, possibly due to the change in sign of the vertical motion in the region. The correlation between the area of disturbed weather and the intense rising motion is very encouraging even though the latent heat parameterization is not properly handled.

C. Trajectory Calculations

The previous case study provides a complete three-dimensional velocity field for a period of approximately 50 hours, which may be used to compute trajectories. Instead of the usual graphical trajectory method, a sophisticated computer program was designed to evaluate the movement of the atmosphere. The program marches backward in short increments from the final map-time, linearly interpolating the wind distribution and vertical motion from the original grid. The advective time-step was chosen to be a 2 hour interval, maintaining very high resolution. This method does not include any approximations, such as the adiabatic condition; it merely uses the calculated velocity fields in the X, Y, P coordinate system for advection. If the derived three-dimensional structure of the atmosphere is considered accurate, then the resulting trajectories from this method can be quite reliable.

The trajectory computation was performed at each grid point for the 800, 600, and 400 mb levels. Figures 55-57 show a randomly selected group of these calculations. The end point (arrowhead) is always at the pressure level indicated on the illustrations. The backward movement takes the parcel of air either below or above the final pressure surface. The pressure, during the extrapolation, is given at maxima or minima and the starting location. The vertical sense of the trajectory is revealed by dotted lines in rising air and solid lines in sinking.

FIGURE 55. Trajectory Calculations

Arrowhead indicates end-point, X indicates starting point, and crosses are positions at synoptic map-times. Solid line means sinking, dotted line means rising. Numbers are pressure at starting point, maximum and minimum.

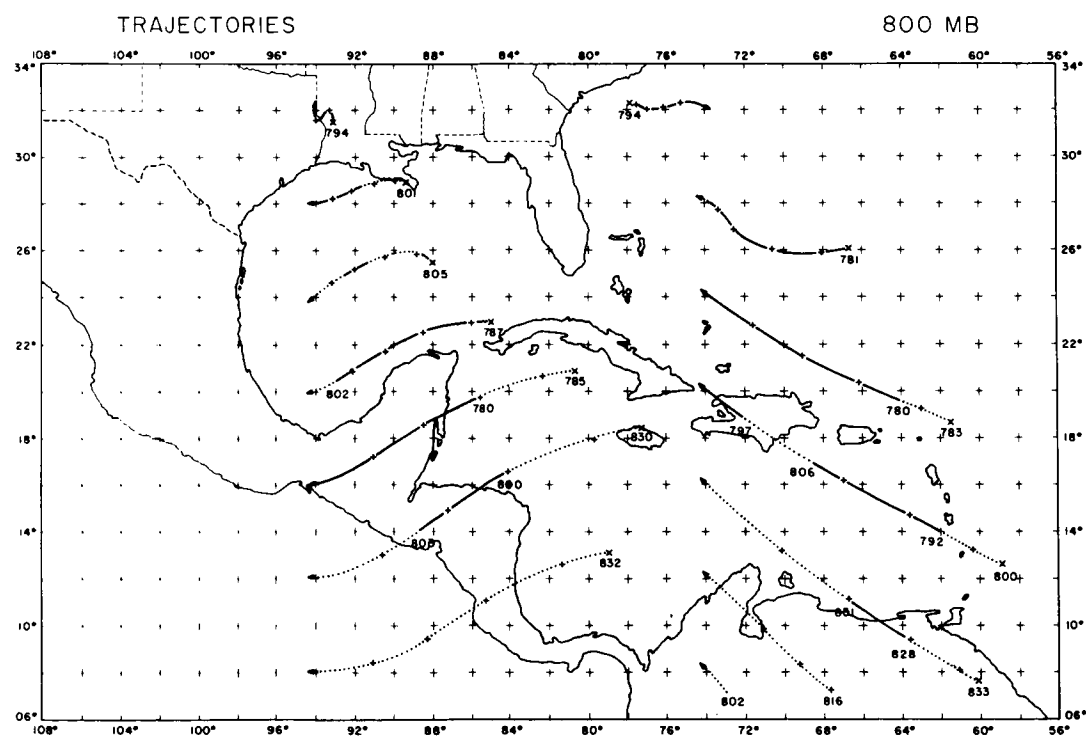
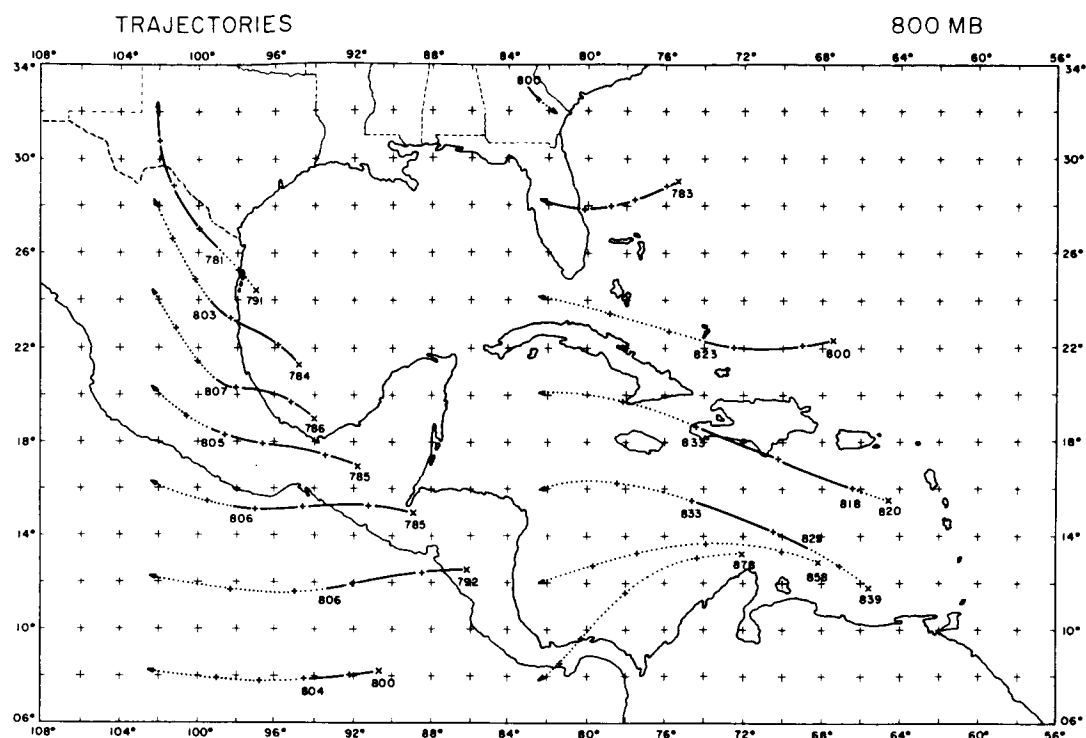


FIGURE 56. Trajectory Calculations

Arrowhead indicates end-point, X indicates starting point, and crosses are positions at synoptic map-times. Solid line means sinking, dotted line means rising. Numbers are pressure at starting point, maximum, and minimum.

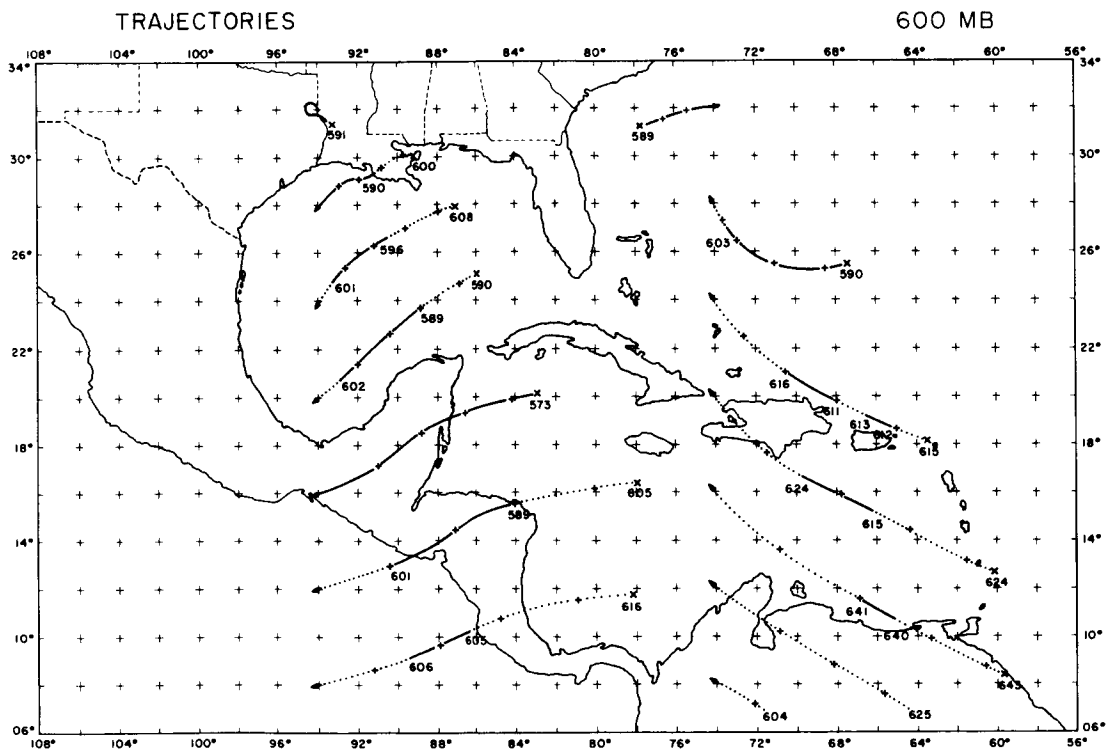
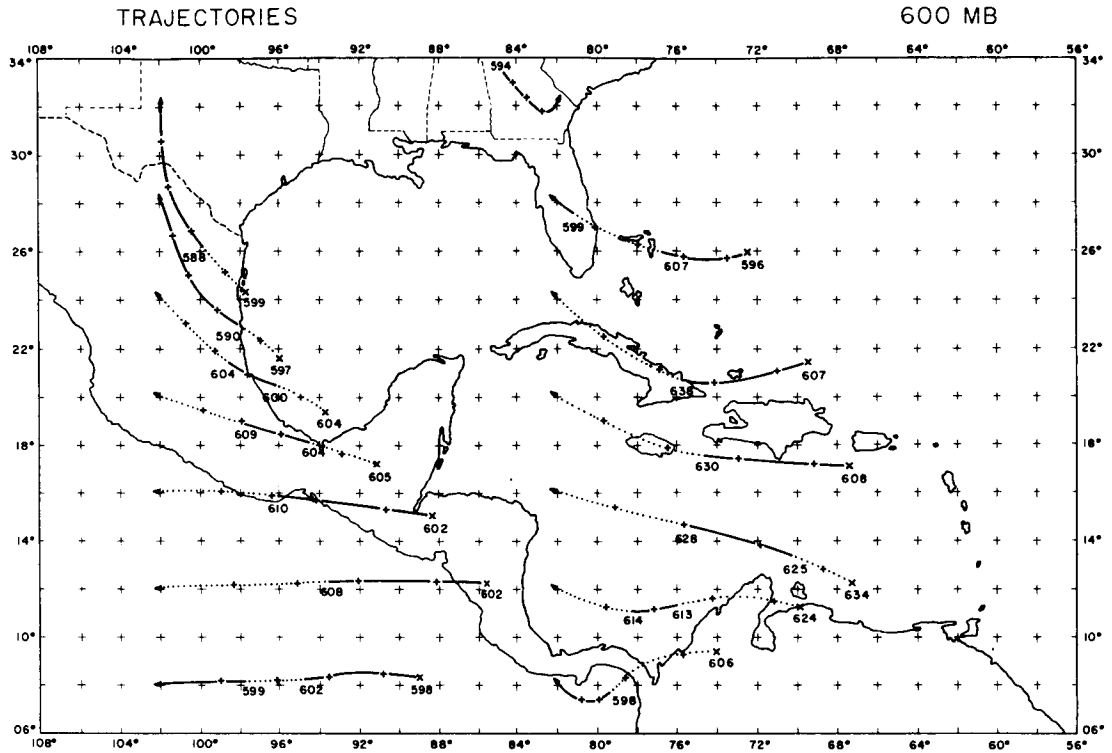
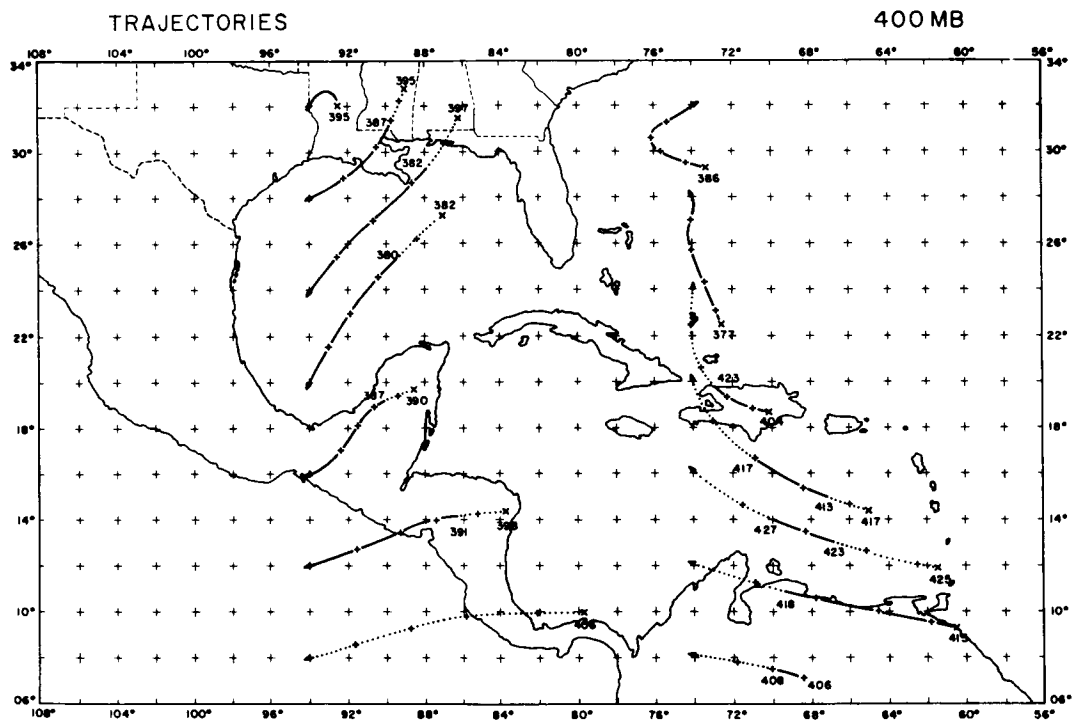
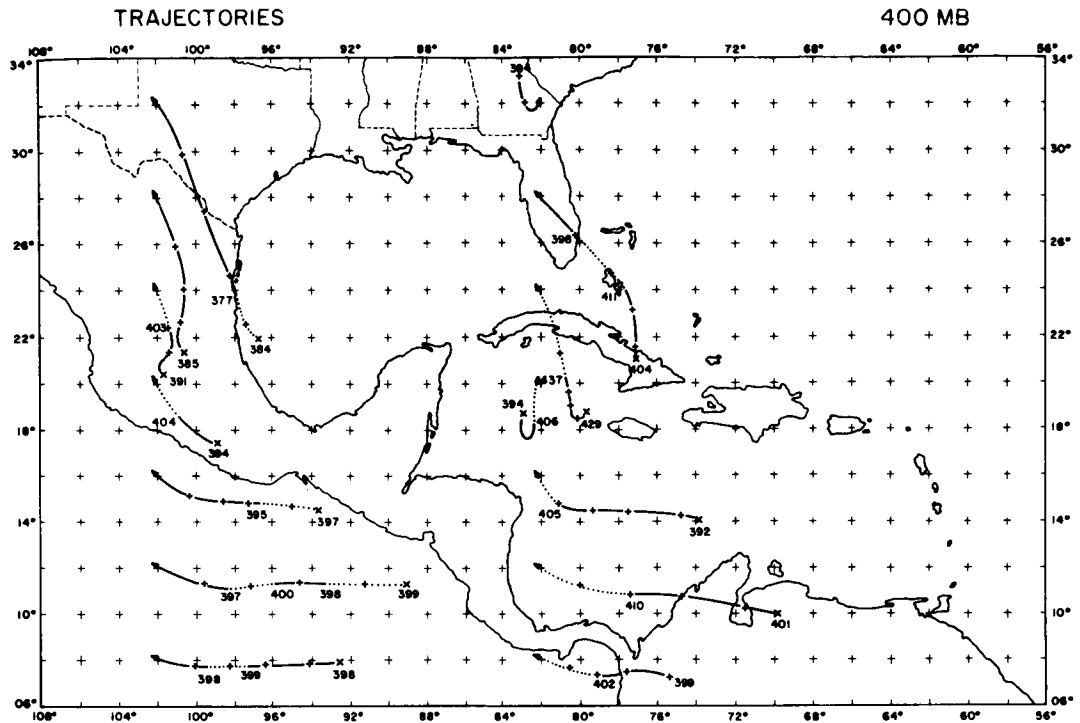


FIGURE 57. Trajectory Calculations

Arrowhead indicates end-point, X indicates starting point, and crosses are positions at synoptic map-times.

Solid line means sinking, dotted line means rising.

Numbers are pressure at starting point, maximum, and minimum.



The basic easterly flow of the tropics with meridional perturbations is in evidence, when the selected trajectories are examined. The average distance the air has moved appears to be about 15° of longitude in the majority of the cases. This is much shorter than typically found in the mid-latitudes which points out the relative slowness of the wind speeds in the tropics. The meridional translation is quite remarkable, with many trajectories crossing 10 degrees of latitude in 50 hours. If a wave in the easterly flow moves to the west with the speed of the wind, then large meridional motion can be expected as seen by the trajectories.

The feebleness of the tropical vertical motion, when compared to extratropical systems, can be seen by observing the starting point pressure. In most cases, the difference is less than 20 mbs. However, several trajectories at 800 mbs indicate rising of 50–75 mbs when the parcel undergoes continuous upward motion throughout the 50 hours. The sinking trajectories do not show as much vertical amplitude as the rising trajectories, which can be explained by the very strong rising center prevalent throughout the latter part of the case study.

The most common objection to the numerical results in the tropics is the fact that the derived vertical motions on the synoptic-scale are too small to have any effect on the weather. This is a valid argument outside the influence of any large-scale circulation in the tropics. The meso- and micro-scale weather systems overwhelm any effects produced by the weak rising

or sinking. However, in a large disturbance, such as a traveling perturbation in the easterlies, the air remains under the influence of the wave for a considerable length of time. The dynamical rising and sinking created by synoptic-scale systems may operate on a parcel of air for 50 to 100 hours or longer, depending on the ventilation of the storm. In the middle latitudes this does not usually occur since the airflow is much more rapid through a particular disturbance.

During the case-study just presented, a large mass of air behind the easterly wave was lifted approximately 50 mbs in 24 hours. If this were to take place over a longer time period, the dynamical vertical motion has the capability of saturating air of 60 per cent relative humidity. Since most of the weather in the tropics is convective in nature, the dynamical rising and sinking merely increases the probability of thunderstorms by raising the relative humidity of the air. An increase from 60 to 80 per cent relative humidity can augment the convective activity considerably. It is the author's contention that the synoptic-scale vertical motion in the tropics can and does influence the convective activity to a large extent by the method previously noted.

D. Concluding Remarks

The application of a diagnostic numerical model to the tropics has, indeed, been very gratifying when the results are considered. However, numerous problems still exist, some of which have been discussed in this paper.

The appropriate choice of a stream function and temperature analysis along with the initial data preparation influence the product of the model to a great extent. The inclusion of latent heat and friction altered the vertical motion fields considerably, proving that these effects are very important in the tropics. Some problems in the parameterization of latent heat of the form presented were apparent in the solutions, however, the results did point out the possible magnitude (1.0–2.0 centimeters per second) the latent heating term may obtain. The possibilities for future research on this topic are very impressive and may lead to the key of tropical storm formation energetics.

The formulation of the non-linear balanced model appeared to be quite adequate for use in the tropics. In fact, it appears to have several advantages over the older, kinematic method of computing vertical motions. It became obvious, when the partitioning was performed, that certain terms in the omega equation were very small and could be neglected in future work. When the model was applied to a particular case study, a fairly good correlation was discovered between the calculated vertical motion and the observed moisture distribution. This fact gives insight on the reliability of the modeling results as well as the effects of the synoptic-scale vertical motion on the tropical weather.

Because of the weak magnitude of the omega fields presented, their contribution to the development of the tropical disturbances and associated moisture surges appear to be obscure. A longer time-scale of influence is

necessary for the dynamical product to operate. As observed from the computed trajectories, this is indeed the case with individual parcels of air remaining under the effect of one system and its associated vertical motion. The dynamical result acts to enhance the meso-scale convective activity of such disturbances by slowly increasing the relative humidity of a large mass of air.

Since it is not a valid procedure to extract too many conclusions from only one case-study, many more such experiments should be performed to verify these conclusions. The answers to a great number of questions may be revealed by a systematic dissection of all the major types of weather disturbances in the tropics using the numerical approach. The problem of prediction with numerical techniques can also be advanced by submitting as the initial state, the results of an accurate diagnostic model.

This research could not have been undertaken without the guidance of Dr. Krishnamurti, who provided the author with the theoretical support, original computer programs, and many useful discussions. The help of Jan Paegle, who helped code many complicated machine programs and the accurate plotting and tabulating of Steve Esbensen and Mirek Borowski is acknowledged. This entire work was performed with free computer time donated by the Computing Facility at UCLA.

REFERENCES

- Charney, J. G., 1962: Integrations of the Primitive and Balance Equations. Proceedings of the International Symposium on Numerical Weather Prediction, Tokyo, The Meteorological Society of Japan. 131-152.
- Charney, J. G., 1963: A Note on Large-scale Motion in the Tropics. Journal of Atmospheric Science, Vol. 20, 607-609.
- Charney, J. G., and Eliassen, A., 1964: On the Growth of the Hurricane Depression. Journal of Atmospheric Science, Vol. 21, 68-75.
- Cressman, G. P., 1963: A Three-level Model Suitable for Daily Numerical Forecasting. Technical Memorandum No. 22, National Meteorological Center, ESSA, 32 pp.
- Danard, M. B., 1964: On the Influence of Released Latent Heat on Cyclone Development. Journal of Applied Meteorology, Vol. 3, 27-37.
- Hawkins, H. F., and Rosenthal, S. L., 1965: On the Computation of Stream Functions from the Wind Field. Monthly Weather Review, Vol. 93, No. 4, 245-252.
- Holl, M. and collaborators, 1965: A Multi-layer Mass-structure Model of the Atmosphere. Scientific Report, Meteorology International, Monterey, California, 16 pp.
- Krishnamurti, T. N. and Baumhefner, D. P., 1966: Structure of a Tropical Disturbance Based on Solutions of a Multi-level Baroclinic Model, Journal of Applied Meteorology, Vol. 5, 396-406.
- Krishnamurti, T. N., Nogues, J., and Baumhefner, D. P., 1966: On the Partitioning of the Baroclinic Vertical Motions in a Developing Wave Cyclone. Scientific Report. (AFCRL 66-419), Air Force Cambridge Research Laboratories, Bedford, Massachusetts, 59 pp.
- Kuo, H. L., 1965: On the Formation and Intensification of Tropical Cyclones through Latent Heat Release by Cumulus Convection. Journal of Atmospheric Sciences, Vol. 22, 40-63.

REFERENCES (Continued)

- Miyakoda, K., 1963: Some Characteristic Features of Winter-time Circulations in the Troposphere and Lower Stratosphere. Technical Report No. 14, Dept. of Geophysical Science, University of Chicago, 84 pp.
- Petterssen, S., 1956: Weather Analysis and Forecasting, Vol. 1, pp. 292-299. The McGraw-Hill Book Co., New York.
- Petterssen, S., Bradbury, D. L., and Pedersen, K., 1961: Heat Exchange and Cyclone Development on the North Atlantic Ocean. Technical Report, AF Grant Number AF 19(604)-7230, University of Chicago.
- Riehl, H., and Malkus, J. S., 1958: On the Heat Balance in the Equatorial Trough Zone. Geophysica, Vol. 6, 503-525.
- Shuman, F. G., 1957: Numerical Methods in Weather Prediction--The Balance Equation. Monthly Weather Review, Vol. 85, No. 10, 329-332.
- Thompson, P. D., 1961: Numerical Weather Analysis and Prediction, 170 pp. The MacMillan Co., New York.
- Yanai, M., 1964: An Experimental Objective Analysis in the Tropics. Technical paper No. 62, Dept. of Atmospheric Science, Colorado State University, 36 pp.

Appendix

The equations used in the text are those discussed by Krishnamurti in Section 1.

N67 - 30789

A Study of a Developing Easterly Wave

T. N. Krishnamurti

and

Julia Nogue

Abstract

A study of wave perturbation in the low level easterly flow during September 13 and 14, 1961 is presented. The wave intensifies into a tropical storm on the 14th acquiring surface winds around 40 knots.

A comparison of this case with a non-developing case is made and some important differences are pointed out. It is suggested that quantities like net moisture convergence in vertical columns and per cent area of synoptic scale occupied by convective clouds need not give a sufficient condition of development, as they seem to do in numerical simulation studies of tropical storm.

1. Introduction

Dunn (1940) reported extensively on the westward moving easterly waves of the Atlantic Ocean. Riehl (1945) presented a number of examples to describe what is now known as an easterly wave model. The frequency of easterly wave passages over a tropical island weather station is quite large, as many as 2 waves per week is a common occurrence. Very few of these however intensify into closed vortices or tropical storms. The example of the non-developing easterly wave, Baumhefner (1966), is characterised by a basic easterly flow in the lower troposphere and a westerly flow in the upper troposphere. The basic zonal wind shear ($\frac{\partial u}{\partial z}$) is positive in the lower troposphere thus the easterly wave is a warm-core disturbance. In the upper troposphere the strong west wind lies to the south of an intense cold-core low. This easterly wave, at its final stage of development is associated with a strong anticyclonic vortex near the 200 millibar surface, the basic zonal wind shear is very small and negative in the region of interest.

An easterly wave with (i) a cold-low aloft or one with (ii) a warm core high aloft are frequent occurrences in the tropics. Baumhefner (1966) investigated an example of (i) that has maximum surface winds around 20 knots. The proposed study here starts out as a case of example (i) but during the later stages its characteristics pertain to example (ii) this system attains tropical storm stage, winds > 40 knots. Neither of these examples reach a hurricane strength.

The motivation of this study has been to study these two examples of easterly waves and see if analysis of fields such as, moisture, vertical motions, three dimensional trajectories, moisture convergence and per cent area covered by convective clouds might reveal some major differences. An interpretation of such differences may be expected to reveal some aspects of tropical dynamics that are hard to see from a visual examination of stream lines, moisture and temperature maps.

2. The developing easterly wave

In order to portray the synoptic history of the developing wave it might be desirable to present detailed analysis of all of the input fields for several map times. This would amount to a large number of drawings, and besides several output fields will have to be portrayed in order to complete a description of the development. We have combined some of the analysis of input fields with some of the computed fields together in same charts to complete a description.

Figures 1,2,3 and 4 show the isotherms (continuous lines) and the wind vectors of the complete balanced wind ($V_y + V_x$) (superimposed) for the 200, 400 and the 1,000 millibar surfaces. We selected these levels to show the upper, middle and lower tropospheric thermal and the flow fields. The following points must be noted in the description.

- i) Our main interest is in a wave located near 75-80°W longitude and 25-30°N latitude.

ii) Four map times of interest are,

September 12, 12Z 1961

September 13, 00Z 1961

September 13, 12Z 1961

September 14, 00Z 1961.

iii) On September 12, 12Z surface maximum wind reports in the region of interest were close to 15 knots (on a synoptic scale). By the 14th of September wind speeds had increased to 40 knots as reported by several ships. A tropical storm of moderate intensity had formed from a weak low level easterly wave.

iv) Somewhat distracting, nevertheless quite pertinent to the study, is another fully developed mature tropical storm that was present over the northern part of the Gulf of Mexico during the period of interest. This is hurricane Carla of 1961. We were not primarily interested in this storm because the balanced dynamics would be inadequate to describe the features of this storm, (Rossby number > 1). Because of the close proximity of the two disturbances we will make frequent reference to Hurricane Carla and discuss some aspects of the thermal and flow fields that are part of this hurricane and whose influence is felt as far away as the developing easterly wave.

3. Thermal and motion fields during the four map times

(Refer to Figures 1, 2, 3 and 4)

1000 mb. The wave perturbation has a cold core during the first 24 hour

period, temperatures are approximately around 22°C and the axis of this cold core is oriented north west – south east during this period. At the last map time the region close to the tropical storm (78°W , 32°N) experiences intense warm air advection from the south and a warm core is distinctly present in the synoptic scale analysis. This portrays the formation of a warm core disturbance during the last 12 hours.

Middle and upper troposphere

At the 400 and the 200 millibar surfaces over the western parts of the Gulf of Mexico and inland over Mexico and Texas a warm core is present. This warm core is a part of the thermal structure of hurricane Carla. The gradual northward movement of the warm air (and the hurricane) is evident in the temperature analysis during the four map times. The temperature field over the Florida peninsula and over Cuba is of considerable interest for this study, especially over the middle and upper troposphere.

A strong cold core low pressure system is present over the eastern tip of Cuban Island on September 12, 12Z which moves northward and appears to warm up considerably and disappears during the 36 hours. At the initial map time the cold low at the 200 mb surface lies over the wave perturbation of the low-level easterlies. In the tropics lower and upper tropospheric weather systems frequently move at different speeds. This appears to be the case here. In the next 36 hours we notice a gradual northwestward movement of the upper low and a slower northward movement of the lower level system. This differential

movement is an important synoptic feature of this case study. During the last map time at 200 mbs a high pressure system, with strong southerly winds over the Florida peninsula, overlies the tropical storm. This feature was investigated by Frank (1963), he postulated that the high pressure system was produced by intense convection. His plausible argument may be restated as follows:

Intense convection over a wide region warms up the air on a synoptic scale thus raising the 200 millibar surface and lowering the heights of the pressure surfaces of the lower troposphere. The synoptic scale rising motions exhibit attendant divergence at upper levels and convergence at lower levels. The intensity of the divergence is strong enough to produce anticyclonic relative vorticity at higher levels and the low level convergence being important for the development of the tropical storm.

The high level anticyclone is located near 30°N where the coriolis parameter $f \approx 7.3 \times 10^{-5} \text{ sec}^{-1}$. The flow field in this region changes from weak cyclonic flow to a weak anticyclonic flow, relative vorticity changes from about $2 \times 10^{-5} \text{ sec}^{-1}$ to about $-2 \times 10^{-5} \text{ sec}^{-1}$, a very small but obviously an important change for tropical dynamics. The wind direction (curvature of flow) changes from cyclonic to anticyclonic, but the associated wind speeds of the large scale flow are less than 10 meters/sec as a result the total change in absolute vorticity is very small. The associated vertical motions are also very weak for synoptic scale motions, ($\approx 1/10 \text{ cm/sec}$). An organized pattern of convergence of mass into the low level developing wave and of divergence of

mass out of the high level anticyclone is present even though the intensities are rather small compared to middle latitude disturbances.

Convection on a synoptic scale is frequently observed in tropical disturbances, but intensification of tropical disturbances is a rarity. A cold core low in the upper troposphere and a wave in the easterly flow in the lower troposphere was present in the non-developing case study discussed by Baumhefner (1966). There was intense convection as evidenced by aircraft reconnaissance flights. There were evidently other important differences in the two cases, some of which we hope to illustrate in this study.

The 400 millibar field is similar to the 200 millibar field over most of the map during the first 24 hours. During the last map time the flow field is not well correlated with either the 200 or the 1000 millibar surfaces over the region of interest. This is not surprising because in the tropical flow fields there are generally two interesting regimes, one near the surface layer and the other near the top of the troposphere. The middle troposphere exhibits properties of lower, upper or neither systems depending on the vertical extent of the disturbances.

Wind speeds are indicated by lengths of the arrows. A northerly jet stream with speeds > 50 knots exists over the Gulf of Mexico at the 200 millibar surface during the 36 hour period. There is a narrow region of cyclonic outflow over hurricane Carla at the 200 millibar surface, outside this region the outflow region is anticyclonic. This jet stream is on the east side of this vigorous anticyclonic outflow. A feature very similar to conditions reported by

Riehl and Gentry (1958) over tropical storm Freida. A strong southerly current (>20 knots) prevails over the Gulf of Mexico at the 1000 millibar surface. Over the developing wave system wind speeds in the southwesterly flow behind the moving wave are considerably stronger than ahead of the wave. Wind speeds attain magnitudes close to 40 knots at the last map time in the southerly flow.

4. Vertical motion, relative humidity and net moisture convergence.

(Refer to Figures 5,6,7 and 8)

The top chart in Figures 5,6,7 and 8 depicts distribution of vertical motion (heavy lines) in units of 10^{-5} millibars/sec at the 900 mb surface. The dotted lines ($\omega = 0$) separate rising and sinking regions. The thin solid lines are isolines of percentage relative humidity. The latter were obtained directly from the observations. Over the northwestern part of the Gulf large rising and sinking motions over hurricane Carla attain magnitudes greater than 100 units. Over the developing wave largest vertical motions attain magnitudes close to -100 units on the 13th at 12Z, however at the last map time when the storm has the strongest surface winds maximum vertical motions are only around -50 units.

In the middle troposphere (500 mb) vertical motions over the developing wave are very weak, intensities are less than 50×10^{-5} mb/sec. Patterns of moisture on the large scale are not very well correlated with vertical motion.

The field of moisture convergence I appears at the bottom of Figures 5,6,7 and 8 for the four map times. Here I is defined by the relation,

$$I = \frac{1}{g} \int_{p_B}^{p_T} \nabla \cdot g \mathbf{v} dp - \frac{\omega g_B}{g}$$

where B refers to the top of the friction layer, p_B is the pressure at the top of the friction layer and p_T the pressure at the top of the troposphere. q is the specific humidity, \mathbf{v} is the horizontal velocity vector = sum of divergent and rotational part, ω is the vertical velocity and g is the acceleration of gravity. Here the units of I are $\text{mb meter}^{-1} \text{ sec}$. Typical magnitudes of I are

$$100 \times 10^{-8} \text{ mb meter}^{-1} \text{ sec},$$

hence we have selected $10^{-8} \text{ mb meter}^{-1} \text{ sec}$ (see as a unit our analysis of maps in Figures 5,6,7 and 8).

In the region of interest, the developing wave, values of I increase from 25 to 75 units during the first three map times. Convection was quite intense in the region where $I > 50$ units. Frank (1963) has shown the Tiros cloud cover for this developing wave. At the final map time when the surface low is most intense the I field is very weak. It may be noted that during the period when the surface winds were increasing moisture convergence I was also increasing, when surface winds reach a maximum speed I had already started to decrease. This might account for the observation that the tropical storm weakened after the 14th and no hurricane strength winds developed out of this system.

5. Three dimensional trajectories

These trajectories were constructed to study conservative and non-conservative properties along paths that lead to the developing wave. From the balanced solution of u , v , and ω fields for four map times trajectories were constructed. Computational aspects of the trajectory program are discussed by Paegle (1966).

Figures (9, 10) show the trajectories leading to grid points at 800, 600, 400 and the 200 millibar surfaces. The 6 hourly positions of a parcel is marked by a cross; these are 42 hour trajectories. An arrow at the end of the trajectory marks the direction of motion of the parcel. Beside each cross the specific humidity, pressure, potential temperature and the absolute vorticity of the parcel are labeled.

Both horizontal and vertical motions of the large scale flow were very small in this example. The horizontal motion of the parcel in 42 hours is only 500 kms. (\approx 300 miles), vertical motion of the parcel during this period is less than 100 millibars. On large synoptic scale, the convergence of mass and moisture were considerably smaller than for the non-developing case discussed by Baumhefner (1966). Specific humidity decreases slightly (0.9 gm/kgm to 0.6 gm/kgm) along a trajectory that leads to 800 millibar surface (and towards the storm center), there is a one degree warming of the potential temperature. A one degree warming over distances of 500 km in tropics is a typical numerical estimate for large scale flows. Changes in potential temperature $\Delta \theta$ along

trajectories are related ^{theoretically} to changes in specific humidity Δq by the approximate relation,

$$\Delta \theta = - \frac{L}{C_p (p/p_0)^{R/C_p}} \Delta q$$

where L is latent heat of vaporization, C_p is specific heat of air, p is pressure, p_0 is a standard pressure = 1000 mb, and R is the gas constant.

Near the 1000 millibar surface, for $\Delta q = 0.4 \text{ gm/kgm}$, $\Delta \theta \approx 1^\circ\text{C}$.

The changes correspond to what is observed for large scale motions. On the cumulus scale these changes would be considerably larger. Trajectories leading to the 1000 mb surface are not constructed, because of boundary extrapolation problems. $\omega = 0$ is a lower boundary condition and these trajectories do not leave the lower boundary as a result. In the real atmosphere turbulent exchange of mass in the surface boundary layer produces a vertical mixing of air. This is parameterized in terms of surface stresses in our general balance model; hence these trajectories in the lowest layers, where frictional and other transfer processes are dominant, is not very meaningful.

Trajectories leading to the developing wave at the 800 and 600 millibar surfaces show very slight indication of development. From similar studies of trajectories leading to centers of developing wave cyclones in middle latitudes we were able to infer various mechanisms that were operating and contributed to development.

The results in the present study are somewhat disappointing when we draw a parallel with the middle latitude analog. Vorticity changes are very small, the intense low level development was on a small scale; only a few synoptic scale

grid points record the information of low level cyclone development. A calculation of a trajectory, leading to the region of the developing wave, at the 200 millibar surface also reveals quasi-barotropic conditions. The largest anticyclonic absolute vorticity of the high level anticyclone is of the order $0.4 \times 10^{-4} \text{ sec}^{-1}$, which as we pointed out earlier is a small change in wind speed with large changes in the wind direction.

6. Partitioning of vertical motions

Vertical motions for the last time, when the surface winds exceed 30 knots in the developing wave, is portrayed for a north-south vertical cross-section, Figure 11.

In this vertical cross-section the heavy dark arrow represents total vertical velocity, at each grid point. The grid points are located at 2° latitude by 200 millibars in this plane. At each grid point four other vertical lines are indicated. They represent the computed components of vertical motion, from left to right they are,

- i) Total
- ii) Vorticity contribution
- iii) Thermal contribution
- iv) Frictional contribution
- v) Latent heat

If a line is not indicated then the correspond magnitude of the vertical motion is $< 3 \times 10^{-5} \text{ mb/sec}$. If frictional contribution is ignored then near 30°N at

the low levels (900 and 700 mbs) the net vertical motion would give negligible vertical motions and at the upper levels there would be rising motions. Large frictional convergence at 900 millibars gives a rising contribution. The frictional contribution damps rapidly with height. Latent heat contribution in this storm were generally very small. In the upper level high rising motions are largely contributed by the differential vorticity advection effects. Thermal advection was very small over most of the region in this example.

Dynamical rising motion in the upper high arising from differential vorticity advection and frictional convergence at low levels appears to be important features of the partitioning of vertical motions presented here.

7. A comparison of the developing and non-developing easterly wave

In studies of tropical storms it is now generally accepted that latent heat release on the cumulus scale is the important energy source. The two scales, synoptic and cumulus are supposed to support each other during the storm development. The concept of parameterization of the small cumulus scale processes for a description of large scale phenomenon in the tropics has been proposed by several meteorologists over the past 6 years. In these studies attention has been drawn on two scales,

- i) Synoptic scale which can be resolved by a finite difference mesh of a few hundred kilometer grid distance.
- ii) Sub-grid scale phenomenon. All of these are classed as cumulus scale phenomenon.

Under this proposition the cooperation of large and small scale processes is envisaged as follows.

Large scale mass and moisture convergence accounts for a per cent of the large scale area which will be occupied by convective elements. The convective or cumulus scale elements are described by some form of a crude cloud model. These clouds grow and release latent heat which is then diffused rapidly to affect the moisture and temperature distributions of the large scale flow. The modified large scale flow determines a new per cent area distribution of convection. Moisture convergence of large scale flow in vertical columns is an important parameter in these studies.

A comparison of calculated fields of moisture convergence I and per cent area a in the developing and the non developing case do not support the proposition that just two scales support each other.

In the non-developing case both ' I ' and ' a ' are much larger than the values for the developing wave. The conclusions that can be drawn from this study are: Lack of sufficient wind and moisture data over the developing wave would give a gross smoothing of these fields and as a result the magnitudes of ' I ' and ' a ' are highly underestimated. The two case studies presented in this report were examined over the same grid net work utilizing synoptic data from about the same number of upper air stations. Data sampling was very similar in these examples. The non-developing wave had an intense trough over the Caribbean Sea where largest values of ' I ' and ' a ' were computed. The developing wave appears east of Florida peninsula which is not sufficiently

well covered with observations to the east.

While it is comforting to explain a discrepancy from lack of observation, the magnitude of the discrepancy noted here is very large and lack of data above cannot provide the reasons for development. Alternatively it is possible that the theories of parameterizations are not very sound. They perhaps lack an intermediate scale of weather phenomenon, not resolved by the existed data network. The cooperation of synoptic and cumulus scales should perhaps be invoked through a mesoscale which at times, when I is large, will not permit a hurricane to form, while at other instances where I is relatively less intense will accelerate the surface development.

Theoretically, large values of moisture convergence will always lead to a large value of ' a ' the per cent area occupied by convective clouds. A warm core is easy to establish under these circumstances, and hurricane strength winds can be realized in a numerical model. In the real atmosphere, Tiros and Nimbus picture show frequently large areas with convective clouds in the tropics but without tropical storms. Large values of ' I ' and ' a ' are thus a necessary but not sufficient condition. Boundary layer instability phenomenon, again not resolvable by the present data networks, on a mesoscale, may be important. Further work is being continued on this topic.

List of References

- Baumhefner, D., 1966. "A study of a non-developing easterly wave". Final Report to AFCRL, Department of Meteorology, University of California. AF 19(628) AFCRL-67-0128.
- Dunn, G., 1940. "Cyclogenesis in the Tropical Atlantic". Bulletin of American Meteorological Society, Vol. 21, pp. 121-146.
- Frank, N., 1963. "Synoptic case study of tropical cyclogenesis utilizing Tiros Data". Monthly Weather Review, Vol. 91, Number 8, pp. 355-366.
- Paegle, J., 1966. "Numerical calculation of three dimensional trajectories utilizing the balanced horizontal and vertical motions". Final Report to AFCRL, Department of Meteorology, University of California, Los Angeles. AF 19(628) AFCRL-67-0128.
- Riehl, H., 1945. "Waves in the easterlies and the Polar front in the tropics". Miscellaneous Report No. 17, University of Chicago, Chicago, Ill.
- Riehl, H., and C. Gentry, 1958. "Analysis of tropical storm Frieda 1954". National Hurricane Research Project Report No. 17, U.S. Weather Bureau.

Fig. 1. Vector representation of the velocity field with the temperature field. Vector length proportional to speed. (0.35 centimeters equals 10 meters per second). Temperature analyzed every 1°Centigrade.

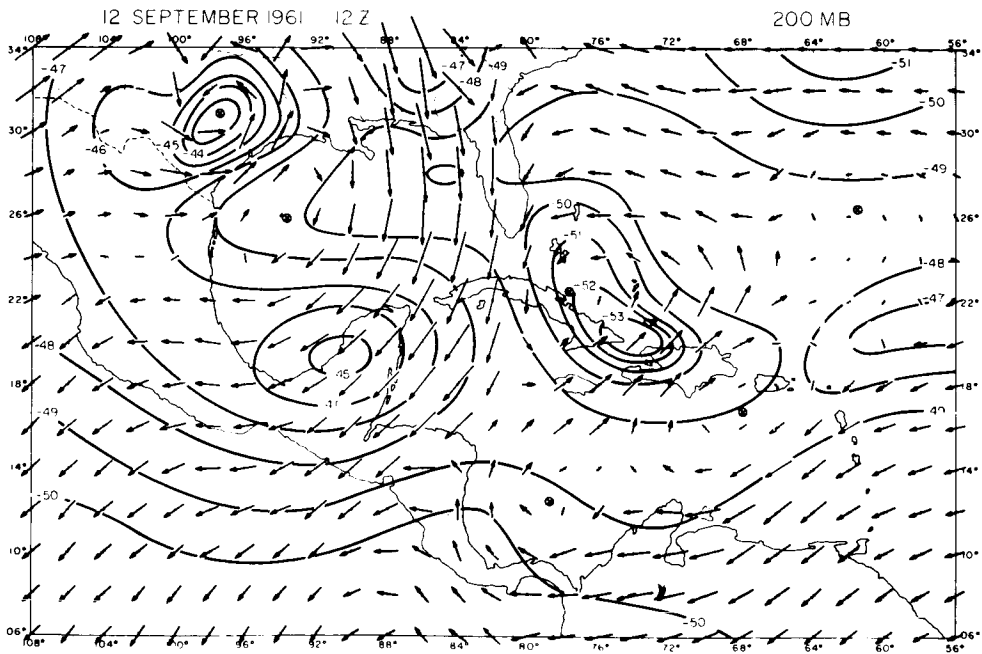
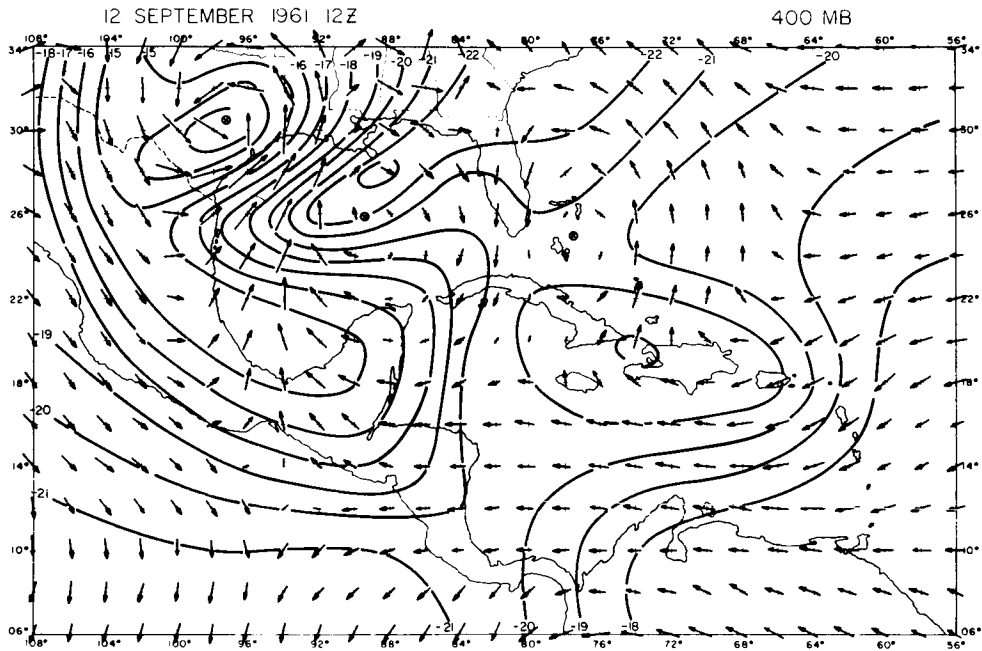
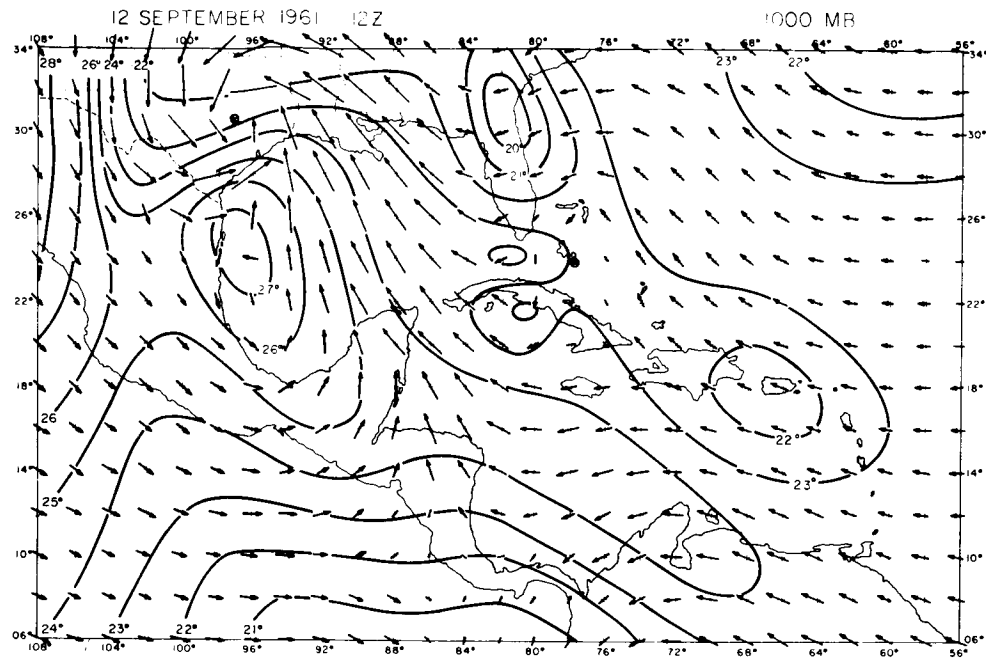


Fig. 2. Vector representation of the velocity field with the temperature field. Vector length proportional to speed. (0.35 centimeters equals 10 meters per second). Temperature analyzed every 1° Centigrade.

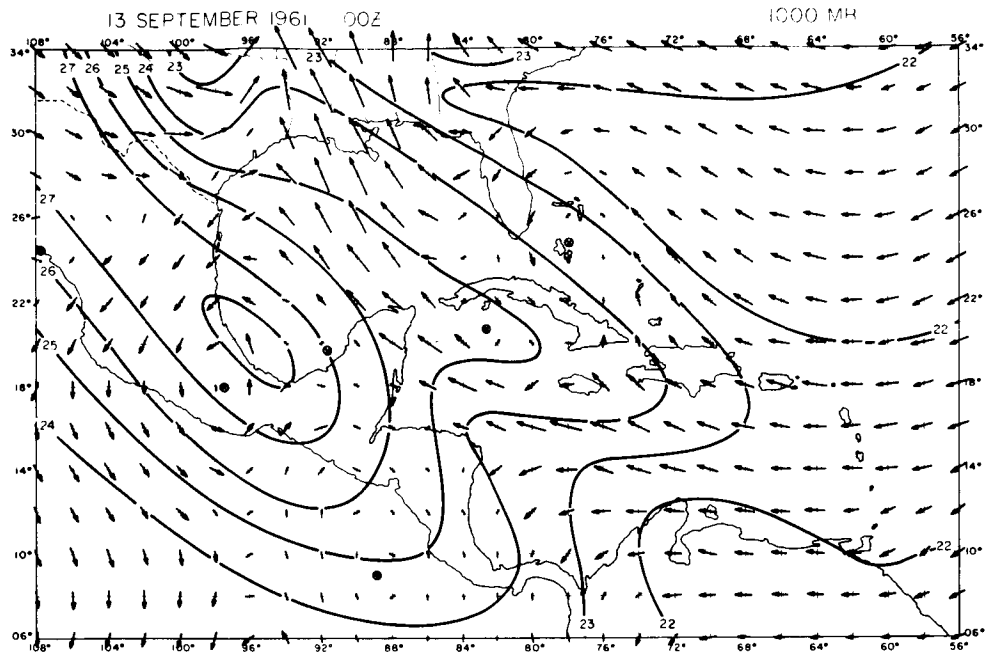


Fig. 3. Vector representation of the velocity field with the temperature field. Vector length proportional to speed. (0.35 centimeters equals 10 meters per second). Temperature analyzed every 1° Centigrade.

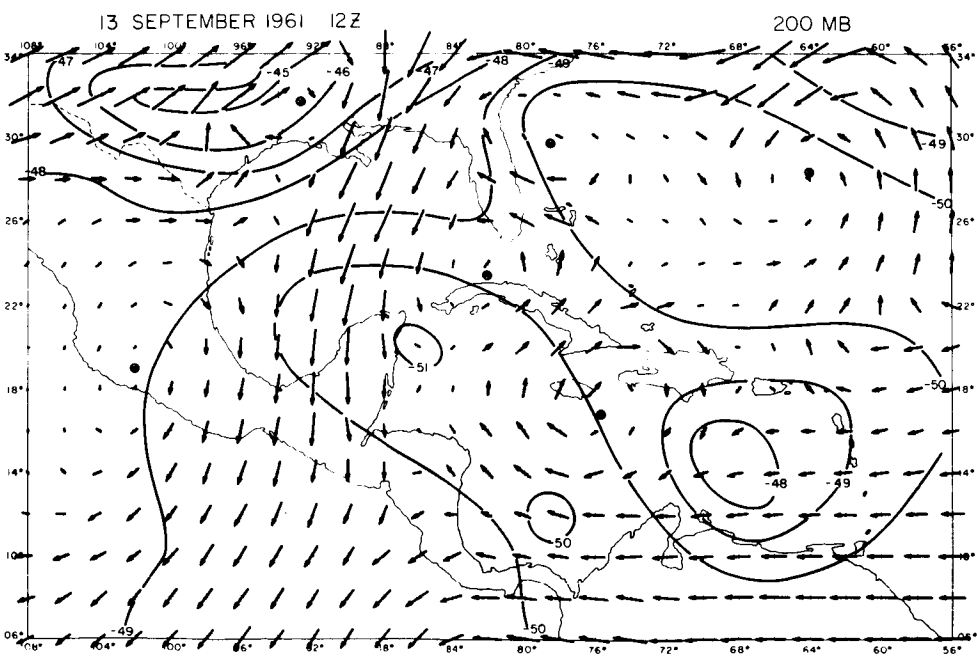
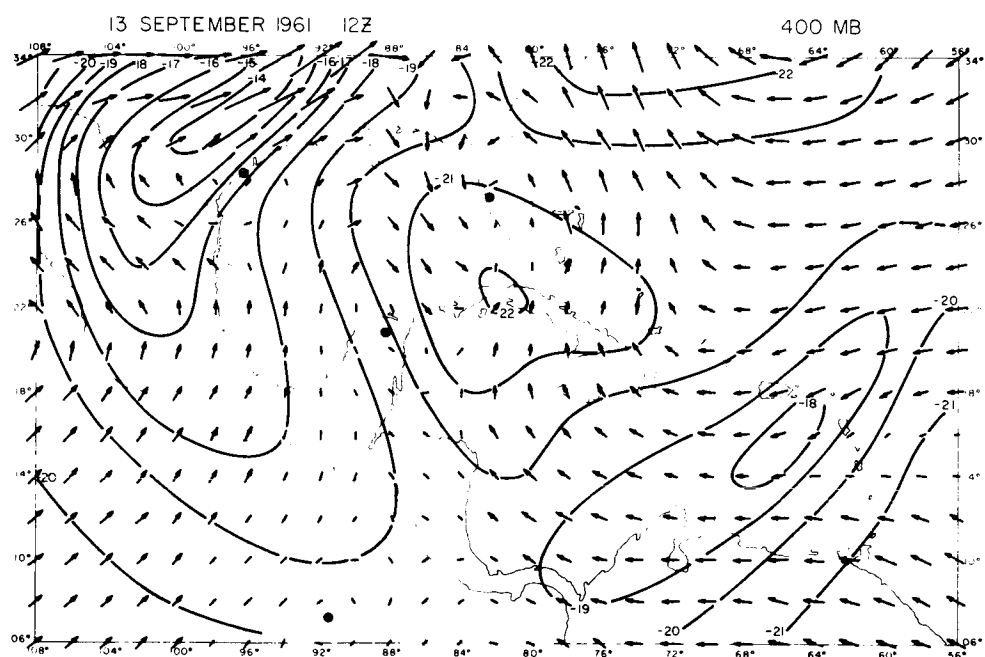
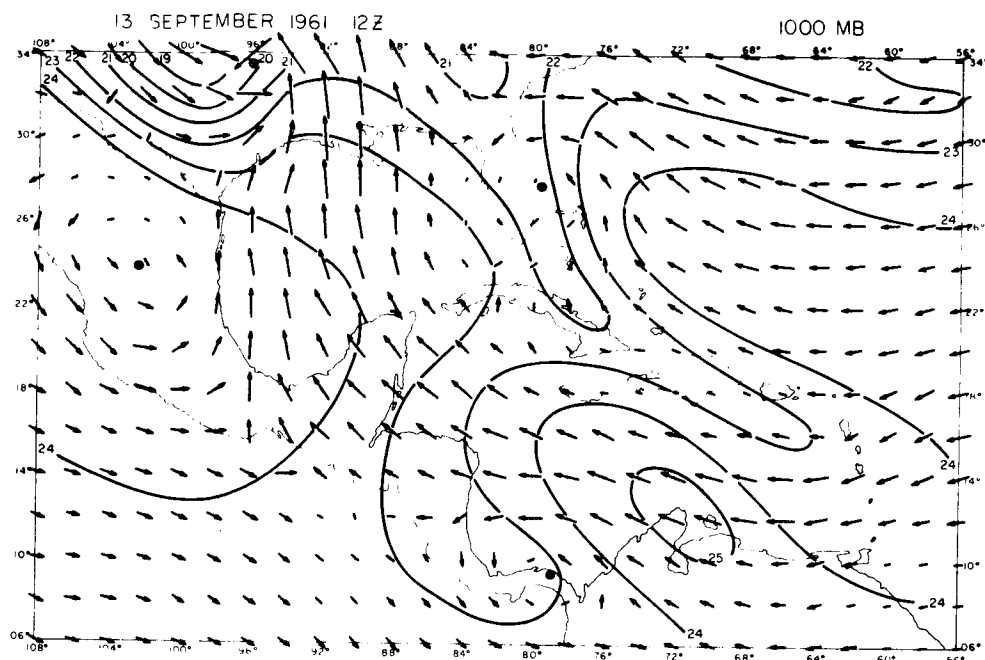


Fig. 4. Vector representation of the velocity field with the temperature field. Vector length proportional to speed. (0.35 centimeters equals 10 meters per second). Temperature analyzed every 1° Centigrade.

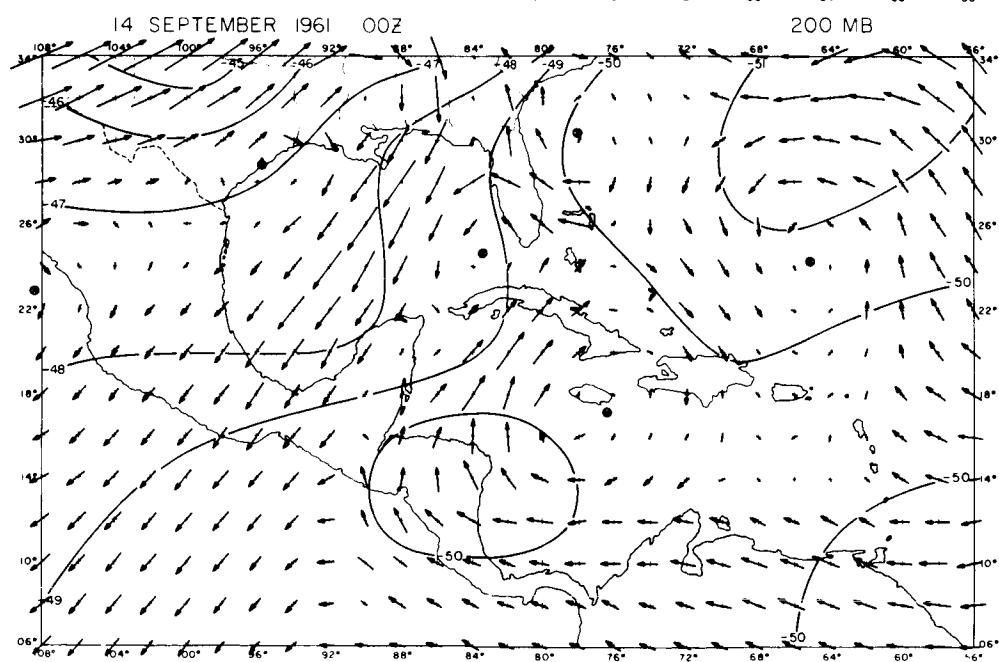
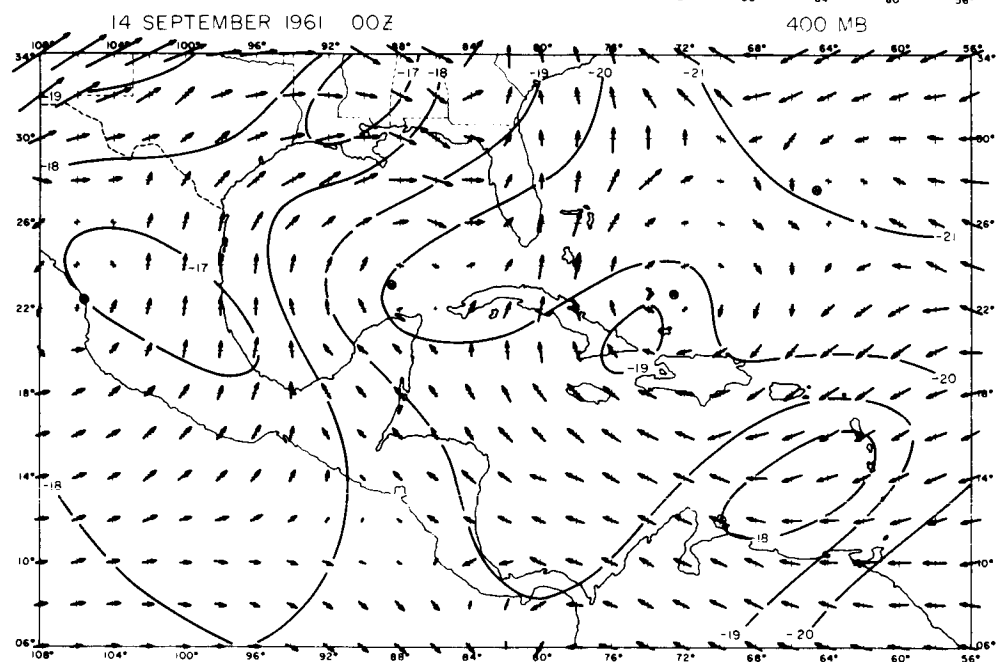
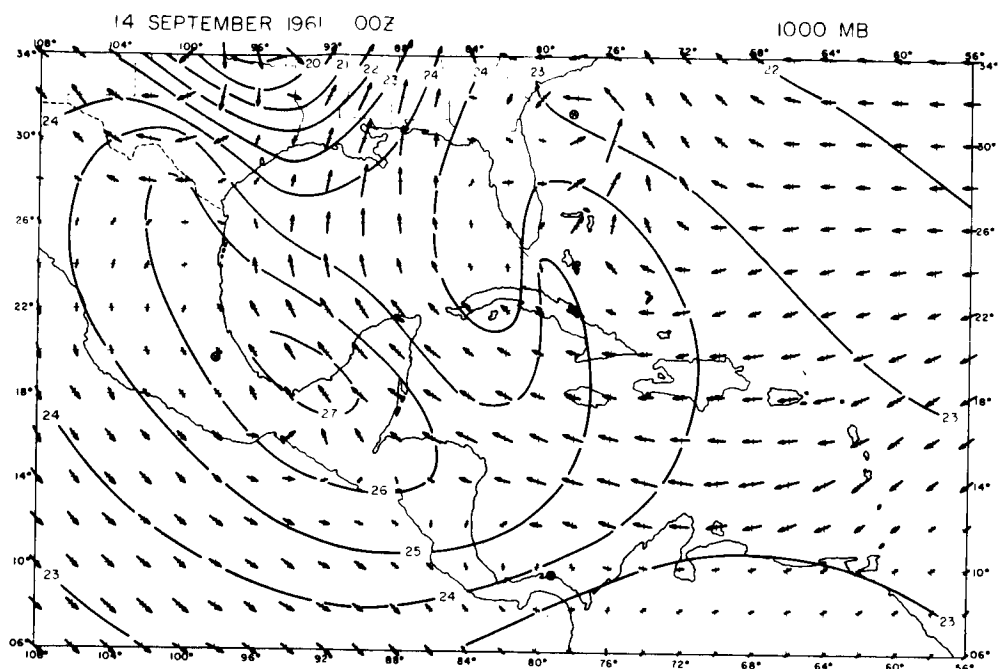


Fig. 5. Top and middle- Vertical motion with the observed relative humidity. Heavy solid lines are sinking, dotted lines are zero vertical velocity and dashed lines are rising motion. Isolines of vertical motion are $20 \times 10^{-5} \text{ mb sec}^{-1}$. Light solid lines are relative humidity analyzed every 10 per cent.

Bottom- Integrated moisture flux. Solid lines are convergence analyzed every $50 \times 10^{-8} \text{ mb sec m}^{-1}$. Dashed lines are convergence analyzed for $25 \times 10^{-8} \text{ mb sec m}^{-1}$. Dotted lines are neutral.

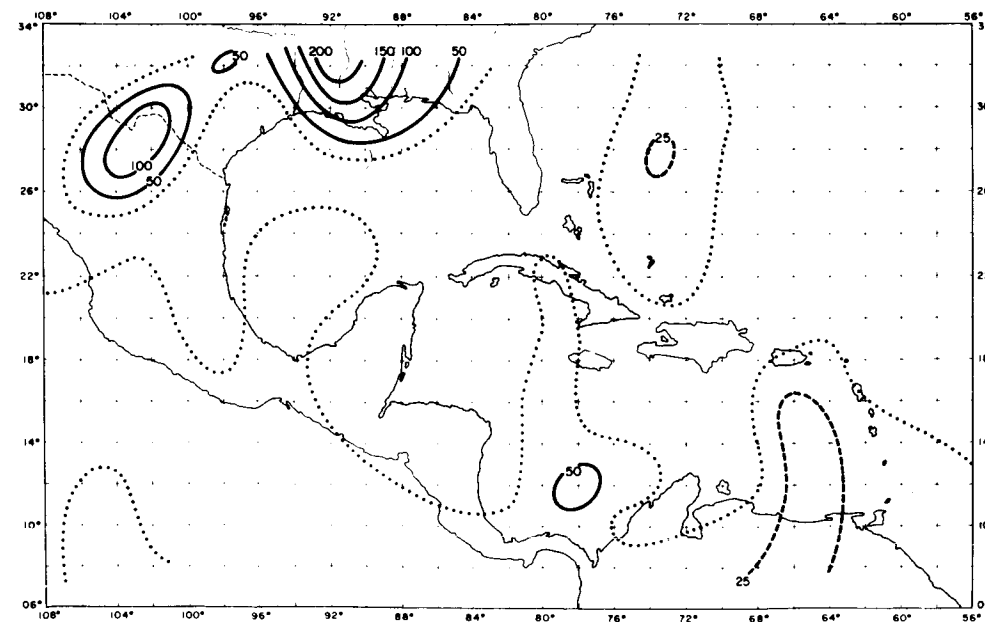
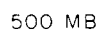


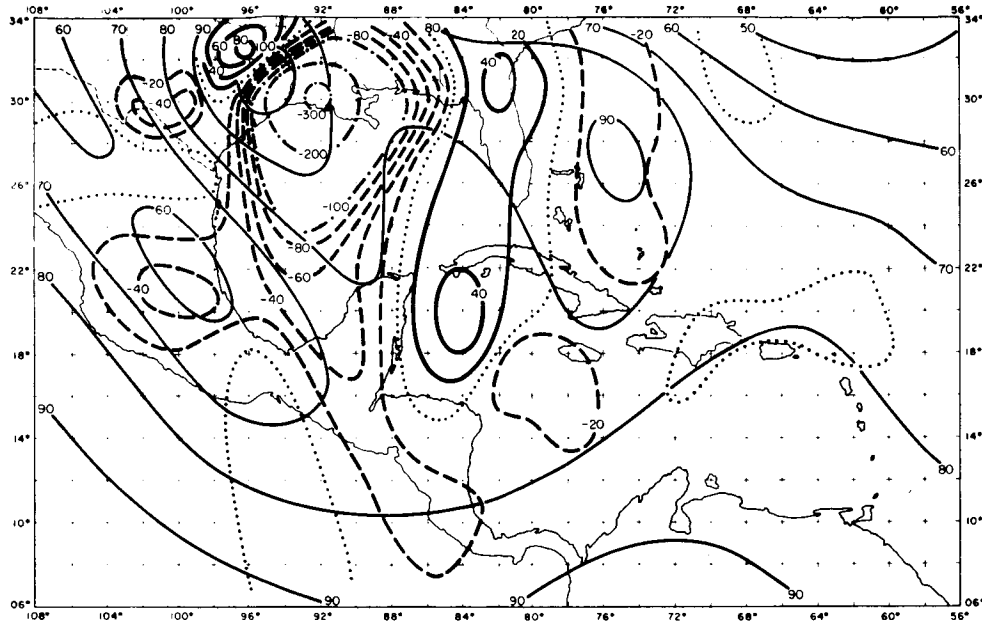
Fig. 6. Top and middle- Vertical motion with the observed relative humidity. Heavy solid lines are sinking, dotted lines are zero vertical velocity, dashed and dash-dotted lines are rising motions. Isolines of vertical motion are every $20 \times 10^{-5} \text{ mb sec}^{-1}$, except the dash-dotted lines which are every $100 \times 10^{-5} \text{ mb sec}^{-1}$. Light solid lines are relative humidity analyzed every 10 per cent.

Bottom- Integrated moisture flux. Solid lines are convergence analyzed every $50 \times 10^{-8} \text{ mb sec m}^{-1}$. Dashed lines are convergence analyzed every $25 \times 10^{-8} \text{ mb sec m}^{-1}$. Dotted lines are neutral.

13 SEPTEMBER 1961 00Z

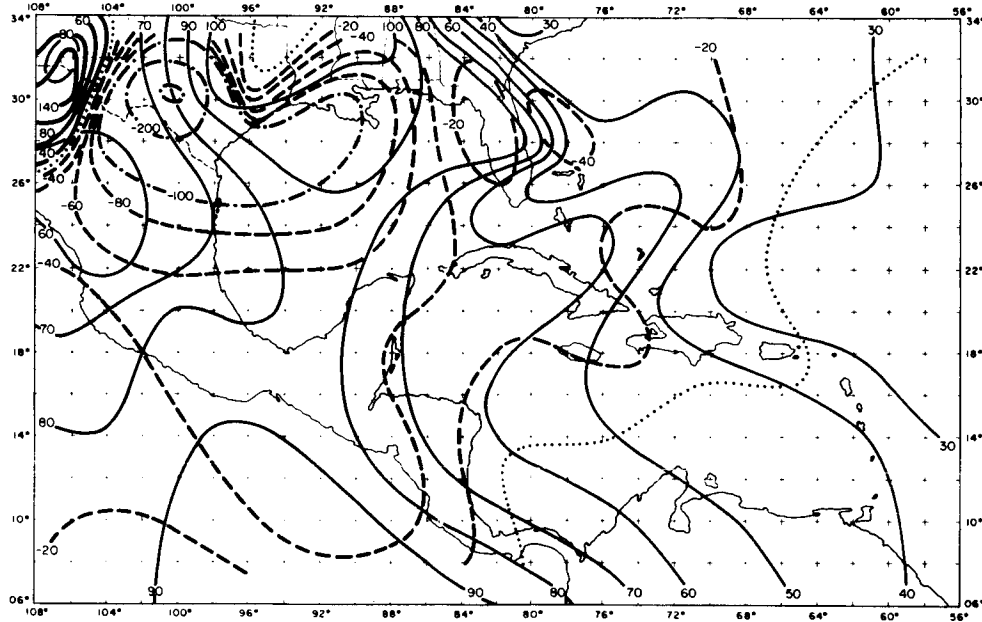
900 MB

27



13 SEPTEMBER 1961 00Z

500 MB



13 SEPTEMBER 1961 00Z

I

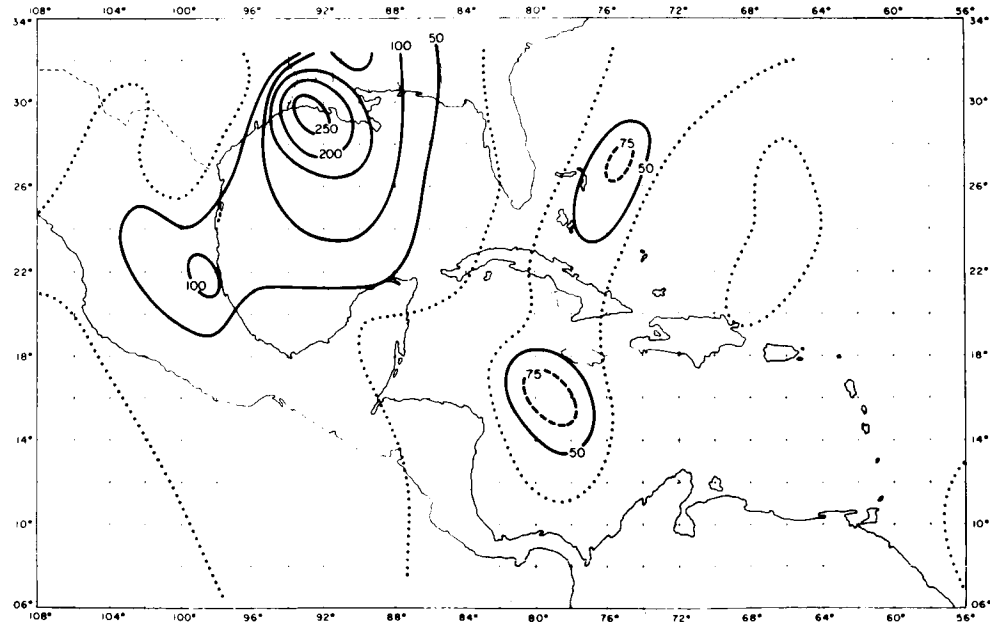
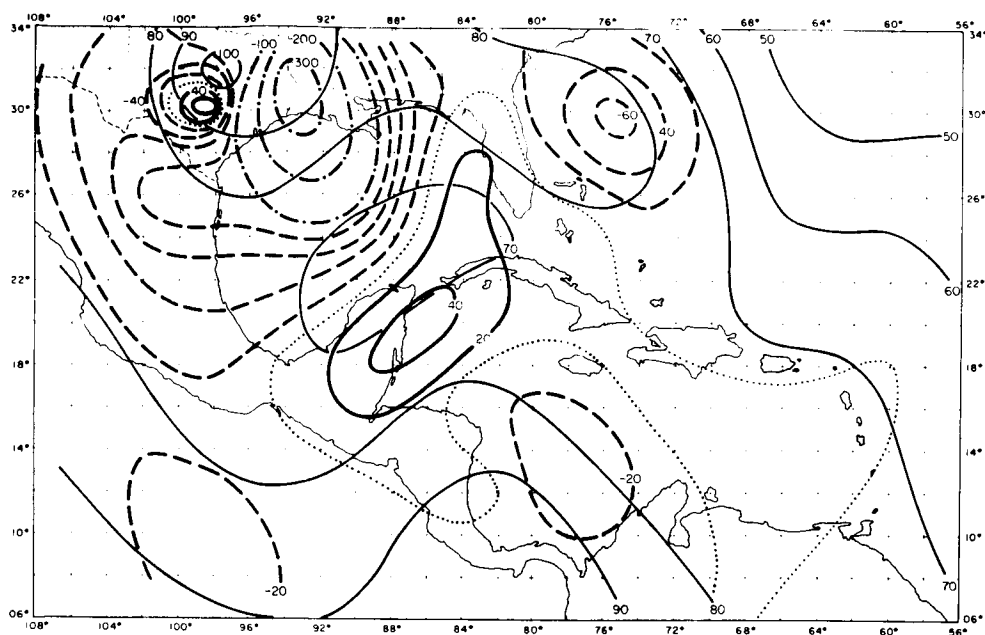


Fig. 7. Top and middle- Vertical motion with the observed relative humidity. Heavy solid lines are sinking, dotted lines are zero vertical velocity, dashed and dash-dotted lines are rising motions. Isolines of vertical motion are every $20 \times 10^{-5} \text{ mb sec}^{-1}$, except the dash-dotted lines which are every $100 \times 10^{-5} \text{ mb sec}^{-1}$. Light solid lines are relative humidity analyzed every 10 per cent.

Bottom- Integrated moisture flux. Solid lines are convergence analyzed every $50 \times 10^{-8} \text{ mb sec m}^{-1}$. Dashed lines are convergence analyzed every $25 \times 10^{-8} \text{ mb sec m}^{-1}$. Dotted lines are neutral.

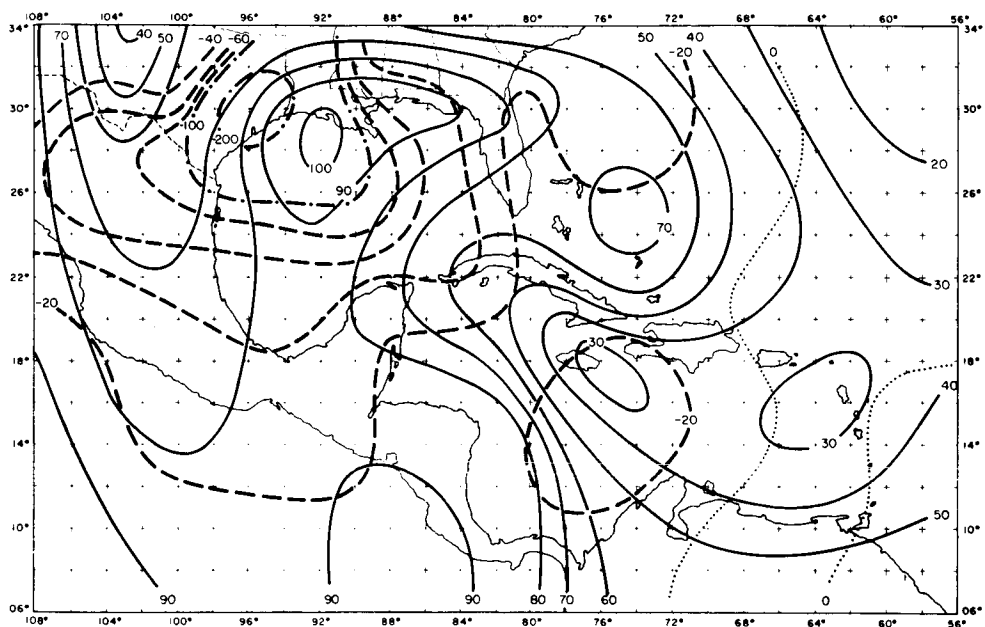
13 SEPTEMBER 1961 12Z

200 MB



13 SEPTEMBER 1961 12Z

500 MB



13 SEPTEMBER 1961 12Z

I

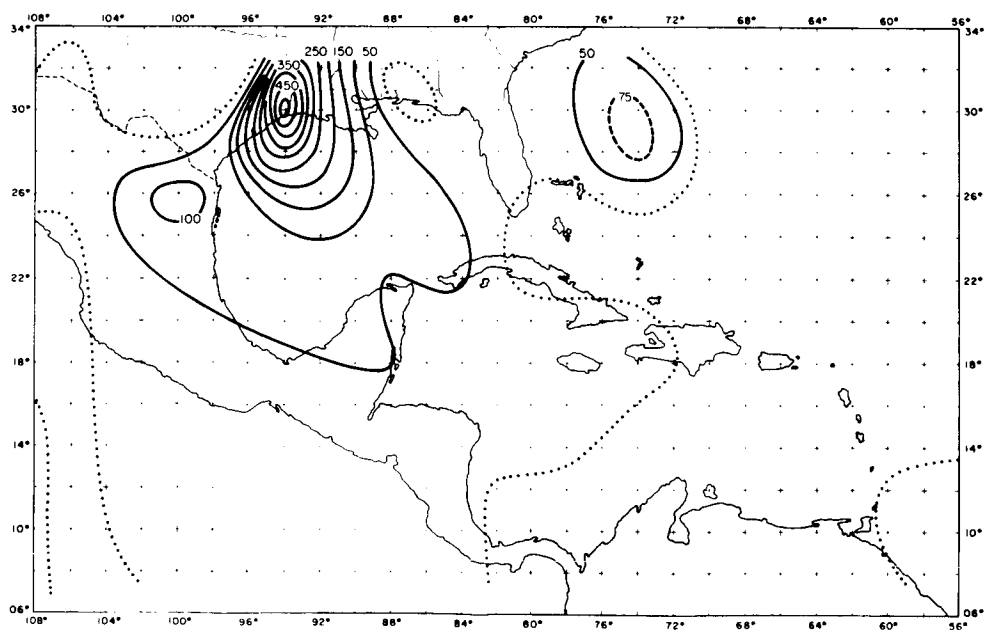


Fig. 8. Top and middle- Vertical motion with the observed relative humidity. Heavy solid lines are sinking, dotted lines are zero vertical velocity and dashed lines are rising motion. Isolines of vertical motion are $20 \times 10^{-5} \text{ mb sec}^{-1}$. Light solid lines are relative humidity analyzed every 10 per cent.

Bottom- Integrated moisture flux. Solid lines are convergence analyzed every $50 \times 10^{-8} \text{ mb sec m}^{-1}$. Dashed lines are convergence analyzed for $25 \times 10^{-8} \text{ mb sec m}^{-1}$. Dotted lines are neutral.

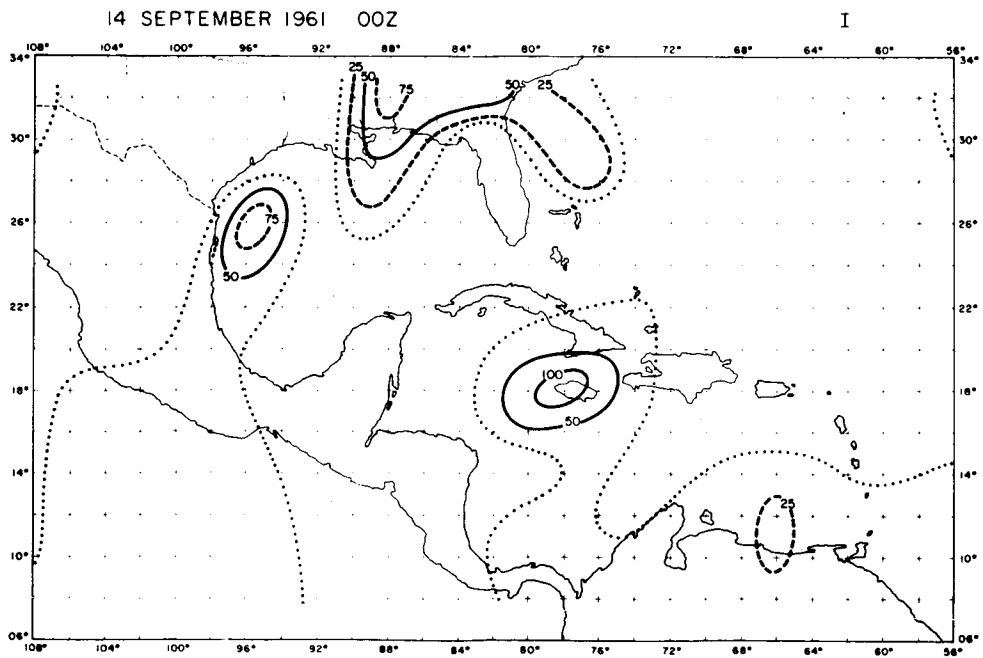
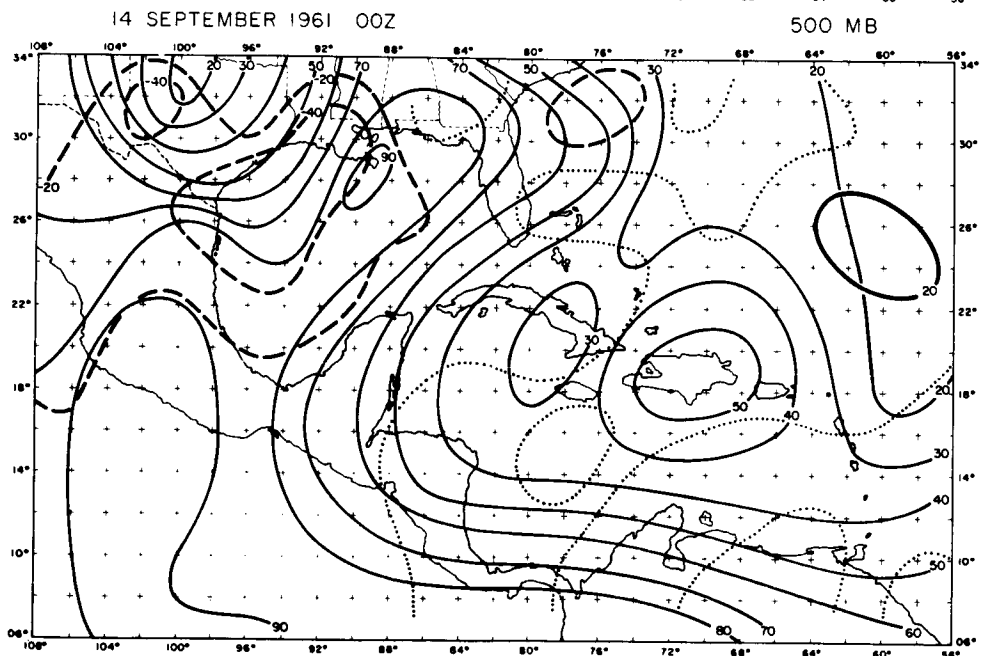
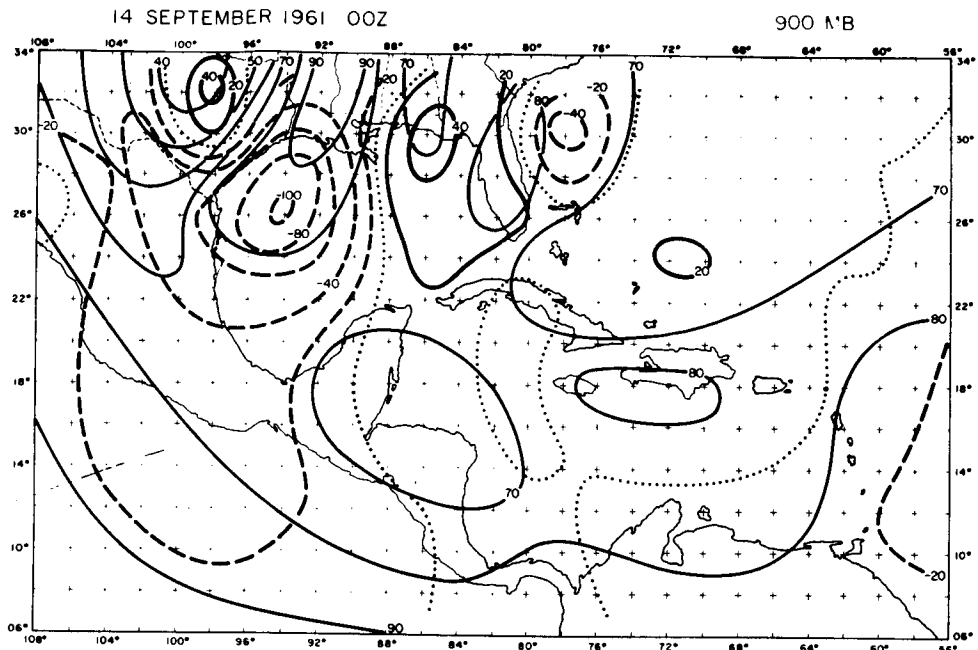
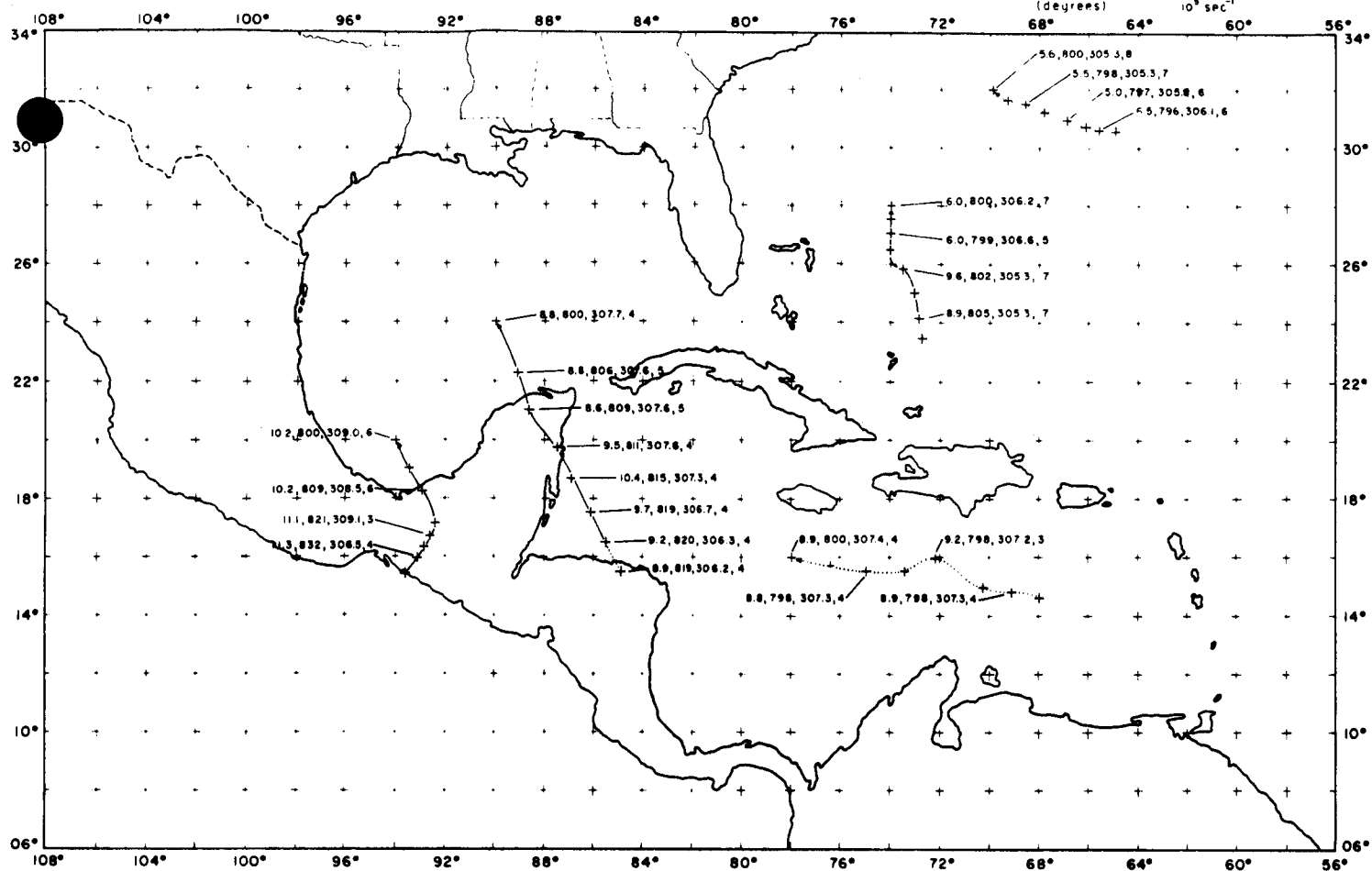


Fig. 9. Trajectory calculations. Arrowhead indicates end point, corresponding to 14 September 1961, 00Z. Crosses are positions each six hours. Solid lines mean rising motion, dotted lines sinking motion. The meaning of numbers is explained in the right upward corner of each figure.

TRAJECTORIES LEADING TO 800 MB

Moisture, Pressure, Potential
(gm/kgm)(mb) Temperature
(degrees) Absolute
Vorticity
 10^5 sec^{-1}



TRAJECTORIES LEADING TO 600 MB

Moisture, Pressure, Potential
(gm/kgm)(mb) Temperature
(degrees) Absolute
Vorticity
 10^5 sec^{-1}

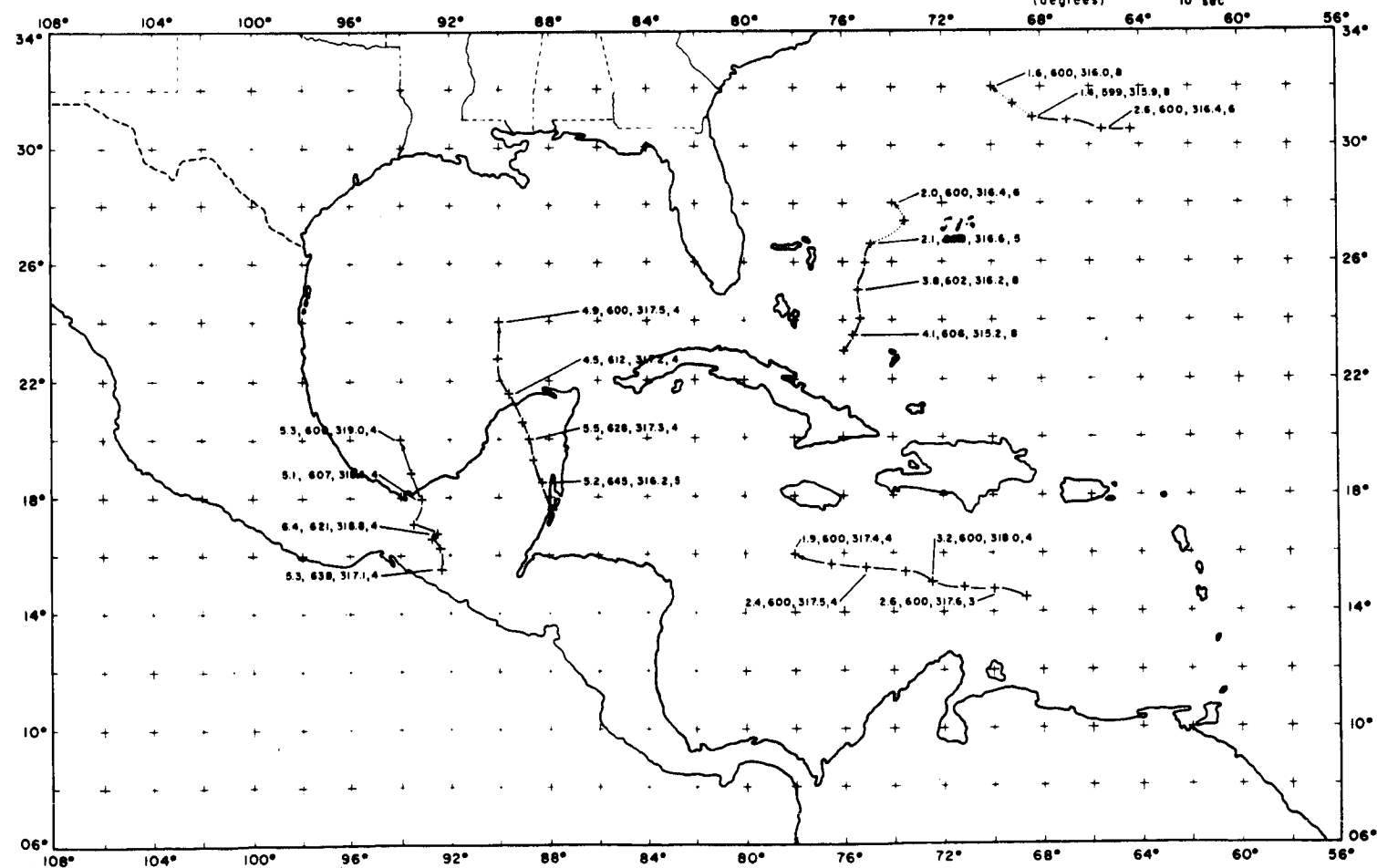
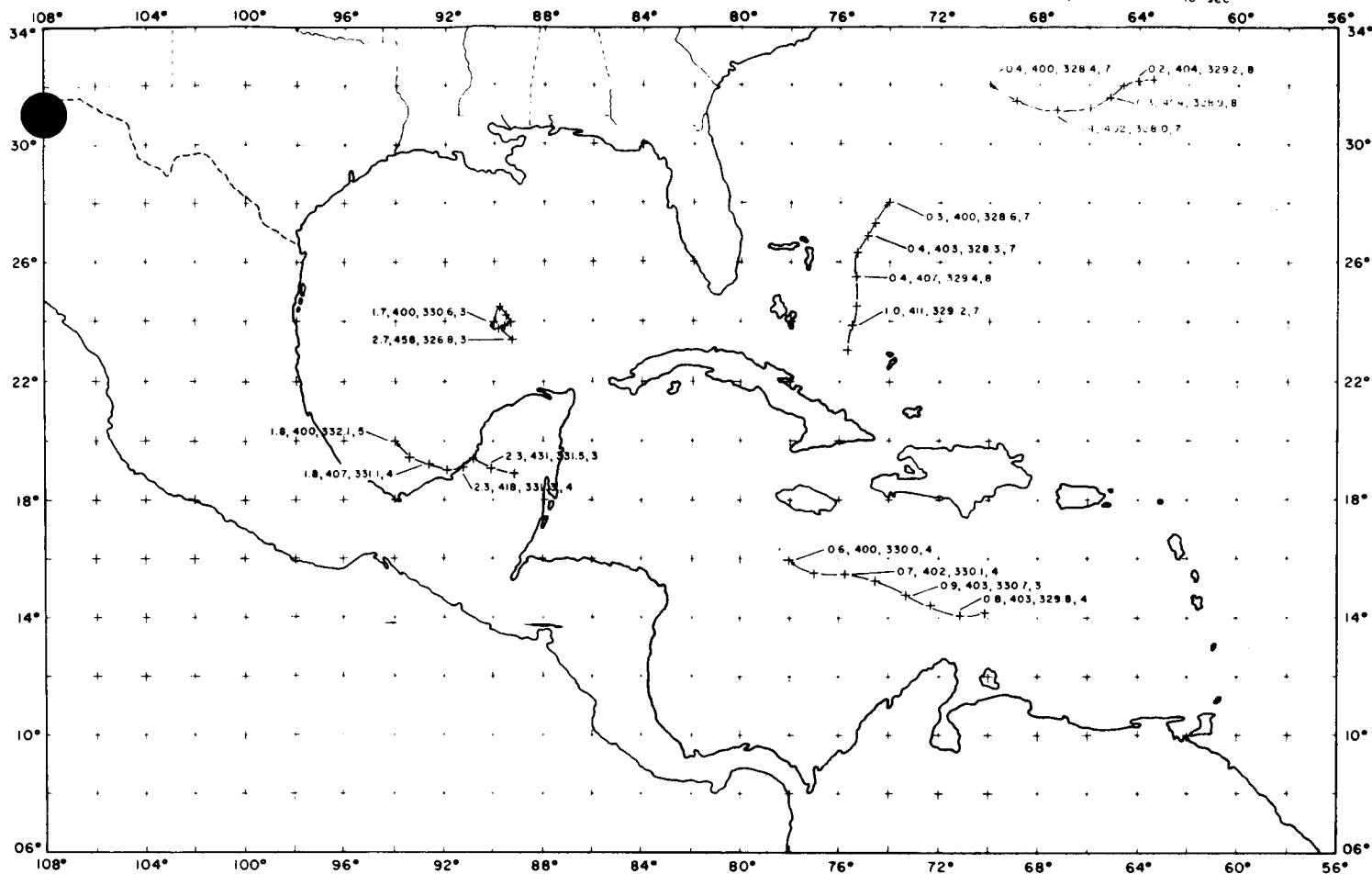


Fig. 10. Trajectory calculations. Arrowhead indicates end point, corresponding to 14 September 1961, 00Z. Crosses are positions each six hours. Solid lines mean rising motion, dotted lines sinking motion. The meaning of numbers is explained in the right upward coner of each figure.

TRAJECTORIES LEADING TO 400MB

Moisture, Pressure, Potential
(gm/kgm)(mb) Temperature
(degrees)Absolute
Vorticity
 10^6 sec^{-1} 

TRAJECTORIES LEADING TO 200MB

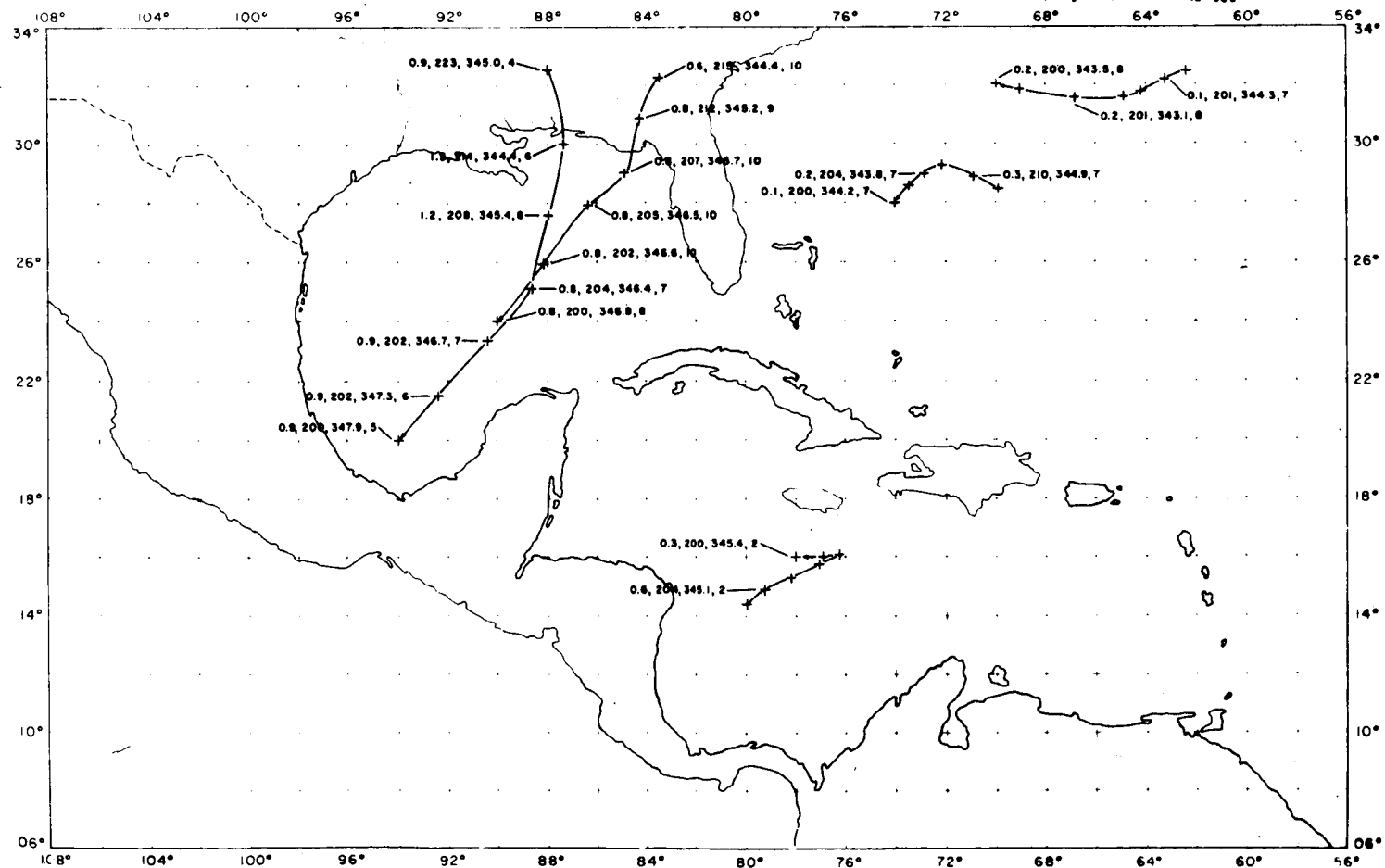
Moisture, Pressure, Potential
(gm/kgm)(mb) Temperature
(degrees)Absolute
Vorticity
 10^6 sec^{-1} 

Fig. 11. Partitioned vertical motion. Heavy vector is the total, light lines are the components. Order at each grid point from left to right: Total, vorticity, thermal, friction and latent heat.

OMEGA CROSS SECTION AT 78° W 14 SEPTEMBER 1961 00Z

0
100
100 = 10^3 MB SEC⁻¹

300 MB



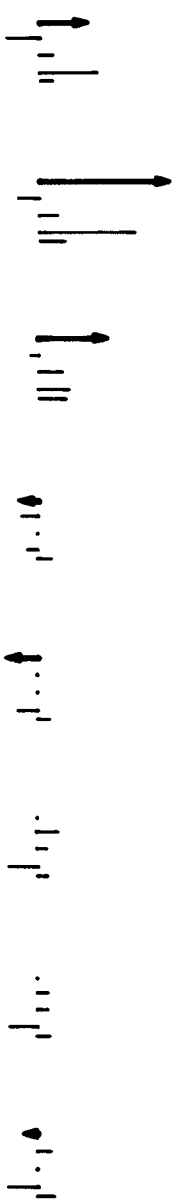
500 MB



700 MB



900 MB



0.5
CM SEC⁻¹

1
34° N

1
18° N

N67-30790

A Calculation of Percentage Area

Covered by Convective Clouds from Moisture Convergence

By T. N. Krishnamurti

ABSTRACT

In the large scale tropical flows one can estimate the percentage area covered by active convective cloud elements according to certain theoretical formulation of parameterization of convective scale motions. We have used Kuo's (1965) model cloud which is based on replacing the ambient tropical atmosphere with a moist adiabatic cloud element over a portion of a synoptic scale grid network. Quantities such as friction layer (1000-800 mb) mass convergence, moisture convergence and other relevant parameters like net moisture convergence over vertical columns extending over the depth of the troposphere are determined to evaluate the per cent area occupied by convective clouds.

An application to a case study of an easterly wave below a cold low is made. Some actual radar pictures are presented for comparison purposes.

1. Kuo's theory of parameterization

According to Kuo (1965) the fraction of a unit synoptic scale area covered by active (newly formed) convective elements is given by the relation,

$$a = I/Q \quad (1)$$

Where I is the net moisture convergence in a vertical column extending from the top of the friction layer to the top of the atmosphere, we may define I by the relation,

$$I = \frac{1}{g} \int_{p_B}^{p_T} \nabla \cdot \mathbf{q} \, dp - \frac{\omega_B q_B}{g} \quad (2)$$

Where q is the specific humidity, p_B is the pressure on top of the friction layer (we have assumed $p_B = 800$ mb) and p_T is the pressure at the top of the atmosphere (we have assumed $p_T = 100$ mb), the subscript B stands for quantities on top of the friction layer. ω is vertical velocity and g stands for acceleration of gravity.

$Q\Delta t$ is the net amount of moisture needed to produce a model cloud over the entire unit synoptic scale grid. The unit grid in our studies is an area approximately 2° latitude square. Kuo defines Q as the sum of two integrals Q_1 and Q_2 which are respectively the amounts of moisture convergence required to i) saturate and ii) warm the column according to simple moist adiabatic ascent considerations.

$$\left. \begin{aligned} Q_1 &= \frac{1}{g\Delta t} \int_{p_B}^{p_T} (q_s - q) \, dp \\ \text{and } Q_2 &= \frac{1}{g\Delta t} \int_{p_B}^{p_T} \frac{c_p}{L} (T_s - T) \, dp \end{aligned} \right\} \quad (3)$$

Where C_p stands for the specific heat at constant pressure, L stands for latent heat from the liquid to the vapor phase, and q_s and T_s are respectively the saturation specific humidity and temperature of a moist adiabatically ascending parcel and they are determined from a knowledge of T_B , q_{sB} . In the vertical above the friction layer (in the cloud region) we assume a conservation of equivalent potential temperature θ_e defined by the relation,

$$\theta_e = \theta e^{Lq_s/C_p T_s} \quad (4)$$

Along a moist adiabat the stability relation

$$-C_p \frac{T}{\theta_e} \frac{\partial \theta_e}{\partial p} = - \frac{\partial}{\partial p} (gz + C_p T_s + Lq_s) \quad (5)$$

is valid, and hence the following equations were solved in an iterative manner for the three variables T_s , e_s and q_s .

$$gz + C_p T_s + Lq_s = C_1 \quad (6)$$

$$e_s = 6.11 e^{25.22 \left(1 - \frac{273}{T_s}\right)} \left(\frac{273}{T_s}\right)^{5.31} \quad (7)$$

and

$$q_s = 0.621 e_s / (p - 0.379 e_s) \quad (8)$$

Equation (7) is a well known relation for expressing saturation vapor pressure e_s as a function of temperature T_s , it may be obtained from the Clausius Clapeyron equation. A similar calculation was performed by Kuo (1965). Δt is an arbitrary parameter, it is a measure of the time required to form a cloud element. We may arbitrarily assign any value, of the order of few hours to represent this time scale, lying anywhere from 1 to 6 hours. The results do, to a certain degree, depend on

the choice of this parameter but as we shall show this is not very critical if we are aware of this arbitrariness of Δt .

2. An application to an idealized situation

We present an idealized example in a two dimensional (x, p) plane of the evolution of the synoptic scale temperature and moisture distribution for a given fixed distribution of $a(x)$ the fractional area covered by convective clouds. Figure (1) top left and top right respectively denote an initial distribution of temperature T and relative humidity in a vertical plane, the horizontal grid distance is 200 km and the vertical grid distance is 50 mb. This initial distribution of temperature is that of a mean tropical atmosphere and the moisture distribution is somewhat arbitrary. It shows relative humidity $> 80\%$ below 900 mb, similar to conditions in the tropics. Along the horizontal axis we assume $a(x)$ to be 0 for the first five and the last five grid points and a linear increase from the 6th to the 10th point, 'a' increasing from 0.01 to 0.1 per cent at the 11th point. At $x = 12$, a is also $= 0.1\%$, and 'a' decreases symmetrically back to zero from the 12th to the 16th point. Assuming that the large scale forcing somehow maintains these values of 'a' fixed for 24 hours we have integrated the thermodynamic energy equation and a moisture conveyance equation for 24 hours to determine heating and moisture advection above the 900 millibar surface. Moisture and temperature values are assumed constant and fixed below the 900 millibar surface. A choice of $\Delta t = 2$ hours is used in these integrations.

In a matter of approximately 12 hours a near steady state was reached in the values of relative humidity, on a synoptic scale q and T approached q_s and T_s and their differences became rather small.

In Kuo's scheme steady state is reached via ' α ' becoming zero when large moisture amounts are at first brought into a region by moisture convergence, and later convergence changes into divergence of flux of moisture because relatively drier air is brought into this region. The six and twelve hour evolutions of temperature and relative humidity are illustrated in Figure 1 middle and bottom. The warm core attains an intensity of +3 degrees and the 80% relative humidity iso-line is carried up through the depth of the troposphere, (a phenomenon on a synoptic scale very familiar to synoptic analysts in the tropics). It may be noted that the synoptic scale changes in Figure 1 were obtained by defining the subgrid scale phenomenon according to a simple cloud model. This Figure 1 should be kept in view in the following calculations of ' α ' in actual meteorological situations. As we shall see in the case study we present, the largest values of ' α ' are only 0.6 per cent hence the efficiency of the heating and of moisture advection are small. In a tropical storm (Hurricane Carla 1961) we found values of ' α ' close to 6 per cent. According to Kuo ' α ' should be interpreted as the percent area occupied by newly formed convective clouds. The theory has several shortcomings:

- i) Moisture convergence always leads to formation of clouds in conditionally unstable states without any formal cloud physics.
- ii) No liquid water is permitted in the moisture conveyance equations.

- iii) Cloud model does not account for any entrainment.
- iv) Heat is released instantaneously as a function of the parameter ' α '.
- v) No dynamical effect of thunderstorm downdrafts are included.
- vi) The parameter Δt is somewhat arbitrary.
- vii) There is a tendency for saturation on a synoptic scale in this

formulation which at first sight seems to be an important drawback, however for reasons stated earlier, it does not appear to be serious.

The entire theory of parameterization is thus very crude. The points in its favor are that Kuo was able to simulate the formation of a tropical storm by releasing heat of the cloud scale motions which is easy to see from Figure (1) presented here. We are looking for a scheme that would have wider application for studies of large scale tropical circulations. Calculation of the parameter ' α ' may give a clue to dynamical processes of development on a large scale, at least to a degree. With this tacit assumption we are presenting results for the case studies.

3. Synoptic description of easterly wave and cold low

Figure (2) portrays the surface and 200 mb maps for August 13, 12Z, 1961. The region of interest is over and south of Cuban Islands. The synoptic situation consists of a wave perturbation of large amplitude in the basic easterly flow in the low latitudes and a closed low (a cold core low) in the upper levels.

Ahead of the upper trough in the region of strong southerly flow the wind shear vector in the troposphere is from the south-southwest and is a region of strong convective banded motions, as revealed in Figures (3) and (4). No tropical storm formed in this situation. Figures (3) and (4) were loaned to us by Dr. William Q. Gray of Colorado State University. An aircraft flight made by the Flight Research Facility of the National Hurricane Research Project provided the data. The flights were made during August 13 and 14 starting from Miami to Kingston, Jamaica and back. As mentioned, convective activity is most marked south-southwest of the Cuban Island and in the Caribbean Sea. Several radar echoes appear very intense surrounded by weaker returns. It is possible to obtain a crude measure of the percentage area covered by hard and soft core echoes in the 2 by 2 degree latitude grid. Largest values for soft echoes were close to 10% and for hard echoes around 2%. A west to east cross-section along 20°N parallel containing isolines of relative humidity is shown in Figure (5) for three map times, August 13 00Z, 13 12Z and 14 00Z 1961. The important feature of this cross-section is the large moisture content > 70% relative humidity through the depth of the troposphere at Kingston, Guantanamo and Grand Turk Island. The funnelling effect of moisture on small convective scale must undoubtedly have resulted in this large scale distribution of moisture. The close similarity of Figure (1) and Figure (5) is perhaps more than a coincidence. Large scale vertical motion for this case study are reported by Krishnamurti and Baumhefner (1966) and by Baumhefner (1966). The largest values of vertical velocity ω were only around 10^{-3} mbs/sec and could

not account for the vertical advection of moisture. A more efficient small scale rapid transfer in convective scale motions must account for this observed large scale distribution of moisture.

4. Some calculated fields

a) Precipitable water below and above the friction layer.

While it is well known that large quantities of moisture in the tropics reside below the trade inversion, frequently large amounts of moisture (after major convective activity) are also found above the friction layer. The normal state above the friction layer is generally dry air with relative humidity less than 50%. In Figure (6) we present a partitioning of the total precipitable water below and above the friction layer (1000-800 mbs). Figure (6) top shows total precipitable water. Figure (6) middle shows total precipitable water above the friction layer and the bottom Figure (6) shows the moisture in the friction layer. These maps were obtained from an analysis of the specific humidity at 1000, 850, 700, 500 and the 300 millibar surfaces. Of pertinent interest here is the large moisture amounts over the region of active convection (Figures 3 and 4), where on a synoptic scale precipitable water amounts are as large as 2.75 cms (water depth) both below and above the friction layer. In the dry region ahead of the easterly wave the air is considerably drier above the friction layer, suggesting strong subsidence above the friction layer. Most of the active convection on August 14, 1961 (the period for which the precipitable water charts were constructed) was found in the

region where the gradient of the moisture field is largest (16°N and 80°W), largest magnitudes of total precipitable water are found in those regions where the convection was active in the preceding 24 hours.

Vertical motion charts are not shown here. They are reported elsewhere by Baumhefner (1966).

Figure (7) shows the distribution of friction layer (1000-900 mb) mass divergence, divergence of flux of moisture, integrated convergence of flux of moisture and an evaluation of the per cent area occupied by convective clouds. Overall in the friction layer there is a good correlation between mass and moisture convergence but there are regions of discrepancy. North of the Gulf of Mexico, where horizontal advection of moisture is large and as a result the fields of $\nabla \cdot \mathbf{v}$ and $\nabla \cdot \mathbf{q}\mathbf{v}$ are not too well correlated. In the region of interest south of Cuba there are fields of strong mass and moisture convergence and over the Gulf of Mexico (the dry belt of Figure 6) we find strong mass and moisture divergence in the friction layer. Lower left, Figure 7 shows the distribution of the net moisture convergence \mathbf{I} in columns. $\mathbf{I} > 0$ has physical significance here, so the region $\mathbf{I} < 0$ is not analyzed. The typical largest magnitudes of \mathbf{I} are of the order 200×10^{-8} millibars meter⁻¹sec. The distributions of moisture convergence $-\nabla \cdot (\mathbf{q}\mathbf{v})$ in the friction layer and that of \mathbf{I} are very similar, as is to be expected. The lower right, Figure 7, shows the distribution of ' α ' the per cent area occupied by convective clouds. It was somewhat unexpected that the largest values of the per cent area covered by

convective clouds came out around 0.6% or near 1%. This number is directly proportional to the parameter Δt which we had assumed = 2 hours. Since Δt cannot be larger than 5 or 6 hours in any case, we may state that the active convection is only present over one or two per cent of the area of the synoptic scale grid network. The correspondence to what is observed as hard echoes in the radar composite charts, Figures 3 and 4, is thus quite encouraging. In Figure 7 we have excluded calculations in regions where $I < 0$, because the parameterization of small scale convection is made only when the following two criteria are satisfied.

$$\begin{aligned} \text{i)} \quad & - \frac{RT}{p \theta_e} \frac{\partial \theta_e}{\partial p} < 0 \\ \text{ii)} \quad & I > 0 \end{aligned}$$

In conclusion it may be stated that we have made a very preliminary investigation of an important problem, whether any of the parameterization approaches are of any value for scientific investigations will have to be tested in considerable more detail.

Figure 1 Distribution of temperature (left) and relative humidity (right) in a vertical plane (x, p) for $t = 0$, $t = 6$ hours and $t = 12$ hours. Vertical grid distance is 50 millibars, and horizontal is 200 kms. The evolution of large scale temperature and moisture distribution from subgrid-scale process is illustrated.

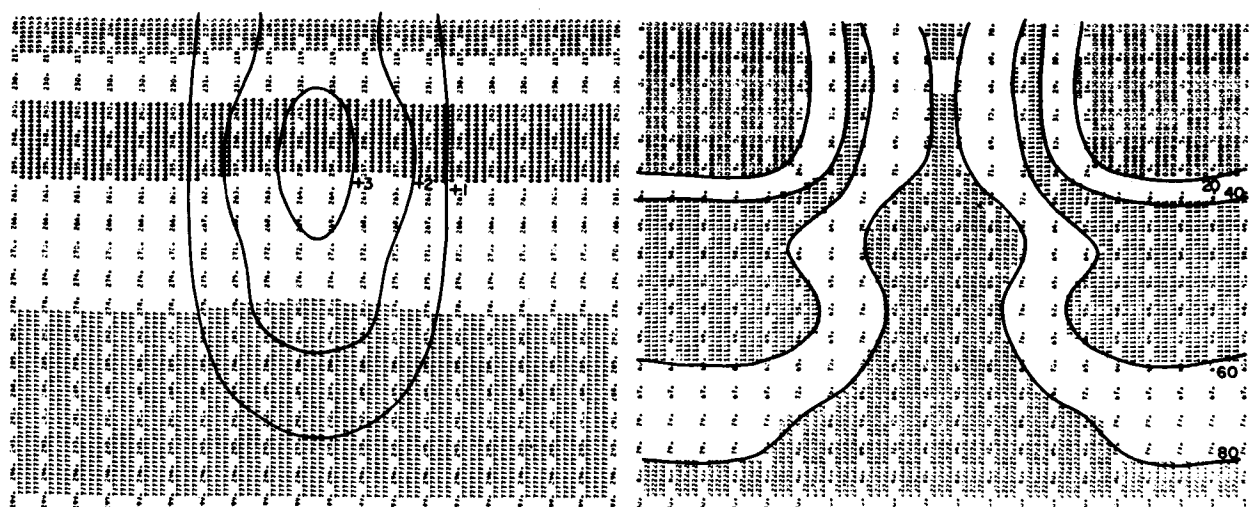
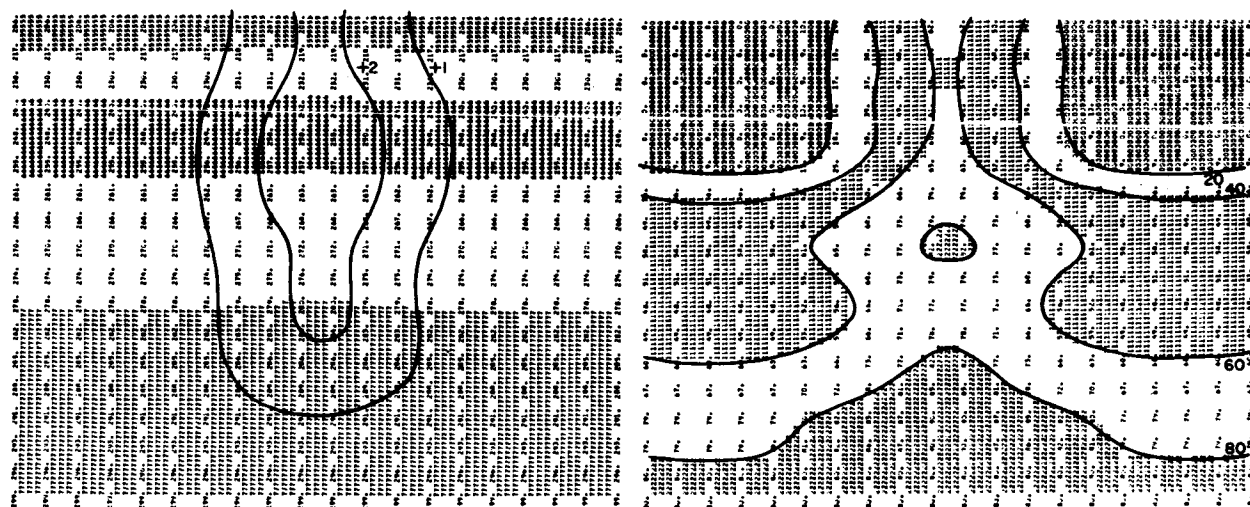
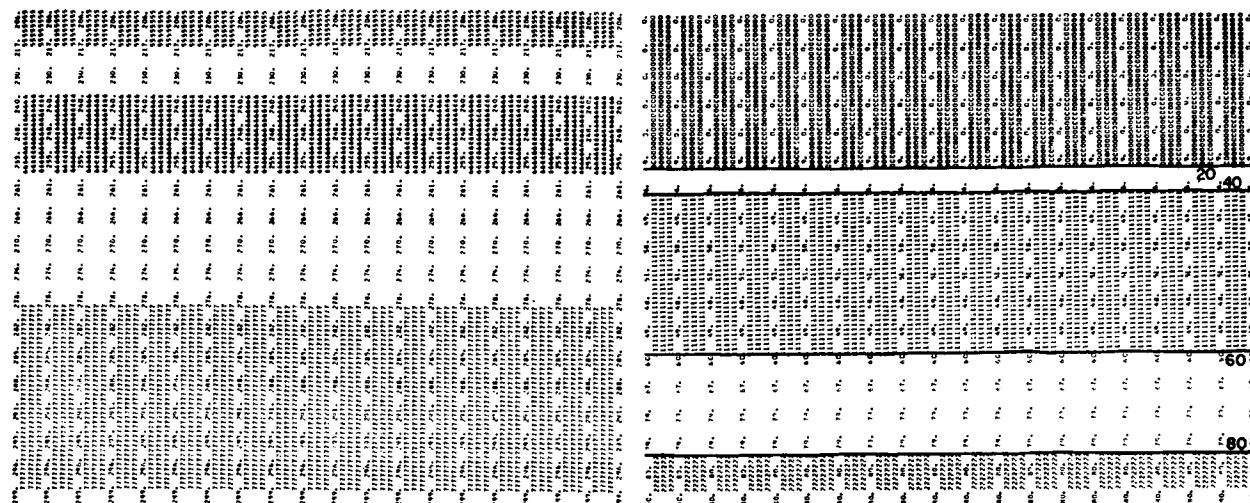
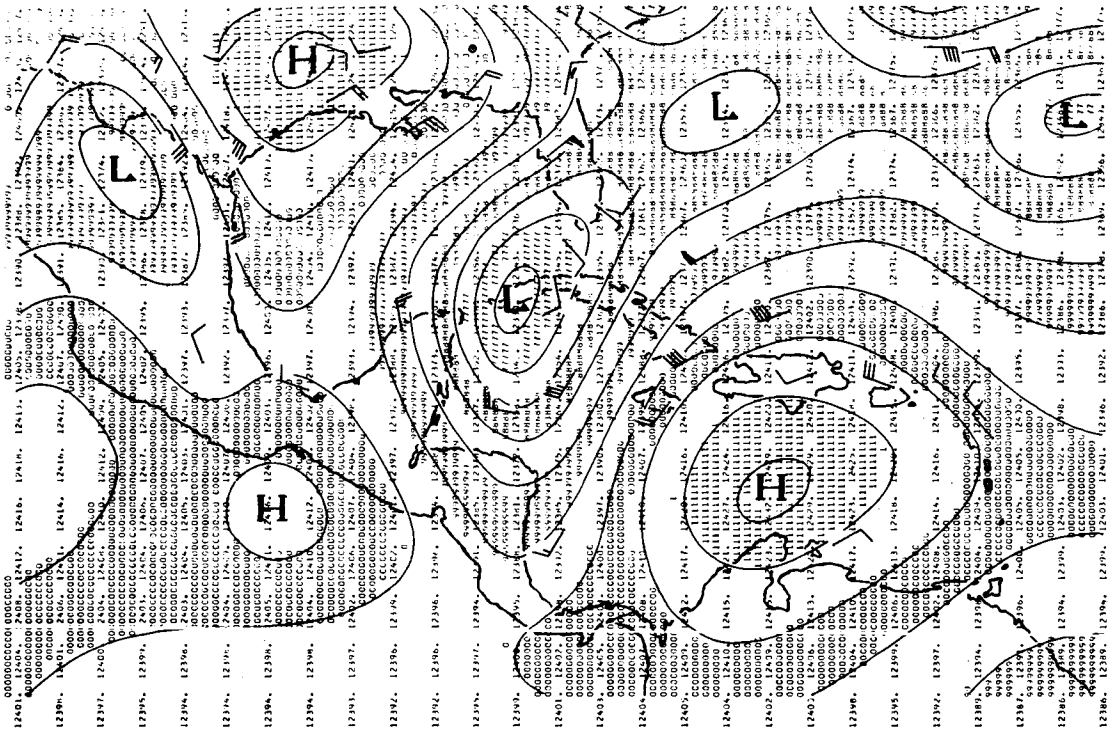


Figure 2 200 mb geopotential heights and surface isobars are shown
for August 14, 00Z 1961. Contours are analysed for every
10 meters and isobars for every millibar.

200 MB (METERS)



SURFACE (MB)

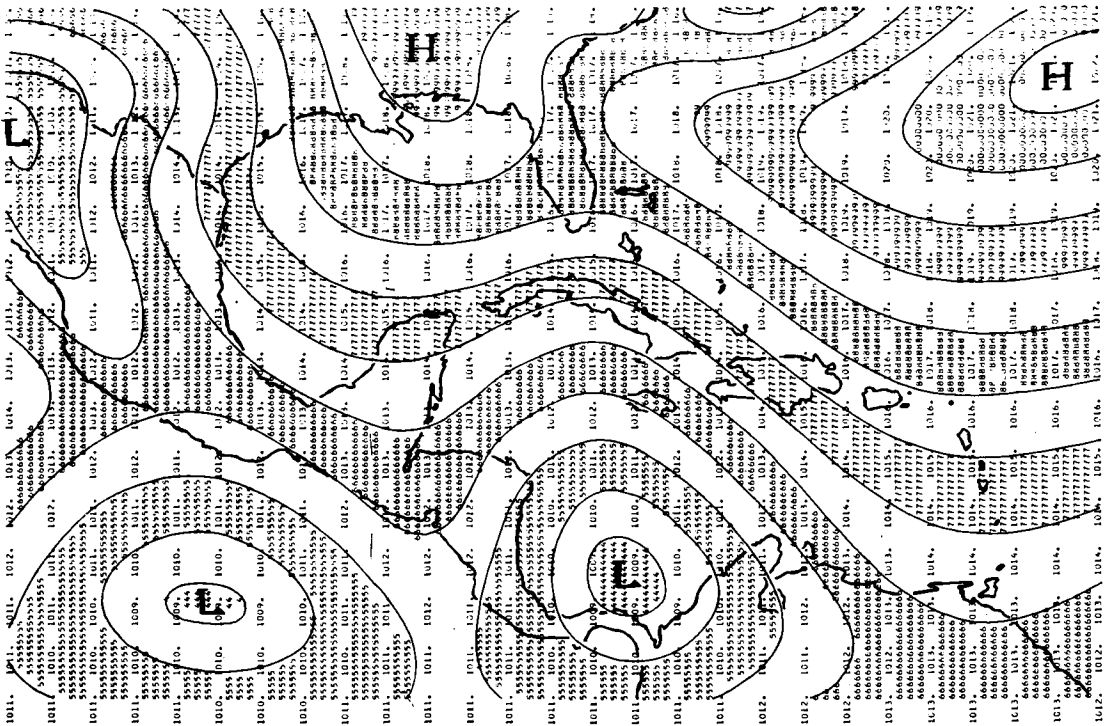


Figure 3 Radar composite chart for August 13-14, 1961. The flight (track shown) originated from Miami and terminated at Kingston. Hard and light echoes are marked by different shading. This chart was obtained through the courtesy of Dr. William Q. Gray of Colorado State University.

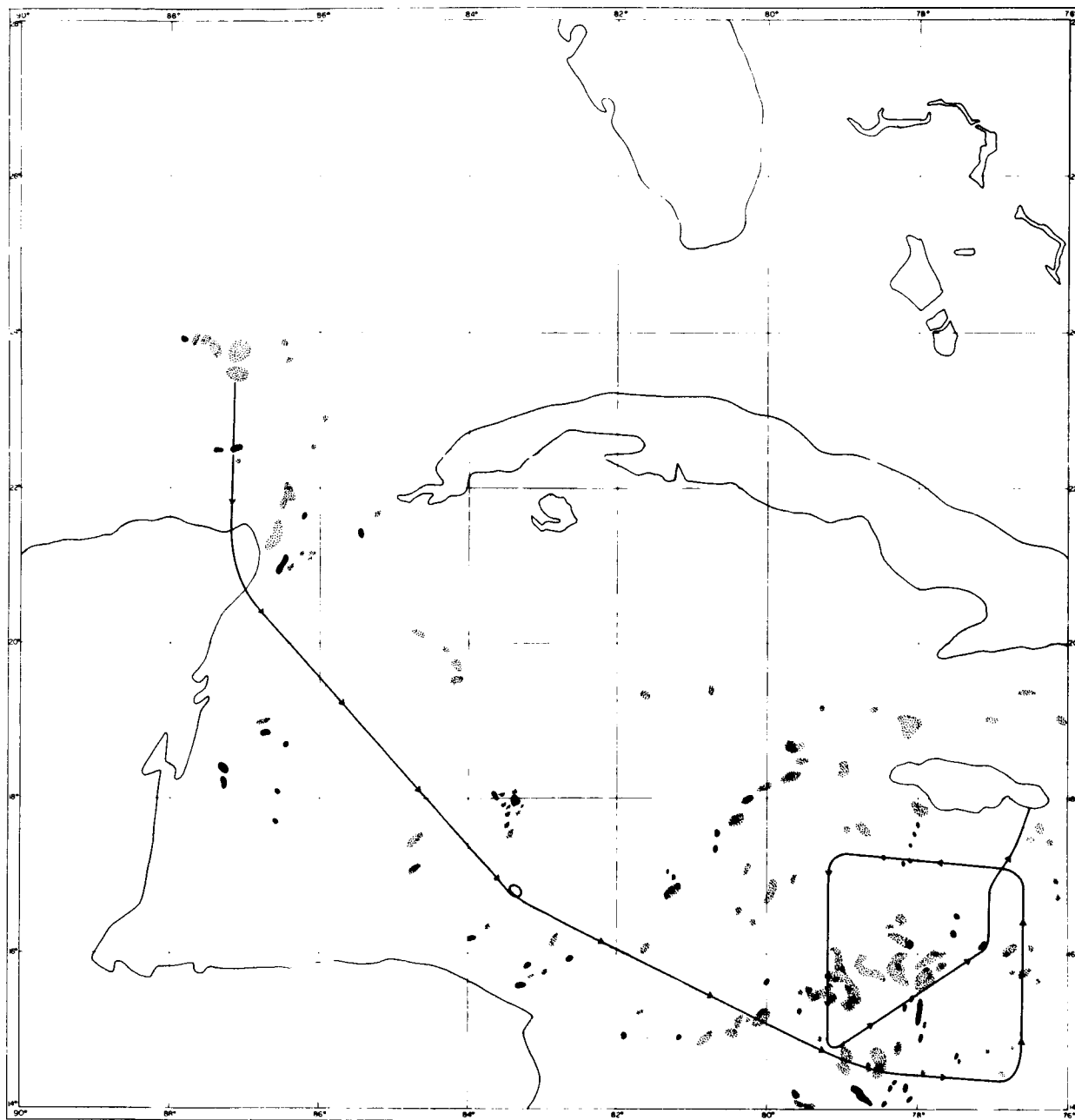


Figure 4 Radar composite chart for August 13-14 1961. The flight (track shown) originated from Kingston and terminated at Miami. Hard and light echoes are shown by different shading. The chart was obtained through the courtesy of Dr. William Q. Gray of Colorado State University.

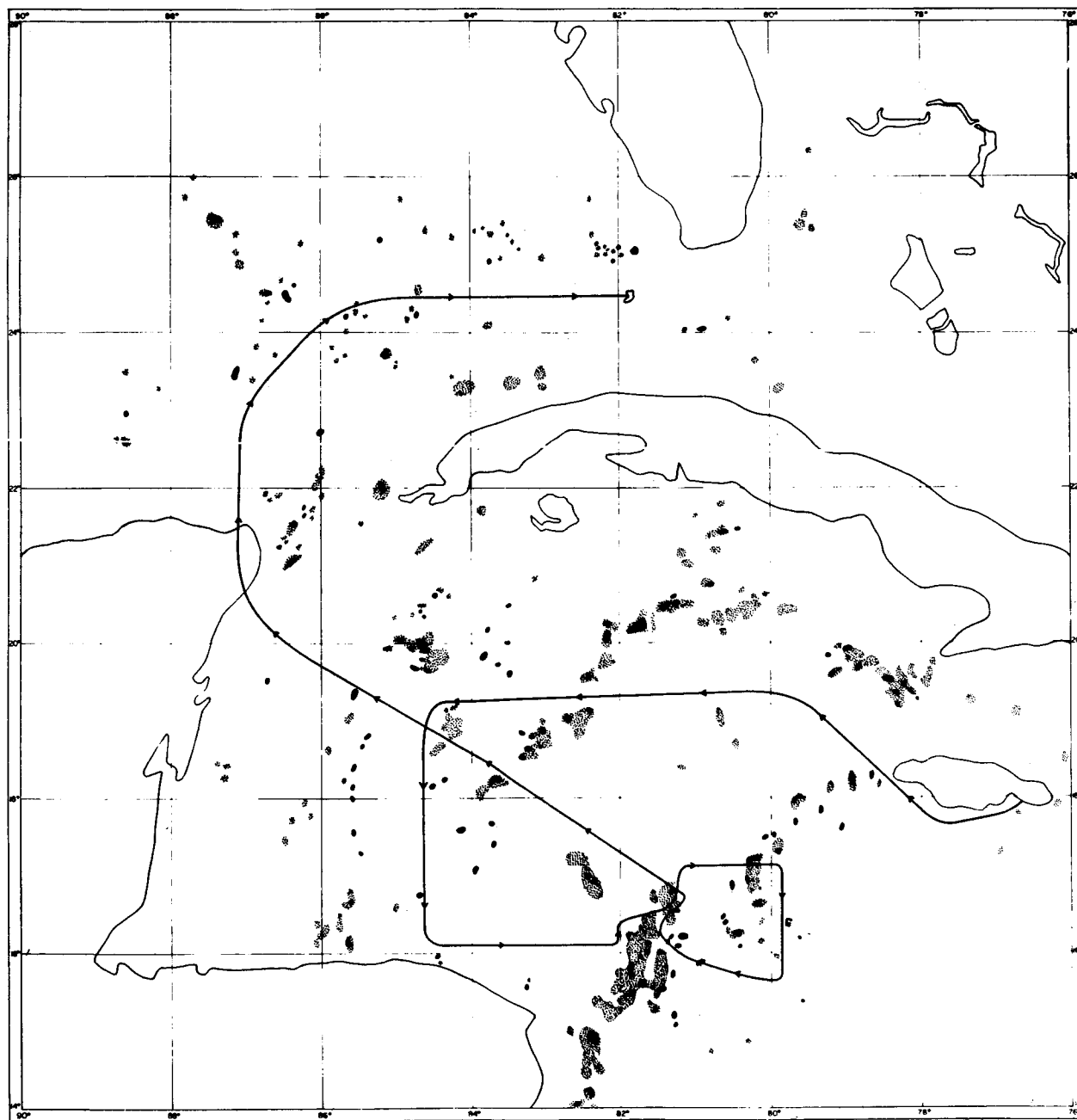


Figure 5 Vertical cross-section of relative humidity at 20°N
from Tacubay (Mexico) to Antigua.

Top: August 13 00Z 1961

Middle: August 13 12Z 1961

Bottom: August 14 00Z 1961

Moist regions are indicated by relative humidity $> 70\%$,
dry regions are indicated by values $< 30\%$.

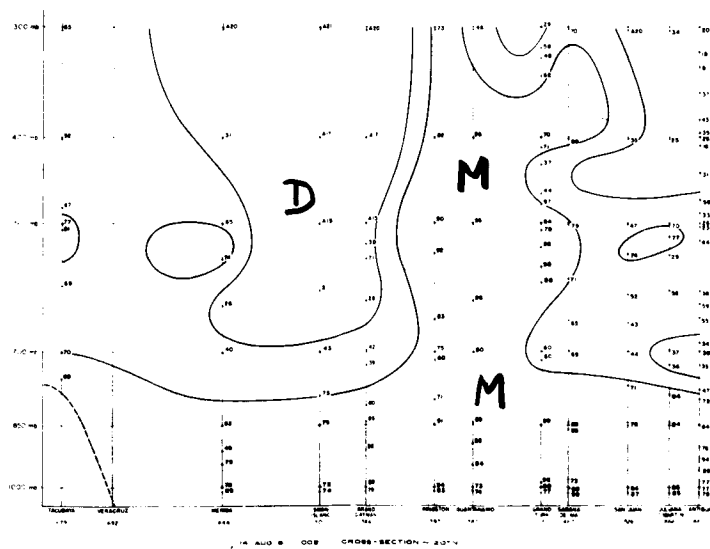
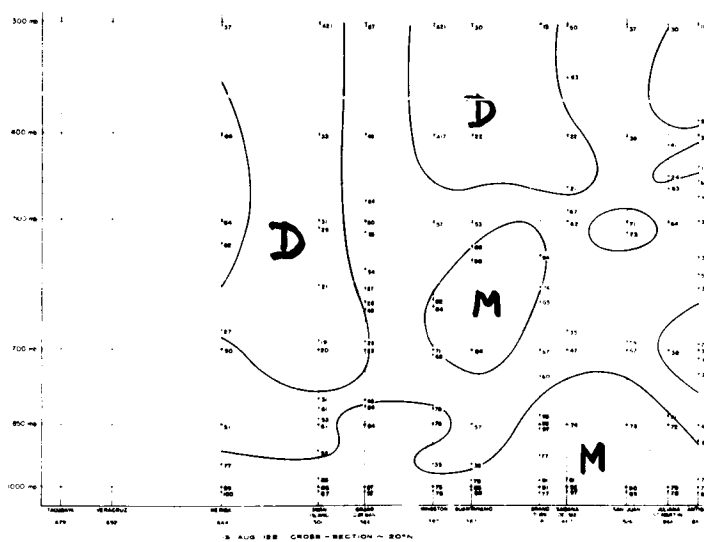
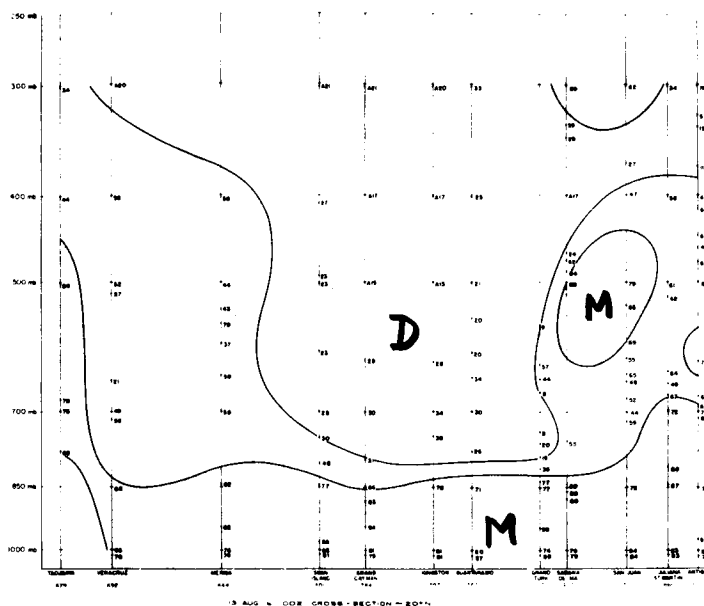
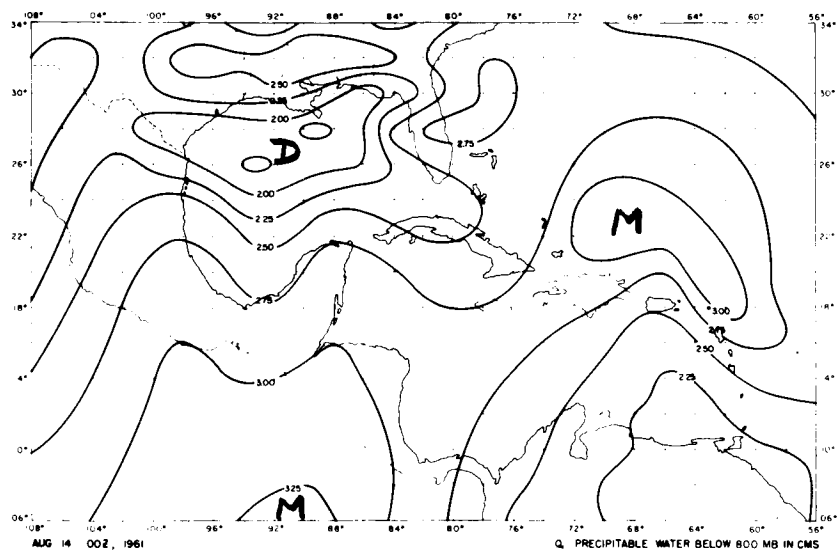
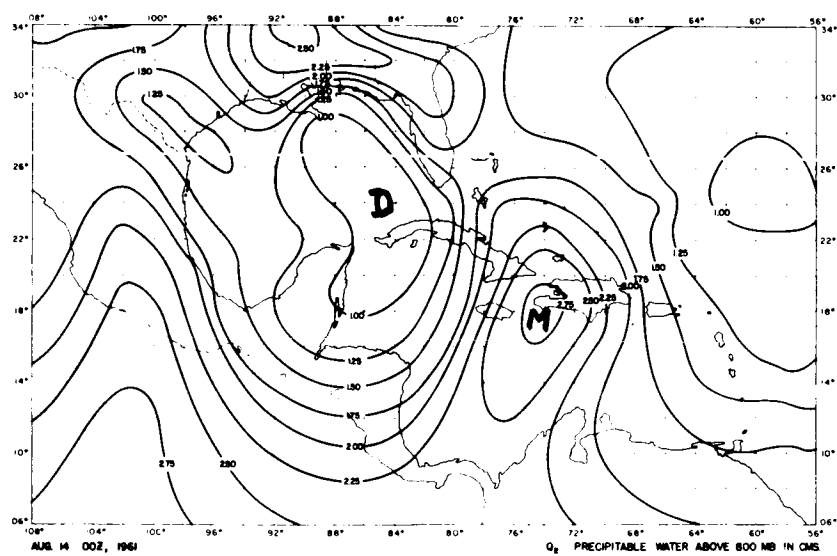
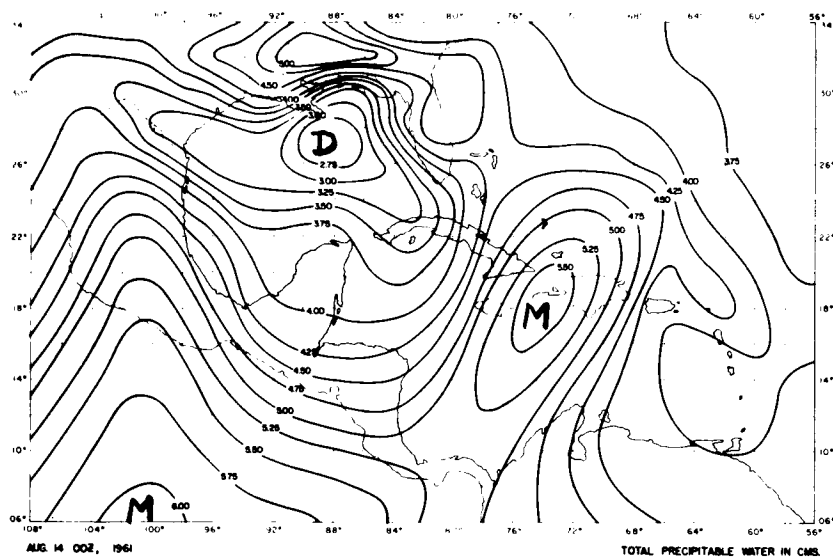


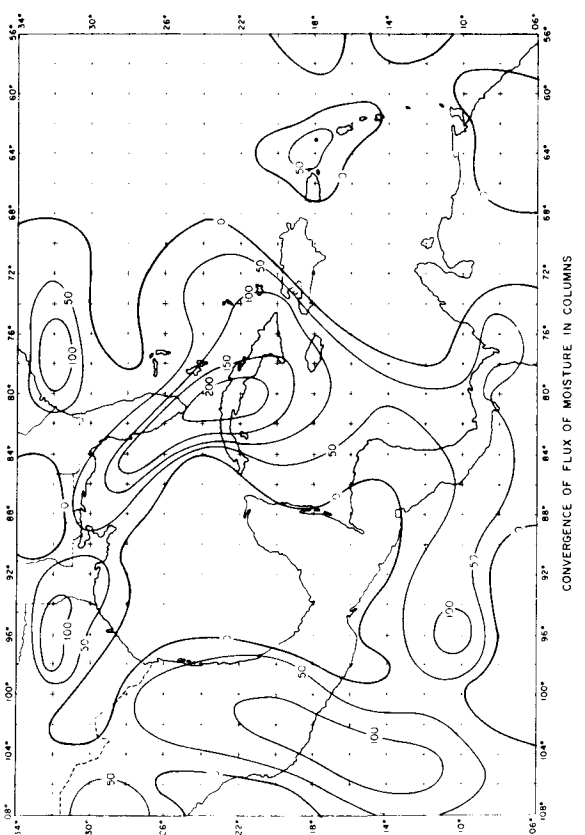
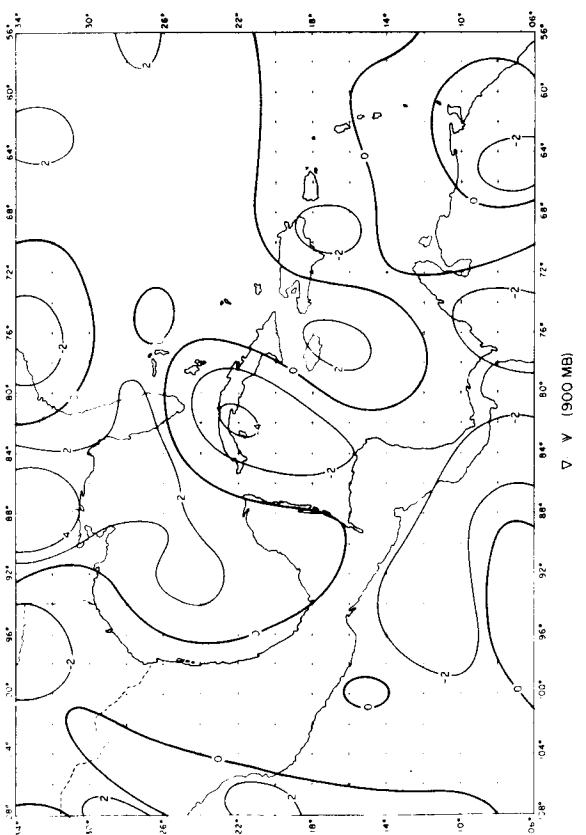
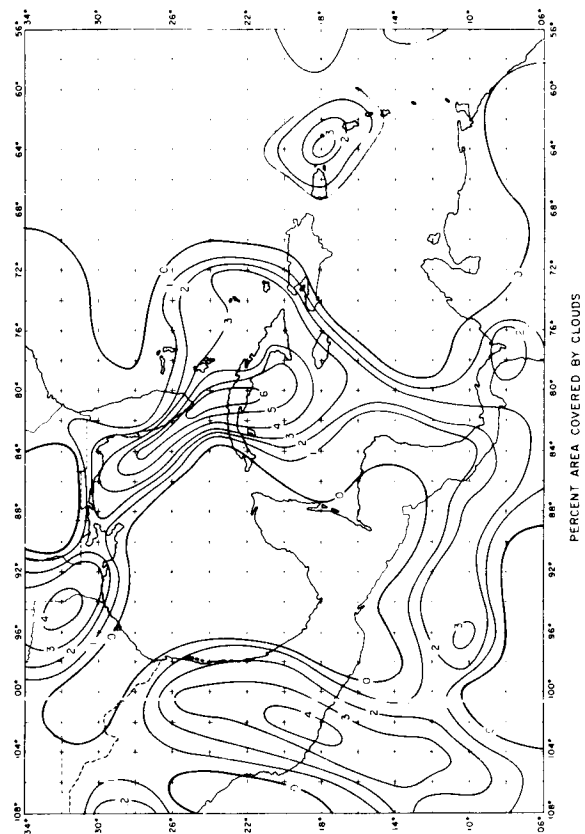
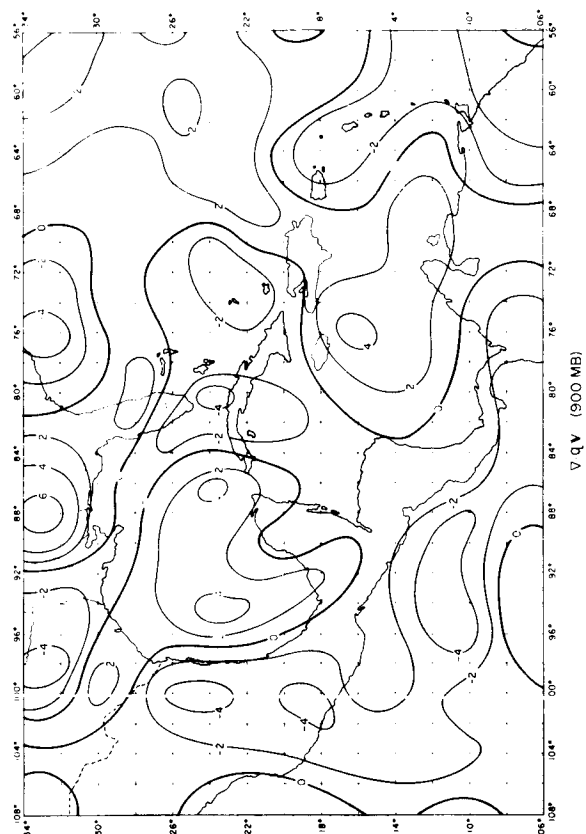
Figure 6 Total precipitable water in cms for August 14, 00Z 1961.

Top: Total

Middle: Above 800 mbs.

Bottom: Below 800 mbs.





List of References

1. Krishnamurti, T. N. and D. Baumhefner, 1966: Structure of a Tropical Disturbance Based on Solution of a multi-level baroclinic model, Journal of Applied Meteorology 5, 396-406.
2. Baumhefner, D., 1966: A Study of a Non-developing Easterly Wave, Final report to AFCRL, Contract No. AF 19(628)-4777. Department of Meteorology, University of California.
3. Kuo, H. L., 1965: On the Formation and Intensification of Tropical Cyclones through Latent Heat Release by Cumulus Convection, Journal of Atmospheric Science 22, 40-63.

Acknowledgements

Principal financial support for the work described in this report was obtained from Air Force Cambridge Research Laboratory, Bedford, Massachusetts, during the period November 1964 - November 1966. This work will continue at Monterey with an extension of support from AFCRL. Dr. Carl Krietzberg of AFCRL and Professor Edwin Danielssen of Pennsylvania State University provided considerable encouragement for the continuation of this work.

Partial financial support was also received from E.S.S.A. grant number: Cwb 11210 through Dr. Fred Shuman, National Meteorological Center, and from N.A.S.A. grant number: NsG 237-62 through Professor Gordon MacDonald, Institute of Geophysics at UCLA.

Professor J. Bjerknes of UCLA suggested the various problems discussed in this report to whom we are all greatly indebted.

Mr. John M. Brown, now a graduate student at MIT, was a part of many of our discussions.

Mr. Robert M. Coie, a senior programmer for IBM at Douglas Aircraft Company at Long Beach, California, was a consultant on some of the coding aspects. He provided considerable clarification and efficiency.

Mrs. Sherry Lovell typed the manuscripts for the report.

Computations were performed on the IBM 7094 computer; we are grateful to the Computing Facility of UCLA for their generous support.

Unclassified

Security Classification

DOCUMENT CONTROL DATA - R&D

(Security classification of title, body of abstract and indexing annotation must be entered when the overall report is classified)

1. ORIGINATING ACTIVITY (Corporate author) University of California Department of Meteorology Los Angeles, California		2a. REPORT SECURITY CLASSIFICATION Unclassified
		2b. GROUP
3. REPORT TITLE Diagnostic Studies of Weather Systems of Low and High Latitudes (Rossby Number < 1)		
4. DESCRIPTIVE NOTES (Type of report and inclusive dates) 30 November 1964 - 30 November 1966 Final Scientific Report Approved February 27, 1967		
5. AUTHOR(S) (Last name, first name, initial) Krishnamurti, T. N. Principal Investigator		
6. REPORT DATE April 1967	7a. TOTAL NO. OF PAGES 360	7b. NO. OF REFS 52
8a. CONTRACT OR GRANT NO. AF19(628)-4777	9a. ORIGINATOR'S REPORT NUMBER(S) Final Report	
b. PROJECT NO. 6698-02		
c. TASK 62405394	9b. OTHER REPORT NO(S) (Any other numbers that may be assigned this report)	
d. 681000	AFCRL-67-0128	
10. AVAILABILITY/LIMITATION NOTICES DISTRIBUTION OF THIS DOCUMENT IS UNLIMITED		
11. SUPPLEMENTARY NOTES National Meteorological Center National Aeronautics Space Agency	12. SPONSORING MILITARY ACTIVITY Hq. AFCRL, OAR (CRH) United States Air Force L. G. Hanscom Field, Bedford, Mass. 01730	
13. ABSTRACT A theory of a general balance model for small Rossby numbers, including effects of latent heat, friction and terrain is presented with some applications in high and low latitudes.		

Unclassified

Security Classification